Detection of Energetic Neutral Atoms and its Application to Heliospheric Science

Inauguraldissertation

der Philosophisch-naturwissenschaftlichen Fakultät
der Universität Bern

vorgelegt von

Martin Wieser

von Hasle bei Burgdorf BE

Leiter der Arbeit:

Prof. Dr. Peter Wurz
Physikalisches Institut der Universität Bern

Detection of Energetic Neutral Atoms and its Application to Heliospheric Science

Inauguraldissertation

der Philosophisch-naturwissenschaftlichen Fakultät
der Universität Bern

vorgelegt von

Martin Wieser

von Hasle bei Burgdorf BE

Leiter der Arbeit:

Prof. Dr. Peter Wurz
Physikalisches Institut der Universität Bern

Von der Philosophisch-naturwissenschaftlichen Fakultät angenommen.

Bern, 16. Juni 2005

Der Dekan:
Prof. Dr. P. Messerli

Abstract

The aim of this work was to develop and test highly sensitive imaging low-energy neutral particle mass spectrometers for application in heliospheric science. Two different neutral particle instruments were built, the Neutral Interstellar Composition Experiment (NICE) and the prototype of the IBEX-Lo sensor of the Interstellar Boundary Explorer mission (IBEX), a mission recently selected by NASA for development and flight. To support the development, a material test experiment for the characterization of charge conversion surfaces was improved in sensitivity and completely automated. New computer based methods for the optimization of ion-optical designs were investigated and successfully applied. For the calibration of these and similar neutral particle instruments, existing ion beam calibration facilities were upgraded to provide a beam of low-energy neutral atoms.

Last compilation: 23rd May 2005

Contents

Chapter 1

Introduction

1.1 The Heliosphere

The solar system is immersed in a large cloud of low density gas, the Local Interstellar Medium (LISM) [Wurz 2000, Fahr 2004]. The solar wind moving supersonically at speeds between 300 and 800 km/s creates a cavity in the LISM, the heliosphere. Relative to the LISM, the Sun moves at about 26 km/s. At the outer edge of the solar system, at a distance of 100 to 300 astronomical units (AU) depending on model [Zank & Pauls 1996], the solar wind continually rams into the LISM, creating the 'interstellar interaction'. Three distinct boundaries are shown in Figure 1.1; the termination shock where the solar wind slows down from a supersonic to a subsonic flow, the heliopause which separates the solar wind plasma from the LISM plasma, and possibly a bow shock or bow wave beyond which the LISM flow is unperturbed by the heliosphere. The LISM is partly ionized but the heliospheric cavity is shielded from the inflow of interstellar ions because the solar wind plasma is highly magnetized compared to the LISM.

A fraction of the inflowing neutral interstellar atoms becomes ionized by charge-exchange with ions (Figure 1.2) that pile up at the so-called hydrogen wall [Linsky & Wood 1996]. This pile-up occurs because the interstellar flow is slowed down, heated and deflected around the heliopause. The surviving interstellar neutral atoms [Fahr 2004, Witte et al. 2004, Zank & Pauls 1996, Thomas 1978] and neutral atoms produced by charge exchange in the interaction region [Gruntman et al. 2001] enter the the heliosphere. At solar distances of a few astronomical units, they become partly ionized by solar ultraviolet radiation or by charge-exchange with the solar wind. These newly created pickup ions gyrate about the interplanetary magnetic field that is frozen into the solar wind and are swept outward from the Sun. Acceleration at the termination shock [Pesses et al. 1981] transforms pickup ions into anomalous cosmic rays (ACR) with energies of 10–100 MeV per nucleon. The other part of the neutral atom population with energies between a few eV to a few keV per atom, can be detected from as close as 1 AU to the Sun as energetic neutral atoms (ENAs), e.g. from an observer in Earth's orbit or on an interplanetary trajectory in the inner solar system [McComas et al. 2004, Barabash

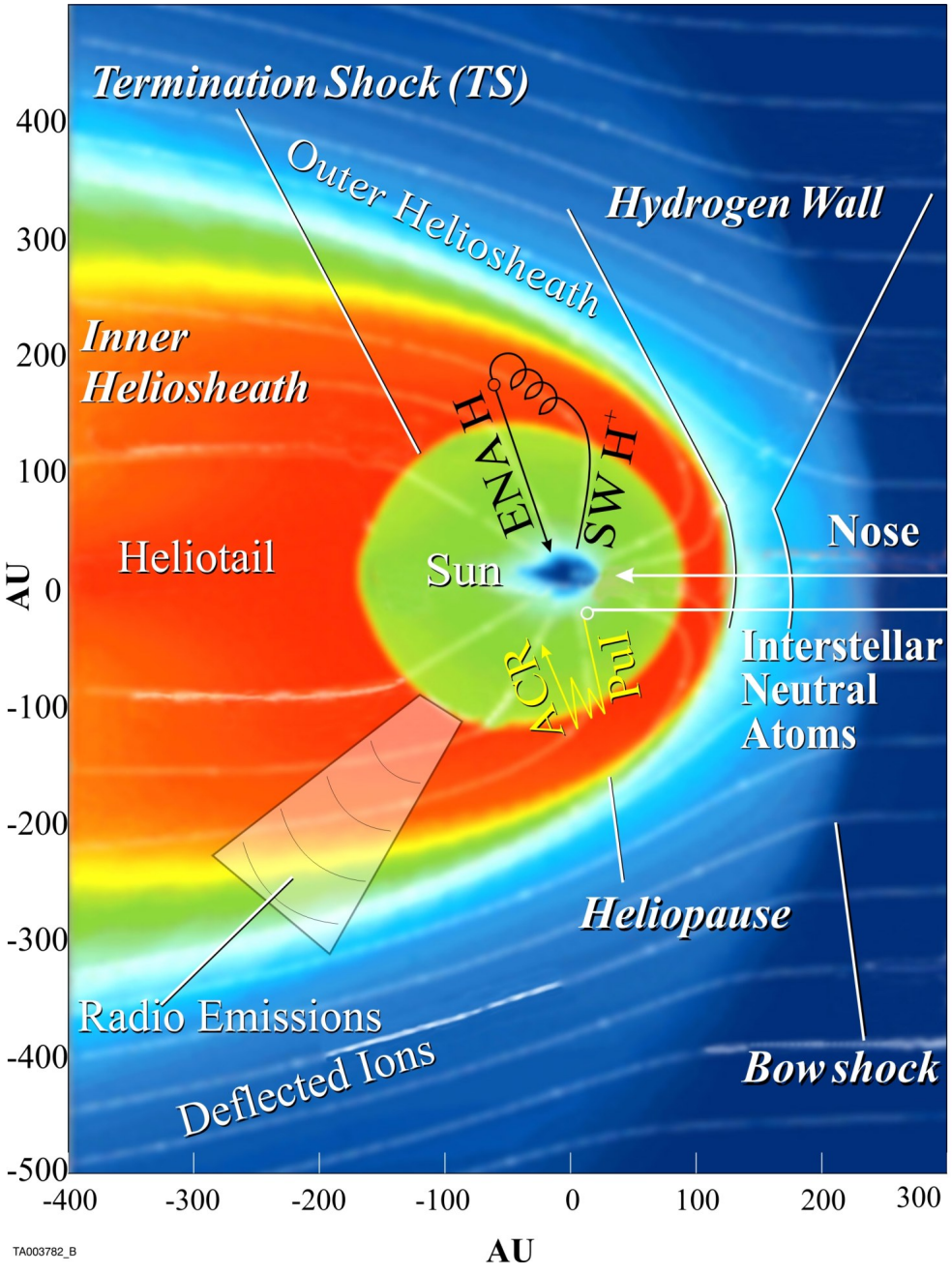

Figure 1.1: The heliosphere. The sun moves to the right at about 26 km/s. Interstellar neutral atoms enter the heliosphere whereas ions get deflected. Neutrals visible from Earth orbit are also produced by charge exchange in the inner heliosheath from solar wind protons, pickup protons, and energetic protons, providing a global image of the interaction region. *Image: IBEX proposal [McComas et al. 2003].*

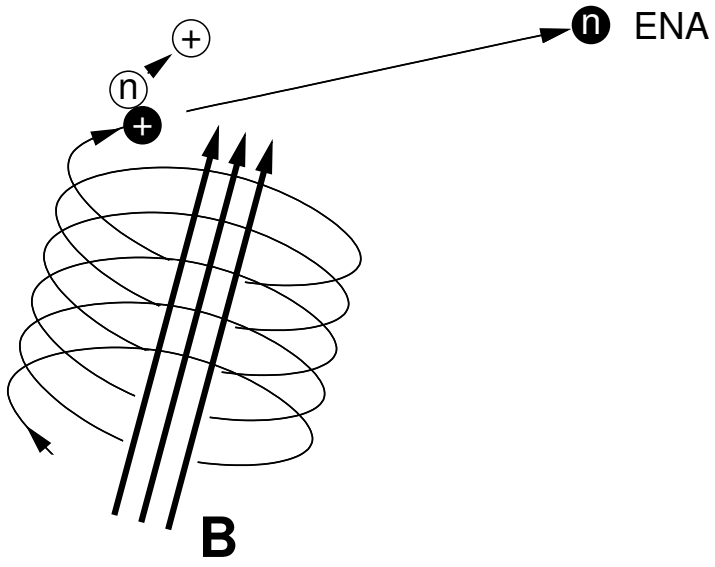

Figure 1.2: Charge exchange process. A fast ion (black, +) bound to the magnetic field **B** hits a neutral atom (white, n). The charge is exchanged between the two reaction partners but their respective velocity vectors at the time of interaction are preserved. The neutralized atom (black, n) is no longer bound to magnetic fields an travels away as energetic neutral atom (ENA) on a ballistic trajectory whereas the newly created ion (white, +) may be accelerated and starting to gyrate around the magnetic field lines.

et al. 2004, Moore et al. 2000]. It is possible therefore to infer the properties of the neutral interstellar gas and the interstellar interaction region by measuring the properties of these ENAs. Such observations of the inflow of neutral helium were done by the neutral interstellar gas instrument (GAS) on the ULYSSES spacecraft [Witte et al. 1992]. However, only limited data are available for other important species such as hydrogen or oxygen.

1.2 Neutral Particle Imaging

Detection of low-energy neutral atoms is much more complicated than detecting ions. Available particle detectors, e.g. micro channel plates (MCP) or solid state detectors (SSD), exhibit an energy threshold below which the detection efficiency drops very quickly to very small values. Furthermore, neutral particles are not subject to electric fields, thus standard ion optical elements such as focusing or energy analyzing elements can not be used directly. In a low-energy neutral particle instrument the neutrals would first need to be ionized and then analyzed using conventional mass spectrometry used in space research. Surface ionization has been identified as the only viable ionization technique to meet the requirements concerning ionization efficiency for the energy range of 10 eV to 1 keV within the limitations imposed by the resources (space, weight, power, etc.) available on a spacecraft [Wurz et al. 1993, Ghielmetti et al. 1994, Wurz et al. 1995, Moore et al. 2000]. A neutral particle hitting a suitable surface at grazing incidence will undergo charge exchange with this surface and emerge with

a certain probability, depending on surface material and species, as negatively or positively charged ion. These ions are then collected, accelerated, and their energy and mass analyzed using conventional ion optical means. For optimal performance, the conversion surfaces used should exhibit a large ionization yield combined with mirror-like reflection properties (i.e., be flat on an atomic scale), be chemically stable, and should not require special treatments as reconditioning or heating [Scheer et al. 2005, Wieser et al. 2002, Jans et al. 2001, Wurz et al. 1997]. If, in addition to the detection the neutral atom, also the direction where it came from is registered, two dimensional maps or images of the ENA flow can be recorded. ENA imaging has made it possible to remotely image space plasmas [Moore et al. 2000, Barabash et al. 2004] and will now be used to image the interstellar interactions and interstellar boundaries at the edge of the heliosphere [McComas et al. 2004].

1.3 Outline of the Work Presented in this Document

In this document work done for the development of low-energy neutral particle mass spectrometers is presented. The document is divided into three parts: in the first part, a laboratory experiment used for the characterization of charge conversion surfaces and support equipment for the calibration of neutral particle instruments is described in detail. The second part is committed to fast methods of ion-optical design. A new method is presented that allows the reduction of development time from year(s) to weeks using computer-based numerical optimization. In the third part, two different neutral particle instruments are presented: the Neutral Interstellar Composition Experiment (NICE) prototype and the prototype of the IBEX-Lo sensor of the Interstellar Boundary Explorer (IBEX) mission [McComas et al. 2004], recently selected by NASA for development and flight.

Part I

Laboratory Experiments

Chapter 2

Imager for Low Energy Neutral Atoms ILENA

2.1 Introduction

The Imager for Low Energy Neutral Atoms laboratory experiment (ILENA) [Schletti 1996, Jans 1999, Wieser 2001, Jans et al. 2001] was built to study the interaction of ions with charge conversion surfaces. The experiment allows the measurement of angular scattering properties and the negative ion and secondary electron yields of small sample surfaces for incident single positivly charged ions at energies from a few tens of eV up to 1500 eV per charge. Samples from 4 mm×4 mm to as large as 60 mm×25 mm have been investigated.

Figure 2.1 is a schematic drawing of the ILENA experiment. ILENA consists of an ion source, a sector magnet, a beam guiding and modulation system, a surface sample stage with housing and a detection unit. All these units are contained in a single vacuum chamber pumped by both turbo-molecular and ion-getter pumps.

Positive ions are produced in a Nier-type ion source [Nier 1940] and accelerated to energies between a few tens of eV and 1500 eV per charge. Ions are mass analyzed in a sector magnet with a mass resolution of $\frac{m}{\Delta m} \geq 45$. The ion beam then enters a focusing, deflection, and intensity modulation unit consisting of an Einzel lens and three pairs of steering plates. The ion beam intensity may be modulated by applying a sinusoidal voltage to one of the beam steering plates. At the exit of the unit, the beam diameter is limited to 1 mm diameter by an aperture.

The impact angle of the ion beam on the surface under investigation can be varied between 90° and 0° with respect to the surface normal. Scattered particles are recorded with a two-dimensional position-sensitive micro channel plate (MCP) detector with a viewing angle of ±12.5° in both azimuthal and polar directions (Quantar Technology Inc, CA, USA, model 3395A-SE/2401B). A retarding potential analyzer (RPA) consisting of four grids is mounted

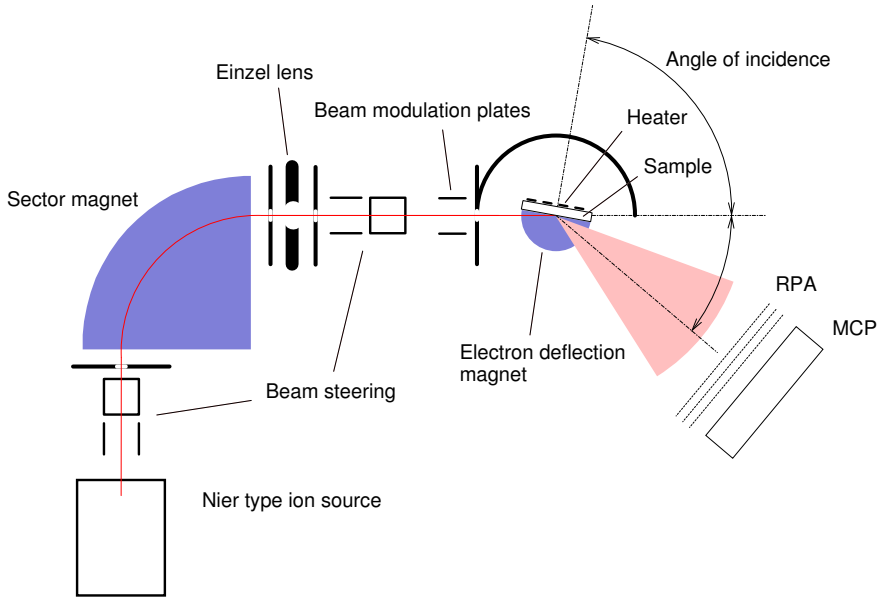

Figure 2.1: ILENA experiment

in front of the MCP detector. The inner two grids of the RPA, are used to prevent positive and/or negative ions from reaching the MCP. An additional grid in front of the MCP detector at negative potential with respect to the MCP front face hinders low energy electrons from reaching the detector - efficiently reducing the background signal measured with the MCP. The detector unit, including the RPA, is shielded electrostatically from the rest of the vacuum chamber.

The electrical current on the sample surface from the ion beam is measured either statically for a non modulated beam down to a limit of 0.1 pA using a pico-ampere meter (model Keithley 6517A) or using a modulated beam and a lock-in amplifier (model Perkin Elmer 7265) combined with a transimpedance preamplifier (model Femto LCA-30-1T) down to a limit of 0.3 fA. A heater attached to the sample holder unit allows the sample surface to be electrically heated up to 150°C. A variable magnetic field parallel to the sample surface and normal to the incident ion beam of ± 3 mT is used to prevent secondary electrons from escaping from the surface, allowing the measurement of the secondary electron yield at low primary ion energies where electrically biasing the sample would disturb the ion trajectories (see [Wieser et al. 2005] reprinted in Chapter 2.4).

A control computer is used to set high voltages and the magnetic field in the sector magnet and the electron suppression magnet. It also interfaces most instruments attached to the setup and allows completely automated measurements over longer time periods.

After baking out the vacuum chamber a residual gas pressure of $4 \cdot 10^{-8}$ mbar is achieved. During operation the pressure may rise into the low 10^{-7} mbar range as a result of the test gas leaking into the ion source chamber.

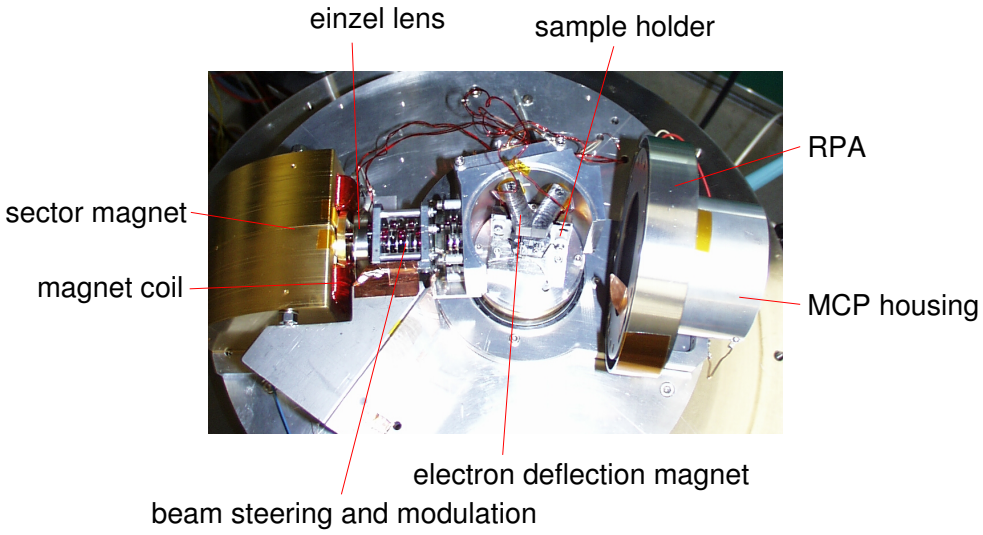

Figure 2.2: Top view of the experiment platform of the ILENA experiment. The diameter of the circular experiment platform is about 38 cm.

Figure 2.2 shows a top view of the experiment platform inside the vacuum chamber. Except for the ion source, which is located under the sector magnet, all main units inside the vacuum chamber are visible in this photograph.

Several features described above were newly added to the experiment during this thesis. The design and performance of these features is described in the following sections of this chapter.

2.2 Mass Resolution

2.2.1 Motivation and Design

Species selection of the ion beam in ILENA was originally done by selecting a suitable test gas to leak into the ionization region of the ion source. This allowed the generation of positive noble gas ions and molecular ions of hydrogen, nitrogen, and oxygen. No mass selection was available because an electrostatic analyzer was originally mounted in place of the sector magnet. Atomic hydrogen or oxygen was present as a minor component in the ion beam when generating molecular ions but could not be separated.

During this work, a sector magnet was built to get access to species such as H^+, D^+, C^+, N^+, and O^+, which are only produced at the percent level in the ion source compared to dominant molecular ions. The 90° sector magnet replaced the previously installed 90° electrostatic analyzer. Both magnet and the coil were placed entirely in vacuum, which is an unusual and technically difficult arrangement. This was an engineering challenge because of the heat

dissipated by the coil and the restricted selection of materials which can be used in ultra-high vacuum. However, having an external magnet was not an option.

Design drivers for the sector magnet were desired a mass resolution of $\frac{m}{\Delta m} > 40$, the capability to handle Argon ions up to 1000 eV per charge at a given bending radius $r = 92.4$ mm, and a beam diameter of <2 mm.

The maximum magnetic field B_{max} required is given by

$$B_{max} = \frac{1}{R}\sqrt{2 \cdot U \cdot \frac{m}{q}} \tag{2.1}$$

For $m = 40$ amu, singly charged particles, and $U = 1000$ V, B_{max} evaluates to 312 mT.

For an electro-magnet with an iron core the magnetic resistivity R_M is defined by

$$R_M = \frac{\Theta}{\Phi} = \frac{l}{\mu_0 \mu_r A} \tag{2.2}$$

where Φ is the total magnetic flux, Θ the magnetomotive force, μ_0 the permeability of vacuum, μ_r the relative permeability of the material, A the cross section of the iron core, and l the length of the medium.

For a magnet with a small gap with a moderate and approximately homogeneous field in the gap, the total magnetic resistivity may be written as the sum of the resistivity of the iron core and the resistivity of the gap:

$$R_M = R_{M\,gap} + R_{M\,core} \tag{2.3}$$

expressed in material properties and geometric variables this yields:

$$R_M = \frac{d_{gap}}{\mu_0 A_{gap}} + \frac{l_{core}}{\mu_0 \mu_r A_{core}} \tag{2.4}$$

where d_{gap} denotes the width of the gap, A_{gap} its effective cross section, l_{core} the effective length of the core, and A_{core} cross section of the core. With a $d_{gap} = 2.5$ mm and $l_{core} \approx 200$ mm and approximately equal values for A_{gap} and A_{core}, the second term in Equation 2.4 may be neglected as long as

$$\mu_r \gg \frac{l_{core}}{d_{gap}} \tag{2.5}$$

i.e., $\mu_r \gg 80$. Simplifying Equation 2.4 and using

$$\Phi = BA \tag{2.6}$$

the magneto motive force Θ required is approximated by

$$\Theta = B_{max} A_{gap} R_{M\,gap} \tag{2.7}$$
$$= B_{max} \frac{d_{gap}}{\mu_0} \tag{2.8}$$

With the mechanical dimensions of the magnet (Figure 2.4) a magnetomotive force Θ = 620A was calculated.

The magnetic core was split in two halves, each one containing one half of the coil, placed on each side of gap. The power dissipated by the coil is given by

$$P_{max} = I^2 R = \Theta^2 \frac{l_{coil}\,\rho}{A_{coil}\,\eta} \tag{2.9}$$

where I is the current in the wire, R the electrical resistance of the coil, l_{coil} the length of one turn of the coil, A_{coil} the available cross section for wires, η the copper fill factor, and ρ the specific resistance of copper ($\rho = 1.78 \cdot 10^{-8}\Omega$m). Note that the power dissipated does not depend on the thickness of the wire used to fill the available cross section.

Due to geometric constraints a total cross section A_{coil} of $2 \times 21\,\text{mm} \times 9\,\text{mm}$ was available. With a fill factor η of 0.7 and an average wire length for one turn of the coil $l_{coil} = 300\,\text{mm}$, a total power dissipation P_{max} of 7.8 W is obtained. The diameter of the wire for the coils was chosen such that the number of turns remained reasonably small and that the maximum current in the wire was of the order of 1 A. Standard enamel insulated copper wire with $0.5\,\text{mm}^2$ copper cross section results in 528 turns, split in two halves of 264 turns each, at a maximum coil current of 1.2 A. The power dissipated in the coils heat the coils considerably. Due to good thermal coupling, heat is conducted to the magnetic core. Thermal conductivity from the magnetic core to the surrounding structure is very small and therefore the temperature of the magnetic core is monitored. If the coils get too hot, increased outgassing occurs and the pressure in the chamber rises to unacceptable levels. The coil current would need to be reduced in this case until the temperature of the magnetic core drops below a experimentally determined threshold and the vacuum is restored.

For a mono energetic beam, the mass resolution for the 90° sector magnet system is approximately given by

$$\frac{m}{\Delta m} = \frac{r}{2 \cdot s_0} \tag{2.10}$$

with r the radius of a nominal particle trajectory, and s_0 the diameter of the object image. With the geometry given in the ILENA experiment, where $s_0 \approx 1\,\text{mm}$ and $r = 92.4\,\text{mm}$, a mass resolution of $\frac{m}{\Delta m} \approx 46$ should be obtained.

At both ends of the magnetic sector field termination plates (Herzog plates) were added to reduce loss in intensity due to beam defocusing. These plates also serve as a collimator to define mass resolution. The Herzog plates were designed according to diagramms given in [Benninghoven et al. 1987]. A drawing of the magnet is shown in Figure 2.3.

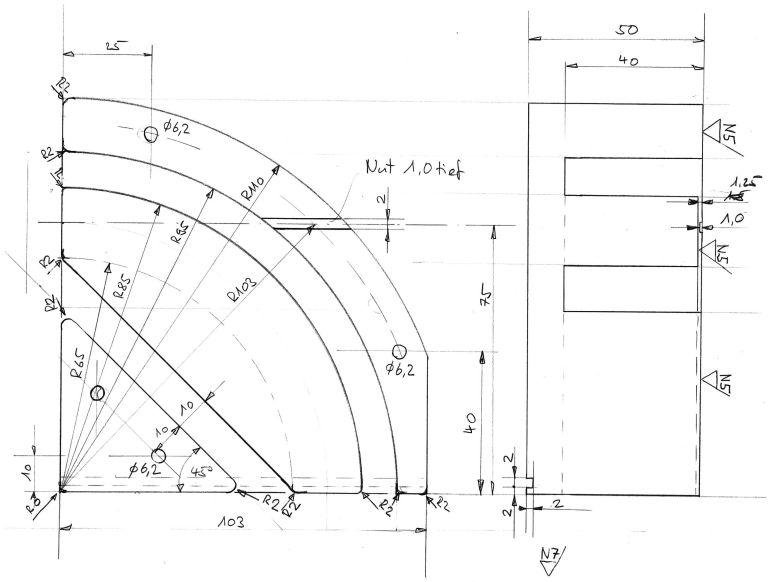

Figure 2.3: Drawing of one half of the ILENA sector magnet core. The other half is mirror-inverted to the part shown. The coil is put into the D-shaped channel. A small horizontal channel along the exiting beam axis is used to align the ion optics between the magnet and the sample surface using a laser pointer.

2.2.2 Manufacturing

Armco Ingot Iron was chosen as the material for the magnetic core. It is high purity iron with excellent magnetic properties. The supplier data sheet specifies a maximum of the magnetic permeability μ_r of 3500 to 6000 after tempering for a lower magnetizing force of about 100 A/m, dropping to about 600 at 2 kA/m. Prior to tempering, this material is easily processed by milling or other cutting techniques. All parts made of Armco Ignot Iron were tempered in house for 100 minutes at 925°C while exposed to a H_2/N_2 atmosphere to maximize the permeability.

Figure 2.4 shows one half of the sector magnet mounted in the ILENA experiment. The magnet core was gold plated to avoid surface charging in vacuum, and oxidation when venting the chamber.

Construction of the coils was rather complicated. The odd coil shape prevented the use of a coil making machine and the coil had to be made by hand on a lathe. Originally, the coil was planed to be completely moulded into a block to minimize the exposed surface of the wires. However, it was not possible to get rid of all air bubbles trapped inside the potting compound resulting in a poor vacuum as every now and then an air bubble burst when pumping down the chamber. Eventually, a coil without any potting compound was built and fitted directly into the magnetic core.

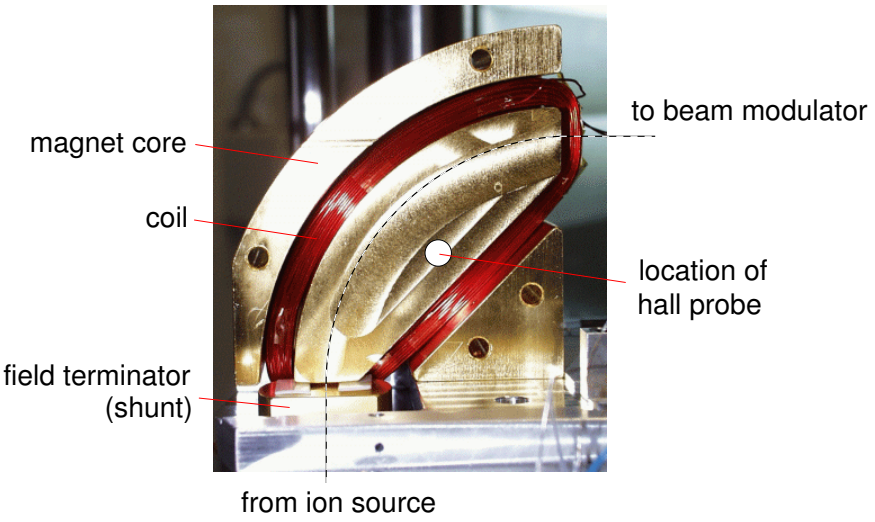

Figure 2.4: ILENA sector magnet with one half of the magnet yoke removed. The nominal ion path is shown as dashed line. Magnetic field terminator plates are placed at both ends of the sector (only the entrance plate is visible, the exit plate was removed).

2.2.3 Magnetic Field Control Loop

To get an accurate magnetic field measurement, a Hall probe was mounted within the magnetic gap as shown in Figure 2.4.

A computer controlled feedback loop allows the desired magnetic field strength in the magnet to be directly set independent of hysteresis effects. The current through the coil is adjusted automatically using the measured magnetic field from the Hall probe. Figure 2.5 depicts the control loop in detail: A computer controls an unipolar power supply, a current polarity reversing relay, a digital to analog converter (DAC) with 12 bit resolution, a range selecting unit, and a LakeShore 460 gaussmeter. To apply current to the coil, the control voltage U_c' needed for the current controlled power supply is calculated. Prior sending data to the DAC, the range select logic is set to the smallest range possible. This allows the smallest possible control voltage step to be decreased for small control voltage values, effectively increasing the DAC resolution. Then the polarity relay and the DAC voltage U_c are programmed and the control voltage is applied to the power supply. The resulting magnetic field is measured using a Hall probe and the control voltage U_c' is adjusted accordingly.

Three different field control modes are implemented to set a magnetic field value:

a) *Closed loop absolute* mode is used to set a field value far away from the current value. In this mode, a previously measured virgin curve of the magnetization (Figure 2.6) is used to get a first approximation of the current I_0 needed in the coil. After setting the initial coil current value and waiting for the settling time, the magnetic field B_0 is measured and the difference ΔB_0 from the nominal field value B calculated. A delta current value ΔI_0 is estimated using the slope of the virgin curve of the magnetization at the point of the measured magnetization

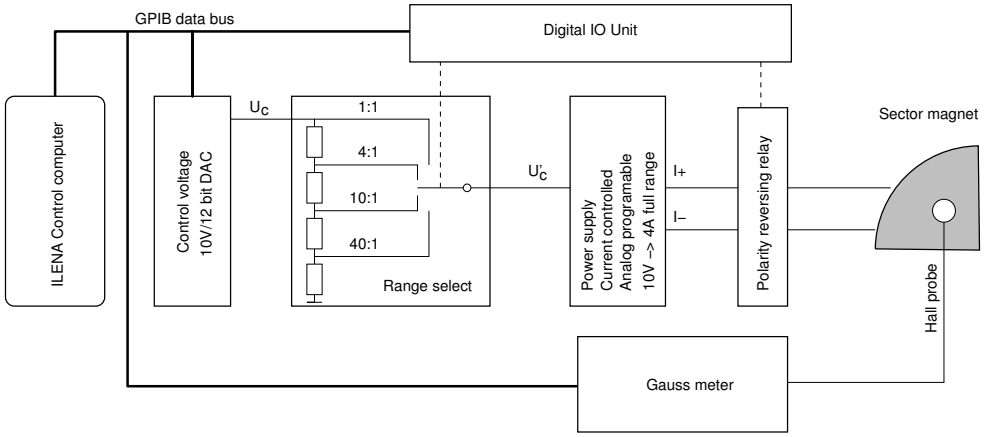

Figure 2.5: Magnetic field control loop

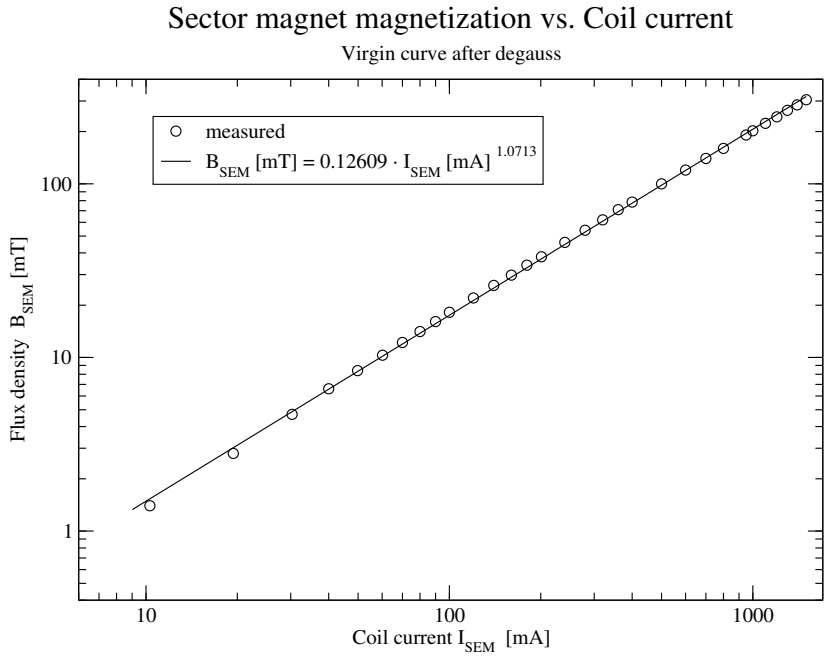

Figure 2.6: Sector magnet field versus coil current. The virgin curve of magnetization is shown. Both coils were connected in series for this measurement. The solid line is an empirical fit to the measured points used in the software to get a first guess of the coil current needed for a certain magnetic field strength.

B_0. The delta current is added to the current already set for the coil, i.e., $I_{n+1} = I_n + \Delta I_n$. After waiting for the settling time, a new field value B_{n+1} is measured and a difference ΔB_{n+1} to the nominal field value B is calculated. The process repeats until ΔB is smaller than 0.03 mT, $\frac{\Delta B_n}{B_n} < 0.003$, or the required current step ΔI is below the resolution of the DAC.

b) *Closed loop incremental* mode is used if both the change in the magnetic field and the estimated change in the coil current are small (ΔB<6 mT and ΔI_0<100 mA). It works similarly to the closed loop absolute mode except that no initial current value is calculated using the virgin curve, but the currently set coil current and magnetic field values are taken as initial conditions for the $\Delta B - \Delta I$ iteration. Both closed loop modes allow the setting of a desired magnetic field value with typically less than 10 iteration steps in less than 4 seconds independent of the previously set values.

c) *Open loop incremental* mode is used for measurements requiring scanning the magnetic field over a predefined range from B_{start} to B_{stop}. In open loop incremental mode, the initial magnetic field value B_{start} is set using closed loop absolute or closed loop incremental mode depending on how different the desired initial magnetic field is from the current magnetic field, resulting in a coil current I_{start}. The coil current is then incremented (or decremented, depending on scan direction) repetitively by a constant small value and the resulting magnetic field measured without any corrections to the coil current step size. Incrementing (or decrementing) stops as soon the measured magnetic field reaches the value of B_{stop}. Both source mass spectra shown in Figure 2.7 and 2.8 were measured using this mode.

The selection of the control mode is done automatically by the program running on ILENA control computer.

2.2.4 Performance

Typical spectra obtained by scanning the available mass range are shown in Figures 2.7 and 2.8. In Figure 2.7 the beam intensity was measured using the lock-in amplifier setup described in detail in Section 2.4. For the spectrum shown in Figure 2.8 the test gas assembly was modified to allow for liquid test substances. The liquid, e.g. heavy water, is poured into a glass flask attached to the test gas feeding system, then the pressure in the feeding system is reduced using a rouging pump until the liquid boils and a large fraction of the gas pressure is due to vapor. This vapor is leaked into the ion source like an ordinary test gas. Heating of the test gas pipes is needed to get rid of the water when changing back to gaseous test species.

The mass resolution of the magnetic sector estimated from data shown in Figures 2.7 and 2.8 is $\frac{m}{\Delta m} \approx 45$ with excellent agreement with calculations presented in Section 2.2.1. Thermal constraints limit the use of the high mass range above 30 amu for ion energies of more than 1000 eV per charge. Data shown in Figure 2.6 also suggests a slight under-performance of the system as a coil current of 1.2 A only results in a field of 255 mT instead of the 312 mT predicted. The reason for this difference is that the condition in Equation 2.5 is not well satisfied for high flux density values where the permeability μ_r of the core material drops to about 600 compared to several thousand at lower flux densities. The nominal value of B_{max}

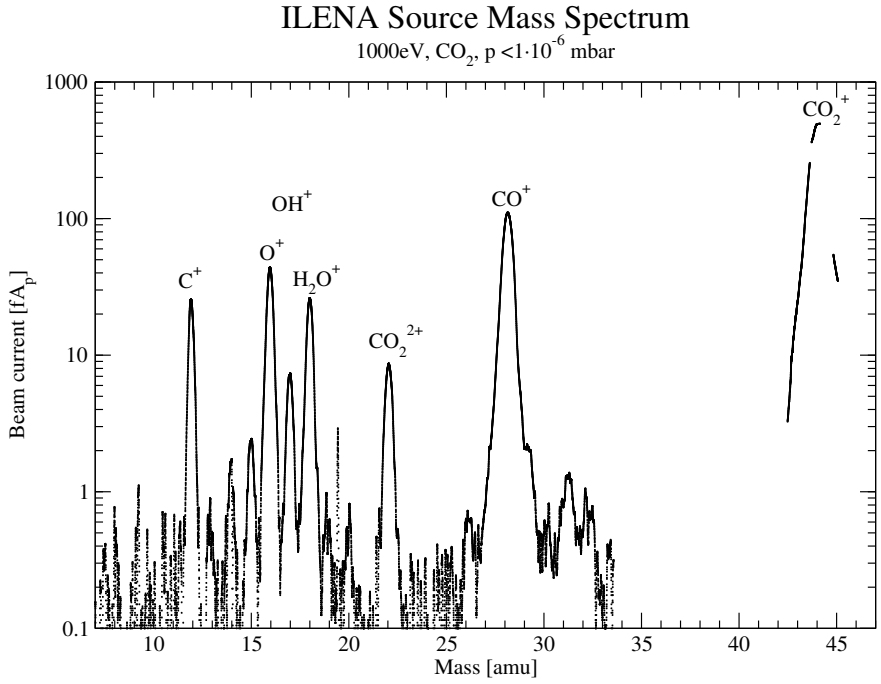

Figure 2.7: Mass spectrum of ILENA ion source. CO_2 was leaked into the ion source and the beam energy set to 1000 eV per charge. The beam intensity was measured using the lock-in amplifier setup described in detail in Chapter 2.4. Note the gaps in the dataset above 34 amu where the magnet coil temperature got too high and measurements had to be interrupted as degassing resulted in a degraded vacuum.

is obtained by increasing the maximum coil current to 1.5 A at the cost of a higher power dissipation. As the main interest is in the low mass, low energy domain this is not a problem.

2.3 Measurement of Ultra Low Ion Beam Currents

2.3.1 Motivation

Measurements of ion beam currents towards ground potential are an essential diagnostic tool in the ILENA experiment. Also, an important aspect of the ILENA experiment are absolute (i.e. quantitative) measurements of scattering and ionization efficiencies. This requires a calibrated MCP detector with known detection efficiencies. In order to directly measure MCP efficiencies, especially at lower ion energies, beam currents of about 1 fA need to be measured. Originally, DC currents were measured down to a lower limit of 0.2 pA. The limit was set by noise picked up from the environment (e.g. the nearby railway lines) and the level of acoustic vibrations (e.g. from turbo pumps). Careful electrical shielding and an improved ground grid in the experiment allowed the reduction of limit to 0.1 pA. Further reduction was

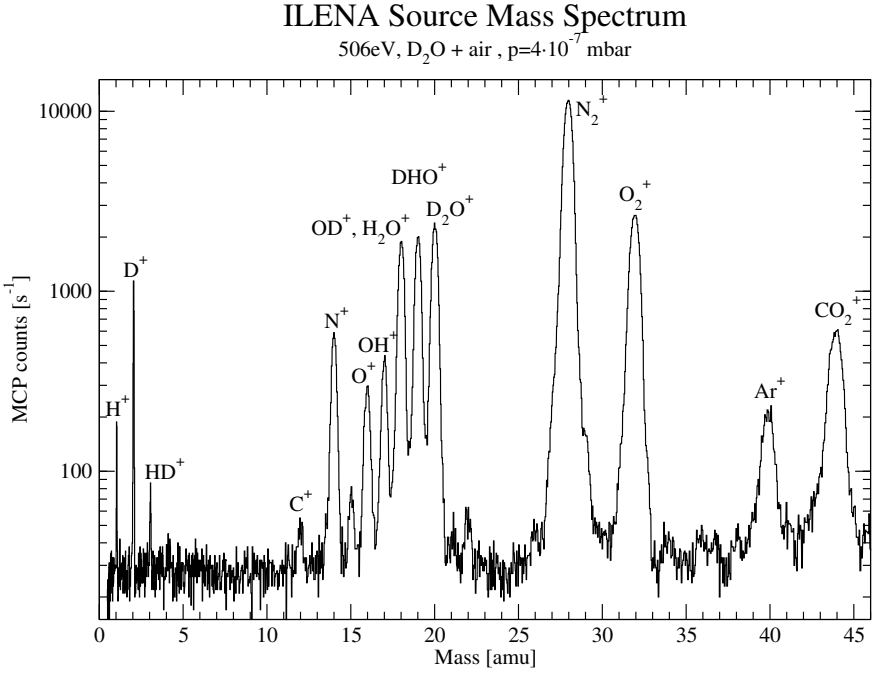

Figure 2.8: Mass spectrum of ILENA ion source measured by directing the ion beam directly onto the MCP detector. A mixture of air and heavy water vapor D_2O was leaked into the ion source. The peak at m=2 consists almost entirely of deuterium and not H_2 as verified by leaking normal distilled water vapor H_2O into the source.

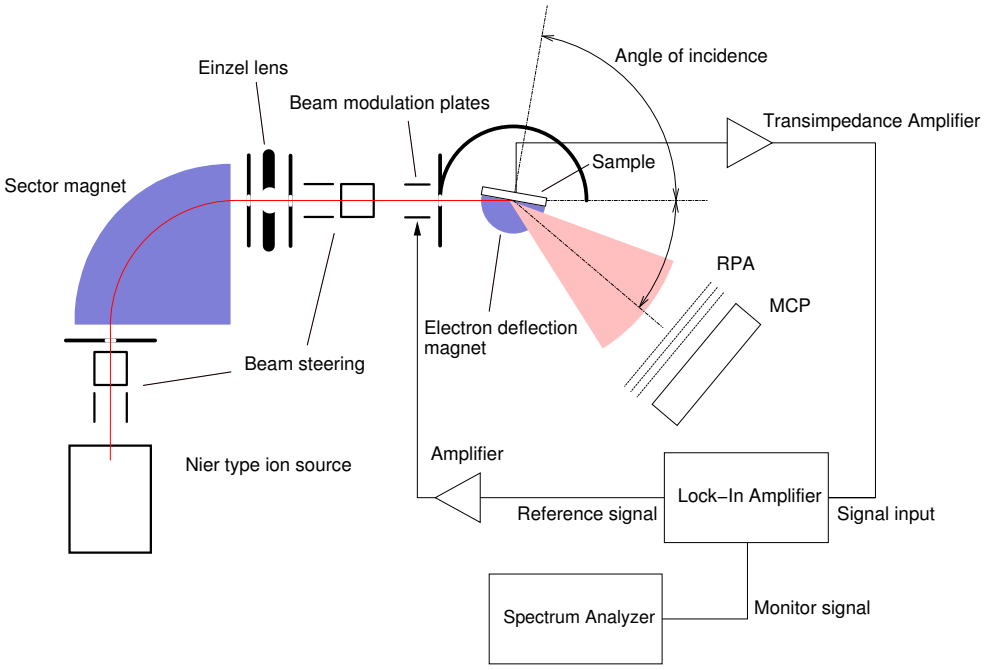

Figure 2.9: ILENA setup including the lock-in amplifier

only possible by switching from a DC to an AC current measurement using a lock-in amplifier. Combined with a transimpedance (current to voltage) preamplifier and improved noise suppression, sub-femto Ampére resolution is demonstrated below.

2.3.2 Implementation

A lock-in amplifier (Perkin Elmer 7265) was installed in the system as shown in Figure 2.9. For diagnostics, the monitor signal measured in front of the analog digital converter (ADC) of the lock-in amplifier was fed into a spectrum analyzer to identify all sources of noise or out of band signals. Figure 2.10 depicts an early background spectrum. A clear signature of 50 Hz line frequency including harmonics up to 1 kHz was identified. Although the line frequency and its harmonics are far off the reference frequency used by the lock-in amplifier of a few Hz, the line noise saturated the preamplifiers of the lock-in amplifier reducing the available dynamic range for the signal. The roughing pump was identified as main source of line noise. Furthermore, a clear signature of the turbo pump used in the system running at 1000 Hz was visible. To eliminate these signals, an ion getter pump was installed. The discharge in the ion getter pump also produces noise, but its spectral density is much lower and the preamplifiers are not saturated that easily.

A problem introduced by the ion getter pump was a particle shower (most likely electrons) injected into the chamber by the pump - severely affecting measurements made using the MCP detector. Up to several thousand background counts per second were detected compared

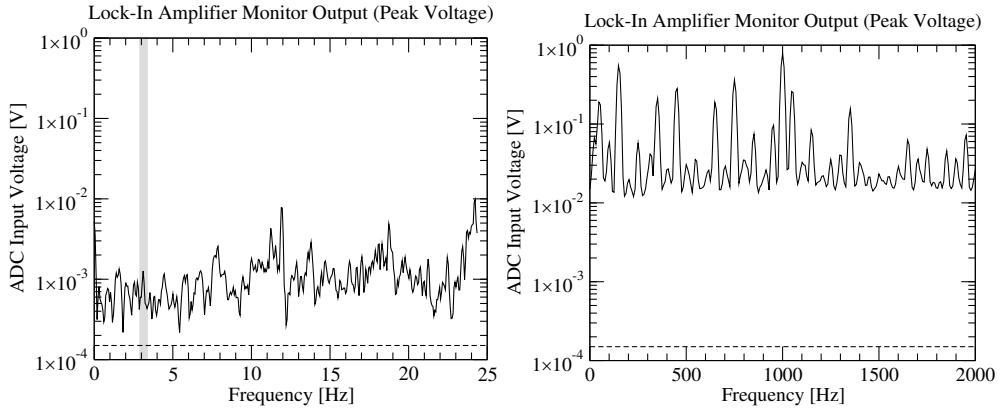

Figure 2.10: Signal spectrum at the input of the analog digital converter (ADC) of the lock-in amplifier for two different frequency ranges. The maximum range of the ADC is ± 10 V. A signal level equivalent to 1 fA is shown as dashed line. The signal frequency of 3.14 Hz is indicated as grey bar in the left figure. Although the spectrum up to 25 Hz looks clean (left panel) , line frequency harmonics and the signature of the turbo pump at 1000 Hz (right panel) saturate the preamplifiers putting the signal at 3.14 Hz outside of the dynamic range of the ADC as the signal to noise ratio for a 1 fA signal at 3.14 Hz is -78 dB.

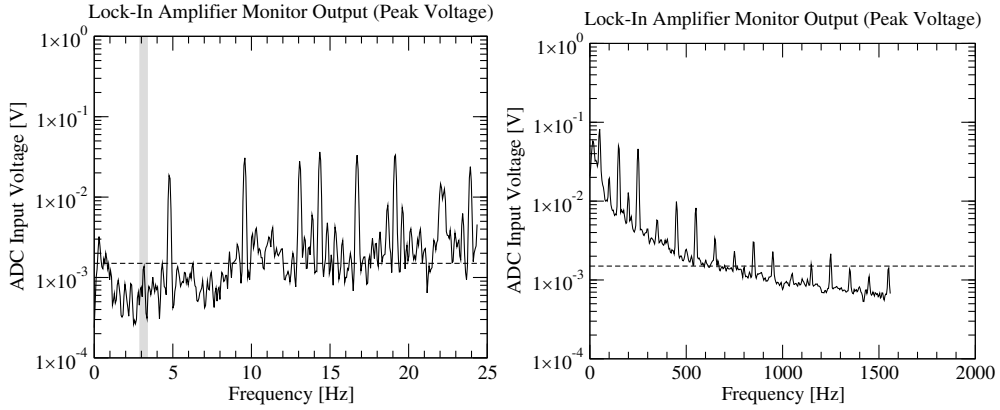

Figure 2.11: Signal spectrum at the input of the analog digital converter (ADC) of the lock-in amplifier for two different frequency ranges after the turbo pump was replaced by an ion getter pump. A signal level equivalent to 1 fA is shown as a dashed line. Compared to Figure 2.10, the preamplifier gain could be increased without running into saturation. The signal frequency of 3.14 Hz is indicated as grey bar in the left figure. Several new features are visible below 25 Hz, but none of them is more than two orders of magnitude larger than the 1 fA signal. At higher frequencies, the fundamental, and the 3^{rd} and 5^{th} harmonics of the 50 Hz line frequency dominate but the peak levels are also within two orders of magnitude of the 1 fA signal level. The signal to noise ratio for a 1 fA signal is -40 dB and thus within the range of the ADC.

to at most 10 when using the turbo pump. Given the available space, suppressing grids placed at high voltage were not a viable solution to get rid of these particles. A set of baffles was installed instead, now requiring several reflections of a particle to get from the pump opening to the MCP detector. However, this had a negative influence on the pumping power of the system.

A further reduction in noise was obtained by lifting the whole experiment a few millimeters onto four air filled shock absorbers - eliminating most structure-borne vibrations from the floor. A copper plate placed underneath the experiment further improved the available local electrical ground reference. The experiment was tied down electrically at all four edges to this plate much reducing the sensitivity of the current measurements to moving objects close to the experiment, e.g. people walking around.

Combined, a considerable reduction in background signal level was obtained placing the 1 fA signal level within the dynamic range of the ADC of the lock-in amplifier. Figure 2.11 depicts a background noise spectrum measured with only the ion getter pump turned on, an improved electrical grounding scheme and mechanical vibration damping installed.

At very low current levels capacitive coupling between beam modulation plates and signal pickup lines becomes an issue. The capacitive reactance X_c needed to couple a current i_c from the beam modulation plates at a voltage of amplitude u_{mod} with a frequency f is given by

$$X_c = \frac{u_{mod}}{i_c} = \frac{1}{2\pi f C}$$

where C is the coupling capacity. For a typical amplitude of $u_{mod} = 1\,\mathrm{V}$ and a modulation frequency of $f = 3.14\,\mathrm{Hz}$, a coupling capacity C of only $5 \cdot 10^{-5}\,\mathrm{pF}$ is needed to couple a current i_c of 1 fA. For comparison, the capacity of two 0.5 mm diameter wires of 10 cm length at a distance of 30 cm is about 0.4 pF.

Very thorough electrical shielding between the sample surface and the beam modulation plates is necessary is keep the value of the coupling capacity low. Fortunately, as long as the capacitively coupled current does not saturate the preamplifiers, is separated from the active current by its phase shift of 90°. An example of the capacitively coupled current versus the active current is shown in Figure 2 of the publication in Chapter 2.4.

Table 2.1 summarizes the sensitivity improvements obtained by the different modifications of the setup. Note that a current amplitude of 1 fA corresponds to 6240 elementary charges per second, a rate that is well within the dynamic range of the MCP detector used.

2.3.3 Applications

The capability to lock onto currents as low as 0.3 fA enables new measurement opportunities. In Chapter 2.4, measurements of the secondary electron yield of a surface are presented using currents in the fA range. Currents in the fA range also allow the direct comparison of current

Setup	lowest measurable current	out of band signal (noise)	signal power to out of band power ratio	signal to noise factor (currents)
DC current measurement	**0.2 pA**$_{DC}$	0.1 pA$_{DC}$	6 dB	2
DC current measurement with improved ground mesh	**0.1 pA**$_{DC}$	0.05 pA$_{DC}$	6 dB	2
Initial AC current measurement Data from Figure 2.10.	$\sim$**30 fA**$_{AC}$	$\sim$ 3 pA$_{AC}$	~ -40 dB	$\sim$ 0.01
Turbo pump replaced by ion getter pump	10 fA$_{AC}$	$\sim$ 1 pA$_{AC}$	~ -40 dB	$\sim$ 0.01
Improved electrical ground mesh	1 fA$_{AC}$	$\sim$ 300 fA$_{AC}$	~ -50 dB	$\sim$ 0.003
Mechanical vibration damping and electrical ground plane	0.3 fA$_{AC}$	100 fA$_{AC}$	-50 dB	0.003
Best AC current measurement Data from Figure 2.11.	**0.3 fA**$_{AC}$	100 fA$_{AC}$	-50 dB	0.003

Table 2.1: Summary of sensitivities depending on experiment configuration.

measurements with count rates obtained from the MCP detector. A method to use this to get absolute detection efficiencies of an MCP is presented in Chapter 2.5. As shown in Chapter 2.6, the method can also be applied to reflection efficiency measurements of sample surfaces [Schletti 1996, Jans 1999, Wieser 2001] where the fraction of particles reflected onto the open MCP area is compared with the total number of particles hitting the sample surface - eliminating the previously needed step of linear interpolation between the measurement of the beam current in the pA range and the recording of the angular scattering image by the MCP using a beam current in the fA range.

2.4 Paper: Secondary electron emission of chemical vapor deposited diamond by impact of slow H^+, D^+, H_2^+, C^+, O^+, and O_2^+ ions

M. Wieser, P. Wurz, R.J. Nemanich, and S. A. Fuselier

(Submitted February 2005 to Applied Physics)

Secondary electron emission of chemical vapor deposited diamond by impact of slow H^+, D^+, H_2^+, C^+, O^+, and O_2^+ ions

M. Wieser[a)], P. Wurz[a)], R.J. Nemanich[b)], and S. A. Fuselier[c)]

[a)] *Physikalisches Institut, University of Bern,*

Sidlerstrasse 5, CH-3012 Bern, Switzerland,

Fax: +41 31 631 44 05, Email: wieser@phim.unibe.ch

[b)] *North Carolina State University, Department of Physics,*

408A Cox, Box 8202, Raleigh, NC 27695, USA and

[c)] *Lockheed Research Laboratories, 3251 Hannover St., Palo Alto, CA 94304, USA*

Abstract

We report on the measurements of the secondary electron yield of chemical vapor deposited (CVD) diamond upon reflection of primary H^+, D^+, H_2^+, C^+, O^+, and O_2^+ ions in an energy range of 50 to 1000 eV per atom at 60° angle of incidence to the surface normal. Depending on species and energy, a secondary electron yield between 0.1 and 2 was observed, and remained unchanged over weeks without further periodic re-conditioning of the surface and in spite the moderate vacuum environment of 10^{-7}mbar. Semi empirical fit functions were found with a dependence on the inverse velocity and the square root of the atomic number of the projectiles.

PACS codes: 68.49.Sf, 79.20.Rf

I. INTRODUCTION

The study of neutral gas in the magnetosphere and in the heliosphere has gained a lot of attention in the recent years [1–3], as it allows to study remotely large plasma populations and their interactions. To investigate spatial distributions of the neutral particle flux, a sensitive imaging neutral particle sensor is needed [4–7]. A well established method of detection includes imaging time-of-flight mass spectrometers as used in the Neutral Particle Detector (NPD) in the ASPERA-3 instrument [7] on the Mars Express spacecraft. In this type of spectrometer, start and stop pulses for time-of-flight measurement are generated by scattering the incident low energy neutral atoms at suitable surfaces and collecting the generated secondary electrons. Combined with an energy measurement, this can be used to determine the mass of the particle. However, only limited data about secondary electron yields of materials suitable for start and stop surfaces are available in the energy range of a few eV up to 1 keV per atom. Chemical vapor deposited (CVD) diamond was identified as promising secondary electron emitting surface as beside the secondary electron yield it may also be polished to a roughness of a few nm rms providing good angular scattering properties for impinging particles and it is chemically stable. We present measurements of the secondary electron yield at a fixed angle of incidence for an energy range of 50 to 1000 eV per atom and for different species.

II. EXPERIMENTAL

A. Setup

The experiment ILENA at the University of Bern (Figure 1) consists of a Nier-type ion source, a sector magnet for mass selection, a beam guiding and modulation system, a sample stage with housing, and a retarding potential analyzer (RPA) followed by an imaging micro channel plate (MCP) assembly. All these units are contained in a single vacuum chamber pumped by a turbo-molecular and an ion getter pump. After baking out the vacuum chamber a residual gas pressure of $4 \cdot 10^{-8}$ mbar is achieved. During operation the pressure may rise into the low 10^{-7} mbar range as a result of the test gas leaking into the ion source chamber. The ion source is floatable to a positive high voltage to adjust the ion energy in the range from 30 eV to 3 keV per charge. Mass per charge selection is done in a sector magnet providing a mass resolution $\frac{m}{\Delta m} \approx 45$. The ion beam diam-

eter when entering the sample housing is about 1 mm. The impact angle of the ion beam on the surface under investigation can be varied between 90° and 0° with respect to the surface normal. The RPA/MCP unit is used to investigate charge state fractions as well as angular distributions of scattered particles.

The electrical current imposed onto the sample by the ion beam is measured using a lock-in amplifier Perkin Elmer 7265. The ion beam intensity is modulated at a frequency of 3.14 Hz by applying the reference signal of the lock-in amplifier to an additional pair of deflection plates followed by a pinhole creating a sinusoidal intensity modulation. The current $\mathbf{i}$ onto the sample is picked up by a Femto LCA-30-1T transimpedance preamplifier and fed back into the lock-in amplifier. Only the current component in phase with the beam modulation signal, $\mathrm{Re}(\mathbf{i})$, is considered. Capacitive coupling between the modulation signal and the sample current measurement wires produces an additional contribution $\mathrm{Im}(\mathbf{i})$ to the measured current, which is separated in the lock-in amplifier by the 90° phase shift relative to the reference signal. Figure 2 shows data of the background signal and an actual measurement recorded with this system. Careful electrical shielding and grounding and mechanical vibration damping of the experiment allows to lock onto the signal for amplitudes down to 0.3 fA.

An adjustable magnetic field ranging from -3 mT to 3 mT parallel to the sample surface and normal to the primary beam allows to inhibit the escape of secondary electrons from the surface. Electrons with energies of a few eV return with a radius of gyration of a few mm to the surface. This is used to separate the contribution of the secondary electrons to the sample current. Compared to applying an electrostatic bias potential to the sample to retain the secondary electrons, magnetic deflection allows to selectively suppress only electrons and to keep the influence on ions negligible.

B. Surface

The surface investigated was supplied by North Carolina State University. A 200 nm thick boron doped chemical vapor deposited (CVD) diamond layer was deposited on a Si waver and polished to a smoothness $<10\text{Å}_{rms}$. The surface was hydrogen-terminated by exposing it to a hydrogen atmosphere at a temperature of a few hundred degrees Celsius.

C. Secondary Electron Yield

For singly positive charged projectiles, the velocity dependent secondary electron yield $\gamma(v)$ is given by

$$\gamma(v) = \left(\frac{\mathrm{Re}\left(\mathbf{i}_{A,\gamma}\right)}{\mathrm{Re}\left(\mathbf{i}_A\right)} - 1 \right)(1+k) \quad \begin{cases} \mathrm{H}^+, \mathrm{D}^+, \mathrm{C}^+ : \; k = 0 \\ \mathrm{O}^+ : \; k = \eta_a^-(v) \end{cases} \tag{1}$$

with $\mathbf{i}_A$ the current onto the sample with a parallel magnetic field (i.e., the primary ion current), $\mathbf{i}_{A,\gamma}$ the current without magnetic field, and k a small correction for the fraction of particles ionized upon reflection of the surface. For hydrogen and carbon, positive and negative charge state fractions are both less than 0.03 per incident atom [8] and cancel approximately ($k \approx 0$). For primary oxygen the positive charge state fraction is below 0.01 per atom and the negative charge state fraction $\eta_a^-(v)$ dominates, however its value is below 0.2 per atom [8]. For molecular projectiles H_2^+ and O_2^+, it was assumed according to data reported in [9, 10] that a molecule produces the same amount of secondary electrons as its equally fast constituents:

$$\gamma_M(v) \approx \sum \gamma_A(v) = 2 \cdot \gamma_A(v). \tag{2}$$

Charge state fractions per atom obtained from hydrogen and oxygen molecules are similar to the charge state fractions obtained from equally fast atoms [8]. For H_2^+ and O_2^+ molecules, the secondary electron yield per atom is thus obtained by

$$\gamma(v) = \frac{1}{2}\left(\frac{\mathrm{Re}\left(\mathbf{i}_{M,\gamma}\right)}{\mathrm{Re}\left(\mathbf{i}_M\right)} - 1 \right)(1+2k) \tag{3}$$

with $\mathbf{i}_M$ the current onto the sample with a parallel magnetic field, $\mathbf{i}_{M,\gamma}$ the current without, and k the correction for the ionized fraction of the reflected particles as in Equation 1.

III. RESULTS AND DISCUSSION

Both Equations 1 and 3 allow the determination of the secondary electron yield using two current measurements, aside from the need of knowledge of the negative ion yield in the case of oxygen.

The two current values are obtained by scanning the magnetic field from negative (field pointing downwards) to positive values (field pointing upwards) as shown in Figure 3.

The secondary electron yield per atom, γ, for all investigated species is shown in Figure 4. For H^+ and H_2^+, the assumption from Equation 2 is well justified a posteriori. For oxygen, however, Equation 2 does not reproduce the data well. The secondary electron yield per atom obtained from O_2^+ was larger by a factor of 1.7 compared to O^+. This is in contrast to data obtained from thin carbon foils [11] where a factor less than one is observed. Within measurement errors, no isotopic dependency of γ could be found between H^+ and D^+ in the investigated velocity range. The values reported for C^+ fit well in the general trend of a higher γ for larger atomic number Z of the projectile. A semi-empirical fit function of the form

$$\gamma = \gamma_0 \cdot e^{-\frac{\nu_0 k}{\nu\sqrt{Z}}} \tag{4}$$

was applied to the data, with ν the particle velocity, $\nu_0 = \alpha \cdot c = 2.18 \times 10^7 \mathrm{m/s}$, k a projectile species independent fitted constant equal 0.215, and γ_0 a free parameter depending on projectile species representing the secondary electron yield per atom obtained from Equation 4 for the asymptotic case $\nu \to \infty$. Table I summarizes the values found for γ_0 depending on projectile type. These fits are plotted in Figure 4 as solid lines.

An approximation for higher velocities is obtained by expanding Equation 4 to a series around $\nu = \nu_0 k$:

$$\gamma \approx \gamma_0 \left(1 - \frac{1}{\sqrt{Z}}\right) \cdot e^{-\frac{1}{\sqrt{Z}}} + \frac{\nu}{\nu_0 k} \cdot \frac{\gamma_0}{\sqrt{Z}} \cdot e^{-\frac{1}{\sqrt{Z}}} + \ldots \quad = a + \frac{\nu}{\nu_0} \cdot b + \ldots \ , \tag{5}$$

which shows the linear dependence of γ with the projectile velocity ν at higher particle velocities. For hydrogen, the constant term a in Equation 5 vanishes, reducing the equation to $\gamma \sim \nu$, which is a well known relation for kinetic secondary electron emission. Secondary electron emission, γ, is generally thought to be proportional to the electronic stopping power S_e [12], and S_e being proportional to ν in the Lindhard-Scharff velocity regime $\nu \leq Z^{2/3}\nu_0$ [13]. This condition is satisfied for all investigated species for $\nu = \nu_0 k$, because k is smaller than one. However, at lower velocities γ is overestimated when using $\gamma \sim \nu$ (see dashed line in Figure 4) and better fits to the data are obtained using Equation 4. A dependence of $\gamma \sim e^{-A/\nu_\perp}$ with A being a constant and $\nu_\perp$ the velocity of the projectile perpendicular to the surface was also reported in [14] where a

surface electron-hole pair excitation mechanism was identified for the emission of secondary electrons from slow Li^+ ions impinging on aluminium, however, no projectile type dependence was reported there. For data reported in [15, 16] for C^+, N^+, and O^+ impinging on a polycrystalline gold surface, surface-assisted kinetic electron emission is identified as dominant mechanism for electron emission. These data are also well fitted with the fit function shown in Equation 4. Similar to findings reported in [17], our data do not show a threshold velocity for secondary electron emission.

IV. CONCLUSION

Measurement of the secondary electron yield by suppressing electrons by a magnetic field is advantageous compared to biasing the sample electrostatically at low ion energies. The energy and trajectory of the primary ions is not changed noticeably by the magnetic field. The secondary electron yields found for CVD diamond for the species investigated were well fitted by an empirical fit function (Equation 4) showing a dependence from the inverse velocity and the square root of the atomic number of the projectile.

Acknowledgment

The financial support by the Swiss National Science Foundation is acknowledged.

[1] P. Wurz, *The outer Heliosphere: Beyond the Planets* (Copernicus Gesellschaft e.V., 2000), chap. Detection of Energetic Neutral Particles.

[2] H.-J. Fahr, Adv. Space Research **34**, 3 (2004).

[3] M. Witte, M. Banaszkiewicz, H. Rosenbauer, and D. McMullin, Adv. Space Research **34**, 61 (2004).

[4] D. J. McComas, F. Allegrini, P. Bochsler, M. Bzowski, M. Collier, H. Fahr, H. Fichtner, P. Frisch, H. Funsten, S. Fuselier, et al., in *Physics of the Outer Heliosphere: Third International IGPP Conference*, edited by V. Florinski, N. Pogorelov, and G. Zank (AIP Conference Proceedings 719, 2004), pp. 162–181.

[5] M. Witte, H. Rosenbauer, E. Keppler, H. Fahr, P. Hemmerich, H. Lauche, A. Loidl, and R. Zwick, Astronomy and Astrophysics **92**, 333 (1992).

[6] T. Moore, D. Chornay, M. Collier, F. Herrero, J. Johnson, M. Johnson, J. Keller, J. Laudadio, J. Lobell, K. Ogilvie, et al., Space Sci. Rev. **91**, 155 (2000).

[7] S. Barabash, R. Lundin, H. Andersson, J. Gimholt, M. Holström, O. Norberg, M. Yamauchi, K. Asamura, A. Coates, D. Linder, et al., ESA-SP 1240 pp. 121–139 (2004).

[8] J. Scheer, M. Wieser, P. Wurz, P. Bochsler, E. Hertzberg, S. Fuselier, F. Koeck, R. Nemanich, and M. Schleberger, Nucl. Instr. Meth. B p. in press (2005).

[9] B. Svensson, G. Holmn, and J. Linnros, Nucl. Instr. and Meth. pp. 429 – 432 (1982).

[10] E. S. Chambers, Phys. Rev. A pp. 1202 – 1207 (1964).

[11] S. M. Ritzau and R. A. Baragiola, Phys. Rev. B **58**, 2529 (1998).

[12] R. Baragiola, Nucl. Instr. Meth. B **78**, 233 (1993).

[13] G. Betz and K. Wien, Int. J. Mass Spectrom. Ion Processes **140**, 1 (1994).

[14] J. Yarmoff, T. Liu, S. Qiu, and Z. Sroubek, Phys. Rev. Lett. **80**, 2469 (1998).

[15] H. Eder, F. Aumayer, and H. Winter, Nucl. Instr. Meth. B **154**, 185 (1999).

[16] J. Lörincik, Z. Sroubek, H. Eder, F. Aumayr, and H. Winter, Phys Rev. B **62**, 16116 (2000).

[17] J. Lörincik, Z. Sroubek, S. Cernusca, A. Diem, H. Winter, and F. Aumayr, Surface Science **504**, 59 (2002).

Figures

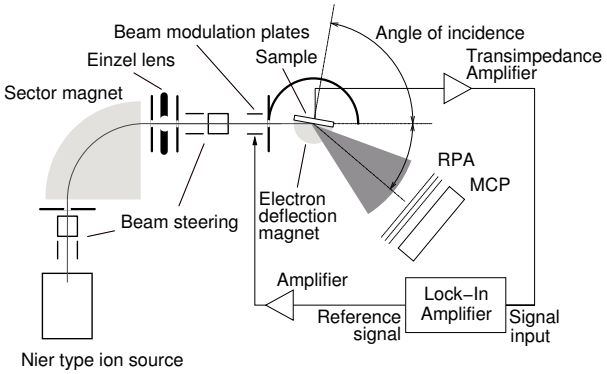

Figure 1: ILENA experiment

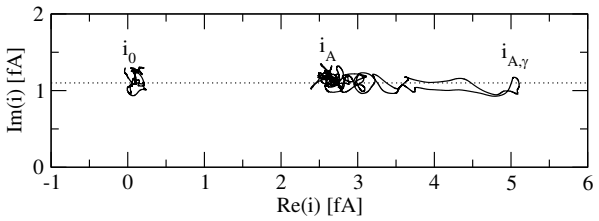

Figure 2: Dataset on the right: Value of current vector **i** measured by the lock-in amplifier while sweeping the magnetic field at the sample from pointing upwards to downwards. A 486 eV H^+ beam impinging at 60° to the surface normal was used. The reference signal used for beam modulation points in positive Re(**i**) direction. The capacitively coupled imaginary component Im(**i**) remains independent of the magnetic field whereas the real component Re(**i**) varies between i_A where the magnetic field is strong enough to hinder electrons from escaping from the surface and $i_{A,\gamma}$ where the field is zero. Dataset on the left: Without beam, Re(**i**) is very close to zero and only the capacitively coupled component i_0 of the signal remains.

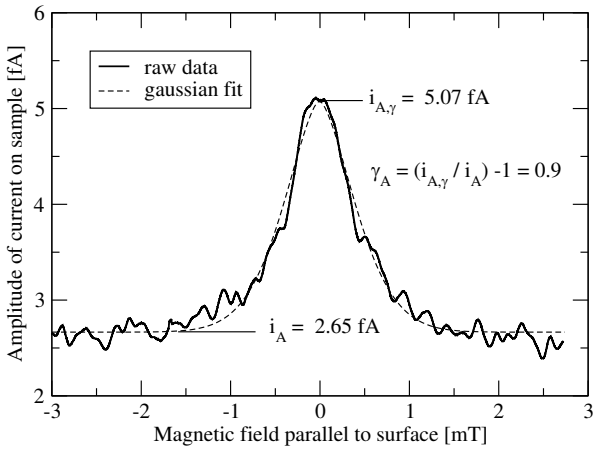

Figure 3: Sample current depending on magnetic field strength. A 486 eV H^+ beam impinging at 60° to the surface normal was used.

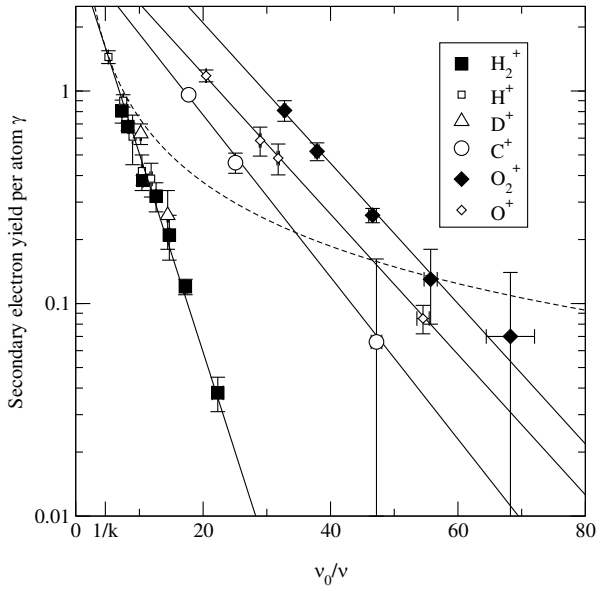

Figure 4: Secondary electron yield for various primary particles impinging at 60° to the surface normal. Fits using Equation 4 with parameters from Table I are shown as solid lines. The dashed line shows the linear approximation obtained for $\nu_0/\nu = 1/k$ used in the series expansion in Equation 5.

Table I: Fit parameters for Equation 4 used in Figure 4. γ_0 is given in units of secondary electrons per atom.

projectile	γ_0
H^+, D^+, H_2^+	4.35
C^+	4.46
O^+	5.51
O_2^+	9.56

2.5 Method for the Measurement of Absolute Detection Efficiency of Multi Channel Plates

2.5.1 Motivation

The knowledge of the absolute detection efficiency of multi channel plates (MCP) is important for may applications. The detection efficiency depends on the field configuration in front of the MCP, the open area of the MCP, the secondary electron yield of the active surface, and the operating mode of the MCPs. For energies above several keV the detection efficiency of an MCP is mainly given by the active area of the MCP as the secondary electron yield exceeds unity. For energies below 1 keV per particle the secondary electron yield drops fast and only limited data for the detection efficiency is available in the literature [Peko & Stephen 2000, Stephen & Pecko 1998]. In this chapter a method is presented that allows to measure the absolute detection efficiency of the MCP assembly in the ILENA setup. The detection efficiency is measured by comparing the count rate from the MCP with the current collected from the MCP front face with high voltages disconnected from the MCP stack. The detection efficiency for all species that can be produced with the ILENA source might be measured - this includes $^{16}O^+$, $^{12}C^+$, $^{20}Ne^+$, $^{22}Ne^+$, H^+, D^+, H_2^+, O_2^+, $^{40}Ar^+$, and He^+.

2.5.2 Experimental Setup

The proposed method is designed for implementation in the ILENA experiment. Although this experiment was built to study the interaction of ions with charge conversion surfaces it may be easily adapted to measure MCP detection efficiencies. The measurement is done using a positive ion beam in the energy range of 40 eV to 1500 eV. The beam is intensity modulated by applying a sinusoidal voltage to one of the beam steering plates. Additional DC offset voltages are applied to ensure an as sinusoidal intensity modulation as possible of the ion beam. The modulated positive ion beam is then directed onto the the MCP. For measurement of the detection efficiency of positive ions, the retarding potential analyzer (RPA) in front of the MCP detector is removed to avoid charge exchange at the RPA grids. Only the grid in front of the MCP detector remains, set to negative potential with respect to the MCP detector to reject low energy electrons from the chamber. The MCP detector is either operated in normal mode with high voltages on or placed in a Faraday cup like configuration where the MCP is insulated except for one connection from the MCP front face to a low current preamplifier. The later is connected to the lock-in amplifier, which also provides the beam modulation reference signal.

2.5.3 Measurement Principle

The MCP detection efficiency is measured by directly comparing the charge deposited on the MCP with the MCP's count rate. For low count rates where the probability that two particles

are detected at the same time is small and for singly charged ions, the detection efficiency η is then given by

$$\eta = \frac{N_{DET}}{\left|\frac{Q_{MCP}}{e}\right|} = \frac{e \cdot \frac{N_{DET}}{t}}{|I_{MCP}|} = \frac{|I_{DET}|}{|I_{MCP}|} \tag{2.11}$$

where Q_{MCP} is the total charge deposited on the MCP front face in the time interval t, N_{DET} the number of counts detected in the time interval t and e the elementary charge. I_{MCP} is the current on the MCP front face from singly charged ions and I_{DET} the equivalent current calculated from the count rate that corresponds to detected particles. As I_{DET} is calculated from the count rate, it is very easy to get good statistics even for very low count rates. Constraints in determining I_{DET} are the background count rate of the detector of the order of 10 counts per second corresponding to about 10^{-3} fA and the maximum allowable count rate of the MCP without saturation of about $1.5 \cdot 10^4$ counts per second corresponding to 2.4 fA_{DC}. A justification for the maximum allowable count rate is given in Chapter 2.5.4. I_{MCP} is more difficult to measure, DC current measurements are very difficult below 100 fA. For a direct comparison the ranges of both currents must overlap. To increase the sensitivity in the measurement of I_{MCP} a lock-in Amplifier is used. This requires the primary beam to be modulated at a frequency f. The absolute detection efficiency η is then given by

$$\eta = \frac{|\Delta I_{DET}|}{|\Delta I_{MCP}|} = \frac{i_{X-DET}}{i_{X-MCP}} \tag{2.12}$$

where i_{X-MCP} is the amplitude of the current in phase with the beam modulation on the MCP front face and i_{X-DET} the amplitude of the equivalent current of the particles detected by the MCP calculated using the modulation in the count rate of the MCP. i_{X-MCP} is directly measured by the lock-in amplifier, it corresponds to the current component with 0° phase shift to the beam modulation signal. The lock-in amplifier also measures the component with 90° phase shift, i_{Y-MCP}. This component is caused by capacitive coupling between the cabling to the beam modulation plates and the MCP front face. It must not be much larger than i_{X-MCP} as this would reduce the accuracy with which the lock-in amplifier is able to measure i_{X-MCP}. The usable range for i_{X-MCP} is limited at the lower end at about 0.3 fA by the ability of the lock-in amplifier to lock on the signal. The high end limit is imposed by the beam source at around 500 fA.

For the determination of i_{X-DET} the counts of the MCP are placed in bins N_k numbered from 0 to $k_{max}-1$ according to the phase Φ of the lock-in amplifier reference frequency f where N_0 corresponds to a phase angle $\Phi = 0$ and $N_{k_{max}-1}$ to a phase angle $\Phi = 2\pi \cdot \frac{k_{max}-1}{k_{max}}$. Each bin covers a phase angle range of $\Delta\Phi_k$. The equivalent currents i_{X-DET}, i_{Y-DET}, and $i_{OFFS-DET}$ are obtained from N by calculating the coefficients of the Fourier series for the fundamental frequency:

$$
\begin{aligned}
i_{X-DET} &= e \cdot \frac{k_{max}}{t_{acc}} \cdot 2 \cdot \sum_{k=0}^{k_{max}-1} N_k \sin\left(\frac{2\pi k}{k_{max}}\right) \frac{\Delta\Phi_k}{2\pi} \\
i_{Y-DET} &= e \cdot \frac{k_{max}}{t_{acc}} \cdot 2 \cdot \sum_{k=0}^{jusok_{max}-1} N_k \cos\left(\frac{2\pi k}{k_{max}}\right) \frac{\Delta\Phi_k}{2\pi} \\
i_{OFFS-DET} &= e \cdot \frac{k_{max}}{t_{acc}} \cdot \sum_{k=0}^{k_{max}-1} N_k \frac{\Delta\Phi_k}{2\pi}
\end{aligned}
\tag{2.13}
$$

where t_{acc} is the total count acquisition time and e the elementary charge. i_{Y-DET} corresponds to the capacitively coupled component i_{Y-MCP} and should be close to zero. This is used as a quality criterion. $i_{OFFS-DET}$ corresponds to the average count rate and is ideally as small as i_{X-DET} indicating a beam modulation depth of close to 100% and that most of the modulation energy is placed in the fundamental frequency f. A further advantage of using a modulated primary beam is that background counts only increase $i_{OFFS-DET}$ and not i_{X-DET}, as they are not correlated with the modulation frequency. The usable range of i_{X-DET} is limited at the upper end by the maximum allowable count rate of the MCP without saturation of $1.5 \cdot 10^4$ counts per second corresponding to 1.2 fA and extends basically to 0 fA at the lower end. The higher end value is half the maximum value for I_{DET} shown above because $i_{X-DET} \sin(2\pi f t) + i_{OFFS-DET} > 0$ for any t as there are no negative counts possible. Comparing this range with the range possible for i_{X-MCP} a comfortable overlap around 1 fA is achieved where the accuracy of the current measurements is better than 10%. For lower detection efficiencies the situation improves as a much higher primary beam intensity is needed to saturate the MCP. The choice of the modulation frequency f is rather critical: The capacitively coupled component i_{Y-DET} increases linearly with frequency. The frequency must be below the frequency used by the nearby railway (16 2/3 Hz) and within the range of the preamplifier used. The measurement time on the other hand should not exceed a few minutes due to the drift in the primary beam intensity. A lower frequency also increases the time the lock-in amplifier requires to lock on the signal. A value of 3.14 Hz was used - the same value as for sensitive secondary electron measurements described in Chapter 2.4.

With some modifications the detection efficiency for negative ions may also be determined. Whereas to measure the detection efficiency for positive ions the primary beam is steered directly onto the MCP, for negative ions the ion beam is directed at grazing incidence onto a tungsten charge conversion surface. Most ions are neutralized upon reflection but a small fraction of 1% to 20% of the particles is negatively ionized. The RPA is included in the setup and configured to reject positive particles. Neutrals originating from the conversion surface and produced in the RPA by surface neutralization [Losch & Niehus 1999] are identified by reconfiguring the RPA such that only neutral particles pass. The neutral particle counts are subtracted prior to further data analysis. As the neutrals amount to more than 80% of all particles longer integration times are required to get good counting statistics after the subtraction of the neutral signal.

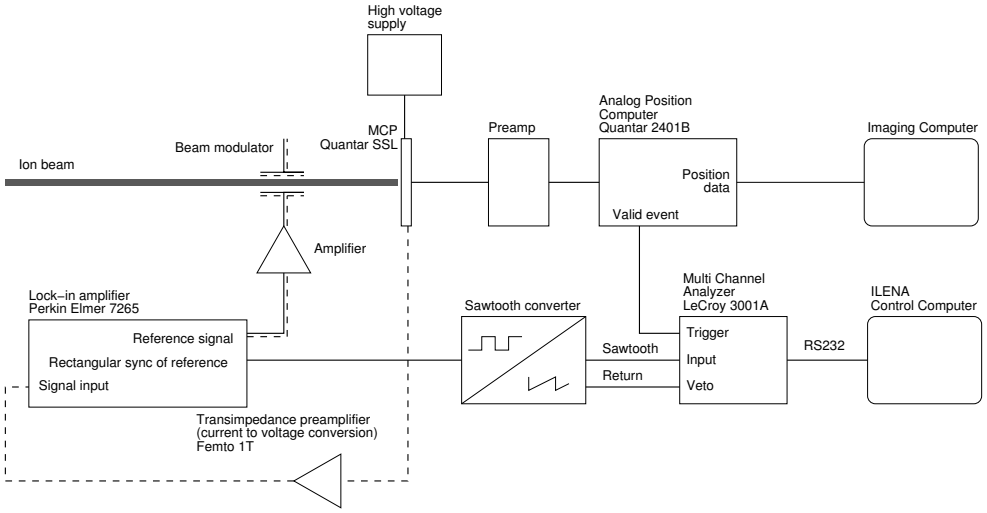

Figure 2.12: Signal flow for MCP detection efficiency measurement. Two measurements are done sequentially: a current measurement (dashed line) with high voltage supply disconnected and the transimpedance preamplifier connected to the MCP and a measurement in particle binning mode (solid line) with the current preamplifier disconnected and the high voltage supply connected to the MCP.

2.5.4 Implementation

The main modification needed compared to the setup described in Chapter 2.4 is the addition of a multi channel analyzer (MCA) that allows the binning of MCP counts according to the phase of the beam modulation voltage. Figure 2.12 depicts a block diagram of the additional modules: To record the phase information, a sawtooth waveform phase locked with the sinusoidal reference signal of the lock-in amplifier is generated. The instantaneous value of the sawtooth waveform is proportional to the phase angle of the sinusoidal reference signal except for a very small interval where the phase angle overflows from 2π back to zero and the instantaneous value of the sawtooth waveform returns from its maximum value to zero. The sawtooth waveform signal is connected to the input of the MCA that is operated in pulse height analysis mode. Every valid event pulse from the position computer triggers a conversion in the MCA and the count is added to the bin corresponding to the instantaneous value of the sawtooth waveform which is a linear function of the current phase angle of the reference signal. Conversion is inhibited during the small interval where the sawtooth waveform returns from its maximum value to zero. As the beam modulation frequency is very low, the signal delay caused by the MCP signal analysis hardware - a preamplifier and a Quantar 2401B analog position computer - until providing a digital valid-event signal is not an issue. The properties of the position computer determine however the maximum allowable count rate. At the end of the accumulation time the ILENA control computer reads the binned counts from the MCA and calculates the values for i_{X-DET}, i_{Y-DET}, and i_{X-OFFS} according to Equation 2.13. For the determination of i_{X-MCP}, all high voltages are removed from the MCP and a sensitive transimpedance preamplifier (current to voltage converter) is attached to the MCP front face and the signal is measured by the lock-in amplifier. Using Equation 2.12 the detection efficiency of

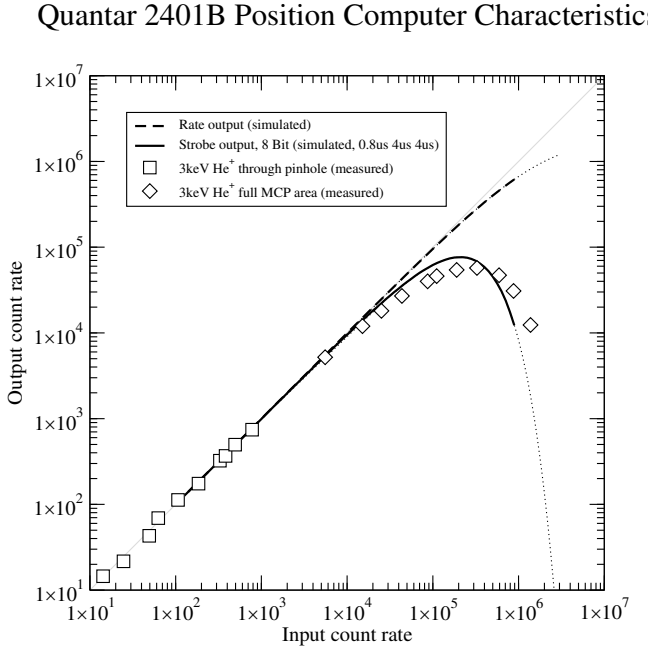

Figure 2.13: Simulated paralyzing properties of the Quantar 2401B analog position computer for the 'strobe' signal output indicating completed position calculations (solid line, simulation) compared with data from measurements obtained using a 3 keV He^+ beam impinging on an MCP (open symbols). If position resolution is not required, the 'rate' signal output could be used up to much larger count rates (dashed line, simulation). For detection efficiency measurements the input rate is kept below below $1.5 \cdot 10^4$ counts per second in the linear range of the position computer.

the MCP is established. In particle binning mode, the spatial distribution of the counts on the MCP area is monitored using the imaging computer to avoid hot spots or a degraded detection efficiency due to a too large particle density on any area of the MCP.

The use of the imaging mode of the position computer reduces the maximum usable count rate of the system. A detailed analysis of the signal chain from the MCP to the preamplifier and to the position computer shows that the later is determining the saturation properties of the whole system. The position computer provides two digital signals upon detection of an event: a fast 'rate' signal without position information generated by a non-paralysable logic with a dead time of 0.5 μs and a slower 'strobe' signal including position information generated by a slower paralysable logic with 4.8 μs dead time. Figure 2.13 depicts a comparison of simulations done using a model obtained from reverse engineering the position computer electronics with actual measurements. Although the model does not exactly model the properties at input rates above 10^5 counts per second since it does not include the preamplifier and the MCP itself, below $1.5 \cdot 10^4$ counts per second from the preamplifier, the position computer does not have a noticeable influence on the measured count rate .

2.5.5 Discussion

The proposed method would allow to directly measure the absolute detection efficiency of an MCP detector by comparing the count rate from a given beam with the high sensitivity current measurements described in Chapter 2.4. The absolute detection efficiency for a large number of species could be determined in an energy range of 1500 eV down to a few tens of eV. For a full implementation in the ILENA experiment about 1 month of work for would be needed, mostly for hardware changes, e.g. replacement of standard high voltage feedthroughs by shielded versions or upgrading cabling inside the chamber, all without having a negative impact on the sensitivity of the system as shown in Table 2.1.

2.6 Relative Reflection Efficiency

A standard tool for comparing scattering properties of a conversion surface is to compare the intensity of the ion beam I_P impinging onto the surface with the total number of particles N scattered into the field of view of the MCP, roughly a cone with 25° opening angle, within the sampling interval Δt. The resulting relative reflection efficiency R is a measure of the scattering properties of a surface that complements the scattering images obtained from the imaging MCP detector:

$$R = \frac{N}{\Delta t\, I_P} \tag{2.14}$$

The intensity of the primary ion beam I_P was originally measured using a DC current measurement from the sample surface towards ground potential with a beam in the pA intensity range, assuming single charged positive particles in the beam. Subsequently, the emission current I_E in the ion source was reduced in several steps until the current from the sample towards ground was below the detection threshold. A further reduction of the emission current I_E in the ion source put the scattered beam intensity $I_S = \frac{N}{\Delta t}$ in the dynamic range of the MCP detector (<20 kcps). Using a linear extrapolation from the DC current measurements, the primary beam intensity I_P^{estim} was estimated for the case where the scattered beam intensity I_S was measured and the estimation for relative reflection efficiency R^{estim} calculated by:

$$R \approx R^{estim} = \frac{N}{\Delta t\, I_P^{estim}}\ ;\ I_P^{estim} \sim I_E \tag{2.15}$$

The interpolation step with the emission current I_E of the ion source is eliminated by measuring the sample current $i_{X-SAMPLE}$ (analog to i_{X-MCP}) with the method described in Chapter 2.3 and comparing it to an equivalent current measured by the MCP i_{X-DET} as described in Chapter 2.5:

$$R = \frac{i_{X-DET}}{i_{X-SAMPLE}} \tag{2.16}$$

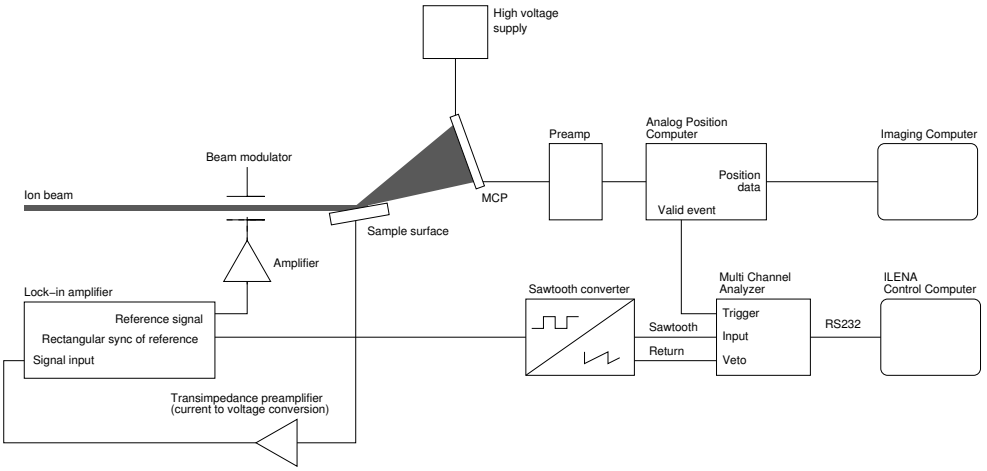

Figure 2.14: Direct measurement of the relative reflection efficiency. All required measurements are done simultaneously, without the need to reconfigure the setup or the beam parameters.

Both measurements are done simultaneously using the arrangement shown in Figure 2.14. Note that the setup is very similar to the setup shown in Figure 2.12. To get a reliable result, secondary electrons from the sample surface would need to be suppressed, e.g. by a magnetic field parallel to the sample surface as shown in Chapter 2.4, and the influence of the charge state fractions of the reflected particles on the detection efficiency of the MCP must be taken into account.

Chapter 3

Neutral Beam Source

3.1 Introduction

Low energy neutral particle mass spectrometers used in space research [McComas et al. 2004, Barabash et al. 2004, Moore et al. 2000] require well characterized neutral atom beams in the energy range of 10 eV–1000 eV for calibration. The Calibration System for Mass Spectrometers (CASYMS) facility [Ghielmetti et al. 1983] and the Calibration Facility for Solar Wind Instrumentation (MEFISTO) [Marti et al. 2001], both at the University of Bern, provide well collimated ion beams in the energy range of interest but do not have a beam neutralization stage. For ease of operation, neutralization by reflecting incident ions at grazing incidence from a polished tungsten single crystal was chosen. Surface neutralization requires no additional pumping systems and the neutralization device acts as additional block in the beam line without modifications to the vacuum system. The device operates under the same conditions as the instrument under test and is easily installed in both facilities, MEFISTO and CASYMS.

3.2 Paper: Production of a low energetic neutral particle beam using surface neutralization

M. Wieser and P. Wurz

(Submitted April 2005 to Measurement Science and Technology)

Production of a low energetic neutral particle beam using surface neutralization

Martin Wieser and Peter Wurz‡

Physikalisches Institut, University of Bern, Sidlerstrasse 5, 3012 Bern, Switzerland

Abstract. For the calibration of low energy neutral particle mass spectrometers a neutralization stage for a charged particle beam was built. The incident positive ion beam is neutralized upon reflection at grazing incidence off a highly polished tungsten single crystal surface. With protons as primary species the device produced a neutral hydrogen beam in the energy range of 10 eV–1000 eV depending on incident ion beam energy with a center energy of 85% to 89% and a FWHM of 11% to 15% of the incident ion energy. The angular spread of the neutral beam was limited by apertures to $4.6^\circ \times 18^\circ$ FWHM. The overall transmission of the device was found to be between 0.005 and 0.013.

Submitted to: *Meas. Sci. Technol.*

PACS numbers: 07.77.Gx, 34.50.Dy, 39.10.+j

‡ To whom correspondence should be addressed (wurz@phim.unibe.ch)

Introduction

Measurements of the physical parameters (temperature, density, composition, and others) of the local interstellar medium (LISM) will give information about the evolution of the solar system and our galaxy. The LISM is separated from the solar system by the heliopause and charged interstellar particles can not cross this boundary to enter the solar system. The neutral fraction of the LISM, however, is not subject to magnetic interactions and can therefore penetrate deeply into the solar system. As the Sun moves with a velocity of approximatively 26km/s relative to the LISM a directed inflow of interstellar neutral atoms can be observed [1, 2, 3]. Furthermore, energetic neutral atoms (ENA) are produced by charge exchange processes at the heliospheric boundary [4] revealing information about the global structure of the heliosphere.

When approaching the Sun the neutral atom populations are affected by gravitation, photo ionization and charge exchange processes. For a spacecraft traveling from Earth toward the heliopause, at a distance of more than about four astronomical units from the Sun these effects become negligible. Consequently it is possible to infer the properties of the neutral interstellar gas and its interaction with the heliosphere by measuring the properties of the inflowing energetic neutral atoms [5]. This has been done for interstellar helium by the Neutral Interstellar Gas Instrument (GAS) on the ULYSSES spacecraft [6]. Even as close as one astronomical unit to the Sun, a fraction of the neutral particle population survives and can be measured by an instrument in Earth's orbit. In Earth's orbit the energies of such energetic neutral particles range from 10 eV to several 100 eV depending on the location of the earth with respect to the interstellar gas flow direction and the inflowing species. Such an instrument is presently in operation on board the IMAGE satellite [7]. A next generation low energy neutral atom mass spectrometer has recently been selected for the Interstellar Boundary Explorer mission (IBEX) of NASA [8].

The calibration of such low energy neutral atom mass spectrometers requires well characterized energetic neutral atom beams in the energy range of 10 eV–1000 eV per atom. The Calibration System for Mass Spectrometers (CASYMS) facility [9] and the Calibration Facility for Solar Wind Instrumentation (MEFISTO) [10], both at the University of Bern, provide well collimated ion beams in the energy range of interest but do not have a beam neutralization stage. We have built and characterized a portable ion beam neutralizer compatible with both calibration facilities, MEFISTO and CASYMS.

Charge exchange

Three different approaches to neutralize an ion beam are reported in literature. A wildly used method is to use charge-exchange between an ion beam and a neutral gas. Utterbach and Miller [11] investigated fast molecular nitrogen beams in the energy range of 5–1000 eV. In a charge exchange cell, an energetic ion, A^+_{fast} collides with a thermal, room temperature, neutral gas atom or molecule, B, picking up an electron via

$$A^+_{fast} + B \rightarrow A_{fast} + B^+$$

resulting in A_{fast} exiting the cell as energetic neutral atom or particle. This is the same process that is responsible to the emission of ENA's from planetary magnetospheres. Neutralization efficiencies up to 10 % can be obtained provided suitable charge capture partners can be found. A common implementation consists of a differentially pumped gas cell filled with a noble gas, e.g. Xenon, followed by a set of deflection section to eliminate the remaining ions. The drawback of a gas cell is that it requires differential pumping as the pressure in the gas cell needs to be much larger (10^{-5}mbar) than the pressure in the instrument test chamber (10^{-7} to 10^{-9} mbar). This results in small apertures for the beam for entering and exiting the gas cell and thus also only a small neutral particle beam diameter.

Photodetachment

An other elegant way to produce a neutral beam is to photodetach an electron from negatively charged ions [12]. Photodetachment is realized with a strong argon-ion-laser (kW power level). As example, ground state O(^{3}P) is produced from O^- using photons with an energy of less than 3.43 eV. Neutralization rates of the percent level are obtained with the kW laser power available. Remaining ions are removed electrostatically. Neutral atom beams of hydrogen and oxygen in an energy range of 4–1000 eV with an energy spread of 1.5 eV given by the ion source have been realized. However the photodetachment technique is limited to species that form stable negative ions and requires a negative ion source. Furthermore the need of a laser in the kW power range imposes additional complications.

Surface Neutralization

A third way to produce a neutral particle beam is to use surface neutralization. When ions are scattered off solid surfaces at grazing incidence, specular reflection of the incoming ion beam will occur if the surface is flat on an atomic scale. In addition, charge exchange reactions between the projectile and a metal surface take place, especially Auger neutralization, resonance neutralization, and quasi-resonant processes, resulting in an efficient neutralization of the scattered particle [13]. A small deflection angle guarantees that a sufficiently long time for charge exchange is available. Large neutralization rates (>90 %) may be obtained this way. This technique for production of energetic neutral atoms is also used in surface science experiments [14]. Recently, Losch and Niehus [14, 15] used a Pt(111) surface to convert an ion beam into a neutral atom beam for surface science studies in an UHV environment. They used grazing incidence at 4.5° for particle scattering. The energy loss was about 100 eV with an energy spread of <40 eV for 3 keV He scattered from a Pt single crystal. Larger angles will cause larger energy loss and larger energy and angular scatter.

Despite the energy loss, energy and angular scatter introduced by the scattering surface, surface neutralization was chosen to build a neutralization device as it has several advantages compared to other methods of neutralizing an ion beam. It requires no additional pumping systems and the neutralization device may be put as additional unit into the beam line without modifications to the vacuum system. Apart of some high voltages, no additional feedthroughs out of the vacuum chamber are needed. The device operates under the same conditions as

the instrument under test, can be built sufficiently small and may be easily installed in both facilities, MEFISTO and CASYMS.

Neutralizer

Figure 1 shows a cross sectional drawing of the ion beam neutralizer. It consists of an electrostatic analyzer, a scattering surface, a set of apertures and an ion deflection system. Figure 2 shows the unit, the rectangular box left of the center of the image, attached to the IBEX-Lo prototype of the Interstellar Boundary Explorer (IBEX) [8] installed in the MEFISTO calibration facility.

A neutral atom beam is produced by reflection of a low energy positive ion beam from a single crystal tungsten surface with (110) surface orientation, polished better than $0.03\mu m_{rms}$. Most ions are neutralized (>90 %) and molecules mostly dissociate upon reflection allowing to use positive molecules as primary particles as well. Molecular ions are produced very efficiently in the CASYMS ion source. The particles experience an energy loss of 11% to 15 % upon reflection. After reflection the remaining charged particles are removed by an electrostatic deflection system. Collimation plates reduce the angular spread of the neutral beam. The result is a divergent neutral beam with a broadened energy distribution.

Possible neutral particles originating from grids in the ion beam line are absorbed in the electrostatic analyzer (ESA) in front of the neutralization surface. This ESA also allows to bend the incident ion beam such that the resulting exiting neutral beam axis is parallel to the incident ion beam axis. A hole in the lower ESA plate allows to separate incident fast neutral particles such that they do not have the possibility to get reflected at the outer ESA plate to the exit of the ESA as ions and to broaden the energy distribution of the produces neutrals. For low energy neutrals (<500 eV) the ion beam energy from the MEFISTO source was held fixed and the neutralizer box was floated to a variable high voltage instead. This allowed to keep the primary ion beam intensity and beam profile from the MEFISTO source constant and to select the neutral beam energy by changing the neutralizer float voltage. The voltage at the ESA plates is adjusted to match resulting ions energy. Neutral Hydrogen down to 10 eV could be produced this way.

Characteristics

The profile of the neutral beam was measured by placing an imaging micro channel plate (MCP) detector (Quantar Technology Inc, CA, USA, Model 3395A-SE/2401B) at various positions behind the exit of the neutralizer. A beam divergence was 18° FWHM in one direction and collimated down to 4.6° FWHM in the other direction by the exit aperture. A typical beam profile measured using 1 keV He^+ primary ions is shown in Figure 3. The transmission of the device was measured for 1 keV He^+ primary ions by comparing the incident ion flux with the neutral flux measured at the MCP detector. The transmission of the device was found to be 0.0054 ± 0.001 at 1 keV, the uncertainty mostly due to the detection efficiency of the MCP. At lower energies direct measurement of the neutral particle flux

gets increasingly difficult as the detection efficiency of the MCP detector is more and more uncertain. However, as almost all ions are neutralized at the tungsten surface, the transmission is determined mainly by the scattering properties of the neutralization surface. Scattering and neutralization properties of the tungsten neutralization surface were measured before in the Imager for Low Energy Neutral Atoms (ILENA) facility at the University of Bern [16]. Figure 4 depicts an angular scattering profile of a highly polished tungsten W(110) surface at an angle of incidence of 82° to the surface normal. This scattering profile is obtained after heating the tungsten surface to more than 1000°C. As the beam neutralizer unit may be floated to high voltage to decelerate the incoming ion beam, heating is not available at the neutralization surface. This results in a broader angular scattering because of the presence of contaminants on the scattering surface which results in a reduced transmission of the device. The flux into the solid angle of acceptance of the charged particle deflection section increases for lower energies as shown in Figure 5 for an angle of incidence of 85° to the surface normal. The absolute transmission of the complete unit was measured using 1000 eV He^+ primary ions by comparing the primary ion flux with the emerging neutral flux, both measured using the MCP detector. Differences in the detection efficiency between neutrals and positive ions were neglected at this energy. A transmission of 0.0054 $\pm$0.001 was obtained. The changes in the shape of the scattering cone produced by primary H^+ions at different energies were used to infer the transmission at lower energies. The narrower scattering cone at lower energies results in an increase of the transmission up to 0.013 at 200 eV as shown in Figure 6. At even lower energies the transmission does not increase anymore as most particles are already collected. In floated operation mode, the defocusing of the primary beam in the deceleration stage in front of the neutralizer must carefully be included into the determination of the total transmission.

A typical energy distribution of the neutral particles is shown in Figure 7. The neutral energy distribution is asymmetric and has a tail towards lower energies. For 1500 eV primary H^+ ions, an energy loss of 11% and a width of 11% FWHM of the primary energy was found. For Hydrogen, the energy distribution of the produced neutrals scales roughly with primary ion energy between 10 eV and 1500 eV incident ion energy, however at energies below 300 eV the mean energy loss increases to about 15% and the width of the distribution to about 15% FWHM of the incident ion energy. The measured energy distribution is similar to energy distributions obtained with similar geometries from other surfaces [16, 17].

Conclusion

We built a portable device to neutralize an ion beam. The device may easily mounted into existing calibration facilities and requires except of high voltages no additional resources for operation. A neutral hydrogen beam over a wide energy range of 10–1000 eV could be produced. The ion beam neutralizer was successfully used for the characterization of the Neutral Interstellar Composition Experiment (NICE) [18] and the prototype of the IBEX-Lo sensor of the Interstellar Boundary Explorer (IBEX) [8].

Acknowledgments

This work was supported by the Swiss National Science Foundation.

[1] H.-J. Fahr. Global structure of the heliosphere and interaction with the local interstellar medium: three decades of growing knowledge. *Adv. Space Research*, 34:3–13, 2004.

[2] G. E. Thomas. The insterstellar wind and its influence on the interplanetary environment. *Ann. Rev. Earth Planet*, 6:173–204, 1978.

[3] G. P. Zank and H. L. Pauls. Modelling the Heliosphere. *Space Sci. Rev.*, 78:95–106, 1996.

[4] M. Gruntman, E.C. Roelof, D.G. Mitchell, H.J. Fahr, H.O. Funsten, and D.J. McComas. Energetic neutral atom imaging of the heliospheric boundary region. *J. Geophys. Res.*, 106(A8):15767–15781, 2001.

[5] P. Wurz. *The outer Heliosphere: Beyond the Planets*, chapter Detection of Energetic Neutral Particles. Copernicus Gesellschaft e.V., 2000.

[6] M. Witte, H. Rosenbauer, E. Keppler, H. Fahr, P. Hemmerich, H. Lauche, A. Loidl, and R. Zwick. The interstellar neutral-gas experiment on ULYSSES. *Astronomy and Astrophysics*, 92:333–348, 1992.

[7] T.E. Moore, D.J. Chornay, M.R. Collier, F.A. Herrero, J. Johnson, M.A. Johnson, J.W. Keller, J.F. Laudadio, J.F. Lobell, K.W. Ogilvie, P. Rozmarynowski, S.A. Fuselier, A. G. Ghielmetti, E. Hertzberg, D.C. Hamilton, R. Lundgren, P. Wilson, P. Walpole, T.M. Stephen, B.L. Peko, B. van Zyl, P. Wurz, J.M. Quinn, and G .R.Wilson. The Low-Energy Neutral Atom Imager for IMAGE. *SpaceSci. Rev.*, 91:155–195, 2000.

[8] D. McComas, F. Allegrini, P. Bochsler, M. Bzowski, M. Collier, H. Fahr, H. Fichtner, P. Frisch, H. Funsten, S. Fuselier, G. Gloeckler, M. Gruntman, V. Izmodenov, P. Knappenberger, M. Lee, S. Livi, D. Mitchell, E. Möbius, T. Moore, D. Reisenfeld, E. Roelof, N. Schwadron, M. Wieser, M. Witte, P. Wurz, and G.P. Zank. The Interstellar Boundary Explorer (IBEX). In V. Florinski, N.V. Pogorelov, and G.P. Zank, editors, *Physics of the Outer Heliosphere: Third International IGPP Conference*, pages 162–181. AIP Conference Proceedings 719, 2004.

[9] A. G. Ghielmetti, H. Balsiger, R. Bänninger, P. Eberhardt, J. Geiss, and D. T. Young. Calibration system for satellite and rocket-borne ion mass spectrometers in the energy range from 5 eV/q to 100 keV/q. *Rev. Sci. Instrum.*, 54:425–436, 1983.

[10] A. Marti, R. Schletti, P. Wurz, and P. Bochsler. New Calibration Facility for Solar Wind Plasma Instrumentation. *Rev. Sci. Instr.*, 72(2):1354–1360, 2001.

[11] N.G. Utterback and G.H. Miller. Fast Molecular Nitrogen Beam. *Rev. Sci. Instr.*, 32:1101–1106, 1961.

[12] T.M. Stephen, B. van Zyl, and R.C. Amme. Generation of a Fast Atomic-Oxygen Beam from O^- Ions by Resonant Cavity Radiation. *Rev. Sci. Instrum.*, 67:1478–1482, 1996.

[13] W. Eckstein. *Inlastic Particle-Surface Collisions*, volume 17, chapter Charge fractions of reflected particles, pages 157–183. Chemical Physics, 1981.

[14] A. Losch and H. Niehus. Structure analysis of the KBr(100) surface - An investigation with a new method for surface analysis on insulators. *Surf. Sci*, 420:148–156, 1999.

[15] A. Losch and H. Niehus. NICASS - A new method for Surface Structure Analysis. *Phys. Stat. Sol.*, 173:117–121, 1999.

[16] M. Wieser, P. Wurz, K. Brüning, and W. Heiland. Scattering of atoms and molecules of a magnesium oxide surface. *Nucl. Instr. Meth. B*, 192:370–380, 2002.

[17] S. Jans, P. Wurz, R. Schletti, K. Brüning, K. Sekar, W. Heiland, J. Quinn, and R.E. Leuchter. Negative ion production by surface ionization at barium zirconate surface. *Nucl. Instr. Meth. B*, 173:503–515, 2001.

[18] M. Wieser, P. Wurz, P. Bochsler, E.Moebius, J. Quinn, S.A. Fuselier, A. Ghielmetti, J.N. DeFazio, T.M.Stephen, and R.J. Nemanich. An instrument for direct mass spectrometric measurement of interstellar neutral gas. *Meas. Sci. Tech.*, submitted, 2005.

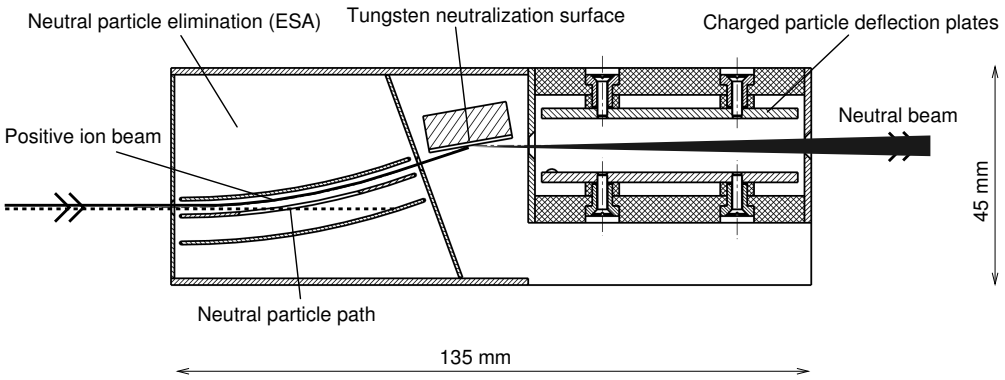

Figure 1. Ion beam neutralizer. Positive ions enter the system from the left. The electrostatic analyzer (ESA) separates any neutrals in the primary beam. Ions are neutralized by reflection at grazing incidence on a polished tungsten single crystal. After reflection, charged particles are removed by the charged particle deflection system on the right side resulting in a completely neutral particle beam.

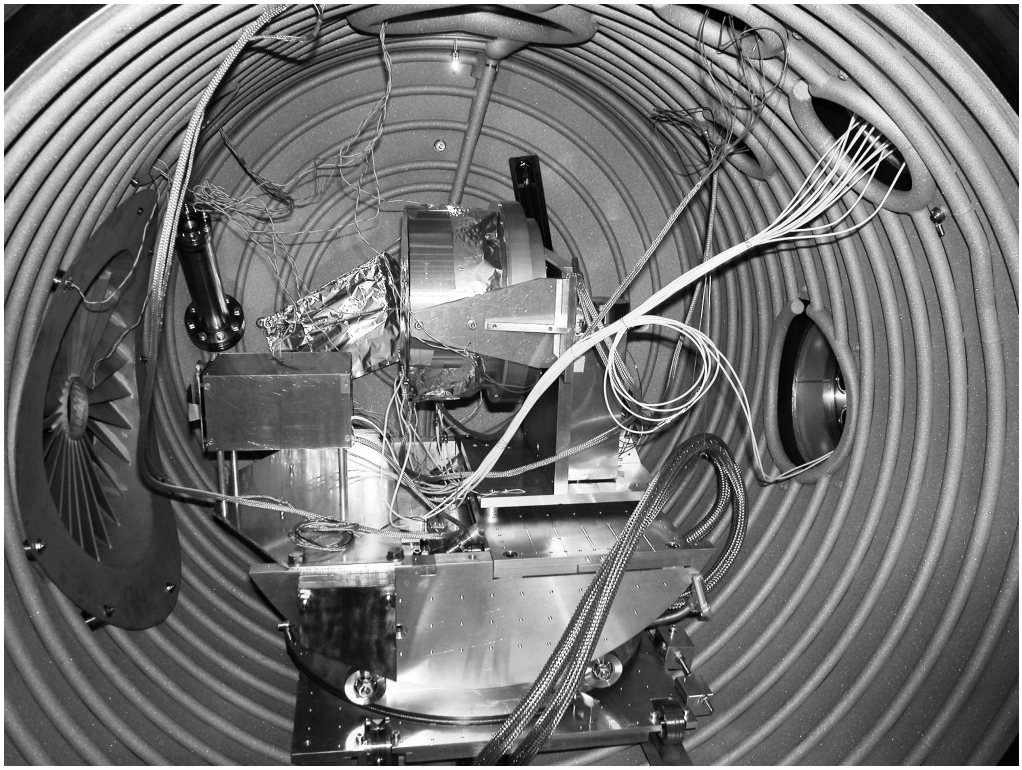

Figure 2. Ion beam neutralizer, inside the rectangular box left of the center serving as high voltage shield, installed in the MEFISTO calibration facility of the University of Bern, Switzerland. The ion beam enters the chamber from the left through the fan shaped opening. The installed instrument is the IBEX-Lo prototype of the Interstellar Boundary Explorer mission IBEX [8].

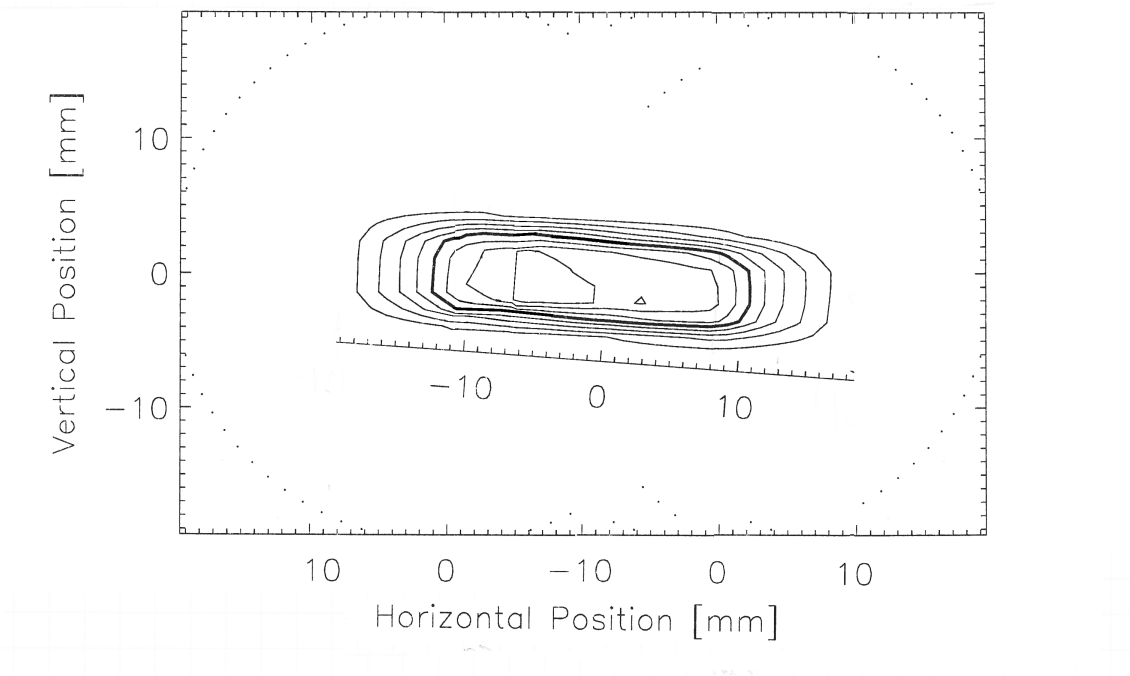

Figure 3. Neutral beam profile at 25 mm distance of neutralizer exit aperture. The lines are equidistant in intensity, the 63% level is marked in bold.

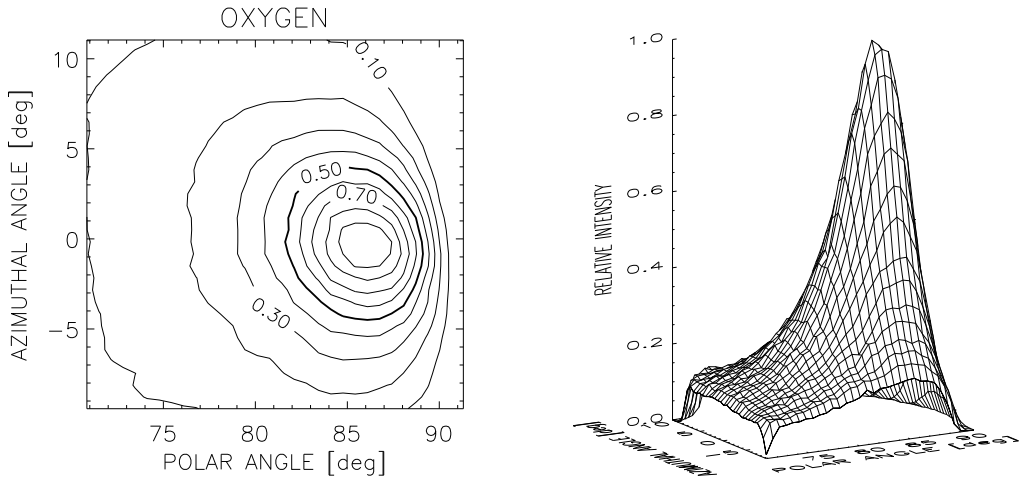

Figure 4. Angular scattering profile obtained from scattering 780 eV per molecule O_2^+ of an highly polished W(110) surface at 82° angle of incidence.

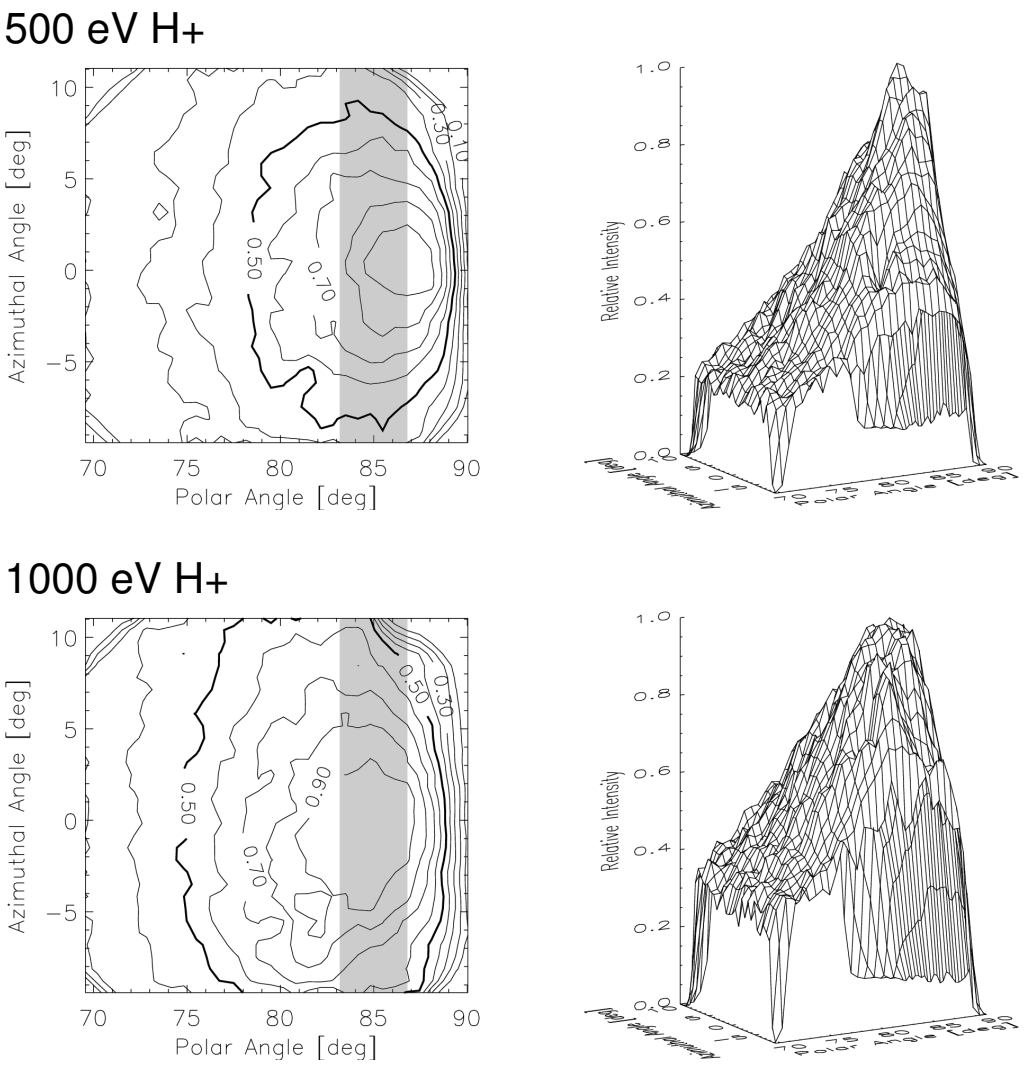

Figure 5. Angular scattering profiles obtained from scattering 1000 eV and 500 eV per atom H^+ ions of an unheated highly polished W(110) surface at 85° angle of incidence. Angular scattering is wider than what was obtained from a heated surface as shown in Figure 4. The solid angle of acceptance of the charged particle deflection section is shown as gray rectangle. At lower energies more particles are scattered into acceptance region.

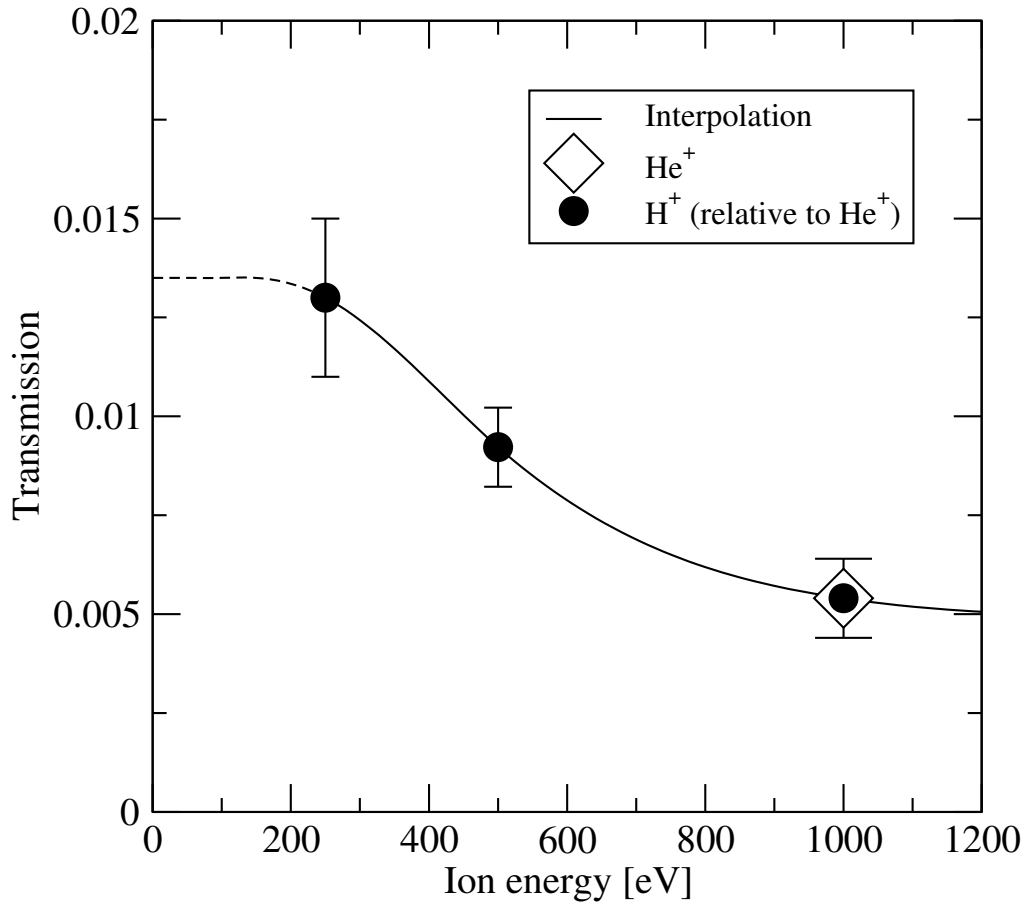

Figure 6. Transmission of the ion beam neutralizer unit. The value at 1000 eV was absolutely measured using He^+primary ions. The changes in the shape of the scattering cone obtained from H^+primary ions were used to calculate the changes in the transmission at lower energies. Below 200 eV the transmission is expected not increase anymore as most neutral particles are already collected.

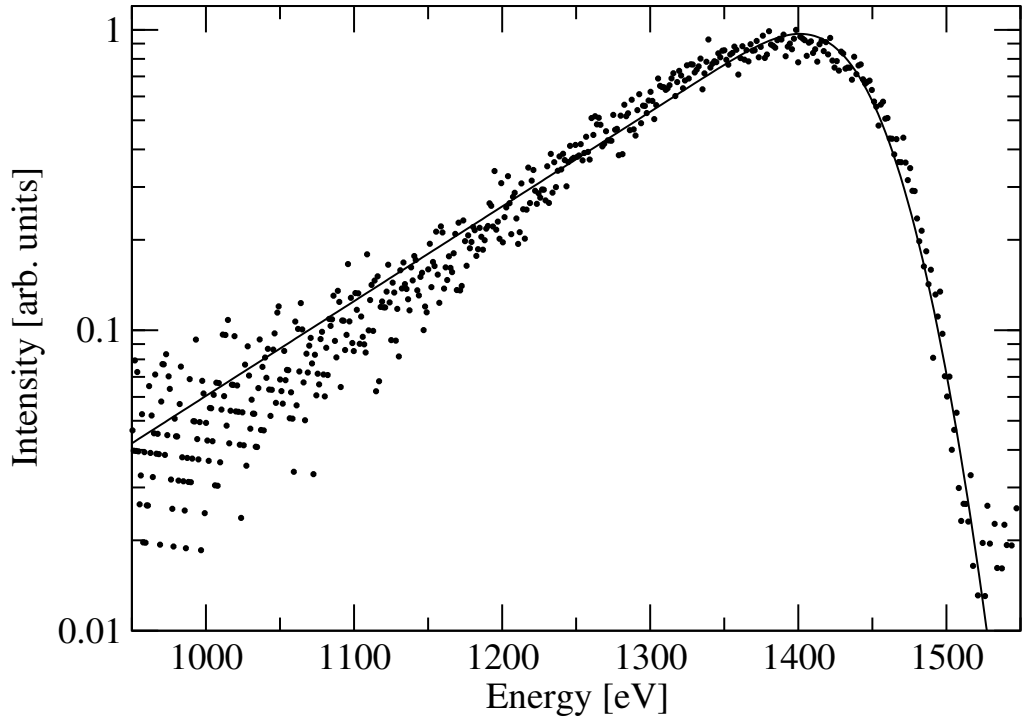

Figure 7. Energy distribution of neutral particles hydrogen reflected off an unheated tungsten derived from a time of flight spectrum. A mono-energetic 1500 eV H^+primary beam at an incidence angle of 85° to the surface normal was used with the time-of-flight detector placed in the specular reflection direction. The mean energy loss obtained is 11 % of the primary energy at a width of the distribution of 11% FWHM of the primary energy. The solid line is a fit to the data and is shown to guide the eye.

Part II

Ion-Optical Design

Chapter 4

Computer Based Optimization of Ion-Optics

4.1 Introduction

Increasingly demanding and complex ion-optical designs used for space instrumentation result in prolongened development times for ion-optical parts. Analytical design solutions are often not available or too complicated to be used. A development scheme based on numerical methods was contrived able to run on a powerful desktop computer: Ion-optical simulation software was combined with custom made optimization modules resulting in a software package that allows to semi-automatically optimize an ion-optical design on a numerical basis. Starting from a initial design a simplex optimizing algorithm modifies the geometry, material properties, magnetizations, and electric potentials to get an improoved version of the design. A key aspect of this design approach is the definition of a well suited objective function to evaluate the performance of a design variant. A description of the ion-optical optimizer along with a reference implementation including an example and applications is presented in the Section 4.2.

4.2 Paper: A software package to automatically optimize ion-optics

M. Wieser and U. Rohner

(To be submitted)

A software package to automatically optimize ion-optics

M. Wieser and U. Rohner

8th May 2005

University of Bern, Physikalisches Institut, Sidlerstrasse 5, 3012 Bern, Switzerland

Abstract

We report the development of a software environment to automatically optimize ion-optical designs. The implementation is based on the SIMION ion-optical simulation package but might be easily extended to support other ion-optical simulators. Several mass spectrometers for application in space were designed using this software and simulation results were successfully verified by hardware built according to these optimization results. The time needed to finalize a design of average complexity could be shortened from the order of typically one year down to a few weeks.

1 Introduction

Development of ion-optics used for mass spectrometers for space instrumentation has become increasingly complex in recent years. Miniaturization, very strict mass margins, expected higher performance than previous designs, and tighter schedules until delivery require new approaches for the design process. Conventional analytical design methods reach their limits because often analytical description of a design no not exist.

We present a novel approach combining ion-optical simulation software with automated optimization procedures. The approach allows to optimize the geometry of the design and the electric and magnetic fields by minimizing an objective function. This function evaluates the quality of a specific design variant, it may rely on any criterion, i.e, transmission, focusing, mass resolution, time-of-flight, or a suitable combination. Depending on the calculated value an optimizer algorithm changes the design geometry, electrode potentials or magnetic fields to get a better design variant.

The described implementation is based on the SIMION ion-optical simulation package. Three mass spectrometers, the Laser Mass Spectrometers LMS 1 [1] and LMS 2 [2], and the low-energy sensor of the Interstellar Boundary Explorer (IBEX) [3], were successfully designed and optimized using this implementation of the optimizer. In all three cases the simulation result was successfully verified with measurements obtained from hardware prototypes.

2 Optimizer Process

In order to optimize a design its geometry must be defined in a parametrized form. This allows the optimizer process to change geometrical dimensions to improve the quality of the solution. It is important that the geometry parametrization is stable even when dimensions change; i.e., that no volume is occupied twice. The choice of what is a free parameter is crucial as it has a direct impact on the quality and speed of the optimization. Fixed and variable electrostatic electrode potentials and direction and amplitude of any magnetizations must be defined and included into the geometry model. For practical reasons, the parameters are grouped into parameters describing the geometry and magnetization g_i and parameters describing electrostatic potentials of electrodes p_j with i and j the index of the parameter within the group. Each design variant is described by a vector $\mathbf{a} = (g_1 \dots g_{imax}, p_1 \dots p_{jmax})$. The two subspaces are optimized separately. Separation of the parameter space into sub domains is normally not a good idea [4]. However, for reasons described below it simplifies the optimizations process considerably. The quality or performance of a specific design is assessed by a

scalar objective function $z(\mathbf{a})$. The optimizer process minimizes the value of this function by changing the components of **a**. Typical design properties used in the object function include ion-optical transmission, time-of-flight resolution, energy, and mass resolution. The value of the objective function is calculated by evaluating particle trajectories within a specific design variant. A large enough number of test particles is needed to obtain reasonable statistics. Depending on geometry and objective function more than 100'000 test particles could be necessary to evaluate each individual design variant **a**.

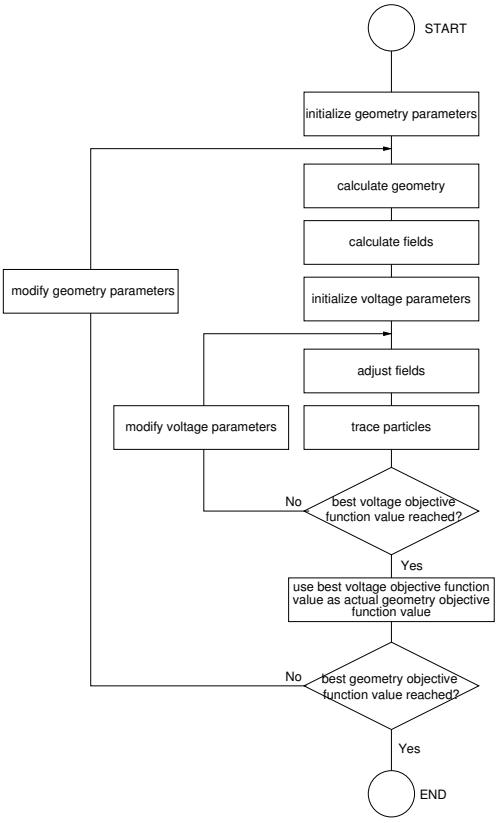

Figure 1: Optimizer program flow.

Figure 1 shows an overview of the optimization process. A ion-optical design is optimized using a two stage process: an inner loop optimizes electrostatic potentials and an outer loop optimizes geometric elements and magnetic fields. While optimizing potentials p in the inner loop, the geometry parameters g of the outer loop are held constant. The best objective function value from the optimization of the potentials p is then used as the objective function value describing the

geometry g and used in the outer loop. The geometry is then changed accordingly for the next iteration. The separation of p and g is needed as any change in geometry requires a recalculation of the electric and magnetic field distributions, whereas for a change of an electrode potential the electric field is calculated very fast due to the fact that the electric potential Φ can be calculated as a sum of the individual potential contributions of each electrode which were calculated separately in first place:

$$\Phi = \Phi_0 + \sum_{k=1}^{jmax} p_k \cdot \Phi_k \tag{1}$$

with Φ_0 the sum of all potentials with a constant value, Φ_k the electric potential generated by the electrode k for a normalized potential (usually 1 V), and p_k the scaling factor for that potential which is equivalent to the electrode potential as long Φ_k is normalized to 1 V. A change in geometry or in magnetization requires to solve the electric and magnetic field differential equations from scratch which is very slow compared to Equation 1 and thus performed as few times as possible.

Different optimization algorithms can be used for the two loops. However, the number of evaluations of the objective function should be kept at an absolute minimum. The simplex algorithm [5] was chosen for implementation because it needs only a few evaluations of the objective function to get an improved solution, it needs no knowledge about the derivatives of the objective function and it is rather simple to implement. As the number of free parameters increases, the simplex algorithm gets less efficient as it gets easier to converge to a local extremum or not to converge at all because of the many dimensions of the parameter space. For less than 10 free parameters for geometry or potentials, good convergence could be obtained most of the time. Alternative algorithms investigated were Particle Swarm Optimizer (PSO) [6], Random [7], Rosenbrock [8], and CONDOR [4]. PSO and Random need many evaluations of the objective function and are thus less efficient as the objective function is computationally expensive. Rosenbrock suffered from convergence problems. CONDOR, a thrust region algorithm optimized for expensive and noisy objective functions, is a promising algorithm. Its larger complexity made it less suited for a first implementation of the optimizer however.

3 Objective Functions

A good choice of the objective function z is essential for a good optimization. As long as only a single property D of a design has to be maximized, e.g., overall transmission, a linear objective function suits well:

$$z = -D \tag{2}$$

The advantage of this type of objective function is that no knowledge about the actual value of D is needed. Note the minus sign which shows that z has to be minimized in our implementation. When m properties D_n of a design need to be considered they can be combined as follows:

$$z = -\prod_{n=1}^{m} D_n \tag{3}$$

as long as all values of each factor D_n are suitably scaled or normalized.

Each factor D_n is calculated from test particles traced through the design and by evaluating their trajectories. The definition of D_n should result in a smooth function with the derivative nowhere zero except at the maximum value. In a realistic design different criteria may apply to the properties considered. It is often desired to keep a property above or below a certain limit whereas an other property has to be maximized. Table 1 shows prototype functions successfully used in different applications.

4 Implementation

The optimizer package consists of several modules: the geometry optimizer program which performs the optimization of the outer loop shown in Figure 1, the voltage optimizer program doing the same for the inner loop, the ion-optical simulation program performing the actual field and particle tracing calculations, a geometry test module used to easily verify parameterizations of the design without the need to launch an optimizer module, auxiliary programs needed for inter module communication, and offline data analysis tools. The implementation of each of these modules is more or less independently and modules can be exchanged to accommodate for different computer architectures and operating systems.

The implementation described here runs on a single computer using the SIMION simulation package [9] running on a Windows™ operating system. Using SIMION is advantageous as its field solver is very fast and well tested. The graphical user interface allows to interactively test geometries. However, SIMION only provides partial support for completely automated simulations using SIMION user programs. Important functions as loading a new geometry into simulation space or starting the execution of a user program can only be done by sending keyboard events to the graphical user interface of the program. This was accomplished using a keyboard event recorder and replayer program [10]. To prevent interference with the physical mouse and keyboard during the simulations

the complete environment was placed inside a VMWARE [11] virtual computer environment (less than 2 % of CPU-time loss compared to a native run without VMWARE). This allowed to detach the physical input devices from the simulation environment. The two optimizer modules and the geometry test module were implemented using the C-programming language for portability to other operating systems and environments.

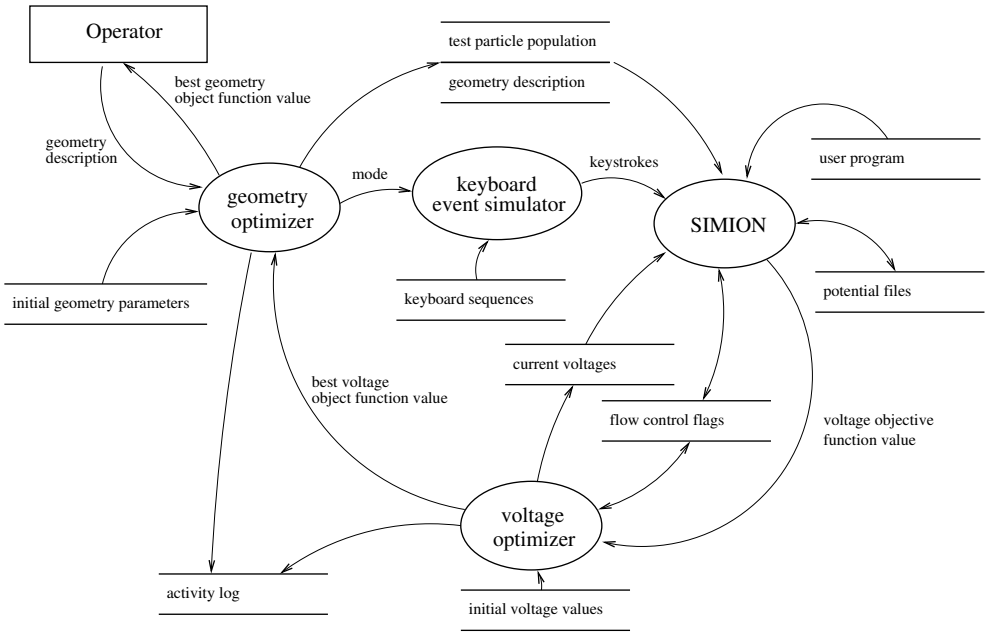

Figure 2: Data-flow of the implementation of the optimizer using SIMION.

Figure 2 shows the data-flow between the optimizer modules for this implementation. The initial geometry description is fed into the geometry optimizer. The geometry optimizer first generates a description of the geometry and the test particle population for SIMION and then launches SIMION and the keyboard event simulator. The later will open the geometry definition within SIMION and initiates the calculation of the potentials and also loads the SIMION user program. After completion of the potential field calculation the control is handed over to the voltage optimizer which will provide the values of the electrode voltages to the SIMION user program by means of a text file. The user program loads the electrode voltages specified in this file and starts the simulation using the test particle population created earlier. After completion of the simulation a objective function value z is calculated by the SIMION user program and returned to the voltage optimizer. The voltage optimizer will calculate new electrode voltages

depending on the returned objective function value or, when the optimum value of the objective function is reached, terminate the SIMION program using the keyboard event simulator and return the control with the best objective function value obtained to the geometry optimizer. The later will then modify the geometry definition, recreate the test particle population fitting to this geometry and launch SIMION again with this new modified geometry. This loop is executed until the best geometry is found or the user decides to change the parametrization of the problem. As a support for the user in in finding the best parametrization of the problem, information about the history of the optimization is collected in all steps and written to log files.

5 Example: Einzel lens

To illustrate the implementation a simple geometry is optimized: In an axial symmetric arrangement a circular parallel positive charged ion beam with $E/q = 10\,\mathrm{eV}$ and a diameter $d_{in} = 10\,\mathrm{mm}$ has to be focused onto a channel plate detector with a diameter $d_{det} = 2\,\mathrm{mm}$ with a time-of-flight dispersion Δt_0 as small as possible and a total transmission T as high as possible. Good spatial focusing and low time-of-flight dispersion are contradictory requirements: with the lens potential at zero volts the time-of-flight dispersion is zero because the beam remains parallel but the overall transmission is low. The transmission may be increased by increasing the lens voltage but this introduces considerable time-of-flight dispersion. A carefully chosen objective function will balance these two competing effects.

Figure 3 shows the initial geometry prior to the optimization. The setup contains five free geometry parameters g_1 to g_5 and one free electrostatic electrode potential p_1. The potentials of the two outer lens electrodes and the detector are kept constant at zero volts. The detector position relative to the center of the lens is fixed, also the start position of the ions (distance detector – ions start point $= 80\,\mathrm{mm}$). Note that the detector is located in a distance of the lens that makes the thin lens approximation for the lens invalid. The quality of a solution is evaluated by flying a set of test particles covering the whole lens entry aperture area starting from the left and by recording the position and timing information when they hit the detector plane on the right. The objective function z has to be minimized and is the product of a factor describing the radial dispersion D_r and a factor describing the dispersion in the time domain D_t:

$$z = -D_r \cdot D_t \tag{4}$$

For an optimal design both factors must be maximized. The influence of each individual factor on the result was evaluated by using alternative objective functions containing only one of the two factors

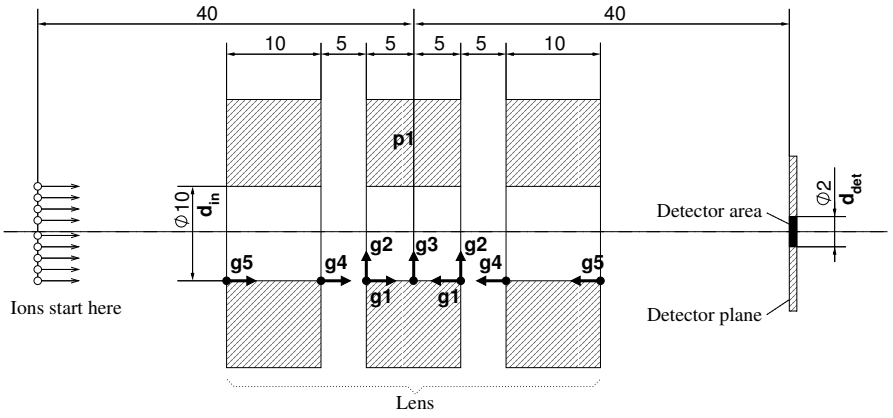

Figure 3: Drawing of the initial geometry. Free geometry parameters are indicated by arrows. The arrows point in the direction. where the corresponding parameter is positive. All potentials except the center electrode p_1 are kept at 0 V. Test particles start from the left and should hit the detector area indicated as black area on the right. All units are given in mm.

$$z_r = -D_r \tag{5}$$

and

$$z_t = -D_t \tag{6}$$

D_r represents the radial distribution at the detector and is calculated as follows

$$D_r = \frac{1}{n}\sum_{i=1}^{n} e^{-\frac{y_i^2}{\omega_0^2}} \tag{7}$$

with n the total number of test particles flown, ω_0 describing the radial width of the radial weighting function, and y_i the radial distance of the point where the test particle hit the detector in respect to the axis of symmetry. A simple box function could have been used also instead of the Gaussian - the box function however has the disadvantage that its value does not change as long a particle hits the area outside the detector area and can thus not provide any information to the optimizer how badly the detector was missed. $\omega_0 = 0.2\,\text{mm}$ was chosen to describe the desired spatial distribution.
The time dispersion D_t is evaluated as follows

$$D_t = \frac{1}{e^{\frac{\sigma_t - \Delta t_0}{k}} + 1} \tag{8}$$

with k a constant, Δt_0 the desired (maximal) time dispersion and σ_t the standard deviation of the particle travel times to the detector in ns of all particles that hit the detector plane at a distance $y < d_{det}$ from the symmetry axis. Particles that hit the detector plane outside the detector area do not contribute to D_t as they are not detected. The value of k has a large influence on the convergence rate of the process. $k = 5\,\text{ns}$ combined with $\Delta t_0 = 20\,\text{ns}$ was chosen as a good balance between a strict interpretation of Δt_0 and a good convergence rate.

The results of three optimization runs with the three different objective functions from Equation 4 to 6 are shown in Figure 4.

When considering only temporal focusing as shown in Figure 4a), the optimizer sets the lens voltage to zero volts to get a parallel beam avoiding any dispersion in time domain. The resulting transmission is low as no focusing takes place. Changes in the geometry have no influence on the objective function as long the detector area is not shadowed by the inner lens electrode. The geometry optimizer gave up soon as no change in the value of the objective function could be obtained by changing the geometry parameters. The required number of iterations in such a case could be further minimized by a better stop criterion.

When only considering spatial focusing as in Figure 4b), the transmission is increased to unity but also a considerable time dispersion occurs.

Both temporal and spatial focusing are included in the objective function for the data shown in Figure 4c). The voltage optimized solution for the initial geometry shows considerable spatial defocusing. The solution is not that bad however as particles that hit the detector plane inside the detector area are separated in time domain from those that hit the detector plane outside the detector area. After 64 iterations of the geometry optimizer both the temporal and spatial focusing has improved, slow particles were moved outside the detector area whereas those remaining inside were moved closer to the center. This, however, by reducing the transmission of the system slightly.

The three examples of the objective function show that is important to review the results produced by the optimizer. Depending on the results both the objective function and the parametrization of the geometry could require modifications in order to produce an optimized result.

6 Applications

Several ion-optical designs were optimized using the described procedure. In all cases the development time for the ion optics could be reduced from the order of one year or more for manual optimization down to a few weeks using the optimizer. In all cases the predicted performance was successfully verified by measurements from prototypes.

Laser Mass Spectrometers LMS 1 [1] and LMS 2 [2], both time-of-flight mass spectrometers (tof-ms), were optimized for transmission and time–of–flight resolution. LMS 1 is an axial-symmetric single reflectron tof-ms with a size of 15 cm, e.g., the size of a soda can. It was designed for the BepiColombo lander (Mercury Surface Element MSE) [12] and should resolve all chemical elements and their major isotopes from the top surface of the planet (regolith). A small part of the regolith had been ionized by a short laser pulse, wheres the mass spectrometer had to resolve the composition out of this ion plume. To get a sufficient high transmission, the ions with their large energy spread caused by the laser induced plasma had to be guided into the spectrometer and for a good mass resolution, focused in time onto the detector. As a boundary condition, all voltages of the spectrometer had to be kept below 500 V (except detector) to save power, mass and space. Also the maximal number of independent electrodes was fixed to 5. Another boundary condition was its size - 15 cm in height and 6 cm in diameter was the maximal allowed size; the performance of a tof-ms can be increased by enlarging the length of the drift path and so increase the time-of-flight of the ions, usually at the extent of increased instrument mass, however. The simulated mass resolution $\mathrm{m}/\Delta\mathrm{m}$ at a 50 % level of the initial geometry was 250 with an ion-optical transmission $T = 10\,\%$ with all voltages optimised and using the whole detector-area. The optimised geometry had a simulated mass resolution of more than 1000 with $T = 4\,\%$ when using the whole detector-area and a simulated mass resolution of 1500 with $T = 1\,\%$ when using only one of the five anodes. The experimentally found mass resolution of the laboratory prototype was above 600.

LMS 2 is a cigarette-box sized double reflectron tof-ms with a size of 7 cm x 3 cm x 1.5 cm (estimated 7 cm x 3 cm x 4 cm with electronics). It was designed for the rover of the BepiColombo MSE. With the same ion-source as in LMS 1, it had been able to resolve the elemental composition of Mercury's surface. The mass resolution prior to the optimisation was below 100 with $T < 1\,\%$. Due to the complexity and limited computer-memory, the whole spectrometer could not be optimised with our optimiser at once - therefore, single ion-optical elements as lenses and the reflectron or the position of the electrostatic analyser or its apertures were optimised iteratively. With the optimisation, the simulated resolution could be increased to above 500 with $T = 1.9\,\%$, depending on the assumed ion-plume parameters[2]. The measured mass resolution was therefore 180 for a multi-shot spectrum (averaged single shots) and 400 for single shots.

The IBEX-Lo sensor of the Interstellar Boundary Explorer mission [3] was optimized for high transmission in consideration of additional mechanical and ion-optical constraints. IBEX-Lo is an axial symmetric single pixel camera for low-energy neutral atoms. It features a ring shaped entry aperture of 26.6 cm outer diameter and $118\,\mathrm{cm}^2$ open area. Particles enter through a collimator for charged particle suppression and field of view determination. Neutral particles

are converted to ions on a conical charge conversion surface, collected by a polodial energy analyser, and finally detected by a time–of–flight detector in the center. The conversion surface section and the polodial energy analyser were optimized for high transmission at a given energy resolution and and considering realistic particle scattering properties at the conical conversion surface. At an energy resolution $m/\Delta m \approx 2$ about 50 % of the particles ionized at the conversion surface are collected compared to less than 10 % prior optimization. The optimizer was also used to reduce the number of electrodes and to simplify their shape while keeping the performance of the design. The simulation results were successfully verified by measurement data obtained from a hardware prototype.

7 Discussion

Computer optimization allows to develop more complexe ion-optical designs in a much shorter time compared to conventional methods. The method was successfully applied for several completely different mass spectrometers [1, 2, 3] and the calculated solutions always agreed very well with measurements obtained from built laboratory prototypes.

For good performance the objective function must be carefully selected and its value periodically reviewed. The parametrization of a design and the objective function should be adapted as the solution evolves. A total of 10 to 15 free geometry parameters at a time proved to be an upper limit for a fast convergence. For more parameters it gets more and more difficult to identify stable solutions. It is important to use enough test particles to get meaningful statistics as all performance parameters are estimated from this set of test particles. If too few test particles are used, the optimizer might adapt the design for the small test particle population and the calculated performance will drop as soon as a larger set of test particles is used. The objective function should be smooth in the parameter space for best stability of the optimizer.

The single computer implementation is advantageous as it runs on an ordinary office computer. The described implementation with SIMION is basically limited by the available computing power and the difficulty to include magnetic fields into the SIMION environment. To avoid these restrictions the optimizer can be adapted to other ion-optical simulation packages as long as the package provides a way to do simulations automatically without user intervention.

Such an alternative implementation of the ion-optical optimizer was done using the TRACE ion-optical simulation package [13] on a cluster computer. The simulation part of TRACE is completely command-line driven making the keyboard event simulator used for the SIMION implementation unnecessary. This was offset by the added complexity of managing the computation tasks distributed

to many computation nodes. The portability of the ion-optical optimizer design to other platforms and other ion-optical simulators could be illustrated with this alternative implementation.

8 Conclusion

Computer optimization of ion-optical designs is a powerful tool to speed up the development process and to get better designs. We developed and successfully used an ion-optical optimizer for the development of mass spectrometers for use in space. The numerical approach combined with fast computers allowed to explore new unconventional designs and optimize their performance. In all cases the development time could be shortened considerably.

Acknowledgements

The authors thank Peter Wurz and Christian Sigrist for their support. This work was supported by the Swiss National Science Foundation.

Desired behaviour	Factors D of objective function
Focus all n particles on region around $x = 0$ in phase space (box version)	$D = \frac{1}{n}\sum_{i=1}^{n}[1 - \mathrm{H}(\lvert x_i\rvert - x_0)]$ H Heaviside step function x_0 region size x_i distance of particle from phase space center
Focus all n particles on region around $x = 0$ in phase space (Gaussian version)	$D = \frac{1}{n}\sum_{i=1}^{n} e^{-\frac{x_i^2}{\omega_0^2}}$ ω_0 area size x_i distance of particle from phase space center
Keep a property d below a threshold t_0 (step version)	$D = 1 - \mathrm{H}(d - t_0)$ H Heaviside step function t_0 threshold value d performance parameter, e.g., average value or standard deviation.
Keep a property d below a threshold τ_0 (Fermi version)	$D = \frac{1}{e^{\frac{d-\tau_0}{k}}+1}$ τ_0 threshold value k threshold 'softness' $(k > 0)$ d performance parameter, as above.
Change the weight of a performance parameter d	$D = b\,d^a$ a weight b normalization d performance parameter, as above.

Table 1: Sample functions used for objective function evaluation.

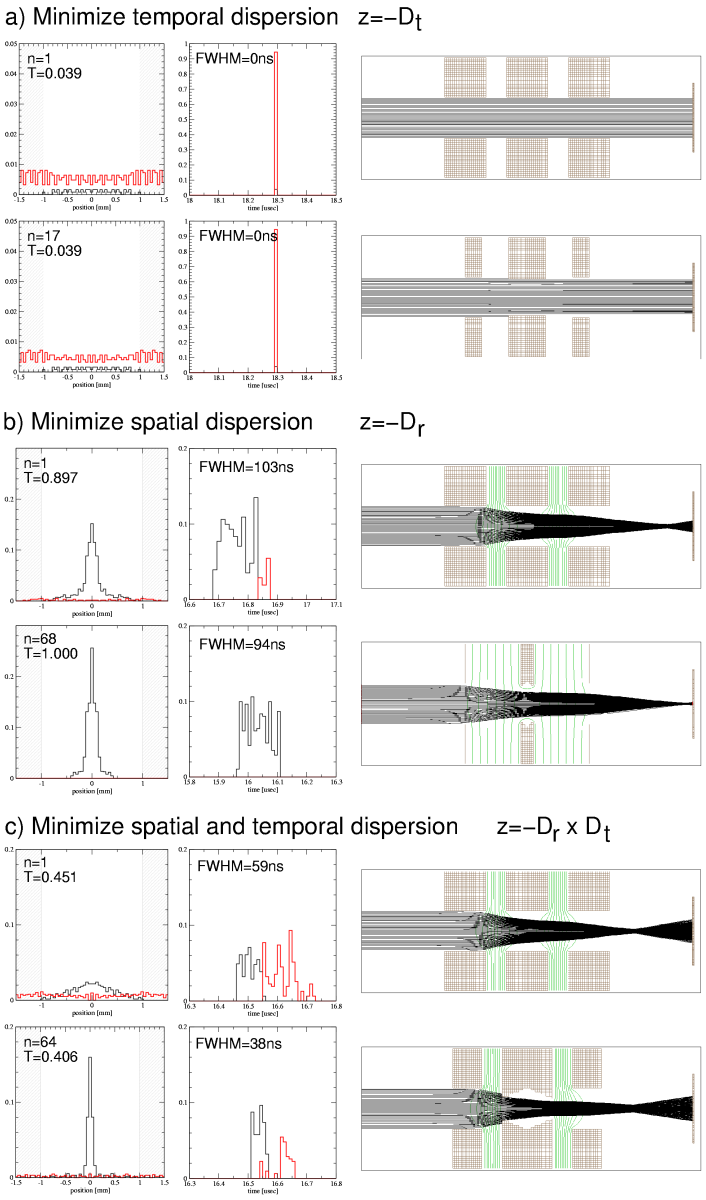

Figure 4: Optimized einzel-lens for three different objective functions. In the upper row of each sub-figure data obtained from optimizing the lens voltage only is shown compared to the lower row where both geometry and potentials where optimized. In each row, the spatial count distribution collapsed to one axis is shown in the left plot whereas the distribution of the time–of–flight is shown in the middle. The black line depicts counts that hit the detector plane inside the detector area and the red line those outside. A sectional drawing of the lens with a selection of trajectories is shown on the right in each row. In the histograms n indicates the number of geometry optimization steps done for the respective row, T represents the transmission, and $FWHM$ the width of a gaussian fit to the time–of–flight distribution of the particles that hit the detector area.

References

[1] U. Rohner, J. A. Whitby, and P. Wurz. A miniature laser ablation time-of-flight mass spectrometer for *in situ*. 2003.

[2] U. Rohner, J. A. Whitby, P. Wurz, and S. Barabash. A highly miniaturised laser ablation time–of–flight mass spectrometer for a planetary rover. *Rev. Sci. Instrum.*, 75:1314–1322, 2004.

[3] D. J. McComas, F. Allegrini, P. Bochsler, M. Bzowski, M. Collier, H. Fahr, H. Fichtner, P. Frisch, H. Funsten, S. Fuselier, G. Gloeckler, M. Gruntman, V. Izmodenov, P. Knappenberger, M. Lee, S. Livi, D. Mitchell, E. Möbius, T. Moore, D. Reisenfeld, E. Roelof, N. Schwadron, M. Wieser, M. Witte, P. Wurz, and G.P. Zank. The Interstellar Boundary Explorer (IBEX). In V. Florinski, N.V. Pogorelov, and G.P. Zank, editors, *Physics of the Outer Heliosphere: Third International IGPP Conference*, pages 162–181. AIP Conference Proceedings 719, 2004.

[4] F. V. Berghen. *Constrained, non-linear, derivative-free, parallel optimization of continuous, high computing load, noisy objective functions.* PhD thesis, Université Libre de Bruxelles, 2004.

[5] J.A. Nelder and R. Mead. A Simplex Method for Function Minimization. *Comp. J.*, 7:308–313, 1965.

[6] J. Kennedy, , and R.C. Eberhart. Particle swarm optimization. In *Proceedings of the 1995 IEEE International Conference on Neural Networks (Perth, Australia)*, pages 1942–1948. IEEE Service Center, Piscataway, NJ, 1995.

[7] J. Li and R. R. Rhinehart. Heuristic Random Optimization. *Comp. & Chem. Eng.*, 22(3):427–444, 1998.

[8] H. H. Rosenbrock. An Automatic Method for finding the Greatest or Least Value of a Function. *Comp. J.*, 3:175–184, 1960.

[9] Inc. Scientific Instrument Services. *SIMION 3D Version 7.0 Ion Optics Program*. 1027 Old York Road. Ringoes, NJ 08551. USA, 1996-2005.

[10] J. Krauer. *Mouse and Key Recorder*. Kra-Tronic Corp., 6037 Root, Switzerland.

[11] VMware, Inc. *VMWARE*. 3145 Porter Drive, Palo Alto, CA 94304.

[12] A. Balogh, M. Bird, L. Blomberg, P. Bochsler, J.-L. Bougeret, J. Brückner, L. Iess, J. Guest, Y. Langevin, A. Milani, J.-A. Sauvaud, W. Schmidt, T. Sphon, R. von Steiger, N. Thomas, K. Torkar, H. Wänke, and P. Wurz. BepiColombo, A Interdisciplinary Cornerstone Mission to the Planet Mercury. Technical report, ESA-SCI(2000)1, April 2000.

[13] A. Fedorov. *TRACE*. Centre d'Etude Spatiale des Rayonnements, 9, avenue du Colonel ROCHE, 31028 TOULOUSE Cedex 4, April 2003. Version 7.0.

Chapter 5

Optimization of Ion-Optics Using a Parallel Computer

5.1 Introduction

To overcome the main limitations of the single node ion-optics optimizer, i.e., long computation times for complex problems and no support for magnetic fields, a new ion-optical simulation code was evaluated and the ion-optical optimizer was adapted for use on a parallel computer.

An energetic neutral particle instrument (ENAMMO-C) for the magnetospheric orbiter of the BepiColombo mission [Balogh et al. 2000] designed by Y. Kazama [Kazama & Barabash 2003] was selected as a test case for optimization by the parallel optimizer. This neutral particle instrument design uses a magnetic sector for mass resolution. The optimizer was used to increase the mass resolution of the design as much as possible while maintaining the other performance parameters.

The parallel version of the ion-optics optimizer was implemented on computers at the Gewerblich-industrielle Berufsschule Bern (GIBB) and the optimization of ENAMMO was successfully run for more than 3 weeks in September 2004. Much insight was gained into the operation of a large cluster computer as well as into the writing of software for parallel computers.

5.2 Hardware

Simulations were run on computers of the Gewerblich-Industrielle Berufsschule Bern (GIBB). GIBB also provided the network connecting the nodes as well as supporting infrastructure.

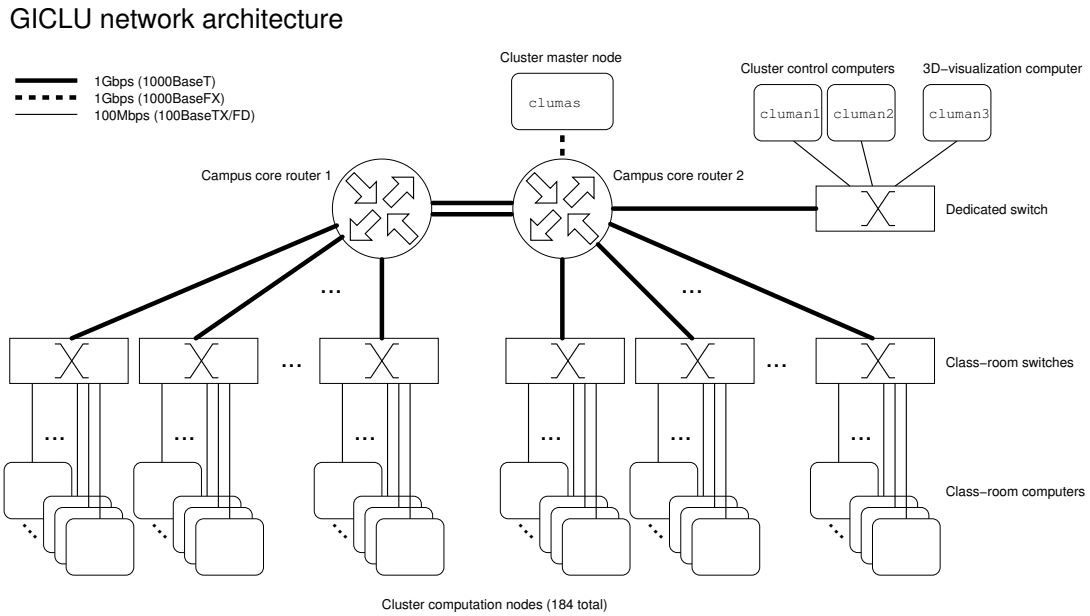

Figure 5.1: Network architecture of the GICLU cluster computer

Figure 5.1 shows an overview of the configuration used for the GIBB cluster computer (GICLU) . 184 standard desktop computers normally used for teaching were aggregated to a cluster for three weeks of school holidays. All computers (nodes) featured at least Intel Pentium IV processors with between 1 GHz and 3 GHz clock frequency and were equipped with 512 MB RAM. The individual computers were connected by 100 Mbps links to class room switches, which were themselves connected to the campus network backbone with a bandwidth of 1 Gbps for each group of 20 to 25 computers. A fast central data storage server (`clumas` in Figure 5.1) for data exchange between the individual cluster nodes was installed with a direct 1 Gbps connection to the campus backbone. This node also served as the cluster master node managing the distribution of tasks to the other nodes. For this master node, dedicated server graded hardware was bought (Hewlett Packard, HP 370 ML) whereas the ordinary cluster nodes were off the shelf no-name desktop computers. Three additional computers, one equipped with fast 3D-graphics hardware were used to control the cluster and to evaluate the calculated results (`cluman1` to `cluman3` in Figure 5.1).

5.3 Software

5.3.1 Overview

The implementation of the ion-optics optimizer on a parallel computer made the reimplementation of various functional blocks necessary.

SIMION was replaced by TRACE, a parallel implementation of a full 3D-ion-optical code by A. Fedorov [Fedorov 2003]. TRACE allows the full 3D-ray-tracing of charged and neutral particles in static electric and magnetic fields. Furthermore, arbitrary particle-surface interactions may be implemented. Integration of TRACE with the optimizer software was straight forward as both the optimizer and the TRACE modules are written in the C/C++-programming language.

A specially tailored task manager software written in `Perl` [Wall 2003] and `Bash` [Fox & Ramey 2002] was developed to distribute the optimizer's computational load as efficiently as possible in a cluster sizing from 4 to 200 nodes.

Visualization software proved to be very important while running the calculations. Software to graphically represent the cluster computer status and the evolution of the objective function value was developed and integrated [Rühl 2004].

For viewing the 3D-instrument geometry and simulated particle trajectories, `FreeWRL` [Lukka & Stewart 1998-2005], a viewer application using the Virtual Reality Modeling Language (VRML) [ISO 1997], was also integrated.

Finally, data export modules were written for the export of the simulated instrument geometry to CAD systems.

5.3.2 TRACE

TRACE is a full 3-dimensional ion-optical simulation software package able to run either on a single computer or in a parallel cluster environment. TRACE is written completely in the C-programming language and available as source code [Fedorov 2003]. Parallel program execution is supported using LAM/MPI, an open-source implementation of the Message Passing Interface specification [Burns et al. 1994, Squyres & Lumsdaine 2003].

TRACE consists of several small modules, each optimized for a specific task. For the integration with the ion-optics optimizer, TRACE was modified and supplemented with additional modules and scripts to speed up calculations, to facilitate the analysis of the data obtained from ray tracing, and to manipulate input and/or output data streams as described in the following paragraphs. As TRACE uses NETCDF [Rew et al. 1997] and plain text files for data exchange between the individual modules, the implementation of new modules was straightforward. Table 5.1 lists the main TRACE modules used. The program flow for a complete TRACE calculation sequence is shown in Figure 5.2, for simplicity without the ion-optics optimizer. Although the modules shown are executed sequentially, each module marked with double lines is a parallel program. Depending on the amount of memory and communication bandwidth needed, parallel programs were distributed to up to 25 execution nodes.

Module name	Purpose
`confmake`-scripts	Generation of the geometry description out of geometric primitives
`BoxPrepP`	Mapping of the geometry onto the simulation universe
`SetEFP`	Calculation of the electric field
`SetMFP`	Calculation of the magnetic field
`CombineEMP`	Linear combining of previously calculated field solutions
`TraceParP`	Particle tracing

Table 5.1: TRACE modules. Modules in the lower half of the table were adapted from examples provided within the TRACE package or newly written for the integration with the ion-optics optimizer. Modules with names ending with -P are implemented as parallel programs.

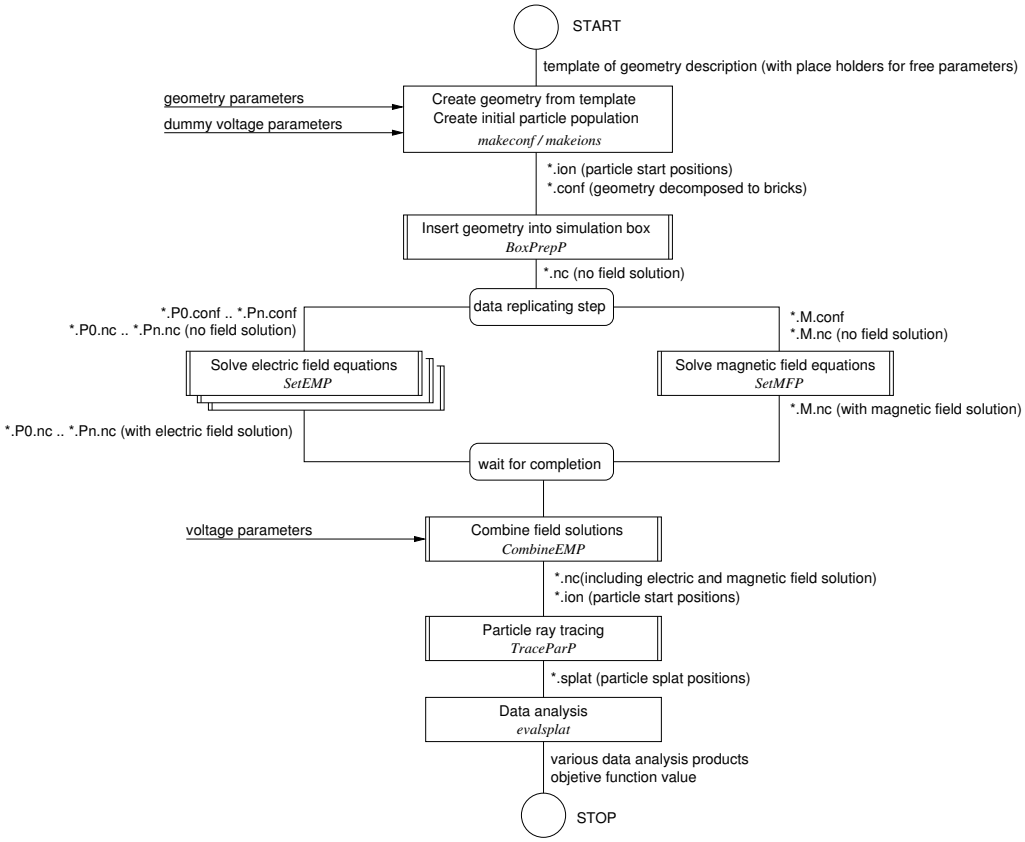

Figure 5.2: TRACE program flow without optimizer. Programs executed in parallel on several execution nodes are marked with a double line in the box. `SetMFP` and all copies of `SetEMP` (one for each independent voltage electrode) are executed concurrently; however all calculations must be completed prior the start of the `CombineEMP` program.

Defining the simulation geometry

Similar to SIMION, the geometry of the instrument is defined using a set of commands describing geometrical primitive objects, such as cubes, cylinders, and spheres, and a set of transformation commands used to scale, translate, and rotate objects. Unlike SIMION, the commands are implemented as small C-programs working on data given in text format. For more complex geometrical objects, these commands are aggregated into small shell scripts, using e.g., bash [Fox & Ramey 2002], although other script languages, e.g., Perl [Wall 2003], can be used as well. Also, unlike SIMION, the geometry in the simulation is not rendered into cubic volume elements (voxels) representing the smallest resolved feature, but is represented by as large as possible irregular rectangular solids called bricks embedded in a coarse grid. The advantage of this design is that the information about the surface orientation of the solids modeled is available during the simulation and can be used to implement particle-surface interactions, something very difficult to do in SIMION.

The representation of the geometry within TRACE requires the decomposition of shapes, such as cylinders and spheres, into bricks. For complicated geometries the number of bricks generated by this process can get rather large, increasing the computation time needed. Another constraint is the mesh size of the underlying grid used for field calculations. Although fields are calculated to machine precision for a brick surface inside a grid cell, having more than two different bricks occupying the same grid cell should be avoided. The scripts from the `confmake` group mostly take care of this problem, but occasional reviewing of the result of the decomposition into bricks is necessary.

In TRACE, material properties such as the magnetic permeability as well as magnetization or the electric potentials applied to individual electrodes are part of the geometry definition. This means that for each changed electrode potential a new geometry must be defined. As long as no electrodes are moved around, previously calculated electric field solutions may be reused by scaling them appropriately resulting in a tremendous increase in performance of the voltage-optimizer module described farther below.

For practical reasons it is useful to have one top-level shell script that generates the whole geometry in one go. This top-level script is realized as a template with place holders for free parameters such as electric potentials, material magnetization, and geometry parameters. By replacing the place holders with values provided by the optimizer modules, a runtime version of the script is generated and executed to produce the geometry used in the simulation. This approach allows calculations to be done with free parameters prior to inserting them into the geometry definition. Geometry definition files are always identified by the `.conf` file name extension.

Mapping the geometry into the simulation universe

The geometry definition obtained from the previous paragraph needs to be mapped into the simulation box volume using the `BoxPrepP` program. The box volume may be smaller than

the size of the complete geometry to save memory and computation time. In this case boundary effects must be taken care of, as elements of the geometry outside the box are not included into the calculation of the electric and magnetic fields. The result of a `BoxPrepP` run is a NETCDF file containing the simulation grid with all bricks inside the box volume assigned to their closest grid cell. These files are identified by a `.nc` file name extension.

Field calculation

The electric and magnetic fields are calculated using the `SetEFP` and `SetMFP` programs. Often more than one independent electrode is contributing to the electric field. The potential field created by each of the individual electrodes is calculated separately. These partial solutions are added together afterwards scaled according to the desired electrode potentials. The time needed to calculate the electric field for a specific electrode potential combination can be shortened considerably this way at the expense of the additional memory needed to store the partial solutions and the time needed to calculate the potential field separately for each electrode in the first place. As the voltage optimizer module will change the electrode potentials very often compared to the number of electrodes this approach is advantageous.

The actual calculation is done by replicating the geometry definition and the simulation box information obtained from `BoxPrepP` for each individual electrode and setting the corresponding electrode potential to unity while all others are set to zero. After the calculation of the electric and magnetic fields in parallel, the `CombineEMP` program combines all partial solutions for the electric potential according to the currently set voltages with the solution for the magnetic field to get the electric and magnetic field used for particle tracing. This functionality is equivalent to the 'fast adjust' feature found in SIMION.

Particle tracing

Particle tracing in TRACE is available through a C-program interface. An example program for particle tracing provided by the TRACE package was generalized. The resulting program `TraceParP` accepts initial particle populations from external ion definition files and writes information about the tracing process to external logging files. Particle tracing is very easily parallelized, each execution node gets the full field configuration and a fraction of the particles defined in the ion definition files. No inter node communication is needed during the calculation, except at the end when results of the individual nodes are combined. Loging files produced by `TraceParP` are analyzed by the program `evalsplat`. This program reads all logging information and calculates an objective function value from it to assess the quality of the simulated design variant. `evalsplat` also generates various other data products, such as mass spectra or 3D-representations of the particle trajectories for viewing with 3D view program.

Visualization

Visualization of the geometry, the electric and magnetic fields, and the particle trajectories is done by two different programs: `FreeWRL` [Lukka & Stewart 1998-2005], a open source 3D viewer, is used for the geometry and particle trajectories and a TRACE supplied IDL [Research Systems, Inc. 2001] program for the electric and magnetic fields.

The IDL program directly reads the NETCDF files generated by `BoxPrepP`, `SetEFP`, and `SetMFP`. The advantage of the IDL program is that no data conversion is necessary to display field information, however it does not allow to easily view the geometry from different viewing angles and it requires an IDL software license to run. `FreeWRL`, a Virtual Reality Modeling Language (VRML) [ISO 1997] viewer application, features fast interactive viewing of a 3D-geometry, allows interactive zooming or rotation of the geometry as needed. It is not suited for the display of field distributions, but it is very powerful tool for displaying particle trajectories inside a given instrument geometry. It requires the transformation of the TRACE geometry definition into the VRML data format prior to viewing. Particle trajectories can be inserted into the the VRML world with different particle types, e.g., different particle mass, differentiated by color coding. `FreeWRL` was used as a standard diagnostic tool during the simulations.

5.3.3 The Parallel Optimizer

The program flow of the simulation including the optimizer is shown in Figure 5.3. The main difference compared to the single node optimizer described in Chapter 4 is the possibility of exploring several variants of a parameter set in parallel before comparing them and deciding what to change to get a better solution. This is done simultaneously for the outer geometry/magnetic optimizing loop as well as for the inner voltage optimizing loop. Ideally, approximately $n_g \times n_v$ parallel threads will be started this way with n_g the number of free parameters used in the geometry/magnetic outer loop and n_v the the number of free parameters used in the inner voltage optimizing loop - exact values depending on optimizer algorithm used.

The simplex algorithm [Nelder & Mead 1965] used in the single node optimizer was first ported to a parallel version. When the algorithm starts, it fills its initial parameter search matrix with values, which can be done in parallel. However, later in the optimization process, simplex will serialize the execution as only one additional design variant is calculated before a decision is made about what to modify. If both the geometry and voltage optimizers use simplex, the initial parallel search for better solutions will completely serialize to only one geometry/voltage parameter set evaluated at a given time. As long as each individual parallel parallel program alone is able to use the cluster to its full capacity, this is not a problem. Experience shows that this is the case up to a size of the cluster computer of 30 nodes. For larger clusters, simplex, in the simple form used, is not a good solution.

Several other optimizer algorithms were investigated, among them the particle swarm optimization (PSO) algorithm [Kennedy et al. 1995] and a promising novel approach (CONDOR)

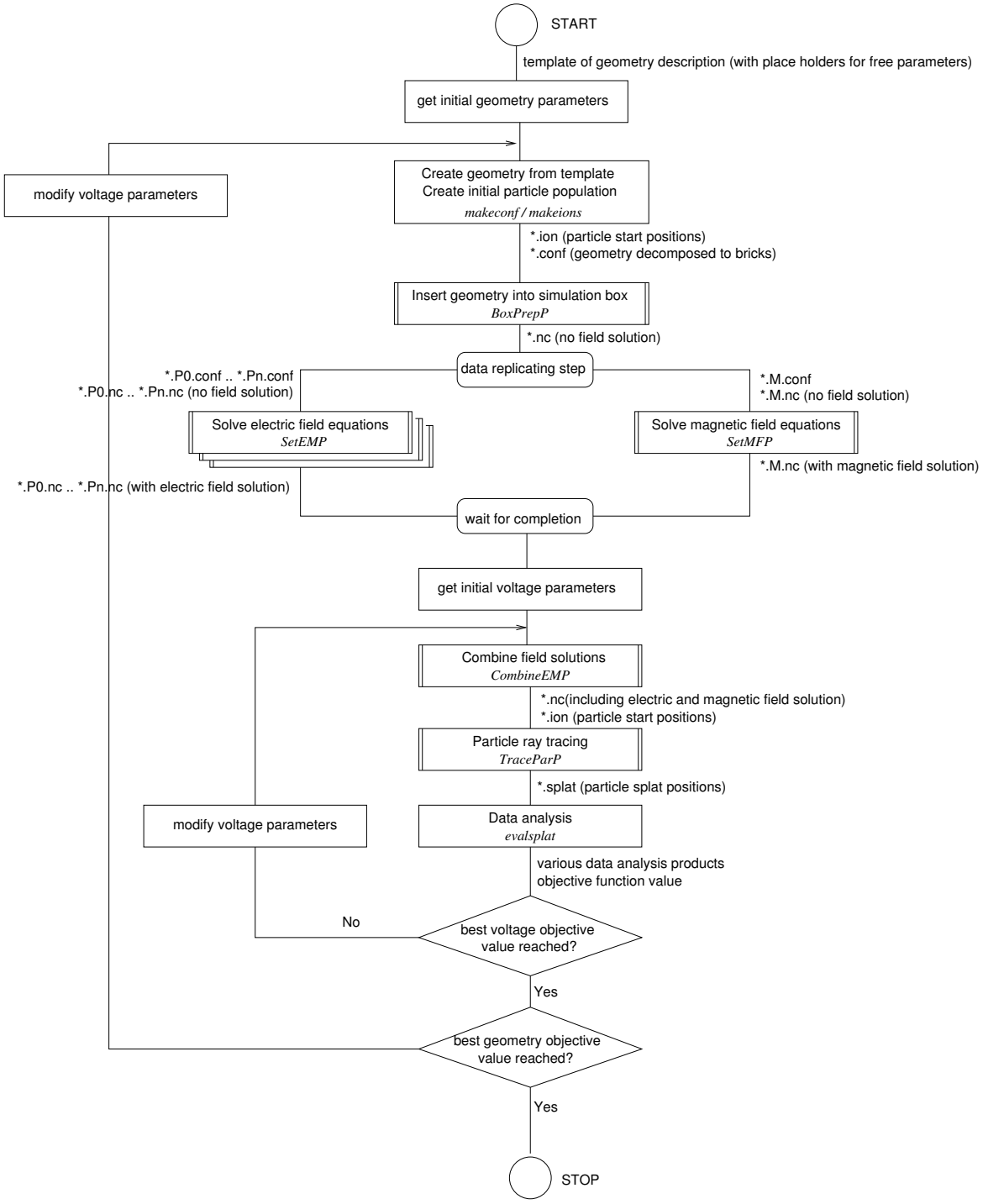

Figure 5.3: Program and data flow with optimizer included.

using a trust region method [Berghen 2004]. However due to the limited time available prior to running the optimizer on the cluster, the already implemented and well understood simplex algorithm was used anyway. To get a reasonable load on a large cluster, up to five independent copies of the optimizer, each with an individual parameterization of the geometry, were launched in parallel. For future optimization efforts, the implementation of a better parallelizing optimizer algorithm is strongly recommended.

5.4 Cluster Configuration and Operation

5.4.1 Cluster Nodes

In the building complex of the school where the cluster computer was run, about 550 personal computers of different performance are installed at the time of writing. Out of them, 184 met the criteria for inclusion in the cluster computer (512 MB RAM and at least an Intel Pentium 4 processor). Most of these computers were located in class-rooms. A key requirement for the use of the class-room computers at GIBB was that no permanent reconfiguration of the installed operating systems (mostly Windows) should be done to minimize the time needed to switch back from a cluster computer configuration to the nominal computer lab mode of operationused for teaching. This was solved by creating a boot-able CD-ROM with all the software needed for a cluster node to connect to a master cluster node where from additional configuration could be loaded.

Linux was chosen as the operating system throughout the cluster. A tailored SuSE Linux 8.2 distribution was fitted onto the boot CD-ROM's. A United Linux 1.0 version was installed on the master node to have access to supplier provided optimization packages for the disk subsystem and the network interface.

5.4.2 Cluster Boot Process

To boot the cluster, a boot CD-ROM had to be inserted in the CD-ROM drive of the node followed by a power cycle or reset, for each of the 184 nodes. As the computers were distributed all over the building complex, 5 people required about 30 minutes to do this. After the initial boot process, the nodes tried to connect to the master node via a Network File System (NFS) share and to register themselves at the master node by means of an information file written to a special subdirectory on the master node's filesystem. The file contained all important informations about the node, such as available memory, network address, processor type and clock frequency. A periodic retransmission of this information file to the master node every 2 minutes was used as a heart-beat signal to identify nodes lost due to program crashes or over-temperature. Also during the registering process, a key exchange took place to allow the master node to connect to a computation node through a Secure Shell (SSH) connection without the need to enter a password. Once each node had registered, a data collecting script on the master node divided the nodes into three performance groups depending on processor

Module	Number of nodes	Comment
`BoxPrepP`	8	Number may be increased for a larger simulation box
`SetEFP`	8	Computation and communication intensive
`SetMFP`	1	Bug in parallel communication schema used for data exchange. Number of nodes was reduced to 1 to eliminate computation errors.
`CombineEMP`	4	Fast but memory intensive task, virtually no communication
`TraceParP`	25	Virtually no communication but very computation intensive

Table 5.2: Number of nodes used for each of the parallel programs used by TRACE.

clock frequency. The script also tagged unreliable nodes that were previously entered into a blacklist to inhibit their further use in the cluster. This was very useful for eliminating nodes that suffered from overheating without the need to physically locate them and to shut them down. The script also generated a list of active nodes used for the subsequent boot process of the LAM/MPI computing universe [Burns et al. 1994, Squyres & Lumsdaine 2003]. Booting of the LAM/MPI computing universe, i.e., making the computation nodes available for computations in the cluster, completed the cluster boot process.

5.4.3 Task Scheduling

LAM/MPI provides methods to launch processes on all or a subset of available cluster nodes. However, to manage several parallel programs working on different data sets, a customised task manager had to be written. For each of the modules described in Table 5.1, the number of nodes to use for optimal computing performance was determined. For tasks where little or no communication between the nodes was required a large number of nodes was assigned whereas communication intensive tasks typically performed better when distributed to fewer nodes. Table 5.2 depicts a summary of the number of nodes assigned to each module.

The task manager ensured that a given parallel program was only distributed to nodes of the same performance group to avoid the waste of computation resources. Using nodes of the same performance group also very likely assigns nodes that are located close together in the network for the same task. This was because computers within one class-room always belonged to the same performance group. Furthermore, the task manager ensured that at any given moment only one task was executed on an individual node to avoid problems with the memory available on the node. No parallel tasks were ever launched on the master node because this node also hosted the central data storage and most of its processing power was used to transfer data from the disk subsystem to the network and vice versa. NFS shares on the master node were used to distribute simulation data to the computation nodes. Tasks remaining on the master node were the parallel optimizer's main program and scripts used for data logging as these did not create much processor load. Also, to take processor and memory load from the master node, non-parallel auxiliary programs used by the parallel optimizer (mostly `Perl` or `bash` scripts for data preparation and analysis) were rolled out to other cluster nodes whenever possible.

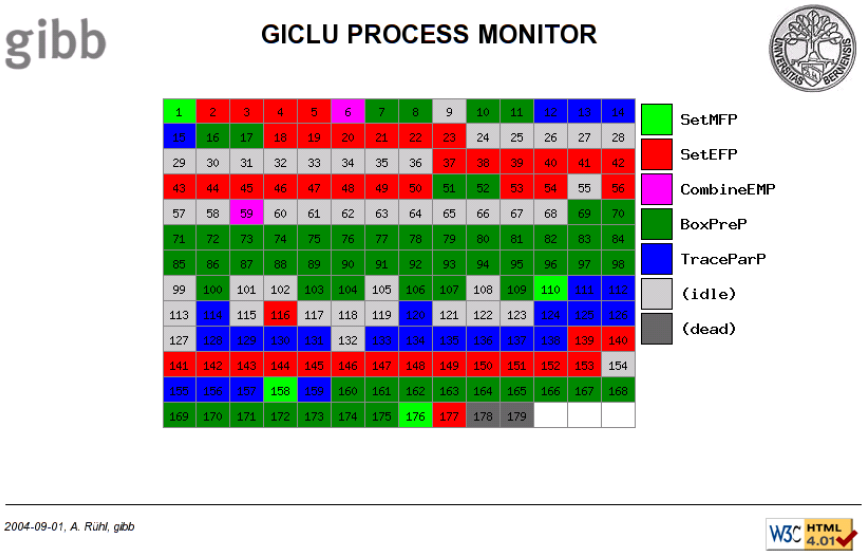

Figure 5.4: Screen-shot of a web-browser window showing the GICLU process monitor while running an optimization on the cluster. Each square represents one computation node with its status in color coded form.

A very important feature provided by the task manager was the unique-number-service. It provided guaranteed unique numbers returned at each call of the service. These numbers were used to create unique filenames for the data sets stored in the central data storage of the cluster master node and to unambiguously identify the tasks launched on the other nodes. The unique number service was implemented by a counter starting at zero and incrementing after each number request. The implementation of the counter ensured that under no circumstances two parallel processes could obtain the same number by accident. As the number provided by the service continuously incremented, it was used to reconstruct the sequence of events in logging files without the need to worry about a globally synchronized clock in the system.

5.4.4 Visualization of the Cluster Status

A web-based application was developed for the visualization of the cluster utilization by A. Rühl [Rühl 2004]. The application features different display modes to show the node status (booting, idle, busy, dead/crashed) or the name of the program running on a node in color coded form for the complete cluster. A screen-shot of a display showing the distribution of the different processes (programs) in the cluster is shown in Figure 5.4. A situation with a total of 177 computation nodes is shown (this was later increased to 184 nodes) . The two last nodes are known to the cluster manager software but were excluded from calculations, because they were placed onto the blacklist due to unreliability.

Display modes that show the evolution of the optimizer's object function value are also available from within this application (see Figure 5.7 for an example).

5.4.5 Linpack Performance

A Linpack performance test [Petitet et al. 2004] was run on the cluster prior to starting the optimization of the ENAMMO-C instrument design. Running Linpack benchmarks on a 4×4 node grid using nodes from two different speed groups (1.8 GHz and 3 GHz processor clock frequency) revealed for both cases a performance of 12.2 GFLOPS (1 GFLOPS$= 10^9$ FLoating point Operations Per Second) indicating a network limited performance of the cluster. However, compared to the communication needs of the TRACE package, the Linpack benchmark overvalues the speed of the network. To better estimate the cluster performance available to TRACE, the complete cluster was divided in groups of 8 nodes as used by the most communication intensive TRACE module, `SetEFP`. When using a 4×2 node grid in Linpack, a performance of 7.7 GFLOPS was obtained for such a group for the high and medium performance nodes and 5 GFLOPS for the low performance nodes. The performance for the high and medium performance node group was still dominated by network throughput, but the configuration reflected the final mode of operation of the cluster much better. Combined for all 184 cluster nodes a performance of 174 GFLOPS was obtained. It should be noted however that this value is a lower limit of the capacity available to TRACE as the most computation intensive TRACE module, `TraceParP`, requires virtually no communication bandwidth and thus the bottleneck of the limited network bandwidth does not dominate its execution time. Also, only limited time was invested in running Linpack; by further tuning of the parameters of Linpack a better benchmark result could be obtained. Another aspect was the maximum network throughput obtained by the master node. Using optimized network card driver software, the link from the master node to the network backbone could be used up to its full capacity of 1 Gbps.

5.5 ENAMMO-C Instrument

A energetic neutral particle instrument (ENAMMO-C) for the Mercury Magnetospheric Orbiter of the BepiColombo mission [Balogh et al. 2000] designed by Y. Kazama [Kazama & Barabash 2003] was selected as a test case for the parallel optimizer. This instrument design uses a conversion surface to ionize low energy neutral atoms and a magnetic sector for mass analysis. The instrument has a cylindrical symmetry (except for the magnets) and a disk shaped $360^\circ \times 11^\circ$ field of view. It scans the whole sky by using the rotation of the spacecraft it is mounted on.

A cross-section of the initial geometry fed into the optimizer is shown in Figure 5.5 and a 3D rendering in Figure 5.6. In Figure 5.5, neutral particles enter the collimator from the right, are ionized to positive ions at the charge conversion surface, pass a wave shaped energy analyzer, cross the center line of the instrument, and enter the magnetic sector structure for mass separation prior detection at the bottom MCP plates. In the design shown in Figure 5.5 also negative ions (from hydrogen and oxygen) can be detected by reversing the voltages in the energy analyzer and using the side MCP's for detection. The mass range for neutrals converted to positive ions starts at helium and extends up to iron. The energy range of the instrument is

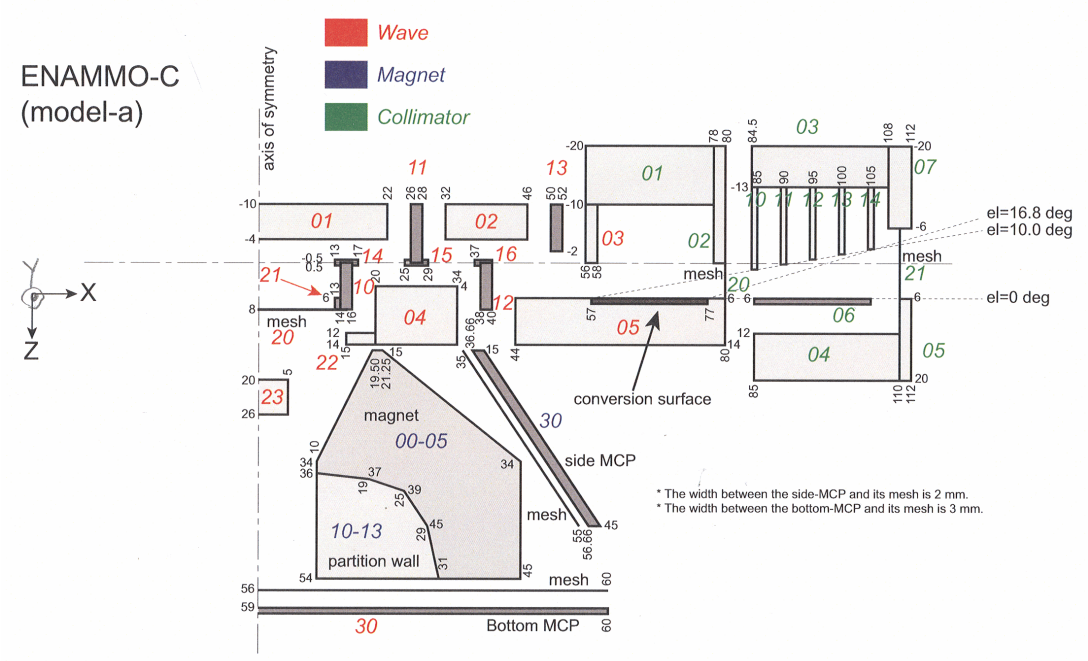

Figure 5.5: Cross section of the cylindrical ENAMMO-C instrument design used as initial geometry for the optimizer. *Drawing by Y. Kazama*

about 10–200 eV for heavy atoms up to 56 amu converting to positive ions at the conversion surface and 500–3000 eV for the two species hydrogen and oxygen, both converting to negative ions at the conversion surface.

For the optimization done with the parallel optimizer, the main focus was on mass resolution with overall transmission the second priority. As is normal for a magnetic sector instrument an increased mass resolution is linked to a decreased transmission. The optimizer was used to keep this effect as small as possible. To simplify the task, only positive ions from the conversion surface were considered, i.e, the side MCP's were dropped from the design. Also not simulated was the collimator in front of the conversion surface. Mainly the shape of the magnets and the electrodes where the particles enter the magnetic sector were subject to modifications. A wide mass range was used for the simulation: He, C, O, Mg, Al, Si, S, Ca, Cr, and Fe. Ions starting with various angles from the conversion surface with an uniform energy spread from 30 eV up to 250 eV were flown through the setup while holding the center energy of the wave constant at approximately 85 eV.

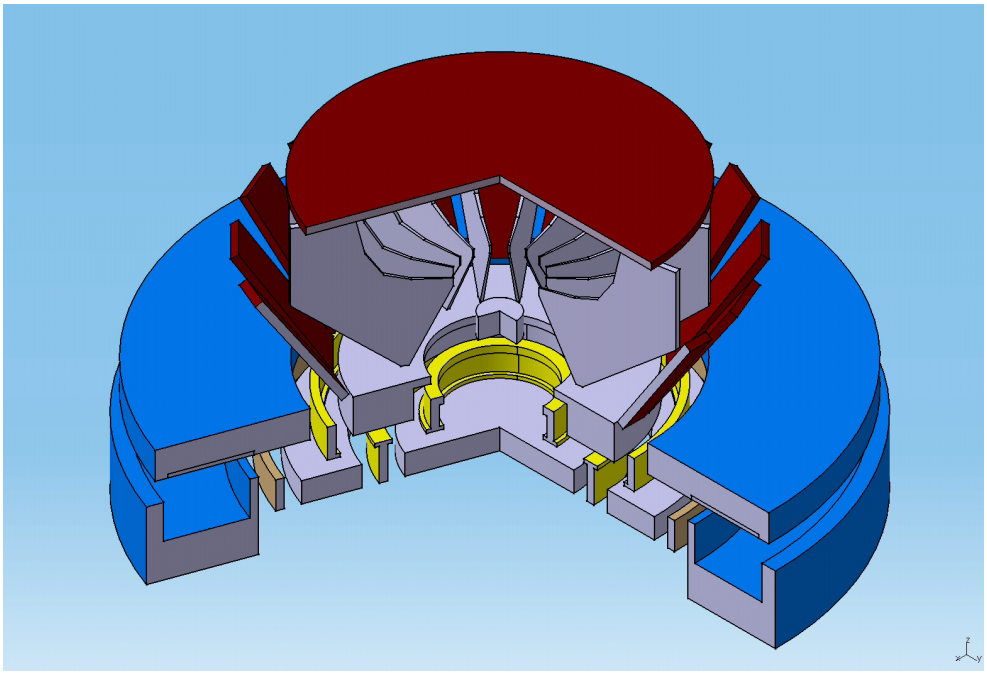

Figure 5.6: 3D cut away rendering of the ENAMMO-C instrument design. Compared to the drawing in Figure 5.5, the instrument is shown upside down. The slices of the magnet forming the magnetic sector are easily identified. *3D-image by S. Fischer, design by Y. Kazama*

5.6 Report: Optimization of a magnet based ENA instrument

The following report was issued after completion of the calculations on the cluster computer. Additional data analysis was done afterwards, the results of these efforts are shown in Section 5.7.

Optimization of a Magnet Based ENA Instrument

Status Report

Date: 01. November 2004

Author:
- Martin Wieser, University of Bern

Table of Contents

Revisions:
21. October 2004, Initial Version, M. Wieser
28. October 2004, Update, M. Wieser
1. November 2004, more elements added, M. Wieser

1 Introduction

A magnet based ENA instrument design provided by Yoichi Kazama was optimized during 3 weeks on a 180 node parallel computer to increase mass resolution. Mass resolution m/dm could be increased to about 11 for Mg. Detailed results from the best mass resolving solution are reported.

2 Instrument

2.1 Base line geometry

Starting from the geometry ' enammo-c' the shape and placement of the magnets as well as electrodes near the magnets were modified. Grids were removed where possible. The simulations did not include the properties of the collimator and the post acceleration stage between the bottom MCP mesh and the MCP itself. Trajectories started at the CS with a uniform coverage of phase space.

2.2 Modifications

2.2.1 New magnet shape and position

The complete magnet structure was moved about 6mm upwards. This improves mass resolution considerably. Magnetic stray fields reaching into the wave section were small, but included in the simulations. The 'partition wall' in the lower center part of the magnet was carefully reshaped.

2.2.2 New center electrodes

Two electrodes in the center of the magnet replace the previously present electrode 'wave_23'. The upper electrode serves as lens to shape the particle path into the magnetic sector as 'wave_23' did. The lower electrode acts as absorber for low mass particles that would otherwise deflected that much in the magnetic sector that they could reach the opposite side of the magnets rendering azimuthal position sensing impossible. This is important for protons and helium ions.

2.2.3 Grids

The grid at the exit of the wave structure could be removed without negative side effects. The grid at the exit of the magnet (the image plane) was kept and biased to a small negative voltage to reject secondary electrons generated by particles hitting parts of the structure in the magnet section. In the simulations the particles stop when hitting the MCP grid plane instead of passing through

the grid and be postaccelerated. This was necessary because of problems with transparent objects that could not be fixed within the time available. When using a fine sized mesh, the omitted postacceleration stage should not have a large influence on the particle trajectories in the magnetic section and also not significantly alter radial splat positions.

2.2.4 MCP's

Only the bottom MCP used for positive ions was included in the simulation. This reduces considerably the detection efficiency for oxygen as the yield for O+ but reduces problems with electrons. Hydrogen does not suffer because approximately as many positive as negative ions are generated at the CS in the energy range of interest.

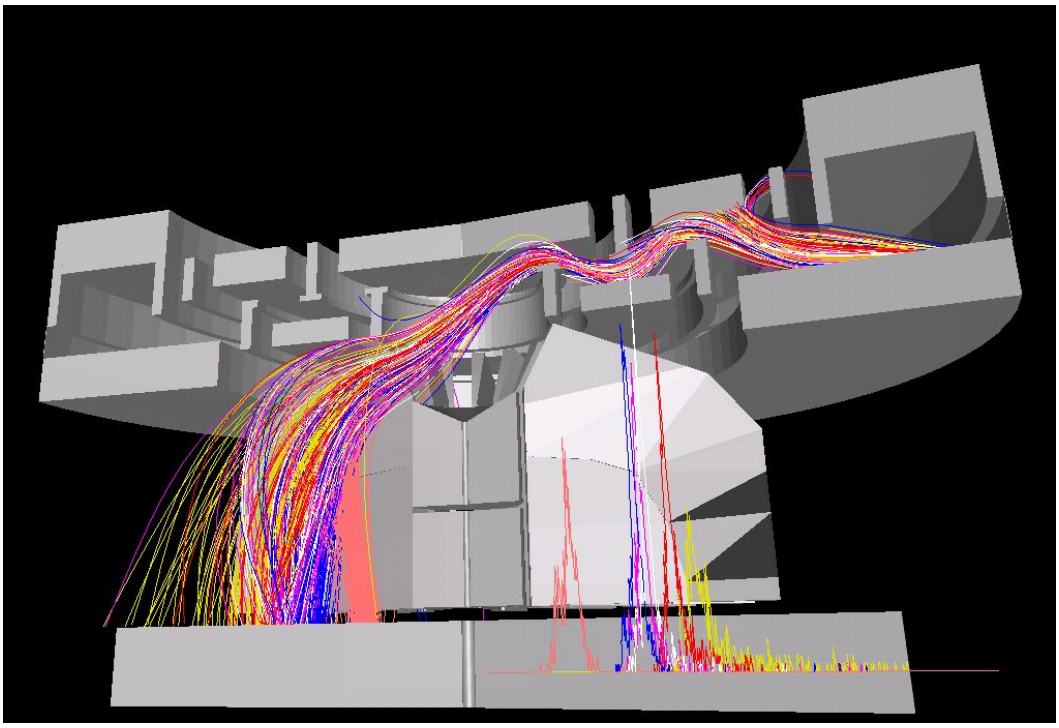

Figure 2.1
3D rendering of enammo-m geometry including a selection of trajectories.

2.3 Parametrization and target function

Up to 5 geometry parameters (mainly magnet shape parameters) and 2 voltages were set as free parameters in each optimization run. The following function F was maximized during optimization:

F = *scale * weighted_intensity * estimated_resolution*

With *weighted_intensity* being a gauss function on the left side of the desired minimum intensity and a slightly increasing linear function towards higher

intensities (right side) of the desired minimum intensity, *estimated_resolution* an estimate of the mass resolution estimated from the radial distribution of the spalt positions on the bottom MCP, and *Scale* an arbitrary scale factor to shift the value of the function into the 0..100 range needed by the optimizer program. The half sided gauss was chosen to prevent the optimizer from simply reducing the transmitted flux to increase the resolution.

3 Performance

3.1 Comparison pre to post optimization

	pre optimization (enammo-c)	***post optimization (enammo-m)***
Energy range	20-100eV	only 85eV post CS was simulated
Energy resolution	50eV	approx: scattering + 10eV -> ~30-50eV
Mass resolution	2 – 3	4 – 14, depending on mass
Field of view	360° x ~12°	360° x ~12°
Angular Resolution	+/- 5-10° x ~12°	+/- 5-10° x ~12°
Sensitivity	~2 x 10^-3 cm^2 sr eV[1)]	~5 x 10^-4 cm^2 sr eV[2)]

1) 10% scattering, 60% MCP, (90%) ^3 grids

2) 0.05 scattering, 0.02 ionization, 67% MCP, (88%) ^2 grids
(grids: 88% Transmission with 0.268 mm mesh size, Buckbee-Mears MG-20)

3.2 Mass Resolution

Mass resolution was first estimated by the separation of Mg and Ca. Later the separation of Mg and Si was used as soon the corresponding peaks got separated.

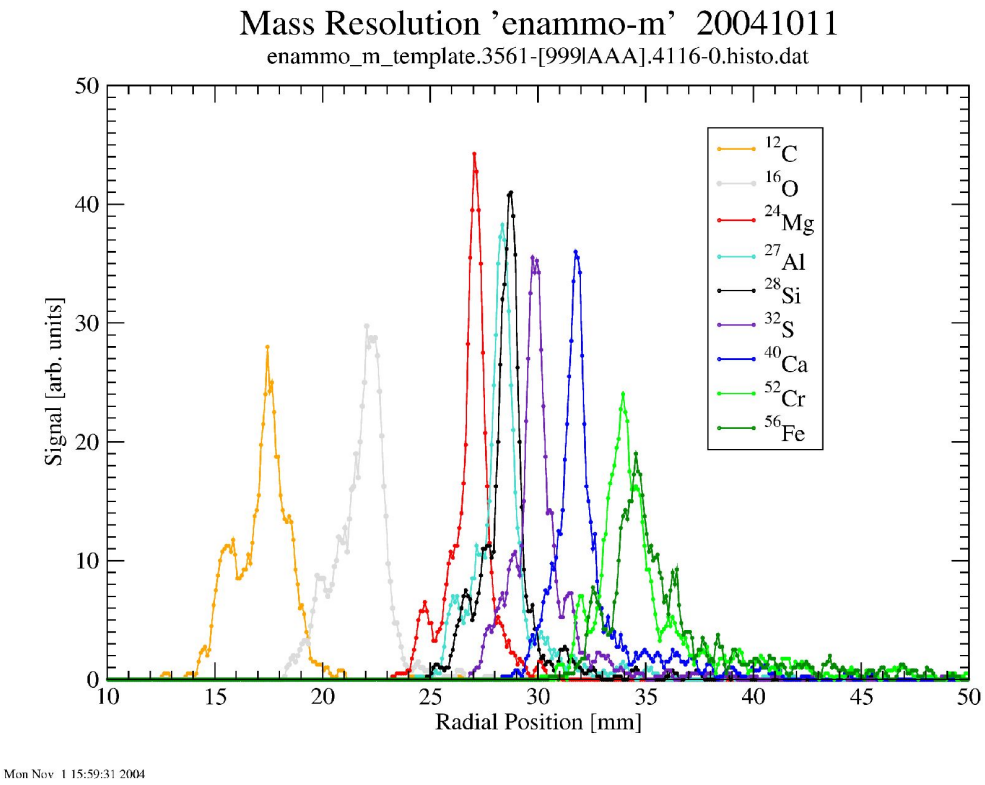

Figure 3.1

Estimated mass resolution of the calculated best solution m/dm was ~11 for Mg. The mass resolution is higher for smaller radii (lower masses). For larger radii the resolution drops considerably. (see Figure 3.3).

An 3rd order transformation polynomial was found to convert radial position to a mass scale:

$m = -9.614 + 3.773\, r - 0.2369\, r^2 + 0.005274\, r^3$

[m] : amu
[r] : mm

Similar polynomials could be found for all simulated geometries.

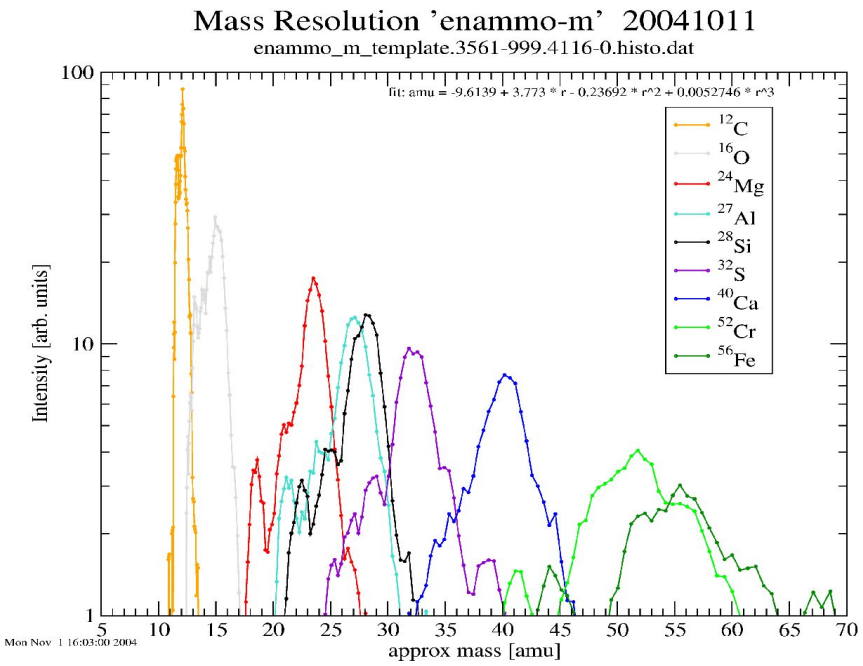

Figure 3.2

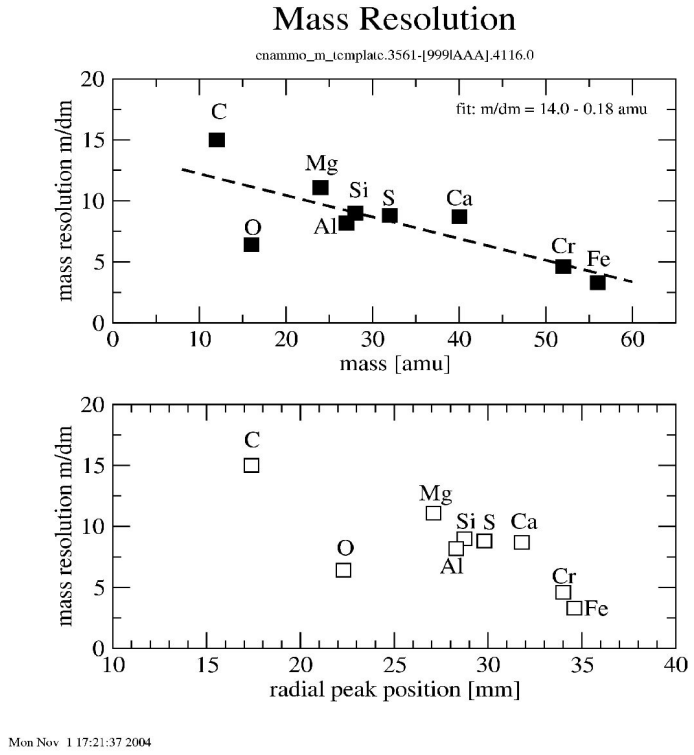

Figure 3.3

By varying the wave center energy the region of best mass resolution can be shifted to higher or lower masses. Selection of primary particles is then done by floating the CS to a suitable potential relative to the wave center energy resulting in preacceleration of particles in most cases. Preacceleration will increase the angular acceptance region of particles reflected away from the CS. Corresponding calculations are already available from enammo-c by Y. Kazama.

3.3 Energy Resolution

The energy resolution is mainly a property of the wave structure and of energy scattering at the CS. Energy scattering at the CS worsens the definition of the energy bins but does not have an influence on the energy width of the particles when entering the magnetic sector. The energy distribution of the particles leaving the CS that make it to the detection plane is shown in Figure 3.4. The resulting overall energy bin shape is a convolution of this curve with the energy distribution obtained from the scattering process at the CS. The energy acceptance of the wave-magnet system is independent of particle mass within counting statistics.

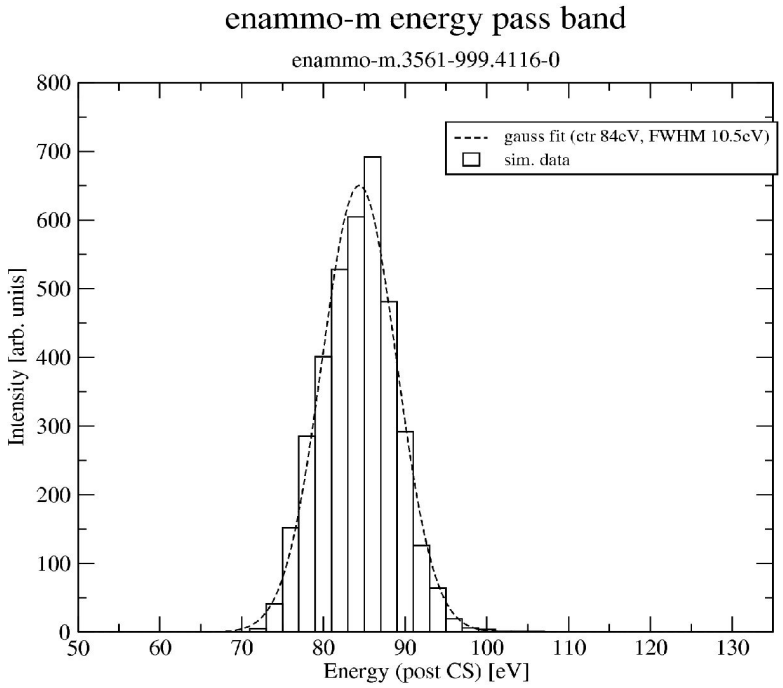

Figure 3.4
Energy resolution of wave-magnet system.

3.4 Angular Acceptance of Wave

Figure 3.5 depicts the angular acceptance of the wave system as scatter plot. Particles started along a radial line across the CS with different elevation and azimuthal offset angles. The scatter plot shows particle trajectories that made it successfully to the bottom MCP grid. The small rectangular region inside the acceptance region is the image on one of the magnet slices. Different colors represent different elements, the color map is identical to the one used in Figure 3.1.

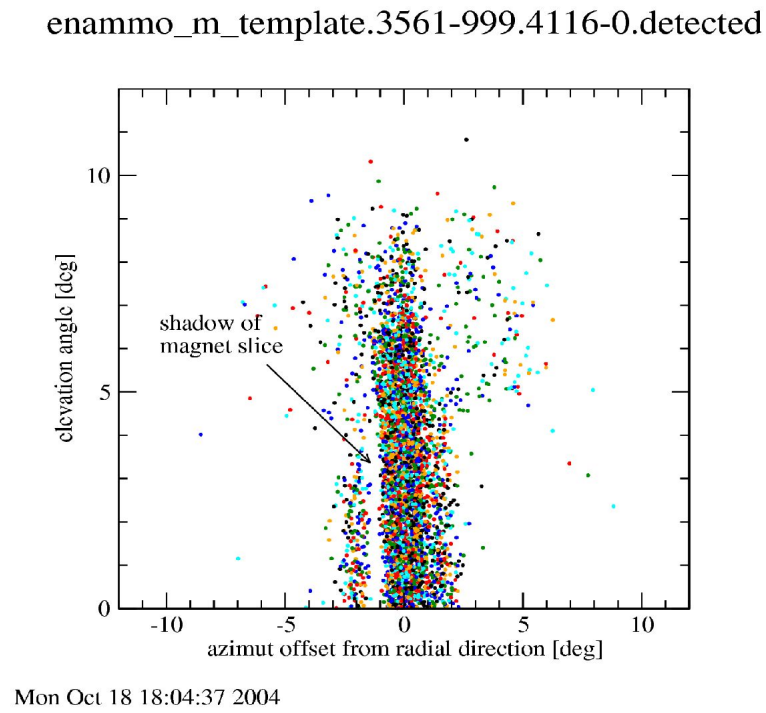

Figure 3.6
Scatter plot of angular acceptance of wave system.

Histograms of the above image projected on each coordinate axis are shown in Figure 3.7.

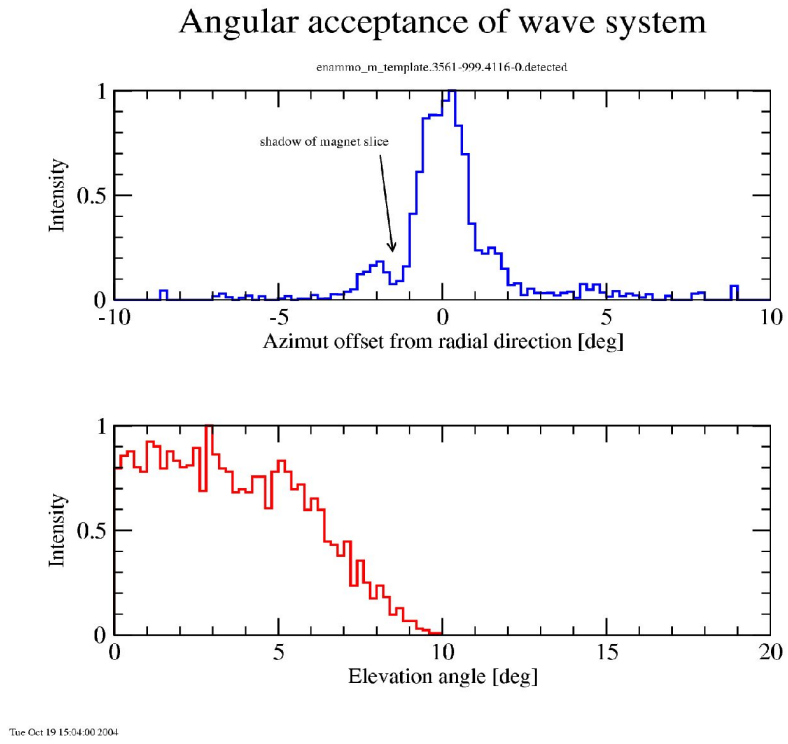

Figure 3.7

Combined with measured angular scattering profiles from real conversion surfaces the geometry factor shown in Chapter was obtained.

3.5 Splat Positions

The distribution of the splat positions of particles that did not make it to the detection plane reveals that apart of the wave structure the upper part of the magnets (away of the MCP) is hit by a large fraction of particles and would merit special surface treatment (roughening or saw teeth). Another important splat region is the cylindrical center electrode between the magnet slices, especially for hydrogen and helium ions.

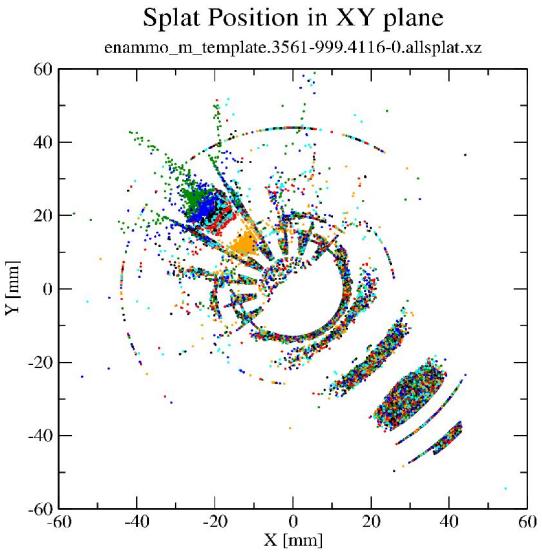

Figure 3.8
View from top in Z+ direction onto instrument. Particles are flown from the bottom right towards the top left. Most particles splat at the first electrodes of the wave structure but a important amount is also absorbed at the magnets. Color coding is identical to Figure 3.1

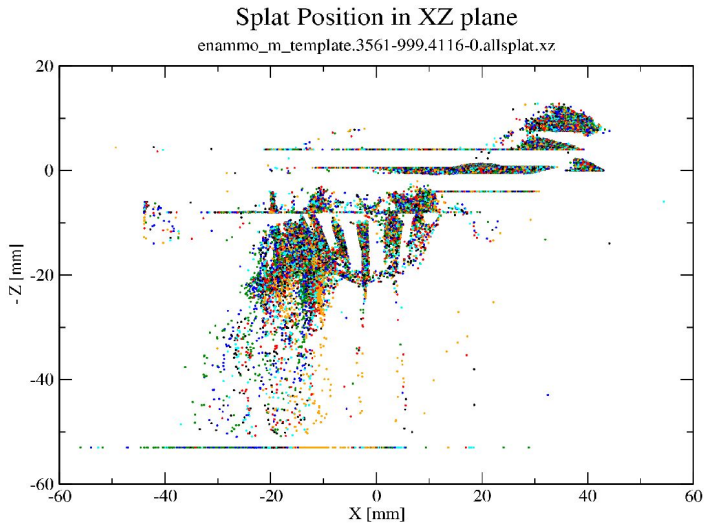

Figure 3.9
Splat positions in XZ plane (note that the Z axis is shown inverse in this plot (z=-57mm in plot equals z=+57mm in the geometry model). Particles are flown from the CS in the top right corner of the image in -X direction into the wave.

4 Discussion

4.1 Geometry

Starting point was the geometry 'enammo-c' by Yoichi Kazama. To simplify matters only positive particles starting at the CS were simulated. Scattering properties of the best available surfaces were assumed when calculating the geometry factor. The collimator was not simulated as it was not changed. Particles were considered as detected when they hit the bottom MCP mesh. Postacceleration from the mesh to the MCP was not included as it has only a minor contribution to the radial spread.

4.1.1 New features

The shape and position of the magnet and the shape and position of the cylindrical center electrode was modified.

4.1.2 Open Issues

a) Size of simulation grid: 0.91mm was chosen as simulation grid size. As the width of the mass peaks at the bottom MCP approaches this value, the effect of the grid size on the simulation result should be verified.

b) Size of simulation volume: The simulation volume was -63/+83mm in X- , +-63mm in Y-, and -13mm / +63mm in Z-direction. Although the instrument was centered along the Z-axis and all trajectories were away from the simulations volume borders, a asymmetry is visible in the particle splat positions (Figure 3.6 and 3.8). This is due to effects from the borders of the simulation volume. Better border conditions (i.e. electrodes with well defined potentials at the border of the simulation volume) would fix that problem. This problem is also the reason for the offset of 1° of the shadow position of the magnet slice in Figure 3.6. Fortunately the deviation occurs close at the CS and not in the magnet region.

c) Repetitive features in the shape of the mass peaks: Each mass peak (see Figure 3.2: i.e. Mg, Al and Si) has distinct 'side lobes' that are most likely due to the discretization of the cylindrical structures in the CS and wave region. Currently all Cylindrical objects are approximated by bricks that cover 5° wide sectors. Other subdivisions should be tested.

d) The calculation of the geometric factor is only en estimate and not very accurate.

4.2 Ion optical code

The ion optical code is a slightly enhanced version of Andrey Fedorov's 'Trace' code. Several new features were implemented and also some bugs fixed. The ion optical code uses LAM MPI as parallel communication library.

4.2.1 New features

a) To speed up calculations, the SetEMP/SetMFP program set was complemented by CombineEMP. CombineEMP imitates the 'Fast-Adjust'-feature in SIMION. It calculates the electric and magnetic field as

Field = M + P0 + k1*P1 + k2*P2 + k3*P3 + ...

with M the result of a magnetic field solution (obtained using SetMFP), Px electric field solutions (obtained using SetEFP) and kx coefficients taken from a configuration file. Details how to use CombineEMP with a sample script are contained in the source code.

b) A more generic (tough not completely generic) version of the particle trace code was implemented in TraceParP. This program accepts a file with particle start parameters and writes splat positions and trajectory data into log files. The particles are evenly distributed between available nodes.

c) Several new shell and perl scripts facilitate the generation of geometry files and the analysis and visualization of trajectories using a VRML (3D) viewer.

4.2.2 Bug fixes

BoxPrepP:
A bug allowing particles to traverse solids was identified and a fix implemented. Main reason for the bug was the fact that each point of the simulation grid only stores one nearest surface of a solid. In geometries where more than one brick populates a simulation grid cell this could result in not detecting the proper inside/outside status of a grid point. The implemented fix does not completely eliminate the problem but makes an occurrence more unlikely.

Furthermore, to points inside a brick the potential of the brick was assigned. This is not necessary for calculations but makes viewing of potential distributions easier. The internal structure of CombineEMP benefits also from this change.

4.2.3 Open problems

a) It is still possible for particles to penetrate solids in case more than 12 bricks occupy a grid cell (this happens i.e. on the center axis of a cylinder).

b) Transparent objects are no longer treated correctly (most likely due to the change in BoxPrepP that assigns potentials to points inside the bricks). Often particles are erroneously reflected from transparent surfaces (probably due to problems establishing the inside/outside status of an arbitrary point in space.

c) SetMFP contains an error that calculates invalid magnetic field solutions at the border between to slices processed by adjacent nodes in parallel mode. The plane affected is one grid cell size wide is oriented perpendicular to the

Y-axis (? verify this) and shows a approximately 2x to low field strength. A quick fix is to not use parallel mode for SetMFP (launch on a single node instead). However this resulted in longer execution time.

4.3 Optimizer

Up to five independent simplex optimizers threads were used. Despite the disadvantages of the simplex algorithms (it tends to serialize jobs and is therefore not well suited for implementation on a parallel computer) it was used because of its well known properties. The 'serialization' problem was compensated by launching up to five parallel independent simplex threads with different start parameters.

4.3.1 New features

No new features were implemented.

4.3.2 Bug fixes

No new bugs were found or fixed.

4.3.3 Open Problems

The simplex algorithm is not well suited for parallel execution on a cluster. Parallelization can only be obtained by using parallel programs for the individual calculation steps and not by parallelizing the optimizer itself. Several other optimizer algorithms (random, PSO, Condor) were tested, but in the time available none could be tested to the same level as the simplex algorithm. Therefore only simplex was used.

4.4 Cluster

4.4.1 Overview

The cluster configuration was adapted specifically to the computing environment used. A fast master node hosts all programs and provides common storage via NFS for more than 180 calculation nodes. Each of this nodes is a standard PC witch is turned into a cluster node by booting from a magic CD. New nodes announce them selfs to the master node where they can be included into the cluster universe.

The optimizer program acts as master program which generates jobs (generate geometry, calculate field distributions, trace particles, evaluate solutions, etc...) and submits them to the sheduler. The sheduler assigns for each parallel program (BoxPrepP, SetMFP, etc.) prior to start a certain number of CPUs and launches the program as soon as enough CPUs are available.

All data files are stored in the common storage on the master node. For each optimization step new filenames are generated. available storage allows to

keep the data equivalent of about 3 days of optimization without deleting anything important. Several visualization tools allow to monitor cluster activity, development of the optimizer performance, calculated geometries and trajectories (using VRML), and node status.

4.4.2 Open Issues

As most of the cluster management software was new, several issues could not be solved in the time available:

a) The cluster is rather static at the moment. It is rather involving to remove a crashed node (i.e. due to temperature problems) from a running cluster and also not so easy to add new nodes while the cluster is running.

b) Most programs write to 'stderr' to report status information to the master node. With more than 100 nodes, the I/O redirect mechanism of LAM MPI often fails to allocate a free network socket resulting in a 'too may files open' error message from the master node and in a prematurely end of the launched parallel program on the cluster. Several attempts were made to fix this problem (including a recompilation of the Kernel with more file handles) but none was effective except the complete suppression of stderr messages.

c) Only one program can be launched on an individual node at the moment. Often a single program does not saturate a node due to time spent in waiting for data sent by other nodes. This is a limitation of the job sheduler used and not of the underlying MPI library.

d) A method to install software on each of the >180 nodes without the need to reboot or to individually log in to each node is needed.

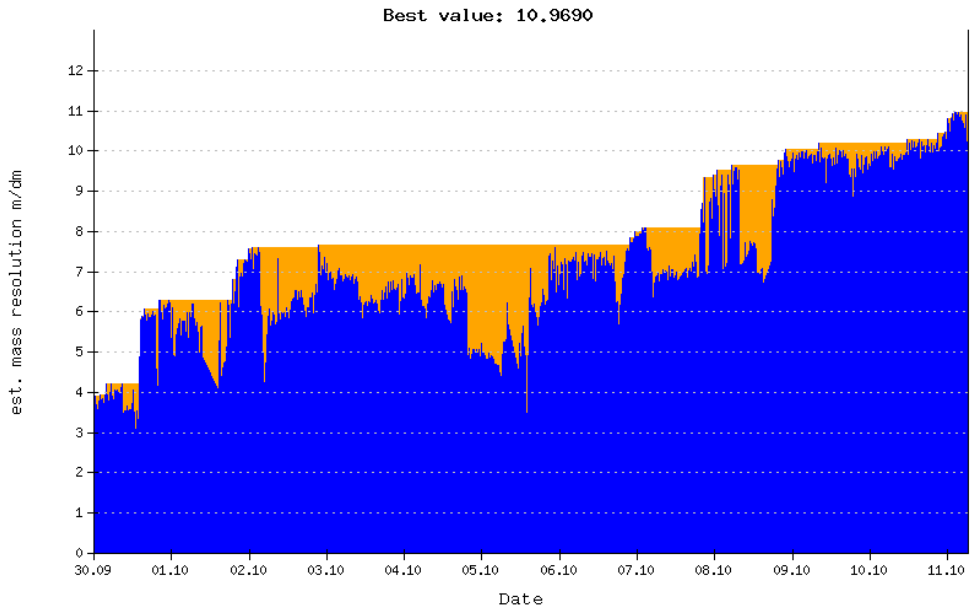

Figure 5.7: Evolution of the mass resolution during the optimization. Data from the second half of the three weeks of available computation time is shown. Blue represents the current value of mass resolution and orange the maximum value obtained so far.

5.7 Additional Data Analysis

5.7.1 Motivation

Although most data were analyzed prior to the submission of the report, more work on the data was done to better understand the performance of the optimizer code, and the properties of the ion-optical design before and after the optimization. Selected results of this work are shown in this Section.

5.7.2 Optimizer Performance

Detailed work was done to assess the performance of the optimizer on a cluster computer. Figure 5.7 shows the evolution of the objective function scaled to represent the mass resolution of the simulated geometry variant for the second half of the three weeks of computation time. Optimization started with a mass resolution $\frac{m}{\Delta m} \approx 2$ about ten days prior the first data point shown in Figure 5.7. The data shown does not, however, present one unattended optimization run. About every 24 hours, the optimization was stopped, the individual values of the objective function carefully analyzed and the parameterization (the free parameters in the optimization process) changed according to the best results obtained so far. Periodic review of the solutions calculated by the optimizer process also allowed the identification of sensitive parameters as

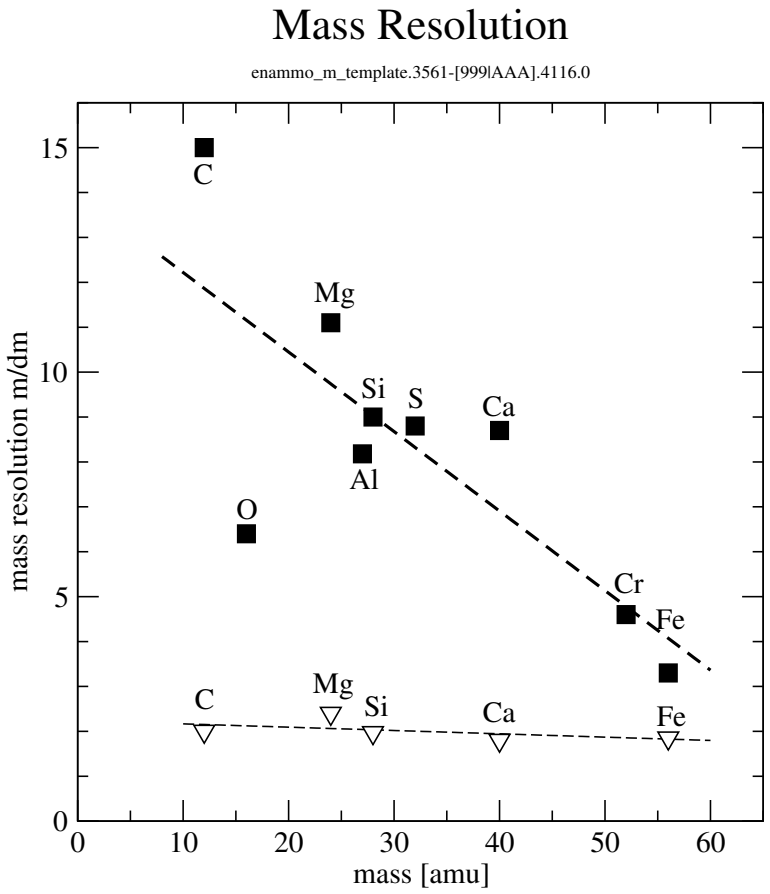

Figure 5.8: Mass resolution before (triangles) and after optimization (squares). The lines are shown to guide the eye. The low value for oxygen after optimization is caused a split of the oxygen particle trajectories in two groups due to the finite elementary block size used to represent the true geometry. As consequence the oxygen peak was broadened resulting in a lower resolution.

opposed to robust ones with no large influence on the result and to prevent the optimizer from being stuck in a local optimum in parameter space.

5.7.3 Mass Resolution

A comparison of the mass resolution prior and after optimization is shown in Figure 5.8. The data shown is a combination of the data shown in the report in Chapter 5.6 with detailed simulations done for the instrument geometry prior optimization. The mass resolution for lighter atoms could be increased considerably more than the resolution for heavy atoms. This is due to the decreasing magnetic field strength in the magnetic sector further away of the center axis of symmetry, the limited diameter of the magnetic section, and the non ideal magnetic sector boundary orientation at the location where atoms with $m > 40$ leave the magnetic sector. The mass resolution for heavy ions, e.g., iron could only be moderately increased.

5.8 Conclusion

The ion-optics optimizer was successfully ported to a parallel cluster computer. Outstanding optimization results were obtained within the time available on the cluster for a complex instrument design including electric and magnetic fields. Only a few remaining problems were identified, the most important two being the need to implement a truly parallel optimization algorithm and the elimination of the communication bug in the `SetMFP` module of TRACE prohibiting the distribution of the computation load of this module to more than one node.

The best value obtained for the mass resolution should be considered as lower limit as the optimization process had to be stopped because the available computation time ran out. It could be shown nevertheless that a low energy neutral particle instrument including mass analysis using a magnetic sector still has a huge potential for further development.

Part III

Instrument Prototypes

Chapter 6

Neutral Interstellar Composition Experiment NICE

6.1 Introduction

The Interstellar Neutral Composition Experiment, NICE, was an earlier attempt to build a high sensitivity energetic neutral atom instrument with mass, energy, and angular resolution. NICE used a small conversion surface combined with an energy resolving ion-optical lens and a time-of-flight mass spectrometer. A prototype without the angular resolution was built and successfully tested using neutral particle beams in two different facilities, in Bern [Ghielmetti et al. 1983] and in Denver, USA [Stephen et al. 1996].

6.2 Paper: NICE: an instrument for direct mass spectrometric measurement of interstellar neutral gas

M. Wieser, P. Wurz, P. Bochsler, E. Moebius, J. Quinn, S.A. Fuselier, A. Ghielmetti, J.N. DeFazio, T.M. Stephen and R.J. Nemanich

(Submitted March 2005 to Measurement Science and Technology)

NICE: an instrument for direct mass spectrometric measurement of interstellar neutral gas

M. Wieser†‡, P. Wurz†, P. Bochsler†, E. Moebius‡, J. Quinn‡, S.A. Fuselier§, A. Ghielmetti§, J.N. DeFazio‖, T.M. Stephen‖, R.J. Nemanich¶

† University of Bern, Physikalisches Institut, Sidlerstrasse 5, 3012 Bern, Switzerland
‡ University of New Hampshire, Dept. of Physics and Inst. for Study of Earth, Oceans and Space, Durham, NH 03824, USA
§ Lockheed Research Laboratories, 3251 Hannover St., Palo Alto, CA 94304, USA
‖ University of Denver, Department of Physics and Astronomy, Denver, CO 80208, USA
¶ North Carolina State University, Department of Physics, 408A Cox, Box 8202, Raleigh, NC 27695, USA

Abstract. The direct measurement of the neutral interstellar gas requires a very sensitive neutral particle imaging instrument in the energy range of 10 eV–1000 eV. For successful detection and identification, the neutral particles have to be ionized first, which will be accomplished via surface ionization. This method is successfully employed in the Low Energy Neutral Atom imager (LENA) instrument on the IMAGE spacecraft launched on 25 March 2000, which still operates well. We present the laboratory prototype of the Neutral Interstellar Composition Experiment (NICE), a neutral particle mass spectrometer dedicated to the measurement of interstellar gas, and will discuss its instrumental characteristics. Performance is evaluated with emphasis on the neutral to negative ion conversion for hydrogen and oxygen and the collection of these ions by the mass spectrometer. Measurements of the detection efficiency of the prototype for primary neutral hydrogen and oxygen atoms are presented. Several conversion surfaces, conductive and insulating, were investigated and all are potential candidates for a next generation neutral particle imaging instrument.

Submitted to: *Meas. Sci. Technol.*

PACS numbers: 07.87.+v, 95.55.Ym, 98.38.Am

‡ To whom correspondence should be addressed (wieser@phim.unibe.ch)

1. Introduction

Measurements of the physical parameters (temperature, density, composition, and others) of the local interstellar medium (LISM) will give information about the evolution of the solar system and our galaxy. The LISM is separated from the solar system by the heliopause and charged interstellar particles can not cross this boundary to enter the solar system. The neutral fraction f the LISM, however, is not subject to magnetic interactions and can therefore penetrate deeply into the solar system. As the Sun moves with a velocity of approximatively 26 km/s relative to the LISM a directed inflow of interstellar neutral atoms can be observed [1, 2, 3, 4]. Furthermore, energetic neutrals are produced by charge exchange processes at the heliospheric boundary [5]. When approaching the Sun the neutral particle populations are affected by gravitation, photo ionization and charge exchange processes. For a spacecraft traveling from Earth toward the heliopause, at a distance of about a few astronomical units from the Sun these effects become negligible. Consequently it is possible to infer the properties of the neutral interstellar gas by measuring the properties of the inflowing neutrals. This has been done for interstellar helium by the Neutral Interstellar Gas Instrument (GAS) on the Ulysses spacecraft [6]. The Ulysses mission was launched on 6 October 1990 and was brought into a polar orbit around the Sun 2 August 1992 using a gravitational assist at Jupiter. Ulysses still operates and is in its third orbit around the Sun. The GAS instrument takes data at selected observation times when the LISM flow vector and the space craft position are favorable. Elements other than Helium can potentially be measured directly using the surface ionization technique [7, 8]. Surface ionization is currently successfully employed by the Low Energy Neutral Atom imager (LENA) instrument on the IMAGE spacecraft for investigations of the terrestrial magnetosphere [9]. LENA surface conversion technology development started late 1992 at the University of Bern. The LENA instrument development started in fall 1995, after NASA's selection of IMAGE as a MIDEX mission.

We have built and tested the laboratory prototype of the Neutral Interstellar Composition Experiment (NICE) instrument for the detection of neutral hydrogen, carbon and oxygen atoms using the surface ionization technique. A velocity range of 10 km/s to 100 km/s corresponding to an energy range of 10 eV–1000 eV depending on species was investigated. This velocity range is expected for the inflow as seen from a spacecraft in a solar orbit or on an escape trajectory from the solar system. NICE is a pinhole camera with angular resolution along one dimension, allowing angularly resolved direct measurements of the interstellar gas flow on possible future missions, such as NASA mission concepts Interstellar Pathfinder [10], Interstellar Boundary Explorer [11], Realistic Interstellar Explorer [12], or Interstellar Probe [13].

2. Prototype Instrument

Figure 1 shows a schematic drawing of the NICE prototype. Neutral particles enter the instrument through an aperture preceded by a charged particle deflection system that hinders charged particles from entering the system. For successful detection the incident neutrals

must be ionized first, which is accomplished by surface ionization [14]. Upon reflection at grazing incidence from a suitable surface a fraction of the incident neutrals is negatively ionized (1% to 30%) [15, 16, 17]. An electrostatic extraction lens collects and accelerates these ions before they are analyzed in a time-of-flight mass spectrometer (TOF) and provides coarse primary particle energy resolution [7, 8]. Several different conversion surface materials were tested with the NICE prototype: A hydrogen passivated CVD diamond surface [17, 18], a polished MgO single crystal [16], a layered sample with a $BaZrO_3$ top layer [15, 19], and a polished poly-crystalline tungsten surface, the LENA/IMAGE flight spare surface [9]. The investigated conversion surfaces (CS) were all polished to a roughness of a few nm RMS, which is necessary for good particle reflection with minimal angular scattering.

Negative ions originating from the entire conversion surface area are focused to a spot at the TOF entrance plane for all emission angles. The position of the spot is a function of the reflected particle energy. Angular scattering at the CS tends to broaden the focal spot. Because this effect is smaller than the energy dispersion of the lens, it is possible to extract moderate energy information from the position across the exit of the lens. Figure 3 depicts a SIMION [20] simulation of the focusing properties of the extraction lens, where a situation with the conversion surface CS on ground potential is shown. Neutral particles enter the lens from the left and are negatively ionized at the CS. Negative ions with three different energies after reflection (14 eV, 50 eV, and 200 eV) and two different scattering angles from the surface (65°, dark colors, and 82°, light colors, to the surface normal) are shown. Particles with different energies are mapped to different positions at the image plane where the TOF entry aperture is located. Different scattering angles at the CS have only a minor influence on the position at the image plane (see inset in Figure 3). In this simulation, the energy resolved spectrum at the image plane is about 15 mm wide (depending on used energy range) for a distance of 115 mm from the CS to the image plane.

The angle of the incident neutrals in a direction out of the paper plane in Figure 1, the azimuth angle, is transformed into an angular position along circular entry slit of the TOF section where the negative ions pass a carbon foil. After passing the carbon foil the particle has changed its charge state to positive and is detected at the stop micro channel plate (MCP). Secondary electrons generated at the carbon foil are also deflected towards the MCP where they generate the start signal. Start and Stop signals are then used to obtain the time of flight. If the TOF unit can measure not only the time of flight of an ion, but also the position at its entrance in two dimensions, then three quantities of the detected particle are measured: mass, energy, and azimuth angle [7, 8]. To minimize the effects of non-specular reflection on azimuth resolution (out of the paper plane in Figure 1) it is necessary to apply a high extraction field near the CS and to have a high ratio of final to initial energy. A lens extraction voltage of 14 kV was used for the current tests compared to a energy below 1 keV per atom of the converted ions. A high ratio of final to initial energy also allows one directly infer the particle mass from the time of flight. The spread in time of flight due to different incident neutral particle energies, the energy loss at the conversion surface and at the carbon foil are small enough to make a good separation of Hydrogen, Carbon, and Oxygen.

The TOF mass spectrometer used in our prototype was an adapted flight spare unit of

the Composition and Distribution Function analyser (CODIF) as being flown on the Cluster satellites [21], which is larger than necessary for the use in NICE since it covers 360° in azimuthal direction where only 180° are needed for NICE. In addition to the TOF unit, electronics and power supply sections of CODIF were utilized while the original CODIF entrance section was replaced by the NICE extraction lens as shown in Figure 1. As the tests were performed with a collimated neutral beam, we did not make use of the angular position sensing capability of CODIF; only one single angular pixel of the TOF section was illuminated. Furthermore, the charged particle deflection plates in front of the CS were integrated into the neutral beam source. The ion energy at the exit of the lens was high enough to achieve reasonable detection efficiencies for all measured species overcoming the inherent decrease in the detection efficiency of the TOF below 1 keV per nucleon due to the carbon-foils used in the TOF to produce the start pulse. The extraction lens assembly including the CS was mounted on a linear translation table to allow for the scanning motion of the TOF entry aperture relative to the lens exit slit to achieve a coarse primary energy resolution. Figure 2 shows the prototype installed in the CASYMS calibration facility.

In a flight instrument the scanning will be performed by either varying the overall lens voltage or by using a position resolving TOF system as is being used on IMAGE/LENA. In the prototype the conversion surface was maintained on –19 kV potential. The negative ions from the conversion surface are then accelerated toward the –5 kV potential at the entrance aperture of the TOF and finally hit the detectors, where the signal is picked up with reference to ground potential. In a flight instrument the potential stack would be shifted such that the conversion surface is at ground potential as shown in Figure 3. The drawback of the configuration with the conversion surface at high negative voltage is increased background signal from sputtered ions caused by positive background ions accelerated toward the conversion surface. This was largely mitigated by thorough electrostatic shielding of the prototype. The instrument was mounted on a turntable to vary the incidence angle of the primary neutral atom beam relative to the conversion surface.

3. Neutral beam sources

Neutral particle sources from two independent facilities, University of Bern and University of Denver, were used for our investigations. In the Calibration System for Mass Spectrometers (CASYMS) facility [22] at the University of Bern a neutral atom beam was produced by reflection of a low energy positive ion beam from a single crystal tungsten surface. This technique for production of energetic neutral atoms is also used in surface science experiments [23]. Most ions are neutralized (>90 %) and molecules mostly dissociate upon reflection allowing to use positive molecules as primary particles as well. Molecular ions are produced very efficiently in the CASYMS ion source. The particles experience an energy loss of approximately 15 % upon reflection [15, 16]. After the reflection the remaining charged particles are removed by an electrostatic deflection system. Apertures were used to limit the angular spread down to 3.6° $\times$ 27° FWHM. The energy distribution of the neutral beam was peaking at 85 % of the primary ion energy with a width of approximately 10 % of the

primary energy [16]. The neutral flux is estimated by measuring the primary ion flux and by using the scattering and neutralization properties of the tungsten neutralization surface, which were calibrated before in the Imager for Low Energy Neutral Atoms (ILENA) facility at the University of Bern [16].

The test facility at the University of Denver supplied an intense pencil-like mono-energetic neutral beam [24]. This neutral atom beam is produced by photo-detaching electrons from negatively charged primary ions. An Ar-ion laser photo-detaches electrons from a fraction of the incident negative ions (<1 %). After removal of the surviving ions, a neutral atom beam remains. The neutral flux is measured by modulating the laser intensity with a chopper wheel resulting in a modulation of the fraction of photo-detached particles. The modulation amplitude of the collected current of the remaining ions at the charged particle deflection plates is equivalent to the neutral particle flux. This source has the advantage of high neutral atom production rate at very low energies ($\sim$20 eV) because at lower energies it takes longer for a particle to cross the laser interaction region. Therefore the probability for electron photo-detachment for an ion increases.

4. Results

The prototype instrument was extensively characterized. This included measuring the sensitivity of the instrument to varying angles of incidence of the primary beam, the energy resolution of the extraction lens, the overall detection efficiency of the instrument dependent on primary energy, and the separation of converted primary neutrals from sputtered particles from the conversion surface.

4.1. Extraction lens

Figures 4, 5, and 6 show ion-optical tests of the extraction lens. An ion beam with a cross section of $20 \times 1\,\mathrm{mm}^2$ was used to map out the ion-optical response of the extraction lens. For these measurements the conversion surface was replaced by a grid through which the ion beam entered. At the exit of the extraction lens an imaging detector was used. The traces in Figures 5 and 6 show collapsed images along the energy dispersive axis of the lens exit. The set of measurements in Figure 5 emulates the angular spread of the particles around the specular direction when scattered off the conversion surface. In this case the range of incident angles through the grid represent a specular reflection angle of 65°, with $\pm$ 15° of scattering about the specular direction. As one can see from the figure, ions leaving the conversion surface at these angles are all focused to line. At energies of 200 eV and more, the angular focusing is degraded. However, the effect is still less than the energy dispersion.

Figure 6 shows energy dispersive properties of the extraction lens for 75° angle of incidence. For an actual instrument incident angles between 80° and 70° with respect to the surface normal are considered, with the NICE prototype using 82° as nominal value. Clearly, the energy dispersive property of the extraction lens can be seen, which relates a radial position at the exit plane to an initial energy of the ion leaving the plane of the conversion

surface. Shoulders at some of the peaks and the double peak structure in the 100 eV panel are introduced due to the finite mesh size of the grid. At 14 eV ion energy there was the additional problem of accurately setting the beam energy, which caused a broadening of the line.

4.2. Angular sensitivity

The scattering properties of a conversion surface depend strongly on the angle of incidence of the primary particles [16]. In the Denver facility, the angle between the incident neutral beam and the surface normal was varied from 76° to 84°. However, because of the angular focusing of the extraction lens (Figures 4 and 5), no significant dependence of the detection efficiency with the angle of incidence was observed. Variations were observed in the count rate due to the relatively small size of the conversion surface used (25 mm diameter) and small beam misalignments on the order of a fraction of a millimeter.

4.3. Energy resolution and sputtering

The energy resolution of the system was investigated by scanning the TOF entry aperture over the exit aperture of the extraction lens. For each position a TOF spectrum was taken. Figure 7 depicts a sample TOF spectrum obtained with a 60eV neutral oxygen primary beam and a MgO conversion surface installed. The negative oxygen peak consists of the converted primary particles and a small fraction of sputtered particles (estimated to be <10% of the total oxygen counts). This upper limit results from measurements at higher energies (300 eV) where the extraction lens separates the sputtered and the converted particle fraction. The hydrogen peak is entirely due to sputtering of surface adsorbates by the primary particles. The sputtered fraction decreased considerably during the two days the surface was under test whereas the conversion efficiency for oxygen remained unchanged.

Figure 8 depicts an energy scan performed by varying the TOF entry slit position at the exit of the extraction lens when using a 150 eV primary oxygen beam and the CVD diamond conversion surface. After subtracting the background, fit functions were applied to the measured peaks in the TOF spectra to separate the observed species at each position at the exit of the lens. The approximate energy scale on the plot was obtained by using different primary energies and by observing the position of the maximum of the oxygen peak. The maximum represents 85 % of the primary energy, as 15 % is the approximate energy loss when reflecting a particle from the conversion surface [15, 16]. The peak is rather broad because the extraction lens has a limited energy focusing capability. That is further degraded by the finite entrance slit width of the TOF section (4 mm). Nevertheless, sputtered particles from the conversion surface can clearly be separated from converted incident neutrals. The energy distribution of the sputtered particles - mostly hydrogen - peaks at a few eV and consequently these particles appear on the low energy side of the spectrum.

4.4. Detection efficiency

The overall detection efficiency η_{total} of the instrument is a product of the efficiencies of the different subsystems and can be expressed as

$$\eta_{total} = \frac{F_{measured}}{F_{incident}} = \eta_i \cdot \eta_L \cdot \eta_F \cdot \eta_T$$

where $F_{measured}$ represents the number of valid TOF counts per second, $F_{incident}$ the number of incident neutral atoms per second that enter the instrument, η_i the fraction of particles that are negatively ionized upon reflection at the conversion surface, η_L the collection efficiency of the extraction lens, η_F the transmission of the C-foil in the TOF, and η_T the detection efficiency of the TOF, which is species dependent. η_i shows a dependence on primary particle energy and species [15, 16, 17]. η_F and η_T depend on species and postacceleration voltage (14 kV in our case), the values used were taken from the CODIF calibration report [25]:

species	η_F	η_T
hydrogen	0.9	0.4
oxygen	0.8	0.2

η_L depends only on the postacceleration voltage as the initial neutral particle energy is much less than 14 keV per atom.

Using the known scattering and ionization properties of the conversion surfaces [15, 16, 17], the collection efficiency of the lens, η_L, was found to be in the range from 0.11 to 0.13 independent of the incident energy and species of the primary particles. The main energy dependence of the overall detection efficiency is thus caused by the energy dependence of the ionization efficiency.

After subtracting the sputtered fraction, the overall detection efficiency is calculated by integrating over the energy distribution at the exit of the lens. Figures 9 and 10 depict the detection efficiency of the prototype for primary neutral oxygen and hydrogen for different conversion surfaces. The results obtained using the two different neutral beam sources, in Bern and Denver, agree very well (see Figure 10, two topmost panels). The efficiencies for truly converted (ionized) atoms are presented with the probabilities for sputtering by primary atoms and background ions accelerated onto the conversion surface resulting in a detected ion. All combinations of primary atoms and conversion surfaces show an energy dependence with increasing efficiency at higher particle energy. The obtained detection efficiency data were fitted by simple exponential functions that are given as grey lines in Figures 9 and 10. Figure 11 depicts a comparison of the instrument performance depending on primary energy, type of conversion surface, and primary species. In this summary plot only the empirical fits, shown as gray lines in Figures 9 and 10, are given. For primary oxygen a strong energy dependence over several orders of magnitudes was observed at low energies, whereas for primary hydrogen the detection efficiency curves are almost flat in the investigated energy range.

4.5. Extracting positive ions

We have also considered using the fraction of positively ionized particles instead of the negative ions, which are also formed upon reflection from the conversion surface. When using positive ions contamination of the measurement by secondary and photoelectrons is not a problem, and their efficient suppression at the conversion surface will not be necessary. The detection efficiency obtained using the positive hydrogen fraction is shown in Figure 12. For energies higher than 150 eV the detection efficiency is higher than the detection efficiency obtained using the negative ion fraction (Figure 9, second panel from top) but at lower energies the detection efficiency drops very fast. As interstellar hydrogen arrives with at most 30 eV in the spacecraft reference frame, the negative ion fraction is preferable because of the higher detection efficiency. Oxygen is not detectable when using the positive ion fraction, because the positive oxygen ion fraction after reflection off the conversion surface is very small (<1%), even at energies up to 2 keV [16, 26]. Using the positive ion fraction does not seem to be an attractive option for an interstellar neutral gas instrument for the energy range and the species of interest.

5. Discussion

5.1. Extraction lens

The energy resolving capabilities of the extraction lens were found to be according to ion-optical simulations. Given the energy spread a particle experiences at the conversion surface, the resolving power of the extraction lens is close to the optimum value. A flight version of the lens would benefit from anti-reflective surface coating of the lens electrodes to minimize signals originating from particles reflected or sputtered at structure parts. While not a problem in the prototype the measured background could be reduced significantly, thus enlarging the dynamic range.

5.2. Angular sensitivity

No dependence of the detection efficiency on the angle of incidence in the range of 76° to 84° was found. This is consistent with earlier findings [16] that showed no dependence of the ionization efficiency of a conversion surface from the angle of incidence for angles between 80° and 85°. Although the width of the angular scattering distribution increases at steeper angles and also at higher particle energies, the extraction lens can focus these angular distributions sufficiently well.

5.3. Energy resolution and sputtering

The energy resolving capability of the extraction lens allows for the separation of sputtered particles from converted incident neutrals. The energy distribution of the sputtered particles peaks at a few eV, thus all sputtered particles appear at the low energy side of the energy spectrum. Hydrogen is the predominant species sputtered from the conversion surface

(Figure 7). The main sources for sputtering particles will be primary helium, carbon, and oxygen neutral atoms as they are the most abundant elements to which the instrument is sensitive after hydrogen. Sputtering due to primary hydrogen is unlikely because of the low energy of the neutral hydrogen atoms (70 km/s $\approx$ 25 eV) and the low mass. Assuming a CVD diamond conversion surface and using elemental abundances of the neutral interstellar inflow from [27], hydrogen sputtered by incident oxygen atoms at a velocity of 70 km/s would contribute about 1‰ to the total hydrogen counts; about 4% of the hydrogen counts will be due to sputtering by helium. Effects that modify the elemental abundances, i.e., at the heliospheric interface, are neglected in this estimation.

In the LISM, oxygen has an abundance of approximately $5{\cdot}10^{-4}$ relative to hydrogen and the sputtering efficiency for hydrogen atoms is about 10^{-3} (from Figure 10, middle panel). The fraction of sputtered hydrogen due to neutral oxygen is therefore of the order of $5{\cdot}10^{-7}$ per incident neutral hydrogen atom, far less than the detection efficiency for an incident 70 km/s hydrogen atom at $5{\cdot}10^{-4}$. Thus, hydrogen sputtered by incident oxygen should amount to about $1{\cdot}10^{-3}$ of the hydrogen counts.

Hydrogen sputtered by incident helium gives stronger constraints: when estimating [28] the sputtering efficiency for helium using the hydrogen and oxygen data, a sputter yield of $1{\cdot}10^{-4}$ is obtained for helium atoms at 70 km/s. Combined with a helium abundance in the LISM of approximately 0.1 relative to hydrogen, $2{\cdot}10^{-5}$ hydrogen counts due to sputtering by helium are expected per incident neutral hydrogen. This yields a 4 % contribution to the hydrogen atom signal.

In our experiment, the conversion surface was transfered from air into vacuum and measurements were started after approximately one day later when the pressure in the vacuum chamber was below 10^{-6} mbar. In the first few hours of measurement a systematic decrease in the sputter rate was observed, indicating outgassing and conditioning of the surface with time. The observed sputter rates are thus considered upper limits. On a mission heading out to the heliopause the instrument would have several years to outgas in a much better vacuum. The NICE instrument could also be combined with a GAS type instrument sensitive to helium to better estimate the sputter rate and also to extend the elemental range to helium.

5.4. Conversion surfaces

Of the four different investigated conversion surfaces, $BaZrO_3$, MgO, CVD diamond, and tungsten, the CVD diamond surface exceeds all others in performance except for oxygen at energies above 150 eV per atom where $BaZrO_3$ shows better performance (Figure 11). Unfortunately the ionization yield for neutral oxygen of the $BaZrO_3$ surface drops very fast below 150 eV per atom. CVD diamond does not show this limitation. The hydrogen terminated CVD diamond surface is furthermore mechanically and chemically very stable and can be polished down to a few nm_{rms} for optimized scattering properties. Although the sample used was a custom made surface, a similar commercially available material, tetrahedral amorphous carbon (ta-C) films, a subset of diamond like carbon (DLC) films, was recently shown to have approximately equal performance [29]. The bulk materials tungsten

and MgO are less favorable, the ionization efficiency of tungsten at low energies depends strongly on surface adsorbates and the insulating properties of MgO causes charging problems due to photoelectrons when illuminated by UV radiation.

5.5. Instrument detection efficiency

Assuming a interstellar neutral density for hydrogen of $0.1\,\mathrm{cm}^{-3}$ and an apparent inflow velocity of 70 km/s (as seen from a spacecraft), locking into the apparent inflow direction, and integrating over the whole angular distribution approximately 75 counts/s for hydrogen and 0.35 counts/s for oxygen can be expected using the current prototype with an active area of $0.35\,\mathrm{cm}^2$.

Without significant changes in the design, the count rate can be increased by a factor of 4 by increasing the open area of the instrument. This is achieved by three measures: The size of the CS is increased from 25 mm to 40 mm in radial direction away from the axis of symmetry, the size of the pinhole in the azimuthal plane is increased until its matches the azimuthal resolution of the TOF of 22.5°, and the average angle of incidence to the CS is changed from from 82° to 78°. This will result in an open area of $1.4\,\mathrm{cm}^2$. All three modifications require no change of the ion-optics of the extraction lens. The CS size presently used for the NICE prototype was chosen for cost reasons. Simulations using SIMION show that the present extraction lens is capable to collect particles from a larger CS area without significant losses.

Another factor of 2 can be obtained by optimizing the extraction lens and the interface between the extraction lens and the TOF. A smaller part of this factor will be obtained by optimizing the field shaping electrodes above the CS using numerical methods. The larger part will be gained by removing the defocusing properties of the TOF entry aperture plate.

A factor of 1.5 is feasible by optimizing the TOF unit itself. For the NICE prototype, the TOF unit was operated with signal outputs referenced to ground potential and with lower internal acceleration voltages in order to reduce the the maximum voltage present in the setup to 19 kV. A TOF unit specifically designed for this application would not be subject to these limitations and therefore have a larger sensitivity.

By combining all these improvements count rates of 900 counts/s for hydrogen and 4.2 counts/s for oxygen would be obtained.

Further optimizations are possible by switching from a 1D-pinhole camera type sensor to a single pixel telescope as used in the GAS instrument. Although major modifications to the ion-optics would be necessary, this would increase the collection efficiency of the lens to almost 100 %, as also particles scattered in azimuthal direction could be focused onto the detector. The detection efficiency would increase by a factor of 3 to 4 compared to the optimized 1D-pinhole camera sensor. Consequently, count rates up to 3600 counts/s for hydrogen and 17 counts/s for oxygen are possible. A single pixel telescope would also allow to increase the open area as proposed for the Neutral Atom Telescope (NAT) sensor of the Interstellar Neutral Atom Detector (INAD) [30], where 38 cm^2 open area is used compared to $1.4\,\mathrm{cm}^2$ in the optimized 1D-pinhole camera sensor. The single pixel telescope arrangement is offset by the need of a scanning platform to measure the full sky angular distribution as

used by the GAS instrument or proposed for the INAD instrument or the need to change the pointing of the spacecraft on a regular basis as it is done on the IBEX mission [11].

6. Conclusion

We have successfully tested a prototype for an instrument for the direct measurement of the interstellar neutral gas. The results from two independent facilities agree very well. The detection efficiency of the present instrument is high enough to get reasonable counting statistics within hours. Sputtered and converted primary neutrals can be separated by their characteristic energies when leaving the conversion surface. The detection efficiency of the prototype can be increased up to a factor of 3 for the design used for the prototype and a factor up to 12 when changing to a single pixel telescope. NICE is planed to be part of the scientific payload of a new interstellar medium exploration spacecraft to be proposed in the MIDEX spacecraft class of NASA's Explorer Program, currently scheduled for the years 2011–2012.

Acknowledgments

The authors thank Matthias Boehm, Ken Crocker, and Mark Granoff for their support when performing the experiments and Adrian Etter for the operation of the CASYMS chamber. This work is supported by the Swiss National Science Foundation and by NASA Grant NAG5-8733.

[1] H.-J. Fahr. Global structure of the heliosphere and interaction with the local interstellar medium: three decades of growing knowledge. *Adv. Space Research*, 34:3–13, 2004.

[2] G. E. Thomas. The insterstellar wind and its influence on the interplanetary environment. *Ann. Rev. Earth Planet*, 6:173–204, 1978.

[3] M. Witte, M. Banaszkiewicz, H. Rosenbauer, and D. McMullin. Kinetic parameters of interstellar neutral helium: updated results from the ULYSSES/GAS-instrument. *Adv. Space Research*, 34:61–65, 2004.

[4] G. P. Zank and H. L. Pauls. Modelling the Heliosphere. *Space Sci. Rev.*, 78:95–106, 1996.

[5] M. Gruntman, E.C. Roelof, D.G. Mitchell, H.J. Fahr, H.O. Funsten, and D.J. McComas. Energetic neutral atom imaging of the heliospheric boundary region. *J. Geophys. Res.*, 106(A8):15767–15781, 2001.

[6] M. Witte, H. Rosenbauer, E. Keppler, H. Fahr, P. Hemmerich, H. Lauche, A. Loidl, and R. Zwick. The interstellar neutral-gas experiment on ULYSSES. *Astronomy and Astrophysics*, 92:333–348, 1992.

[7] A. G. Ghielmetti, E. G. Shelley, S. Fuselier, P. Wurz, P. Bochsler, F. Herrero, M. F. Smith, and T. Stephen. Mass spectrograph for imaging low energy neutral atoms. *Opt. Eng.*, 33:362–369, 1994.

[8] P. Wurz, M.R. Aellig, P. Bochsler, A. G. Ghielmetti, E. G. Shelley, S. A. Fuselier, F. Herrero, M. F. Smith, and T. S. Stephen. Neutral atom imaging mass spectrograph. *Opt. Eng.*, 34(8):2365–2376, 1995.

[9] T.E. Moore, D.J. Chornay, M.R. Collier, F.A. Herrero, J. Johnson, M.A. Johnson, J.W. Keller, J.F. Laudadio, J.F. Lobell, K.W. Ogilvie, P. Rozmarynowski, S.A. Fuselier, A. G. Ghielmetti, E. Hertzberg, D.C. Hamilton, R. Lundgren, P. Wilson, P. Walpole, T.M. Stephen, B.L. Peko, B. van Zyl, P. Wurz, J.M. Quinn, and G .R.Wilson. The Low-Energy Neutral Atom Imager for IMAGE. *Space Sci. Rev.*, 91:155–195, 2000.

[10] G. Gloeckler, M. Banaszkiewicz, P.A. Bochsler, H.J. Fahr, L.A. Fisk, P.D.C. Frisch, H.O. Funsten, J. Geiss, M.A. Gruntmann, D.L. Judge, M.A. Lee, D.J. McComas, D.G. Michell, E. Moebius, E.C. Roelof, H.R. Rosenbauer, M. Witte, P. Wurz, T.H. Zurbuchen, N.A. Schwadron, R.M. Johnson, J. Woch, R. Kallenbach, R. Lallement, P.A. Isenberg, M. Popecki, J.M. Quinn, R.L. McNutt, J.T. Gosling, V. Baranov, M.E.C. Hilchenbach, U. Mall, K. Scherer, M. Tosi, T. Linde, J.V. Vallerga, D. Rucinski, M. Bzowski, J.D. Slavin, and L. Fortson. Interstellar Pathfinder - A Mission to the Inner Edge of the Interstellar Medium. A proposal to the NASA in response to AO 98-OSS-03 for a Medium-Class Explorer, 1998.

[11] D. J. McComas, F. Allegrini, P. Bochsler, M. Bzowski, M. Collier, H. Fahr, H. Fichtner, P. Frisch, H. Funsten, S. Fuselier, G. Gloeckler, M. Gruntman, V. Izmodenov, P. Knappenberger, M. Lee, S. Livi, D. Mitchell, E. Möbius, T. Moore, D. Reisenfeld, E. Roelof, N. Schwadron, M. Wieser, M. Witte, P. Wurz, and G.P. Zank. The Interstellar Boundary Explorer (IBEX). In V. Florinski, N.V. Pogorelov, and G.P. Zank, editors, *Physics of the Outer Heliosphere: Third International IGPP Conference*, pages 162–181. AIP Conference Proceedings 719, 2004.

[12] R.L. McNutt, G.B. Andrews, R.E. Gold, A.G. Santo, R.S. Bokulic, B.G. Boone, D.R. Haley, J.V. McAdams, M.E. Fraeman, B.D. Williams, M.P. Boyle, D. Lester, R. Lyman, M. Ewing, R. Krishnan, D. Read, L. Naes, M. McPherson, and R. Deters. A Realistic Interstellar Explorer. In M. Velli, R. Bruno, and F. Malera, editors, *Solar Wind Ten, Proceedings of the Tenth International Solar Wind Conference*, pages 830–833. AIP Conference Proceedings 679, 2002.

[13] P. Liewer, R. Mewaldt, A. Ayon, and R. Wallace. NASA's Interstellar Probe Mission. Technical report, NASA Jet Propulsion Laboratory, Space Technology and Application International Forum STAIF, January 2000.

[14] P. Wurz. *The outer Heliosphere: Beyond the Planets*, chapter Detection of Energetic Neutral Particles. Copernicus Gesellschaft e.V., 2000.

[15] S. Jans, P. Wurz, R. Schletti, K. Brüning, K. Sekar, W. Heiland, J. Quinn, and R.E. Leuchter. Negative ion production by surface ionization at barium zirconate surface. *Nucl. Instr. Meth. B*, 173:503–515, 2001.

[16] M. Wieser, P. Wurz, K. Brüning, and W. Heiland. Scattering of atoms and molecules off a magnesium oxide surface. *Nucl. Instr. Meth. B*, 192:370–380, 2002.

[17] P. Wurz, R. Schletti, and M. R. Aellig. Hydrogen and oxygen ion production by surface ionization using diamond surfaces. *Surf. Sci.*, 373:56–66, 1997.

[18] P.W. May. Diamond thin films: a 21st-century material. *Phil. Trans. R. Soc. Lond. A*, 358:473–495, 2000.

[19] R. Yanochko, W. Brock, J. Krzanowski, J. Quinn, and R. E. Leuchtner, editors. *Pulsed laser deposition of barium zirconate thin films for neutral particle imaging applications*. Mat. Res. Soc. Symposium. Proc. Boston, MA, USA, December 1-6 1996.

[20] Inc. Scientific Instrument Services. *SIMION 3D Version 7.0 Ion Optics Program*. 1027 Old York Road. Ringoes, NJ 08551. USA, 1996-2005.

[21] H. Rème, J.M. Bosqued, J.A. Sauvaud, A. Cros, J. Dandouras, C. Aoustin, C. Martz, J.L. Médale, J. Rouzaud, E. Möbius, C. Krocker, M. Granoff, L.M. Kistler, D. Hovestadt, B. Kleckler, G. Paschmann, M. Ertl, E. Künneth, C.W. Carlson, D.W. Curtis, R.P. Lin, J.P. McFadden, J. Croyle, V. Formisano, M. Di Lellis, R. Bruno, M.B. Bavassano-Cattaneo, B. Baldetti, G. Chionchio, E.G. Shelley, A.G. Ghielmetti, W. Lennartsson, A. Korth, H. Rosenbauer, I. Szemerey, R. Lundin, S. Olson, G.K. Parks, M. McCarthy, and H. Balsiger. The Cluster Ion Spectrometry Experiment. *ESA SP-1159*, 1993.

[22] A. G. Ghielmetti, H. Balsiger, R. Bänninger, P. Eberhardt, J. Geiss, and D. T. Young. Calibration system for satellite and rocket-borne ion mass spectrometers in the energy range from 5 eV/q to 100 keV/q. *Rev. Sci. Instrum.*, 54:425–436, 1983.

[23] A. Losch and H. Niehus. Structure analysis of the KBr(100) surface - An investigation with a new method for surface analysis on insulators. *Surf. Sci*, 420:148–156, 1999.

[24] T.M. Stephen, B. van Zyl, and R.C. Amme. Generation of a Fast Atomic-Oxygen Beam from O^- Ions by Resonant Cavity Radiation. *Rev. Sci. Instrum.*, 67:1478–1482, 1996.

[25] L. M. Kistler. Cluster CODIF Calibration Report. Technical report, University of New Hampshire, NH, USA, 2000.

[26] H. Verbeek, W. Eckstein, and R. S. Bhattacharya. Negative hydrogen ion formation by backscattering from solid surfaces. *Surf. Sci.*, 95:380–390, 1980.

[27] J. Geiss and M. Witte. Properties of the interstellar gas inside the heliosphere. *Space Sci. Rev.*, 78:229–238, 1996.

[28] E. Taglauer. Surface Cleaning Using Sputtering. *Appl. Phys. A*, 51:238–251, 1990.

[29] J.A. Scheer, M. Wieser, P. Wurz, P. Bochsler, E. Hertzberg, S.A. Fuselier, F.A. Koeck, R.J. Nemanich, and M. Schleberger. High negative ion yield from light molecule scattering. *Nucl. Instr. Meth. B*, page in press, 2005.

[30] S. Levi, E. Moebius, D. Haggerty, M. Witte, and P. Wurz. An Interstellar Neutral Atom Detector (INAD). In M. Velli, R. Bruno, and F. Malera, editors, *Solar Wind Ten, Proceedings of the Tenth International Solar Wind Conference*, pages 850–853. AIP Conference Proceedings 679, 2002.

Figures

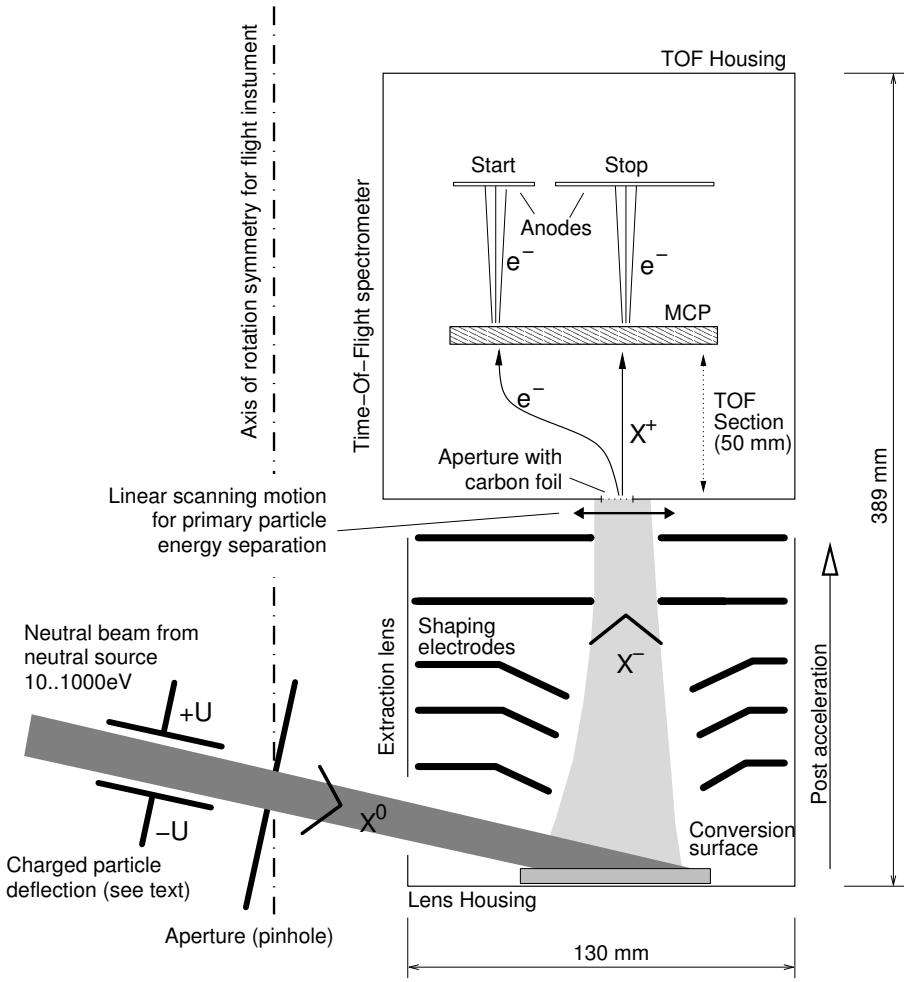

Figure 1. Schematic view of the NICE prototype with envelope dimensions. The indicated height includes the electronics box, power supplies, and digital processing unit needed for the time-of-flight spectrometer.

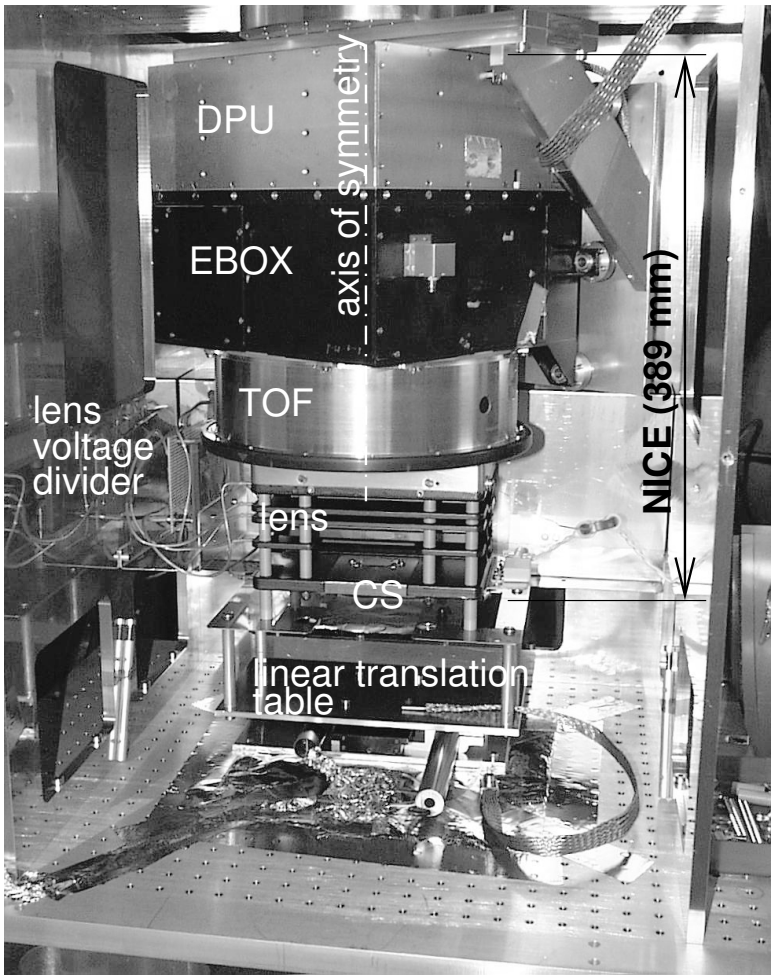

Figure 2. NICE prototype installed in the CASYMS [22] calibration facility at the University of Bern. Most electrostatic shielding and the ion beam neutralizing unit with the collimating entry aperture were removed for this picture. The small circular feature on the lowest plate in the lens right above the label 'CS' is the conversion surface. The time-of-flight mass spectrometer above the lens is an adapted flight spare unit of the Composition and Distribution Function analyser (CODIF) as being flown on the Cluster satellites [21]. The time-of-flight section is labelled with TOF, the electronics box containing the preamplifiers and the power supplies for the micro channel plates with EBOX, and the associated digital processing unit with DPU.

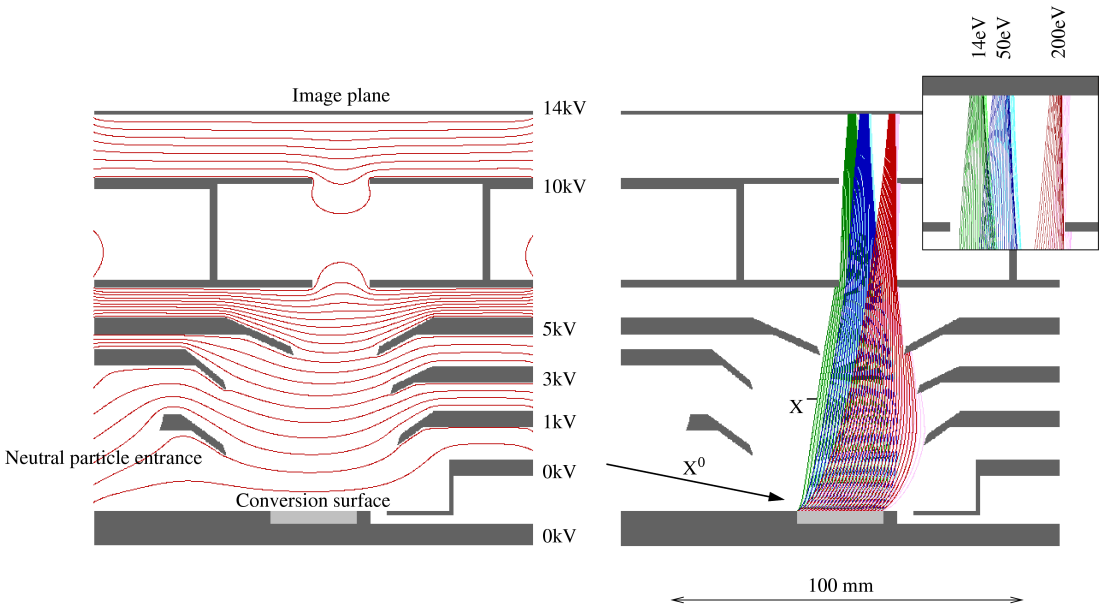

Figure 3. SIMION ion-optical simulation of the extraction lens. Equipotential lines with 500 V step size are shown in the left panel. Particle traces with different energies are shown in the right panel. Dark colors correspond to an angle of 65° and light colors to an angle of 82° to the surface normal at the conversion surface. Only a minor dependence of the position in the image pane on the angle of incidence at the conversion surface is visible (inset).

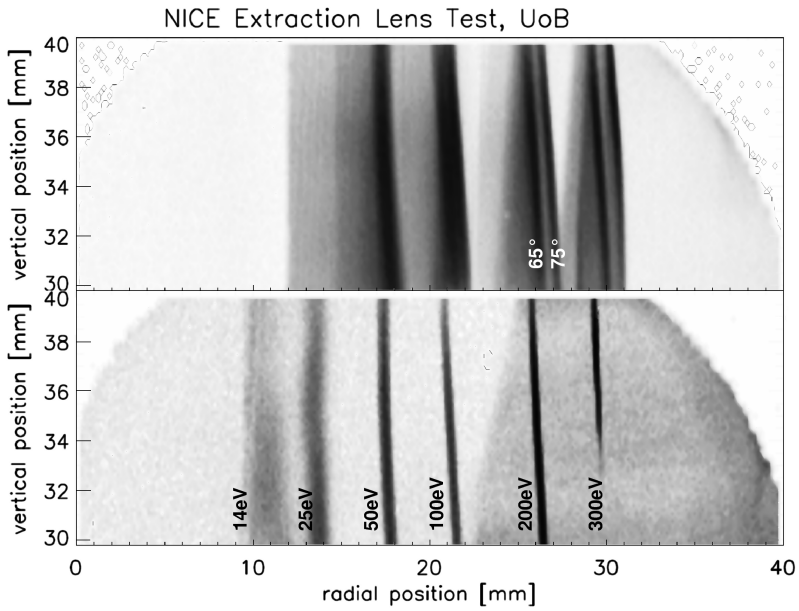

Figure 4. Energy resolving power of the extraction lens measured with an imaging detector placed at the exit of the lens. The response of the lens to beam energies from 14 eV to 300 eV at a constant angle of 75° to the conversion surface normal is shown in the lower panel. The upper panel shows the response to two different angles, 65° and 75°, for energies of 50 eV to 300 eV. As shown in Figure 3, angular focusing improves towards lower energies. The arc like structure in both panels is due to the field of view of the detector used. Note that the color scales of the two panels are both logarithmic and also different to enhance the visibility of details.

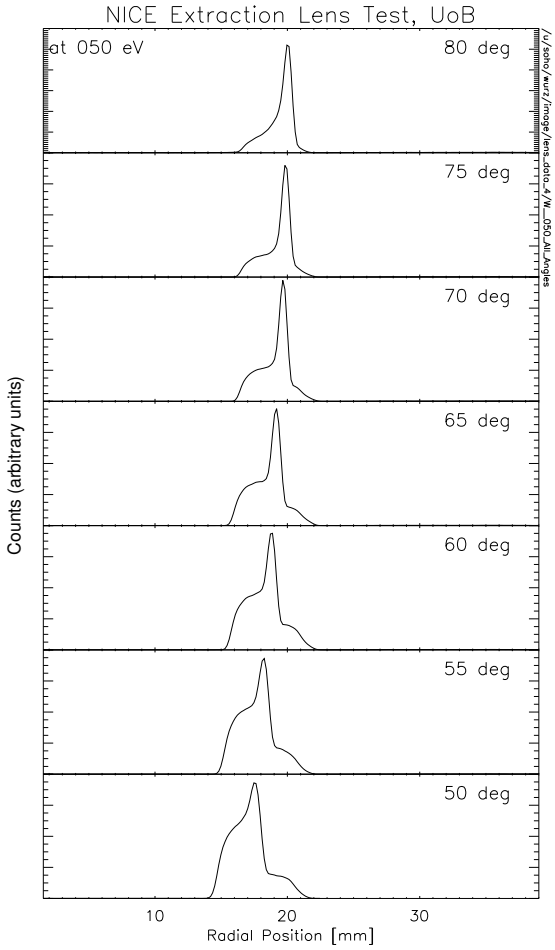

Figure 5. Result of ion-optical tests of the extraction lens. The seven panels show traces for a beam energy of 50 eV for a range of incident angles measured from the surface normal.

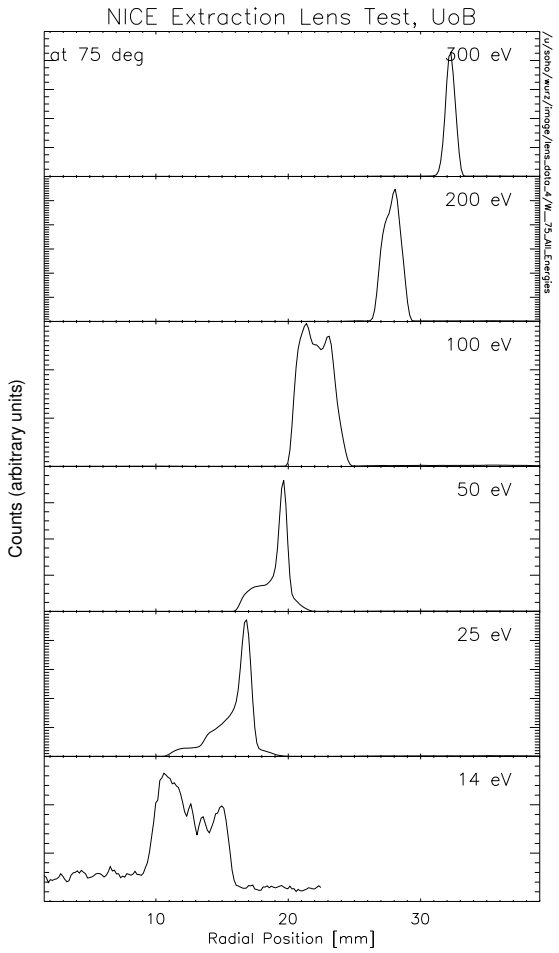

Figure 6. The six panels show traces for energies in the full range the extraction lens is designed for for an incident angle of 75° with respect to the surface normal.

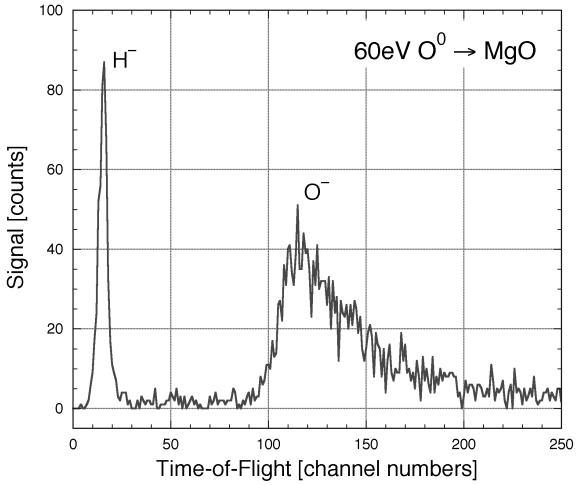

Figure 7. Sample TOF spectrum out of a scan over the exit of the extraction lens when using a 60 eV neutral oxygen primary beam and a MgO conversion surface. The time of flight increases with channel number.

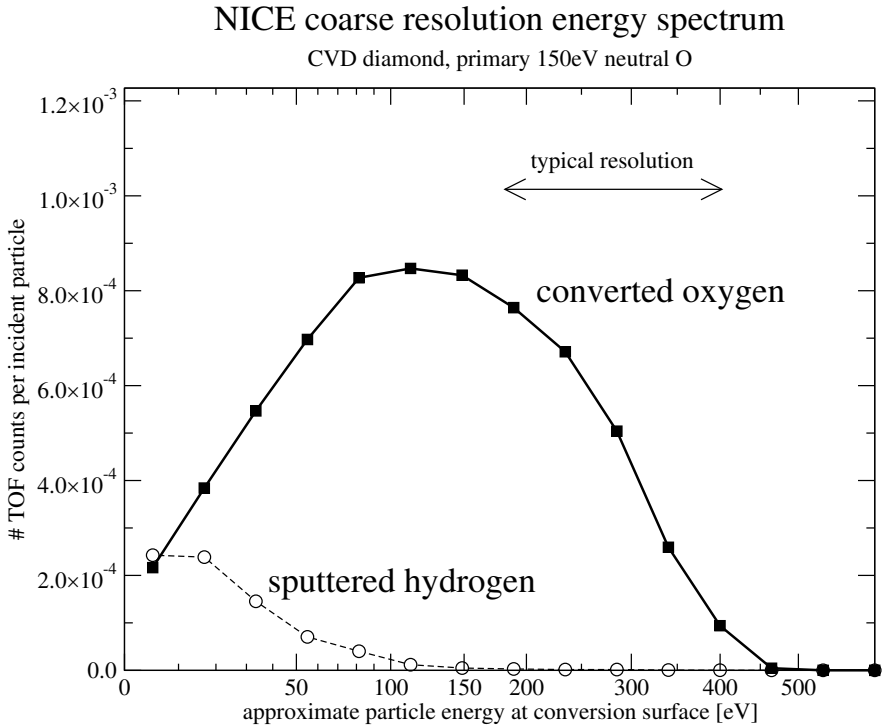

Figure 8. Scan over the exit of the extraction lens. Neutral oxygen was used as primary beam and negative charged particles were collected.

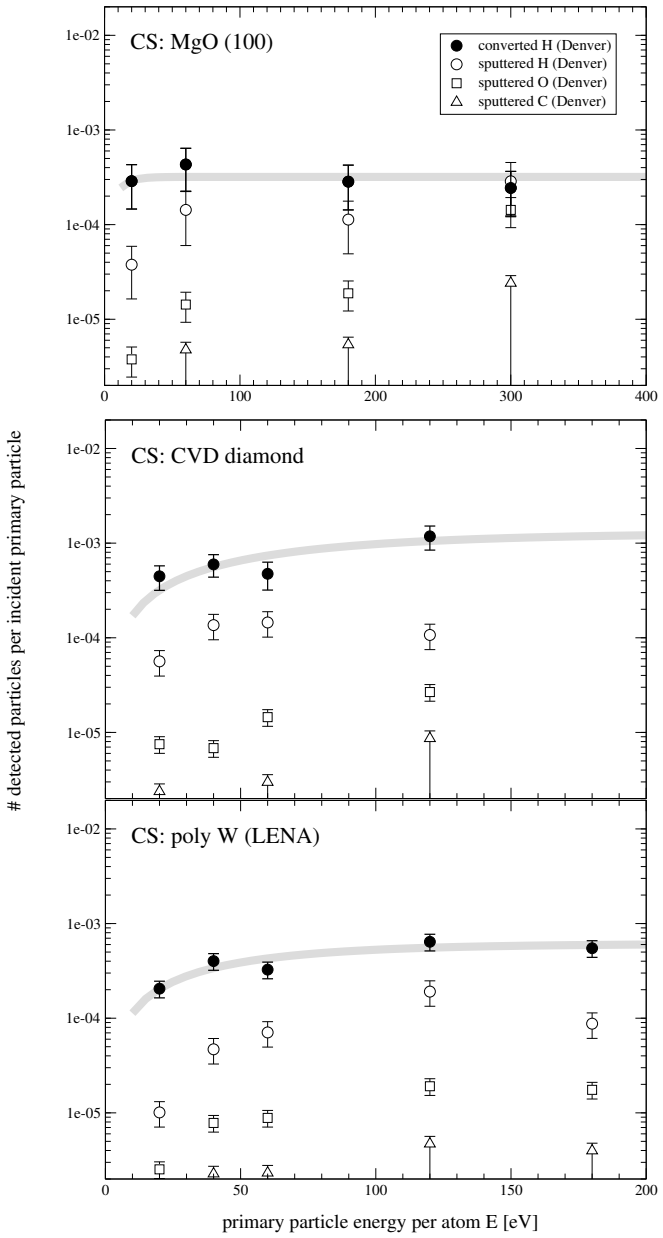

Figure 9. Detection efficiency for hydrogen obtained for different conversion surfaces (CS). Note the different energy axis scaling in the top panel.

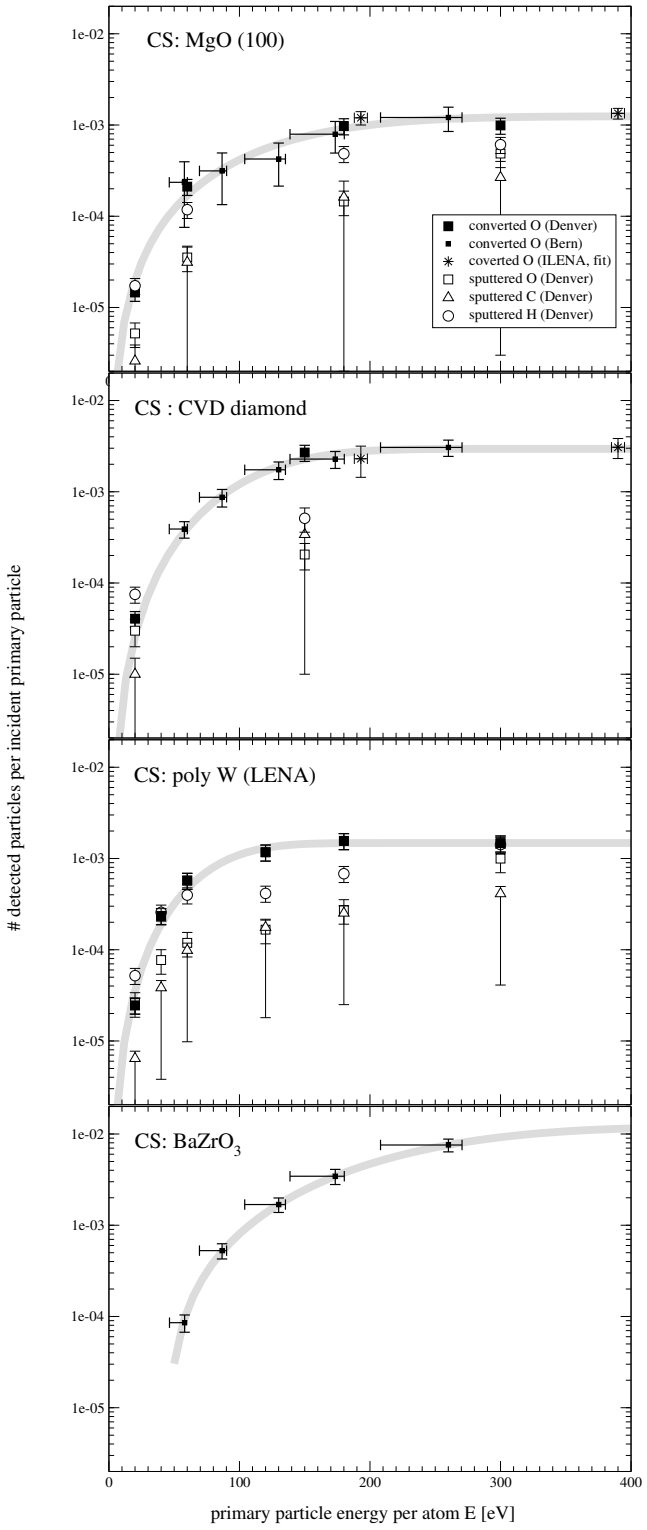

Figure 10. Detection efficiency for oxygen obtained for different conversion surfaces (CS). The data set labelled ILENA was taken from [16].

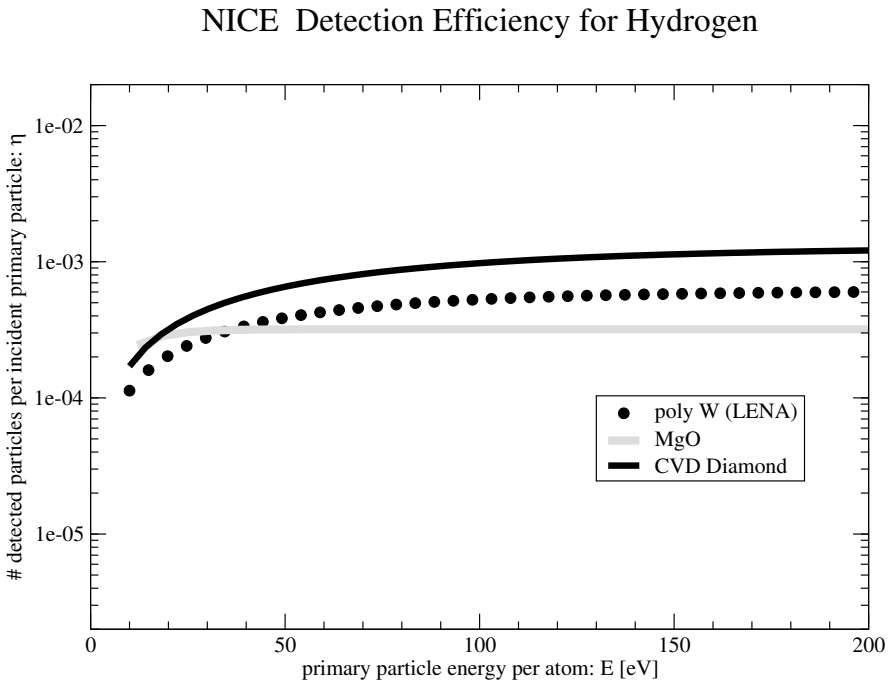

(a)

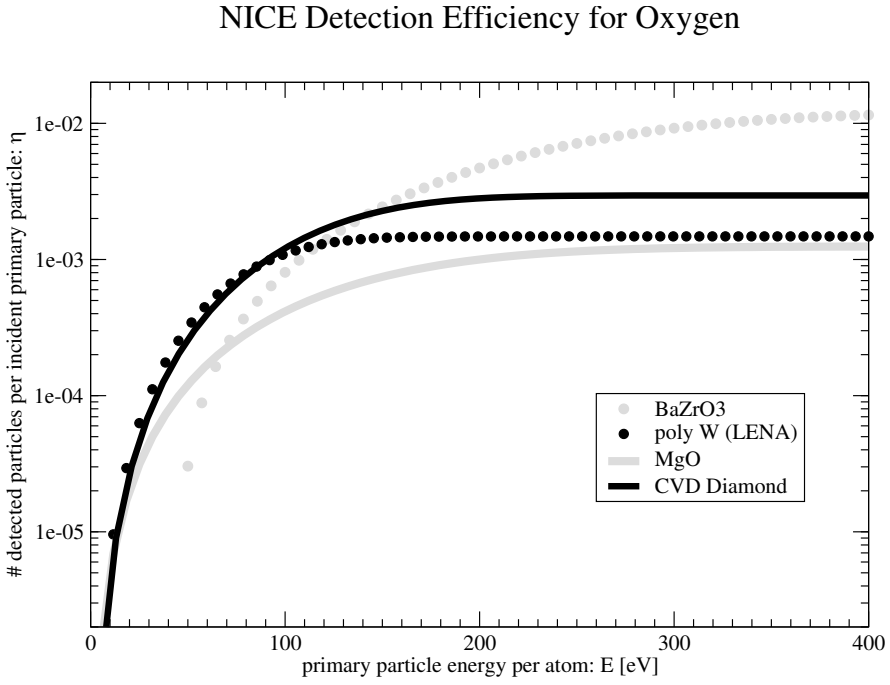

(b)

Figure 11. Summary of empirical detection efficiencies for different conversion surfaces

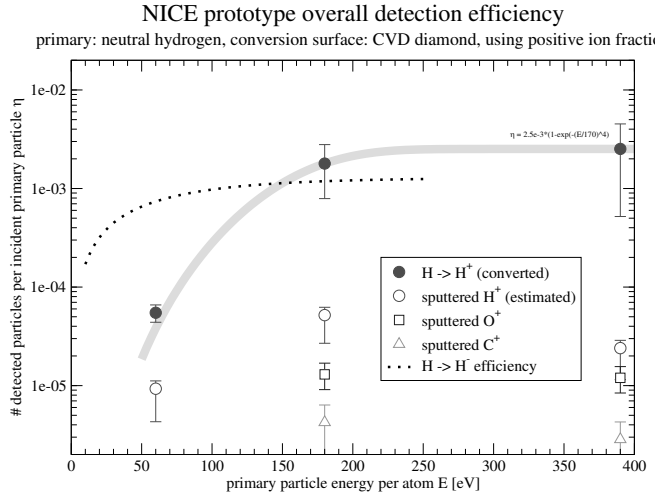

Figure 12. Detection efficiency for primary hydrogen and the CVD diamond conversion surface when using the positive ion fraction. The detection efficiency obtained when using the negative charge state fraction is shown for comparison (dotted line, from Figure 9, middle panel).

Chapter 7

Interstellar Boundary Explorer IBEX

7.1 Introduction

In January 2005, NASA's Office of Space Science selected the Interstellar Boundary Explorer (IBEX) mission [McComas et al. 2004] for development and flight. IBEX will provide the first global views of the Sun's interstellar boundaries by taking angular resolved images of the global energetic neutral atom (ENA) flux in an energy range of 10 eV to 6 keV.

IBEX will answer the following key questions about the global interaction between the solar wind and the interstellar medium:

I: What is the global strength and structure of the termination shock?

II: How are energetic protons accelerated at the termination shock?

III: What are the global properties of the solar wind flow beyond the termination shock and in the heliotail?

IV: How does the interstellar flow interact with the heliosphere beyond the heliopause?

To answer these questions, IBEX carries two ultra-high sensitivity ENA single pixel cameras on a spinning spacecraft. Scheduled for June 2008, IBEX will be launched into a highly elliptical Earth orbit to get a view of the outer heliosphere beyond the Earth's relatively bright magnetospheric ENA emissions (Figure 7.1). The spin axis of the spacecraft will remain Sun pointed throughout the year, enabling both sensors to produce a nearly full sky map of the ENA flux every six months. Depending on the strength of the termination shock (TS), the resulting map will look different. Figure 7.2 depicts the expected hydrogen ENA flux for a strong and a weak TS as obtained from simulations. Large differences between the two cases can be seen.

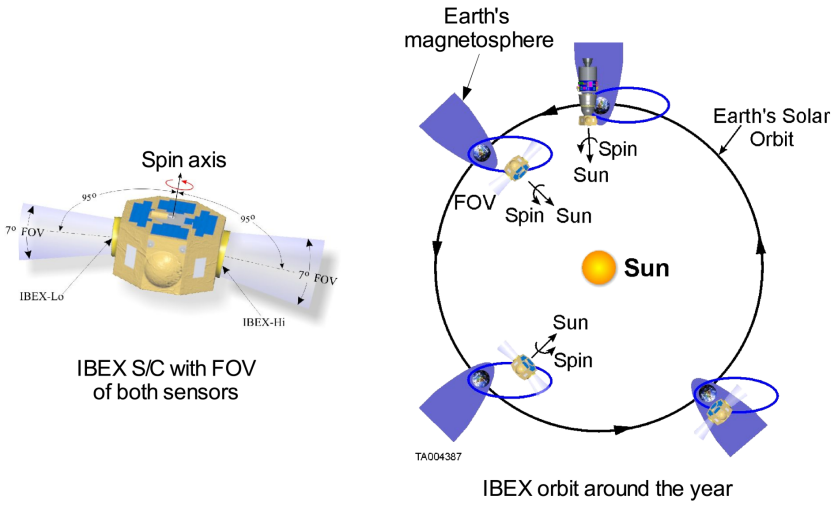

Figure 7.1: IBEX spacecraft and its orbit throughout the year, *Image: IBEX proposal [McComas et al. 2003]*

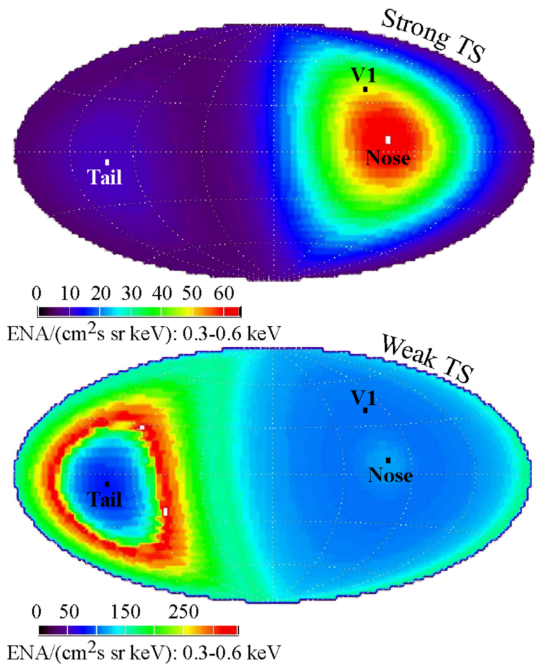

Figure 7.2: Simulated ENA flux for 0.3–0.6 keV hydrogen as seen by IBEX shown in solar ecliptic coordinates with the center of the figure at 0° latitude and 180° longitude. Results predicted for a strong gas-dynamical termination shock (TS) are shown in the top panel and for a weak TS due to a large pickup ion pressure in the bottom panel. Nose depicts the upstream and tail the downstream direction of the inflow of interstellar material. The position of the Voyager 1 spacecraft is indicated by V1. *Image from [McComas et al. 2004]*

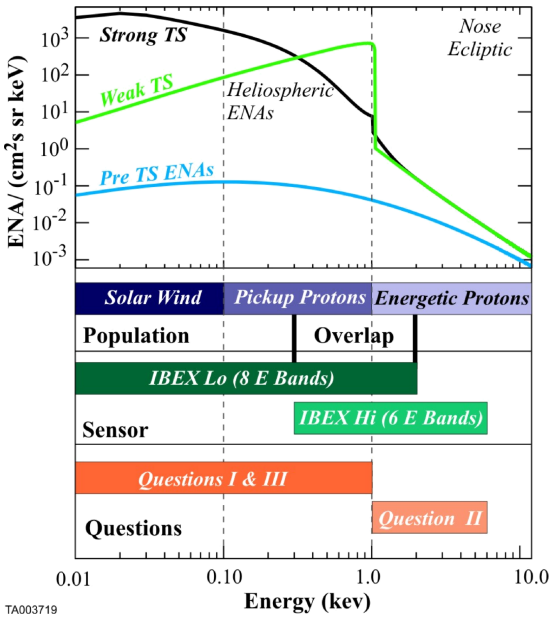

Figure 7.3: Upper panel: Predicted hydrogen ENA flux near heliospheric nose direction for a strong (black) and weak (green) termination shock (TS) [Gruntman et al. 2001]. Based on model assumptions, large variations in ENA flux are possible. Lower panel: Overlapping energy ranges for neutral hydrogen for both IBEX sensors related to the science questions. *Image from [McComas et al. 2004]*

The two sensors cover a different energy range with an overlap: IBEX-Lo is sensitive for 10 eV to 2000 eV neutral hydrogen and neutral oxygen atoms, whereas IBEX-Hi covers the range from 300 eV to 6 keV for neutral hydrogen only. Figure 7.3 depicts the energy ranges of both sensors and how they relate to the science questions from above. The capability to detect neutral oxygen is a feature of IBEX-Lo only and will be used to answer science question number IV as shown in Figure 7.4.

Both sensors are built out of similar functional modules: A collimator for setting the field of view (FOV) and rejection of charged particles at the sensor entrance, followed by a conversion unit that transforms the incident ENAs to ions, a polodial shaped electrostatic analyzer (ESA) for energy band selection, and a detector unit. Whereas in IBEX-Hi incident ENAs are positively ionized upon passage of a thin carbon foil, IBEX-Lo uses a charge conversion surface (CS) to convert the incident ENAs to negative ions. The detectors used are also different, IBEX-Hi, sensitive to hydrogen only, uses a coincidence detector, whereas IBEX-Lo features a time-of-flight section to be able to separate hydrogen and oxygen.

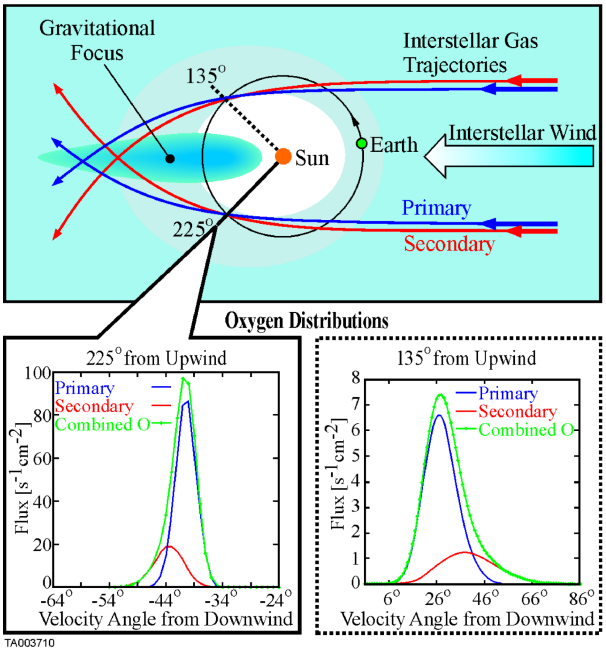

Figure 7.4: Observation of neutral oxygen inflow by IBEX-Lo (science question IV). The secondary population was heated and slowed down in the interaction region whereas the primary component entered the solar system undisturbed. The two components will be separated using the asymmetric distributions shown in the lower two panels. *Image from [McComas et al. 2004]*

7.2 IBEX-Lo Sensor Prototype

7.2.1 Introduction

Crucial for the successful final selection was the construction of sensor prototypes. The IBEX-Lo sensor prototype was designed, built and tested as part of this work at the University of Bern. The ion-optical design was done using the ion-optics optimizing software described in Chapter 4, taking full advantage of the shortened development time this tool offers. A detailed report about data obtained from the different prototype versions is shown in Section 7.2.7.

The main focus in the development of the prototype was set on the conversion surface material [Scheer et al. 2005, Wieser et al. 2002] and on the ion-optical design of the CS and ESA sections. Design drivers were a high overall transmission when using realistic particle scattering properties at the CS combined with an energy resolution sufficient to divide the 10 eV to 2000 eV energy range into eight bins as shown in Table 7.1:

Energy bin #	Range [eV]
1	10–19
2	19–38
3	38–73
4	73–141
5	141–274
6	274–532
7	532–1030
8	1030–2000

Table 7.1: IBEX-Lo energy bins

The sensor concept at this early stage is shown in Figure 7.5. The sensor has a cylindrical symmetry. ENAs enter the sensor from the right through a collimator who sets the field of view and also suppresses charged particles. The ENAs then hit the CS where a fraction is negatively ionized. After moderate pre-acceleration (PreAC) and by passing the poloidal ESA [Moestue 1973, Ghielmetti & Shelley 1990] the negative ions are focused towards the center axis of symmetry. At the exit of the ESA the ions are post-accelerated to 20 keV prior entering the TOF section where they are detected. The post-acceleration helps to reduce the angular spread of the ion trajectories at the exit of the ESA. Without, the spread would be increased compared to the spread at the entry of the ESA because the area of the exit aperture is smaller than the area of the entry aperture. As the energy of the particles does not change inside the ESA, increased spread would be inevitable due to phase space conservation (Liouville). post-acceleration is also needed for the detection of oxygen as the TOF uses carbon-foils to generate the start pulse for the TOF measurement and only particles above 1 keV/nucleon pass these foils easily.

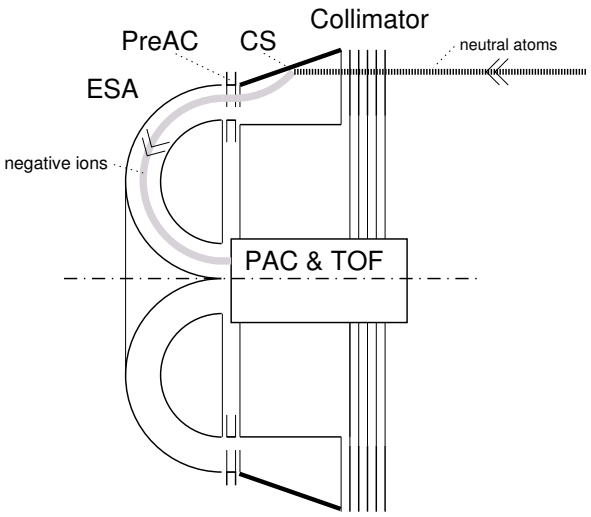

Figure 7.5: IBEX-Lo sensor prototype concept

The total exposed CS area of the sensor was fixed to 125 cm^2 corresponding to an outer diameter of the CS cone of 133 mm with the CS tilted 15° with respect to the incoming neutral particles. These values were kept for the prototype and for the flight design developed afterwards although the orientation of the exposed surface of the CS changed from pointing inwards as used in the prototype to pointing outwards in the flight design (see Section 7.3).

7.2.2 Baseline Version

The baseline version of the prototype was built from a design snapshot taken after three weeks of calculations with ion-optical optimizer. The transmission at the center of an energy bin of the design could be increased from the initial 10% to about more than 50% while keeping the energy resolution $\frac{E}{\Delta E} > 2$. This was possible by introducing a pre-accelerator stage between the CS and ESA sections, by placing suitable field shaping electrodes opposite of the CS, and by carefully reshaping the ESA electrodes.

The hardware prototype consisted of the CS section, the polodial ESA, and, as substitute for the TOF section, an imaging MCP detector (Quantar Technology Inc, CA, USA, model 3395A-SE/2401B). In the CS section only a quarter of the whole circumference was equipped with conversion surface tiles to reduce complexity and cost. The collimator was omitted in first place and developed separately at the University of New Hampshire. A neutral atom beam was produced using the ion beam neutralizer described in Chapter 3.

The first measurements done with the prototype were the mapping of the ion-optical properties of the CS extraction electrodes and the ESA section using an ion beam. For this purpose, the CS was replaced by a pinhole through which pencil like positive ion beam was injected in to the prototype. By varying the angle of this pencil beam to the CS normal vector a detailed angular

dependent transmission function of the ion-optical system could be recorded. Measurements with neutral particles were also done using a magnesium oxide [Wieser et al. 2002] CS but due to the limited beam intensity of the ion source in the CASYMS facility only a few data sets could be obtained. Nevertheless this data was used for the initial proposal of IBEX submitted to NASA [McComas et al. 2003].

Several modifications were added to the prototype at a later stage, each described in the sections below. Figure 7.6 shows a assembly drawing of the prototype including all added features. Data about the performance of each of these modifications is shown in the report reprinted in Section 7.2.7.

7.2.3 Fins

After NASA's selection of IBEX to Phase A of the selection process, the prototype was modified to address open questions. To reduce particle scattering at electrodes, the outer ESA electrode was replaced by a fin-like structure as shown in Figure 7.6. The fins, 0.3 mm thick and made of copper, were built using electro-forming. All other ESA electrodes were copper plated and finally blackened together with the fins using Schering Rapid [Collini Flühmann n.d.], which creates a foam-like UV and particle absorbing copper sulfide top layer. Figure 7.7 depicts a electron microscope picture of such a blackened surface, the ragged absorbing surface is clearly visible.

The mounting of the individual fins onto the outer ESA support plate was a rather involved process, as the blackened surface must not be touched in order not to damage the copper sulfide coating. The fins were mounted using a special mounting tool that allowed to lift the individual rings onto the support structure without touching the surfaces. Figure 7.8 shows the mounting sequence of the fins. The fins reduced the amount of scattered particles by at least two orders of magnitude as shown in the report reprinted in Chapter 7.2.7.

7.2.4 Conversion Surface Unit

To be able to heat the conversion surface, a new CS support unit with less thermal inertia was built (Figure 7.9). The new CS unit was equipped with newly acquired diamond-like carbon (ta-C DLC) conversion surfaces [Scheer et al. 2005]. This CS material was later selected for the flight-CS because of its excellent scattering and ionization properties and its excellent chemical and mechanical stability. All measurements using neutral particles shown in the report in Chapter 7.2.7 were done using ta-C DLC surfaces. The new ta-C DLC tiles were glued using conductive silver epoxy glue onto tantalum strips, which were mounted individually onto the aluminum support structure. A heater was attached on the backside of the tantalum strip mounted in the center. The CS could be heated up to 100°C this way.

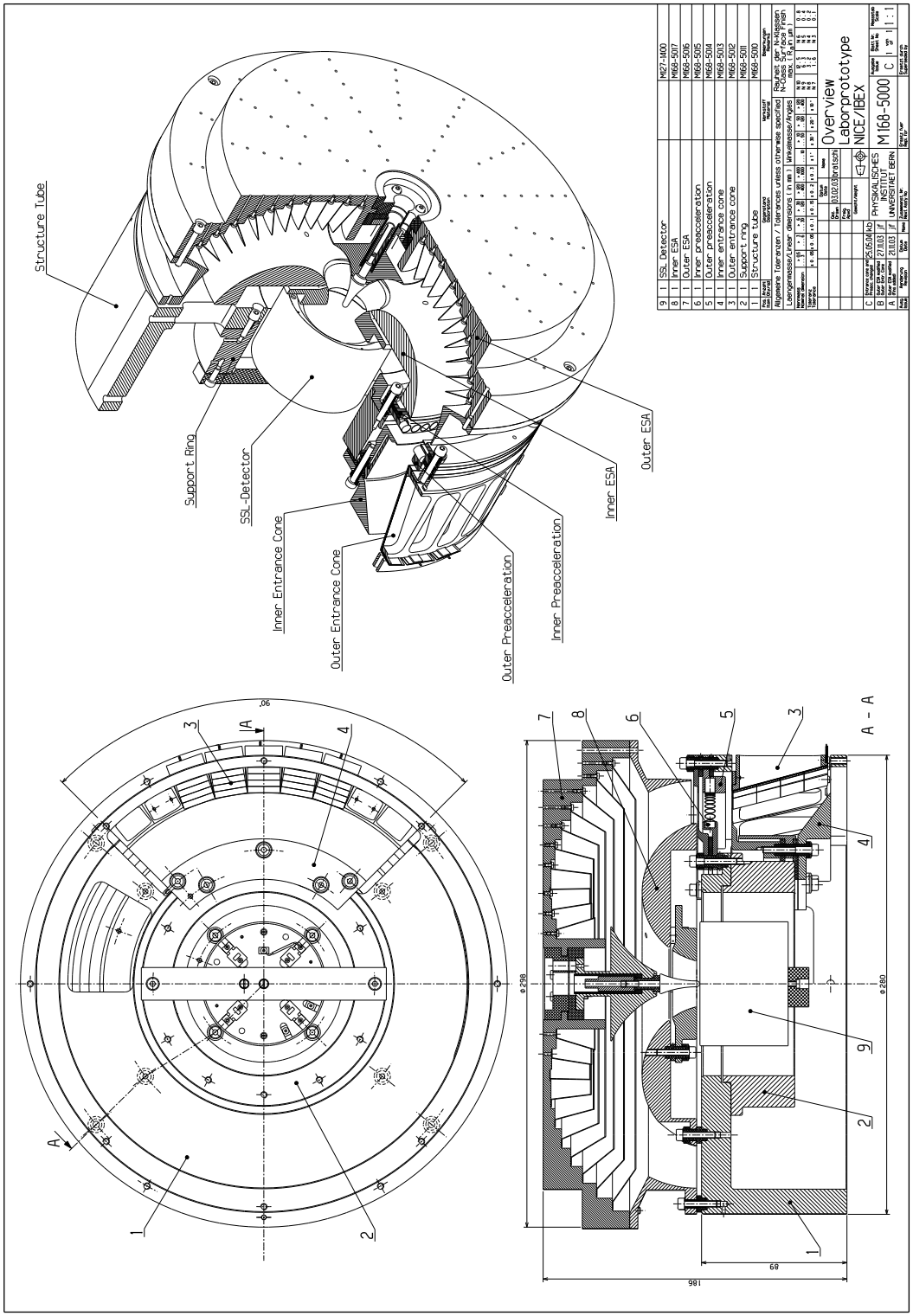

Figure 7.6: Drawing of IBEX-Lo prototype version including blackened fins and magnets.

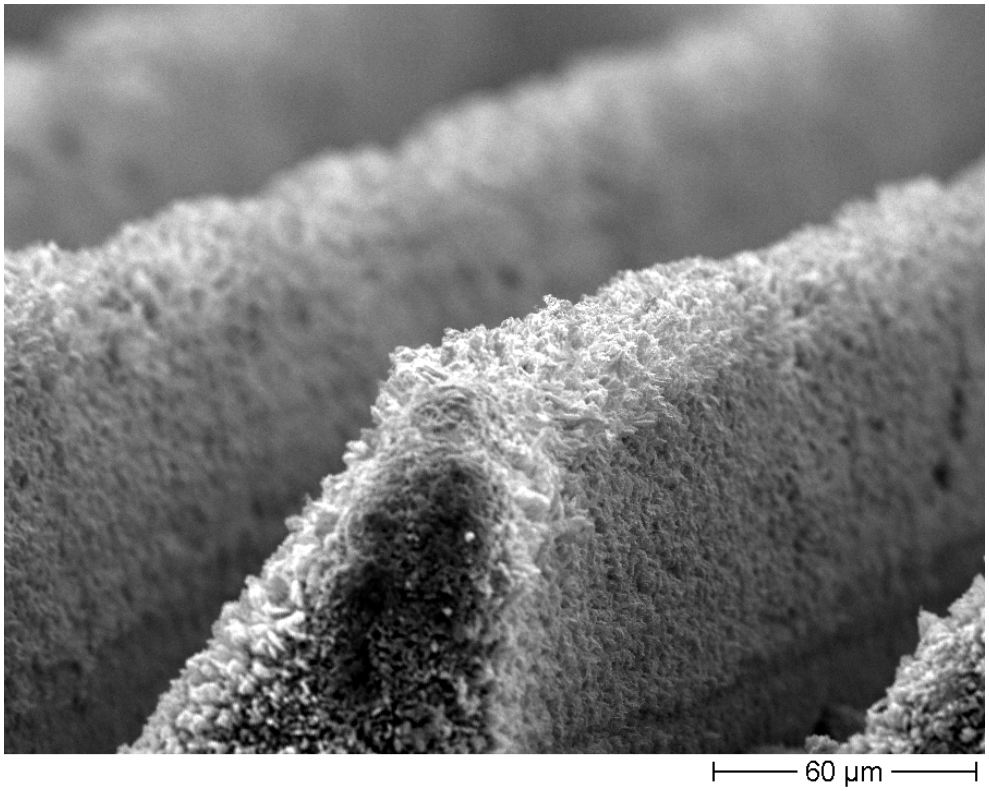

Figure 7.7: Electron microscope image of copper sulfide blackened saw-teeth structure, *Image by E. Krähenbühl, Institute of Applied Physics, University of Bern*

7.2.5 Electron Suppression Magnets

As major third modification, electron suppression magnets were added between the CS and the ESA. As negative ions are extracted from the CS, secondary electrons created at the CS and the surrounding electrodes need to be suppressed. Permanent magnet rods made of standard AlNiCo magnet material were embedded in the field shaping electrodes between the CS and the ESA. Figure 7.10 shows the outer accelerator electrode between CS and ESA equipped with these magnets.

Figure 7.11 depicts how the magnets were placed in the prototype producing a magnetic field of 60–300 G in the gap, large enough to deflect electrons away from the direction where they could reach the exit of the ESA.

Figure 7.12 shows the prototype with all modifications installed in the MEFISTO calibration chamber. Measurements with neutral hydrogen and neutral oxygen atoms were done with this setup.

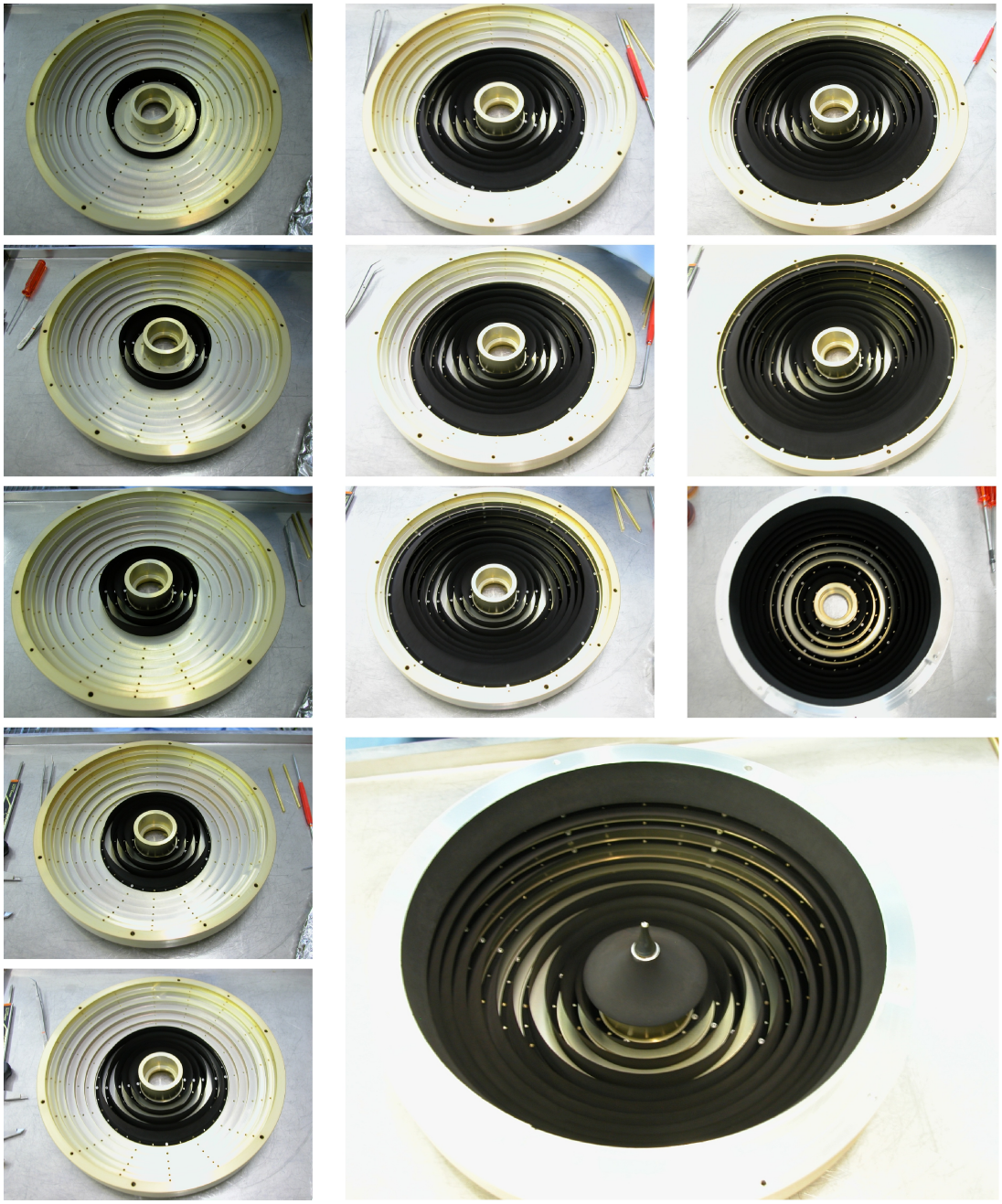

Figure 7.8: Mounting of the blackened fins onto the outer ESA support structure. The sequence starts on the top in the leftmost row and finishes in the third image on the rightmost row. The big inset shows the fully mounted outer ESA structure including the center field shaping electrode. Note the overexposure of the outer surface of the structure due to the long exposure time needed to resolve the blackened surfaces inside.

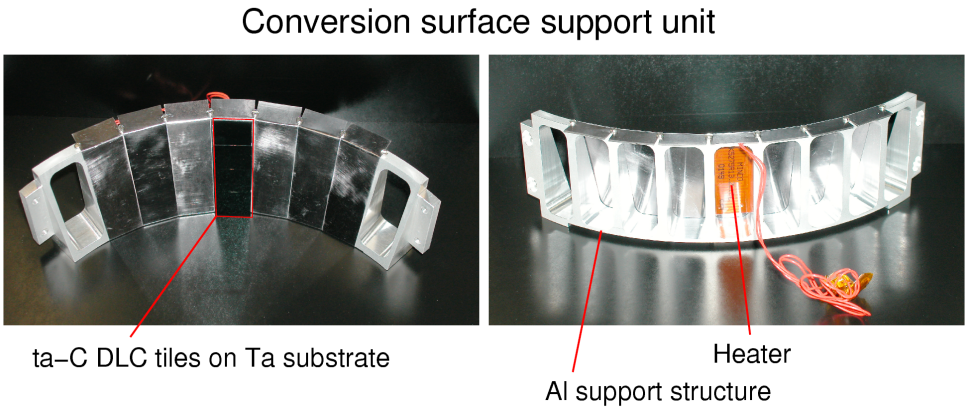

Figure 7.9: Conversion surface support structure. The unit covers one quarter of the circumference of the prototype. The left panel shows four ta-C CS tiles mounted on the center tantalum strip. The four tiles outlined by the red box are 20 mm×15 mm in size each. For measurements, only this center strip was illuminated by the neutral beam. The right panel shows the CS-heater glued onto the backside of the center tantalum strip.

Figure 7.10: Outer pre-accelerator electrode with embedded permanent magnets for secondary electron suppression. The individual embedded magnet rods are 6 mm in diameter.

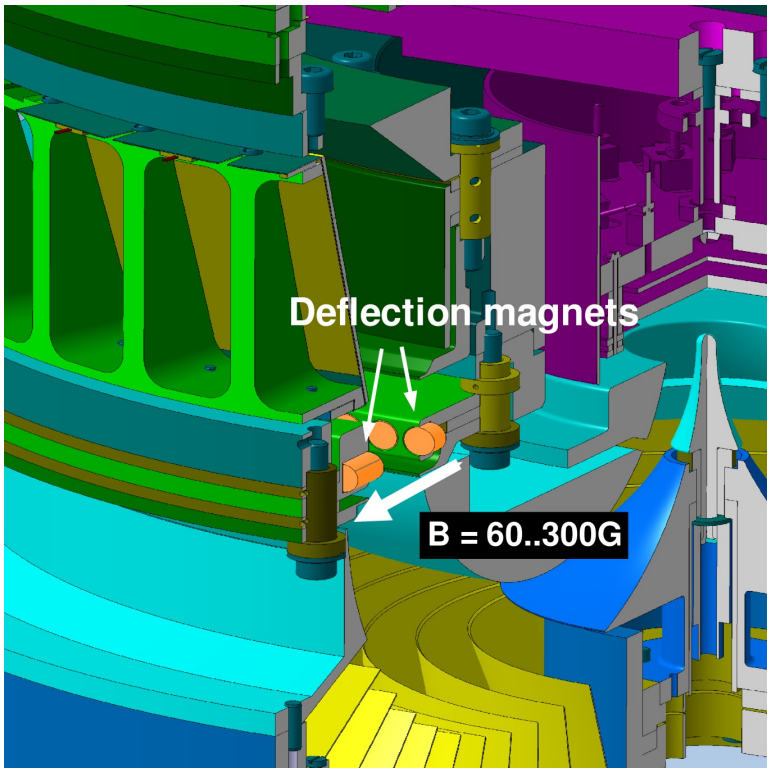

Figure 7.11: Placement of the secondary electron deflection magnets (orange). A cut through the CS section (green) is shown. The fins of the outer ESA plate are shown in yellow and the imaging MCP detector in dark purple. The magnetic field in the gap varies from 60 G between the electrodes and 300 G directly at the magnet poles.

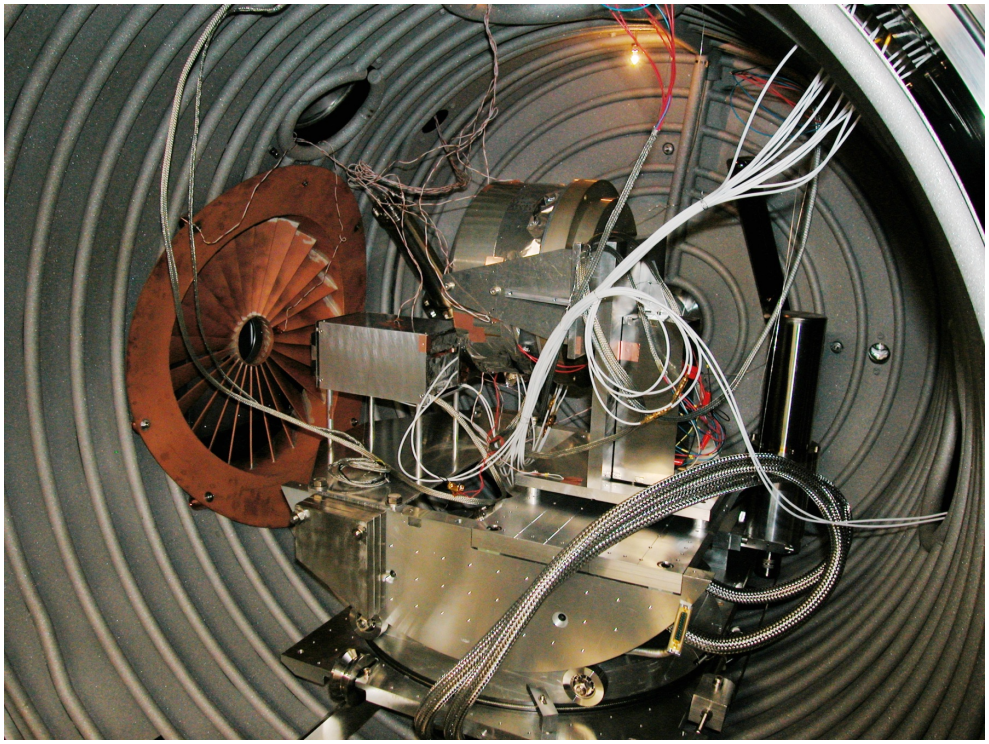

Figure 7.12: IBEX-Lo prototype in MEFISTO calibration facility. The ion beam enters the chamber from the left through the fan-shaped opening and is neutralized using the ion beam neutralizer described in Chapter 3. This neutral beam then hits the CS of the prototype in the center. The pipes along the chamber wall belong to the cryogenic shroud of the chamber. During operation the shroud is filled with LN2 and and acts as very efficient pump after cooling down to -196°C. The prototype was placed on a heater plate to prevent temperatures below -10°C at the imaging MCP detector installed at the place of the time-of-flight section. Measurements with neutral hydrogen and neutral oxygen were done with this setup.

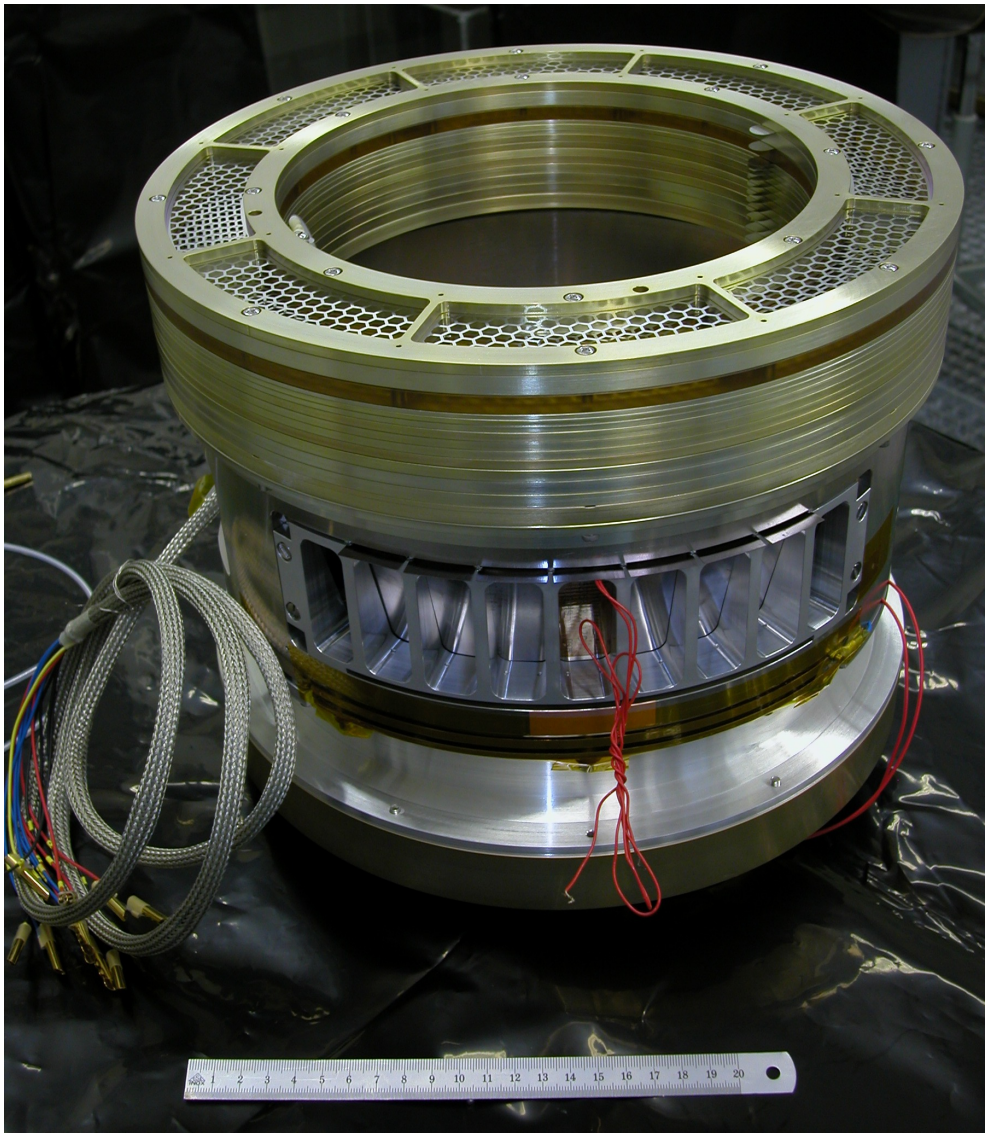

Figure 7.13: IBEX-Lo prototype with collimator. The units visible are the collimator on the top, the main structure tube with the CS support unit with the red power wires for the heater in the middle, and the ESA section on the bottom. The cable on the left supplies high voltages to the electrodes and the detector inside.

7.2.6 Mating with the Collimator

Finally the prototype was mated with the collimator build at the University of New Hampshire. Figure 7.13 depicts a view onto the prototype including the collimator. The collimator was tested independent of the rest of the prototype [Möbius et al. 2004], however, it was built to fit onto the main structure tube of the prototype nevertheless to enable possible future combined measurements.

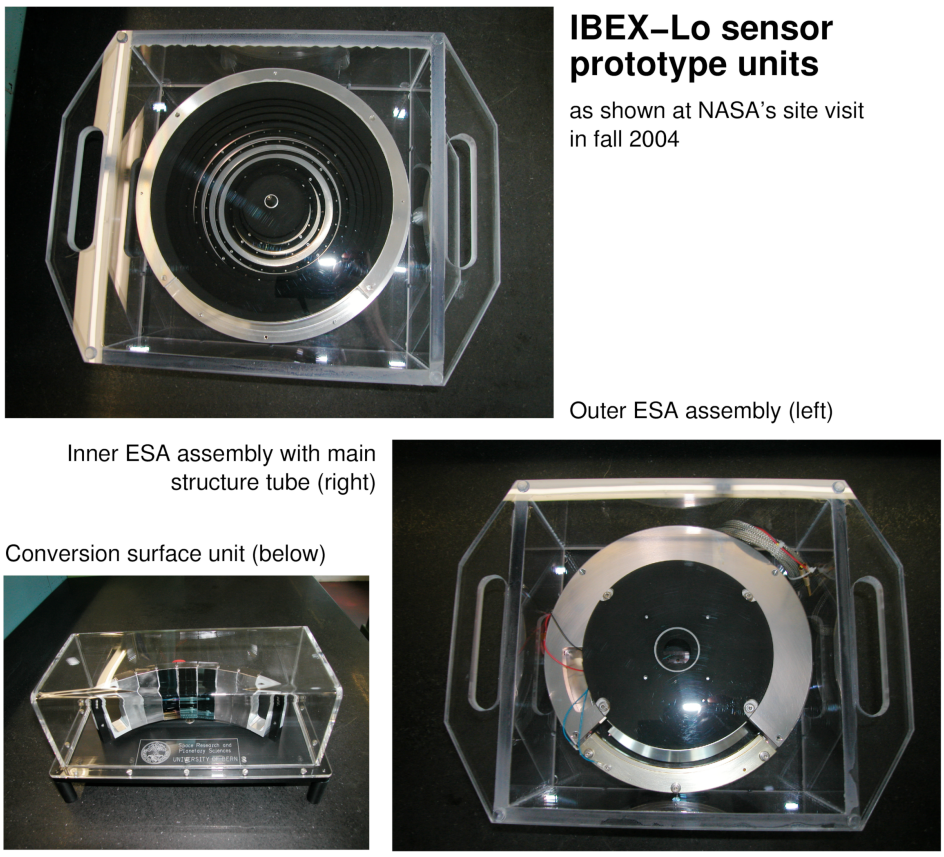

Figure 7.14: IBEX-Lo sensor prototype as shown at NASA's site visit

7.2.7 Report: IBEX-Lo Prototype

The following report summarizes the tests and measurements done with the IBEX-Lo sensor prototype and was issued originally for the Phase A proposal submitted to NASA's Office of Space Science in April 2004. The version printed here is an updated version including more results and was issued for NASA's site visit at Orbital Science Corporation in September 2004. For the site visit the prototype was fitted into sturdy polycarbonate boxes and presented on-site as exhibit as shown in Figure 7.14.

IBEX-LO Prototype Testing in Bern

Status Report

Date: 20. August 2004

Authors:
- Martin Wieser, University of Bern
- Peter Wurz, University of Bern
- Eric Hertzberg, Lockheed Martin

Table of Contents

Revisions:
14. April 2004, Initial Version, M. Wieser
21. April 2004, Linguistic Update, E. Hertzberg / M. Wieser
6. Mai 2004, Effects of fins and blackened surfaces, M. Wieser
20. August 2004, Oxygen data and Magnets, M. Wieser / P. Wurz

1 Introduction

Two different test arrangements were used to characterize the prototype:

1) Ion optical tests of the angular acceptance of the ESA and CS extraction optics using positive ions.

2) Measurement of End-to-End prototype performance using neutral primary particles.

2 Ion Tests

2.1 Setup

The setup for ion measurements used in the CASYMS facility is shown in Figure 2.1.

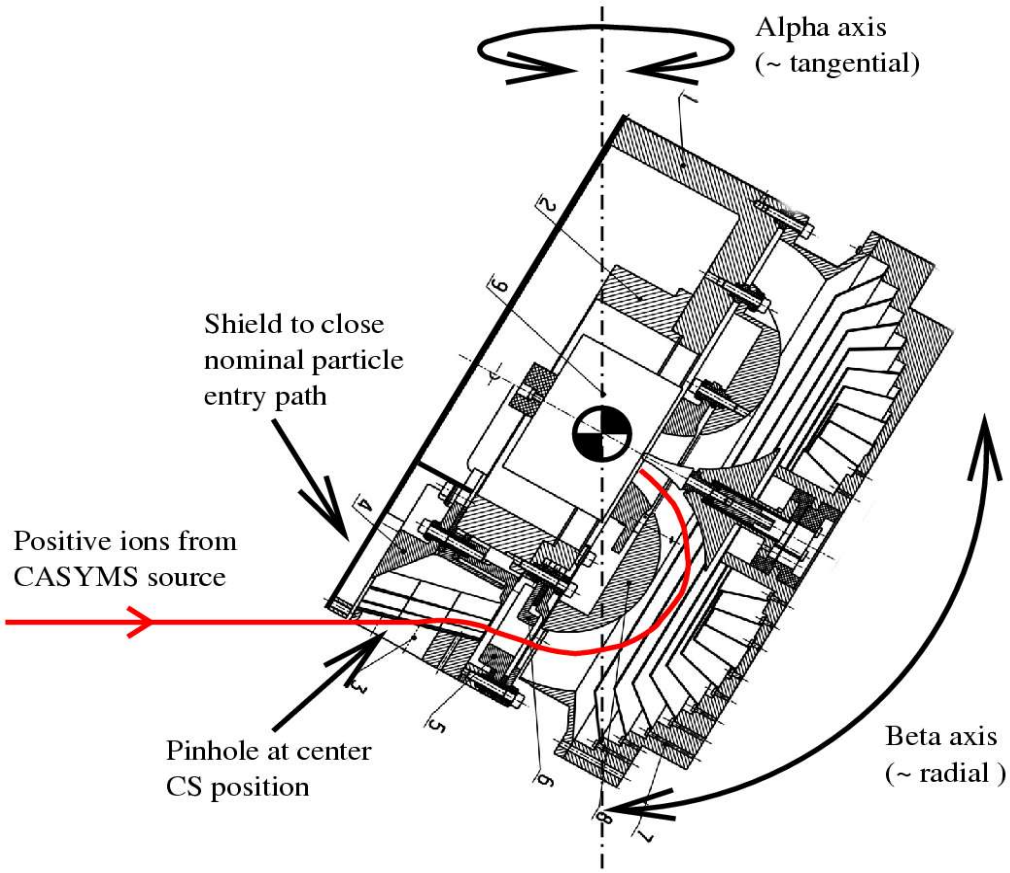

Figure 2.1

A positive mono energetic ion beam (He+) in the energy range of 25eV to

2.5keV is directed from various angles through a pinhole centered on the CS to simulate various scattering angles at the CS.

A position sensitive Quantar SSL detector was used instead of the TOF unit. Due to limits in the maximum allowed detector float voltage, the detector was mounted closer to the exit of the ESA than the nominal TOF entry position. This allows for improved collection of ions exiting the ESA for incident energies at the CS up to 255 eV.

To accommodate positive instead of negative ions starting at the CS, all electrode potentials were reversed in polarity in the prototype.

The angle of acceptance of the ion optical system was verified for different primary energies. Two angles could be varied: tangential and radial.

Two different scan modes were used:

1) Primary beam at nominal energy (ESA center energy), 13 * 13 angular positions
2) Primary beam energy varied in 25 steps (log spaced) from 25 to 2500 eV with 5*5 angular positions at each energy step.

For all these tests the prototype ESA center energy was set for 255eV ion energy which corresponds to an incident neutral atom energy of 300 eV, falling about midway between energy bin #5 and #6.

2.2 Results

2.2.1 Scattering

Figure 2.2 shows the estimated amount of scattered and directly transmitted particles vs. reflection angle, when starting with a pencil beam at a position centered on the CS. During the measurements angles of incidence[1] through the CS were varied radially and tangentially,to the CS were varied and for each set of angles a 2D image at the exit of the ESA was taken. Figure 2.2 is a composite of this entire set of runs. Note that a test beam corresponding to a perfectly spectral reflection of an incident neutral beam parallel to the prototype symmetry axis would appear at radial angle = 15° and tangential angle = 0°.

The prototype was not equipped with blackened surfaces or fins for these first measurements. This plot was developed from the raw data shown in Figure 2.3.

[1] 'Tangential angle' corresponds to 'Azimuthal angle' and 'Radial angle' to (90° - 'polar angle') in the ILENA scattering images. Radial/Tangential = 0/0 points parallel to the CS towards the ESA, -15/0 would be parallel to the symmetry axis of the instrument, and 75/0 point to the center of the instrument.

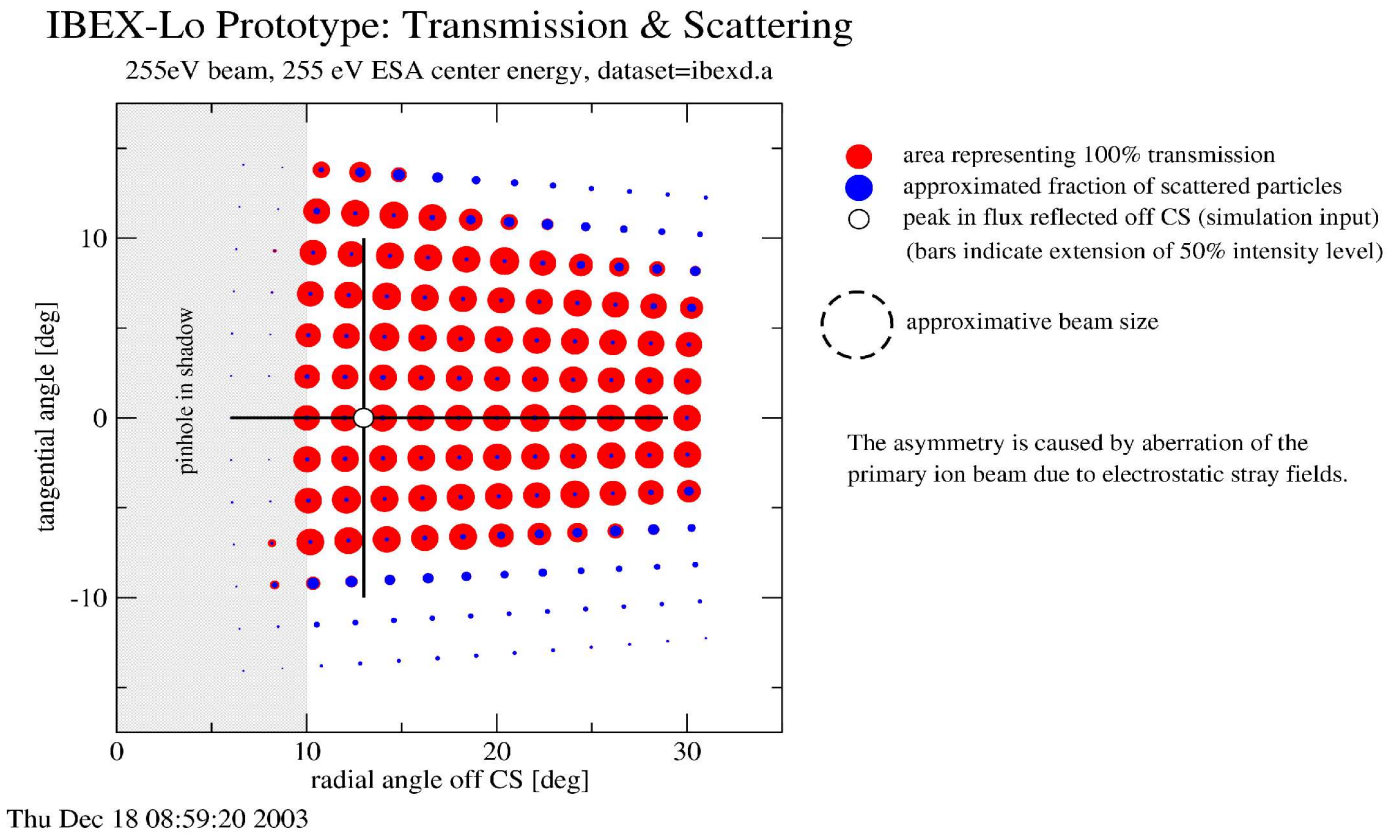

Figure 2.2

Clearly scattered particles appear at the edge of the transmission phase space (blue dots in Figure 2.2).
Figure 2.3 shows the raw images arranged in the same way as the data in Figure 2.2. Scattered particles were estimated by integrating all counts outside the image of the pencil beam starting from the CS. The area covered by the direct image of the pencil beam is shown in light blue, whereas scattered particles appear as dark red 'background'.
The numbers below each individual image give an estimate of total transmitted and scattered particles in percent normalized to the maximum center beam flux (due to some uncertainty in the primary flux determination the total flux number can exceed 100%).

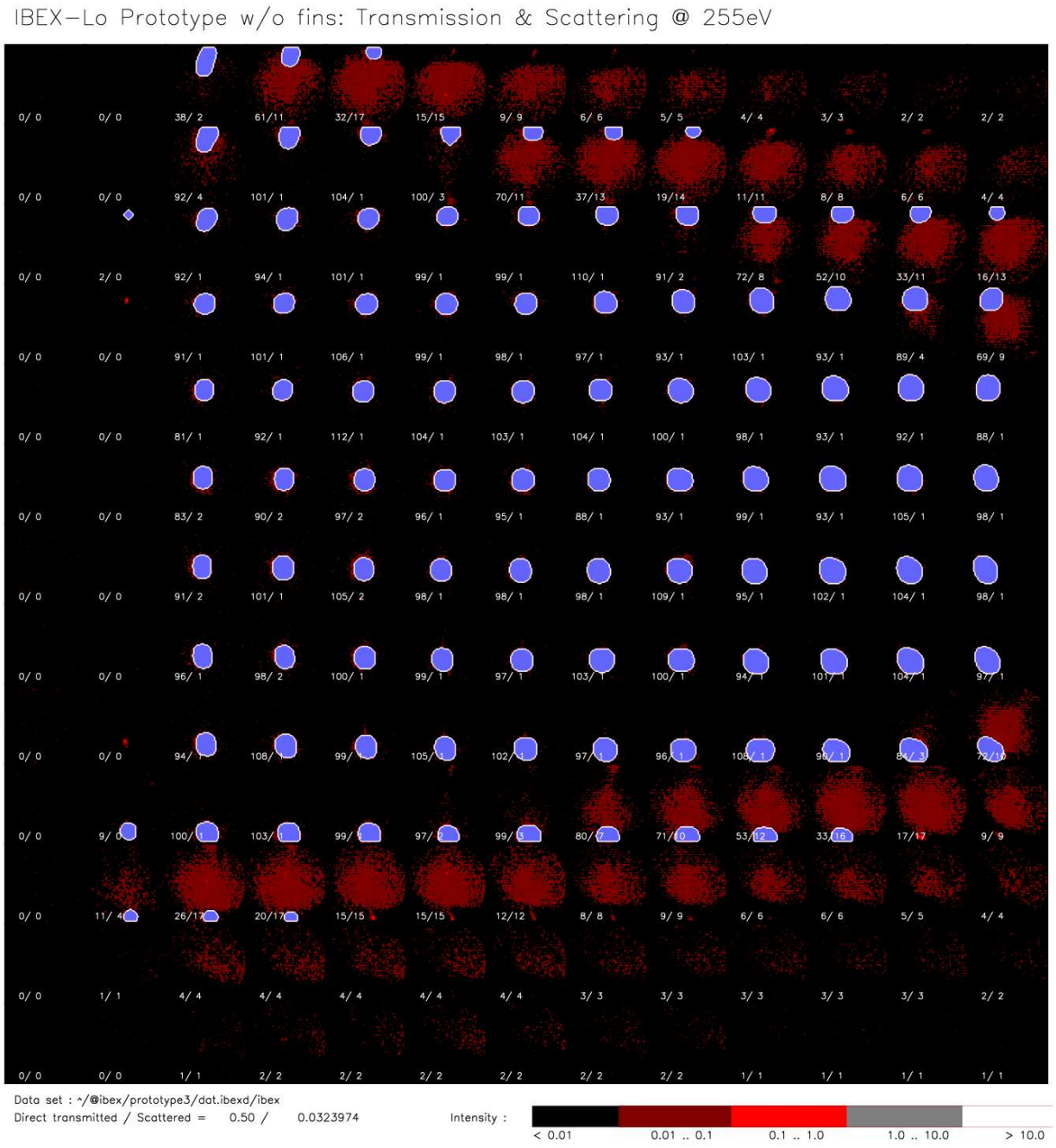
IBEX–Lo Prototype w/o fins: Transmission & Scattering @ 255eV
Data set : ~/@ibex/prototype3/dat.ibexd/ibex
Direct transmitted / Scattered = 0.50 / 0.0323974
Intensity :
< 0.01
0.01 .. 0.1
0.1 .. 1.0
1.0 .. 10.0
> 10.0

Figure 2.3

Figure 2.4 shows beam transmission as a function of angle after installing fins and blackening surfaces, but otherwise maintaining the same conditions as in Figure 2.3.

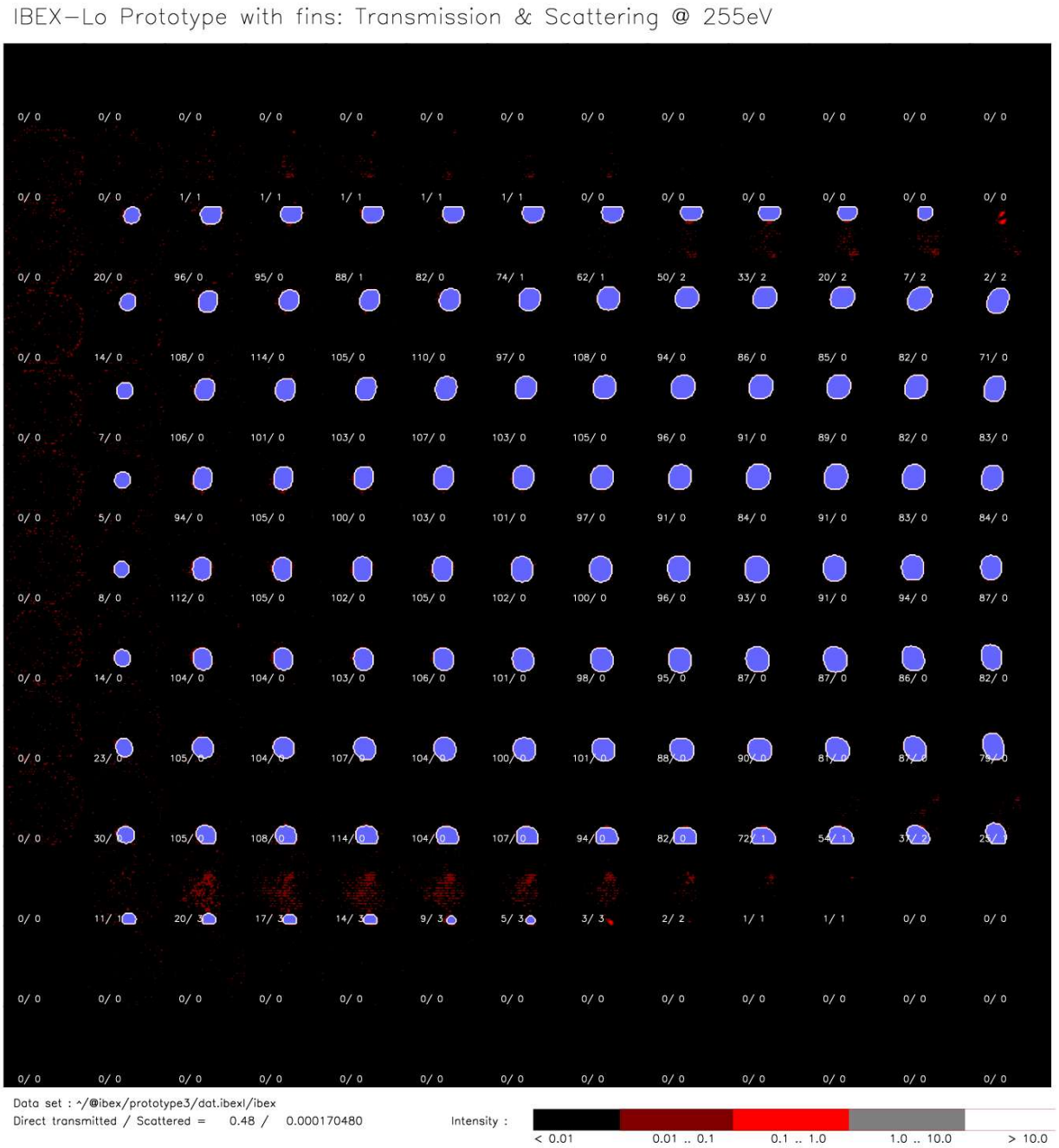

Figure 2.4

A substantial reduction in the number of scattered particles becomes evident by comparing Figures 2.3 and 2.4: while the directly transmitted fraction (shown as light blue area) does not vary significantly, the scattered fraction (shown in dark red) is reduced by a factor of **190** (see Table 2.1)[2] :

	Fraction of directly transmitted particles	***Fraction of scattered particles***
no blackening, no fins	0.50	0.0324
blackened surfaces, with fins	0.48	<1.70E-4

Table 2.1

2.2.2 Angular Acceptance

Figure 2.5 shows the simulated energy dependent angular range of acceptance of the ESA optics for particles starting at the center of the CS. A SIMION Monte Carlo simulation using about 100'000 particles was run to obtain these results.
The center energy of the ESA is set to 100eV (for transiting negative ions) in this simulation. As expected, the largest area (shown in red) corresponds to the energy closest to the center energy of the ESA.

Due to excessive file size, the corresponding measurements are shown in a separate file: `mapkcap.pdf`.

5 x 5 images were taken for different radial and tangential angles as indicated below each individual image. For this data set the ESA was set to 100eV (for transiting positive ions), as in the simulations but with charge sign reversed, and the primary beam energy was then varied from 25eV up to 1311eV. Note that the noise visible in the images taken at lower energies and smaller radial angles (the left hand columns on each page) is due to counting statistics and not caused by scattering. The energy dependent acceptance from the simulations is well reproduced by measurements even though only 25 data points are available per primary energy.

[2] The accuracy of the suppression factor of 190 is limited by background counting statistics of the detector. A detailed analysis shows that the suppression is larger than 38 with 99% confidence. No upper limit can be given since the data is also compatible with infinite suppression within the 99% confidence interval.

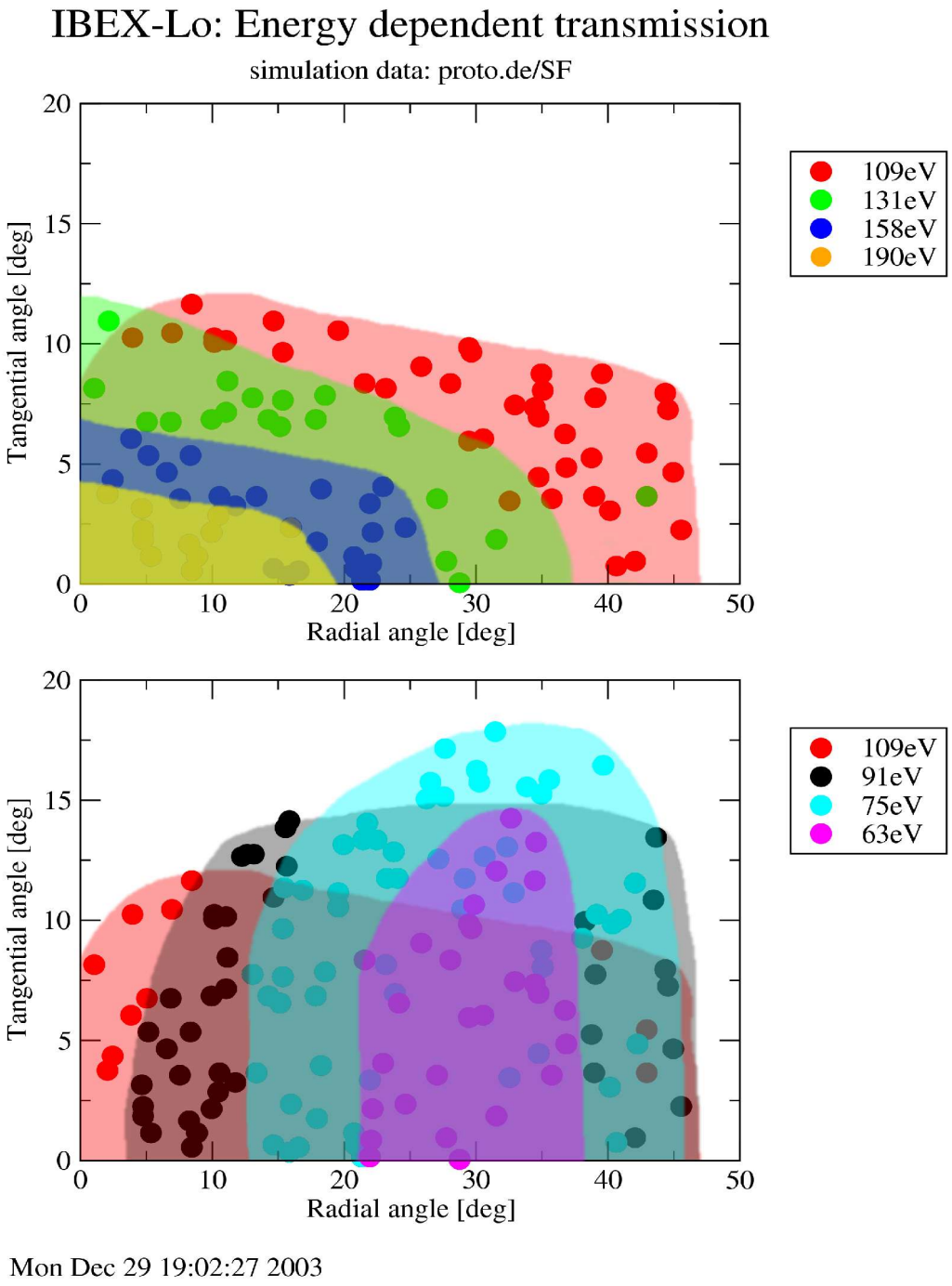
IBEX-Lo: Energy dependent transmission
simulation data: proto.de/SF
Tangential angle [deg]
Radial angle [deg]
109eV
131eV
158eV
190eV
Tangential angle [deg]
Radial angle [deg]
109eV
91eV
75eV
63eV
Mon Dec 29 19:02:27 2003

Figure 2.5

3 Neutral Particle Tests

3.1 Setup

Neutral particle tests were done in the MEFISTO ion beam facility using a beam neutralizer. The setup used is shown in Figure 3.1

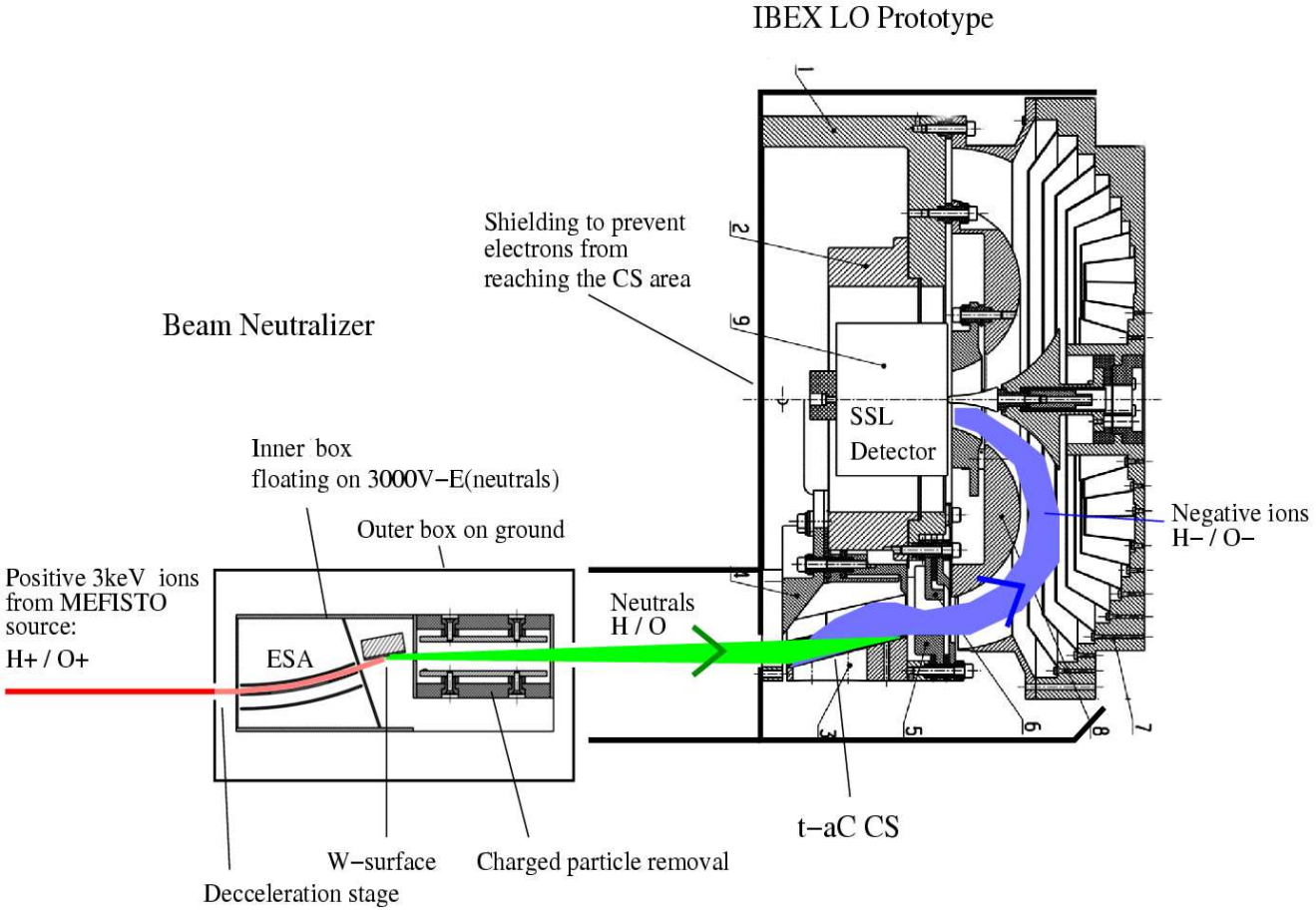

Figure 3.1

For these measurements a neutral beam was produced by reflecting a positive ion beam (H+ or O+) of fixed 3000 eV energy off a highly polished tungsten neutralization surface that can be biased (floated) to any potential up to 3000V.

By changing the neutralizer inner box float voltage, the energy of the produced neutrals can be varied. For incident hydrogen, the resulting neutral beam has a 15% lower mean energy than the incident positive ions and an energy straggling FWHM of 15% of the incident energy (see Chapter 3.3.1 for a discussion on energy loss for oxygen). The energy distribution displays a pronounced tail towards lower energies and a sharp drop towards higher energies. The data shown in Figure 3.2 represent the energy spread obtained

by neutralizing a 1617 eV H+ beam on a MgO surface (data taken at the University of Osnabrück). The distribution obtained when using a W surface as in the neutralizer is very similar. For a model of energy spread valid for oxygen see Chapter

The angular divergence of the exiting neutral beam is approx 10° tangential x 4° radial FWHM after clipping of the profile at the prototype entry aperture. A 95% transmission grid at ground potential was fitted to the entry aperture of the prototype where the neutral beam passes through the shielding plane (see Figure 3.1).

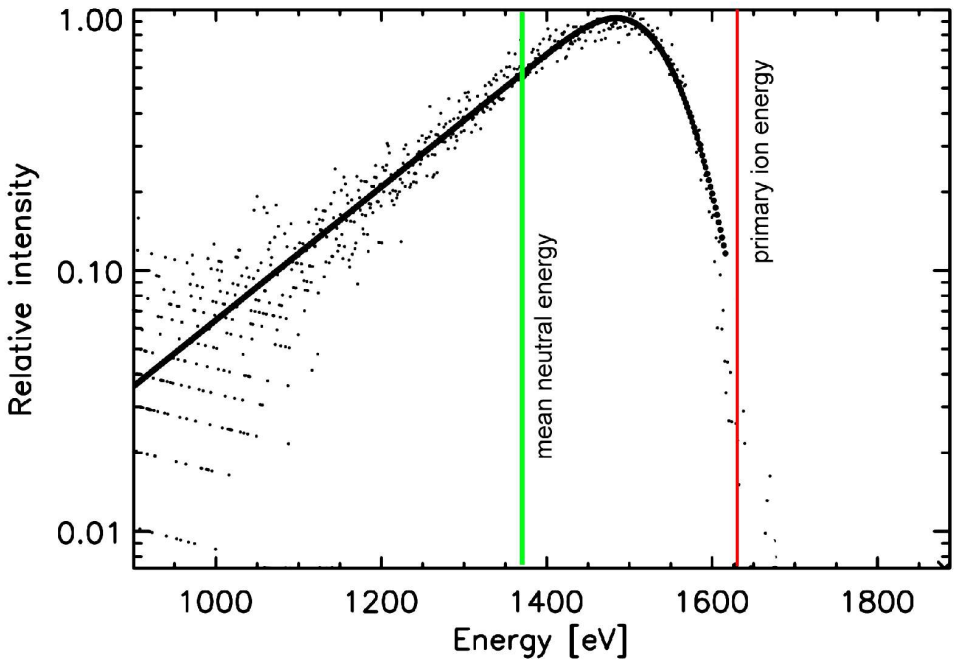

Figure 3.2

No angular motion is available in the present instrument setup in MEFISTO except a small tilting motion of a few degrees to facilitate primary beam pointing.

A Quantar (SSL) detector was used to record the beam emerging from the ESA exit area. The advantage of using this detector is that images of exit beam shapes can be recorded. The disadvantage is that the maximum allowable voltage to which this detector can be floated is 2000V, making energy bins 6 through 8 inaccessible. Originally a CEM detector with a fiber optical signal coupling was intended for these measurements (as already done for the ion beam tests in CASYMS), but difficulties with low temperature sensitivity forced its abandonment for the time being.

Later measurements were done with a heating plate installed below the

prototype to keep its temperature above 0°C in any case. Tough the optically coupled CEM was not used even with the heating plate due to limitations in the available chamber time, the heating plate allowed to use the cryogenic shroud for pumping ensuring a pressure in the low 10^{-8} mbar range

Only ta-C DLC surfaces (samples L06 - L09) have been neutral beam tested in MEFISTO so far. These samples were not hydrogen passivated.

Pressure in the MEFISTO chamber was 2 to $4x10^{-8}$ mbar during the measurements and prototype temperature varied between -20°C and 20°C for the data shown (> 0°C for all measurements with secondary deflection magnets).

3.2 Results for Hydrogen

3.2.1 Efficiency

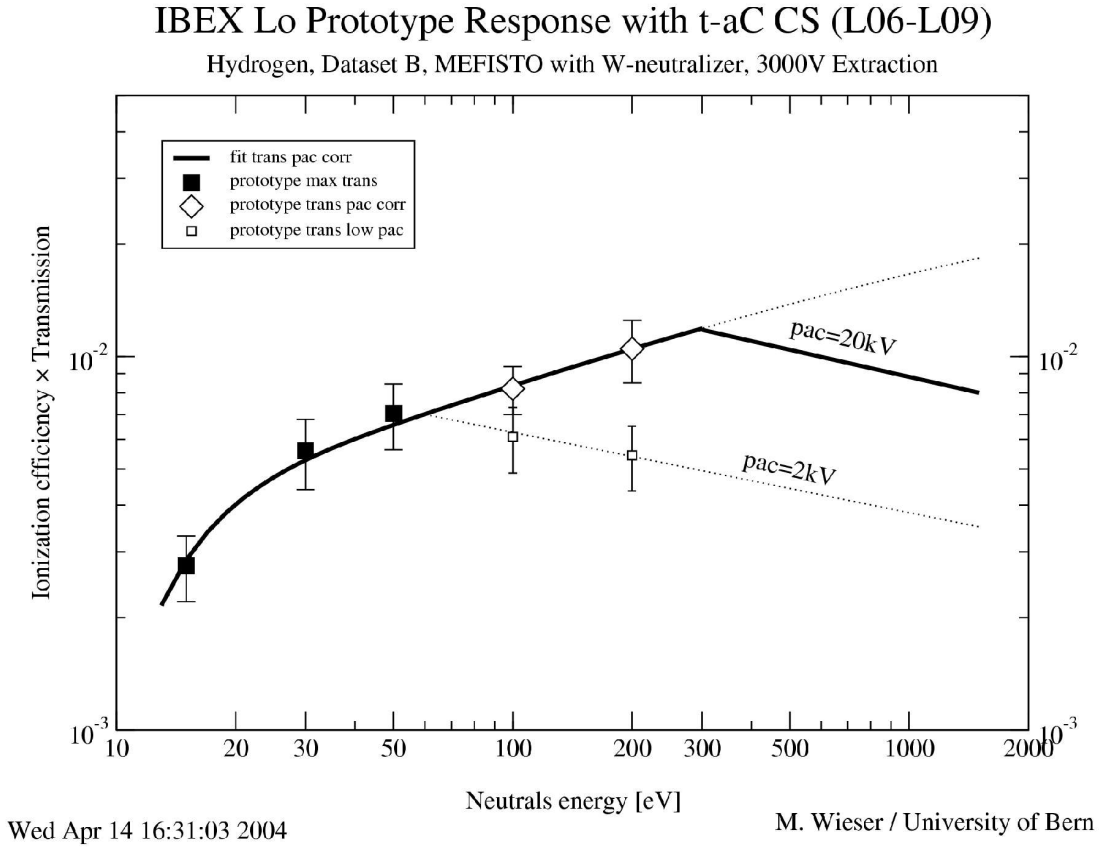

Figure 3.3

Figure 3.3 depicts a compilation of all available datasets for the L06-L09 t-aC CS samples mounted in the prototype. The bold solid line shows performance with a nominal post acceleration voltage of 20kV. The leftmost 3 data points were taken unaltered from the peak values in the transmission curves of bins #1 to #3. The small open squares represent corresponding data points for

bins #4 and #5, however due to the low post acceleration voltage the values are lower than for nominal post acceleration. The large open diamonds are the same data corrected for a nominal post acceleration voltage using ion optical simulations.

The solid line includes an added estimated decrease above 300eV incident neutral particle energy due to increased divergence, hence loss, of ions exiting the ESA. As the post acceleration voltage is a fixed value, it becomes more and more difficult to focus increasingly energetic negative ions onto the detector. For the lower post acceleration voltage used in these measurements, the effect of beam divergence and loss already appears in bins #4 and #5, as noted above. The dotted line at the upper right shows ideal performance with no post acceleration losses.

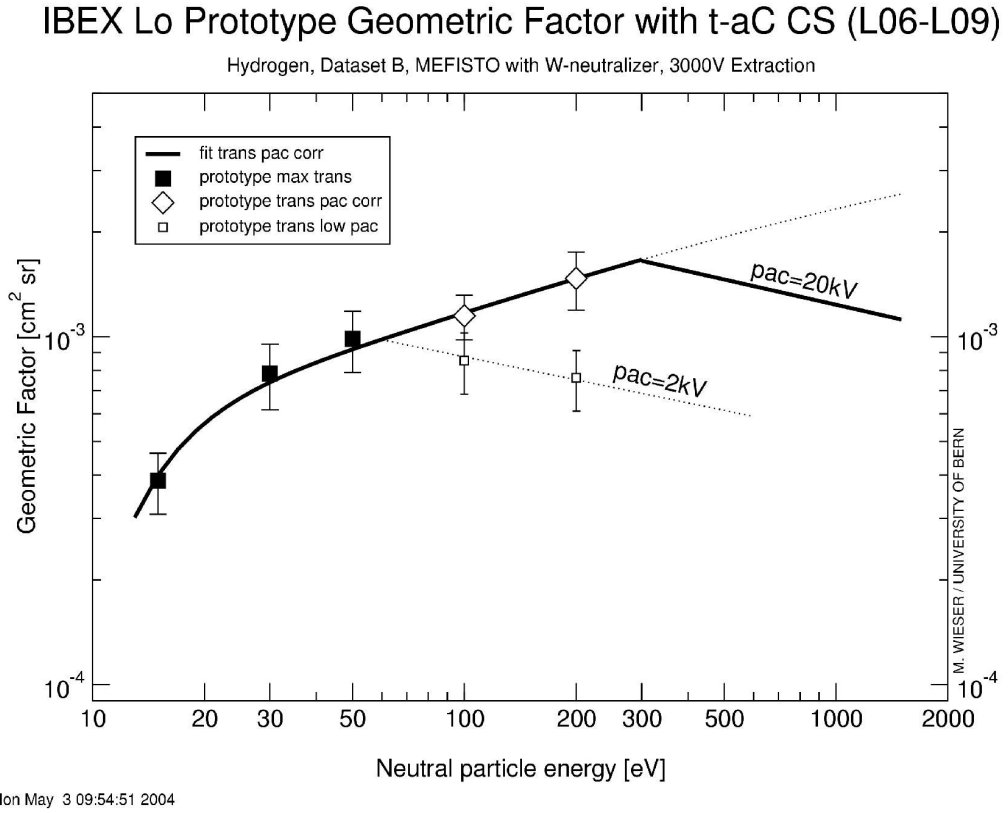

Figure 3.4

The geometric factor curve calculated from the data shown in Figure 3.3 is shown presented in Figure 3.4. A neutral beam having 7° x 7° angular extent, rather than the existing 4° x 10° angular spread, would produce a slightly higher geometric factor curve.

3.2.2 Ionization Efficiency

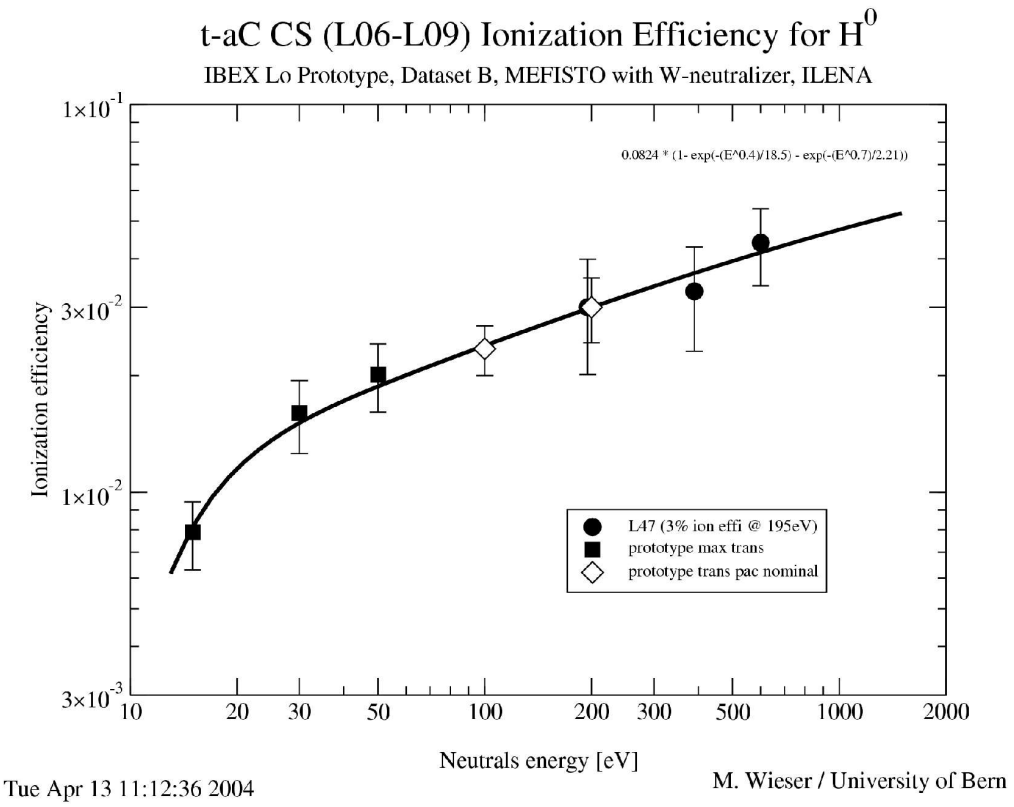

Figure 3.5

Figure 3.5 was derived from the data in Figure 3.3 by removing the energy dependent ESA transmission factor (Figure 3.6), with special attention paid to scattering losses near the CS. Ionization data from the ILENA test setup (University Bern) using sample L47 are added at higher energies. (Sample L47 is the same material as samples L06-L09, and like L06-L09, was not H passivated).

3.2.3 Transmission

An estimate of the energy dependent transmission of the prototype using nominal post acceleration voltages, Figure 3.6, can be made only for energy bins #1 to #5, since no higher energy bins have yet been measured. From geometrical constraints one can assume that the transmission in the lower energy bins is constant but begins to drop as energy exceeds the threshold beyond which post acceleration can no longer capture all negative ions exiting the ESA. The shape of the drop at higher energies was estimated from the drop observed in energy bins #4 and #5 when using the reduced 2kV post acceleration (Figure 3.6). Simulations that ignore post acceleration losses show transmission to be constant in energy from 10 eV to 2000 eV.

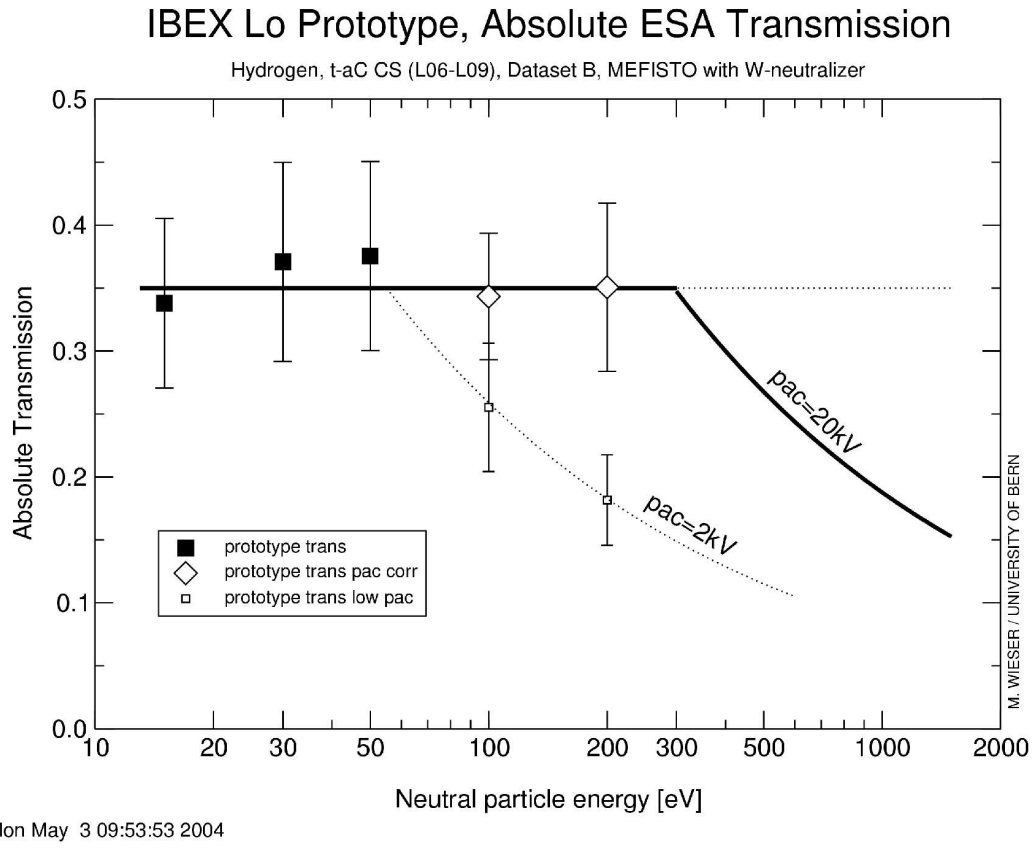

Figure 3.6

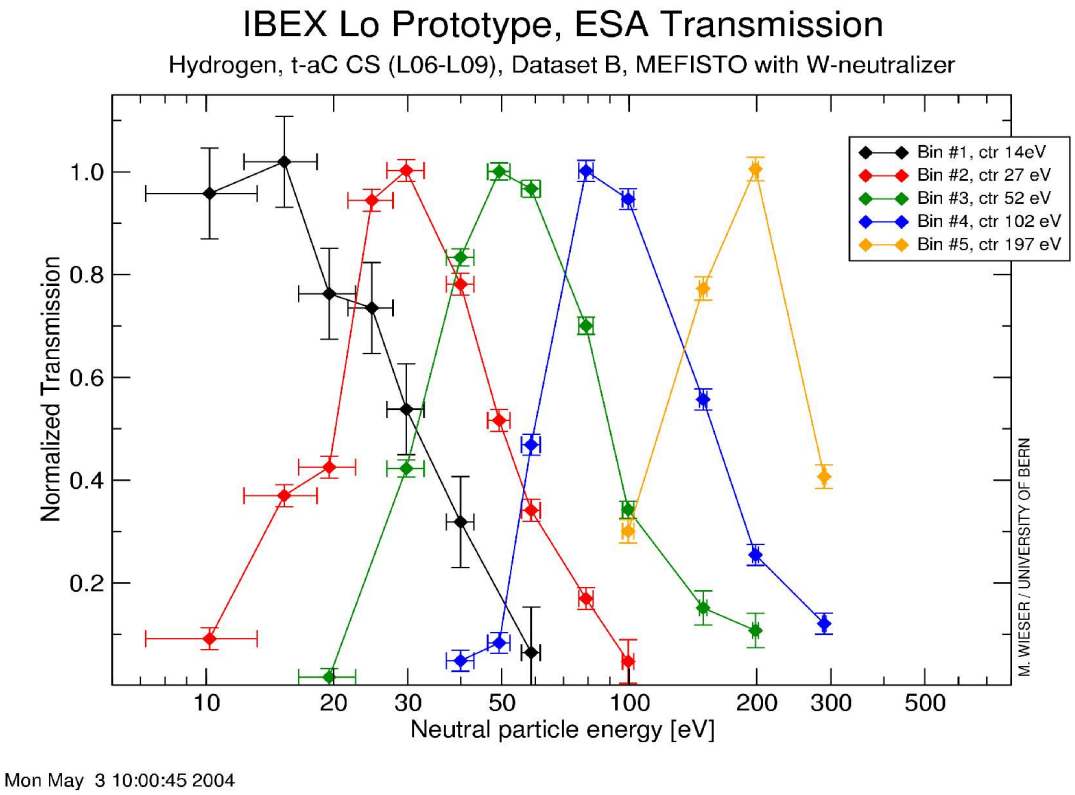

Figure 3.7

3.2.4 Energy Bin Shape

The energy resolution obtained for the 5 lowest energy bins is shown in Figure 3.7. In bins #1 and #2 a secondary electron contribution appearing at higher primary energies (>50eV) was subtracted. Energy bin shapes have not been corrected for the effects of the incident neutral beam energy spread (see Figure 3.2).

The energy width of the neutral hydrogen beam produced by the neutralizer is 15% FWHM of the primary ion energy, E0. The peak shape is approximately a skewed triangle as shown in Figure 3.2. The primary energy distribution is very steep on the high energy side with a pronounced tail towards lower energies.

The measured prototype energy bin shape is a convolution of the 'true' bin shape with the primary energy distribution. The measured bin width is therefore overestimated in Figure 3.7 where each measured bin extends further towards higher energies than the ' true' bin shape would.

The measured transmission peak width is approx 100% of E0, FWHM. By deconvolving the neutral particle energy spread of 15% FWHM, the total width of the transmission curve is approximately 90% of E0, FWHM, with the 10% 'cut away' at the high energy tail of the transmission curve. Nevertheless even without this correction, the measured bin shape agrees well with ion optical simulations (Figure 3.8) of the prototype geometry, which is designed with wider energy bins (ΔE/E~0.7) than the proposed flight geometry(ΔE/E~0.5).

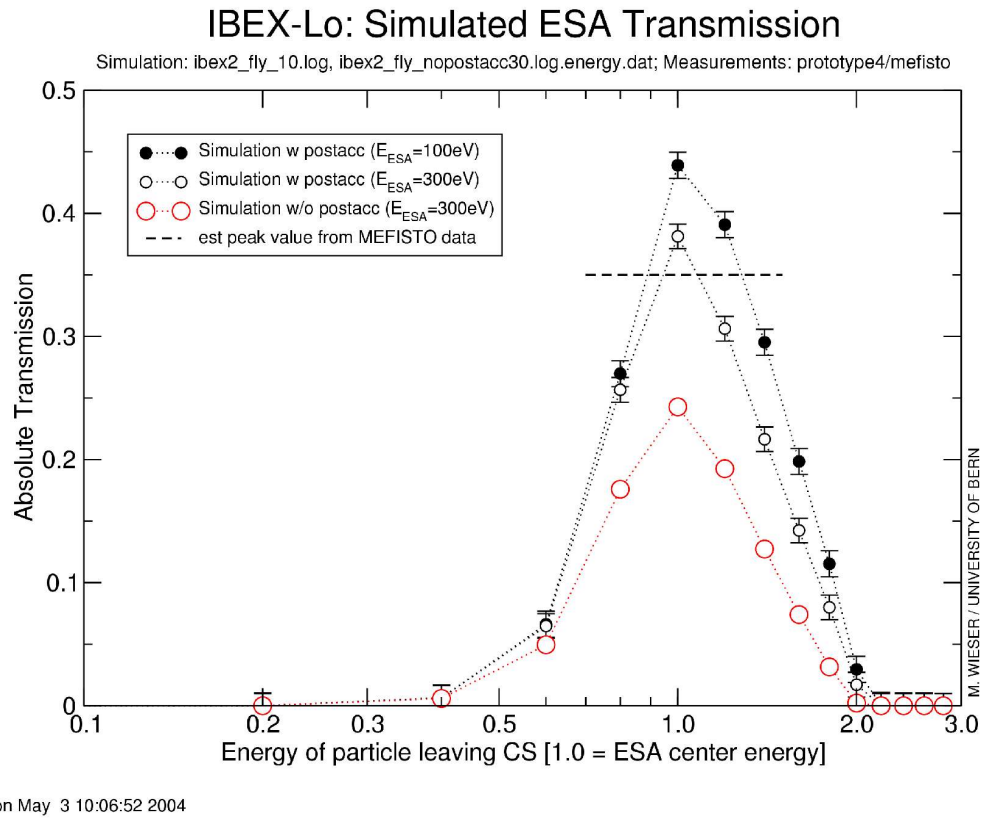

Figure 3.8

Note that none of the curves shown in Figure 3.8 represent the exact situation in the MEFISTO test setup. The horizontal dashed line shows the estimated peak value derived from MEFISTO Dataset B (used in Figures 3.3 to 3.7). A peak value of 0.35 is reasonable as the real post acceleration falls somewhere between cases with and without post acceleration. Also the bin shape compares well to the 5 measured bin shapes shown in Figure 3.7.

3.2.5 Secondary Electron Suppression

To suppress secondary electrons permanent magnets[3] were mounted in the electrodes that accelerate the particles into the ESA. The strength of the radial field varied from 30mT at the inner electrode to 6mT in the center of the gap to 17mT at the outer preaccelerator electrode. A comparison of the measured signal with and without magnets is shown in Figures 3.9 to 3.11 for energy bins 1, 2 and 3:

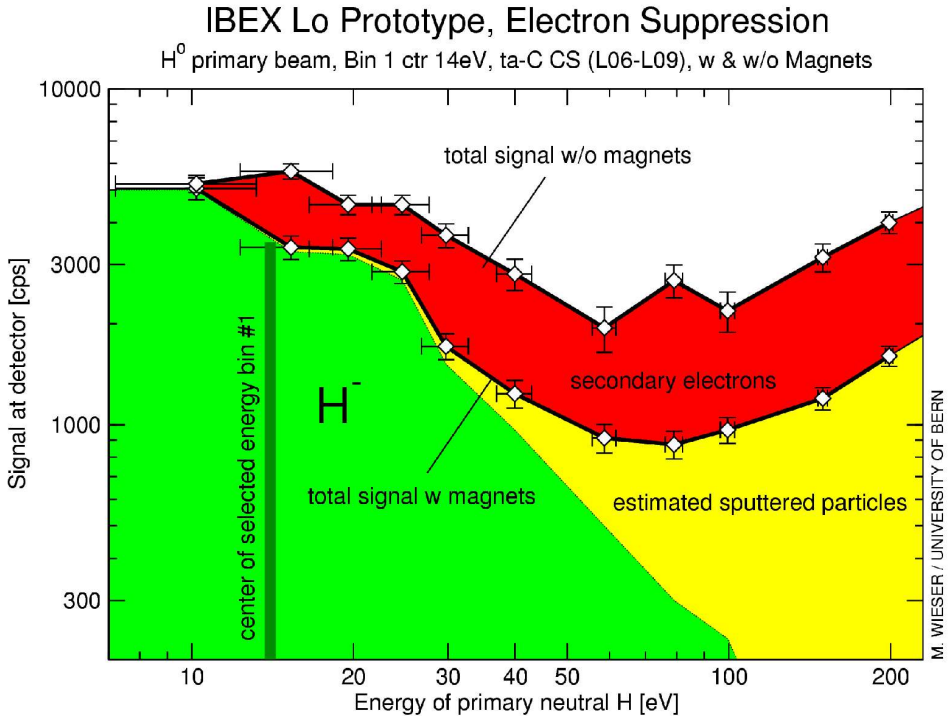

Figure 3.9

[3] Off the shelf AlNiCo rods of 6mm diameter with axial magnetization were cut in 5 and 10mm long pieces which were the glued in suitable holes in the electrodes in question.

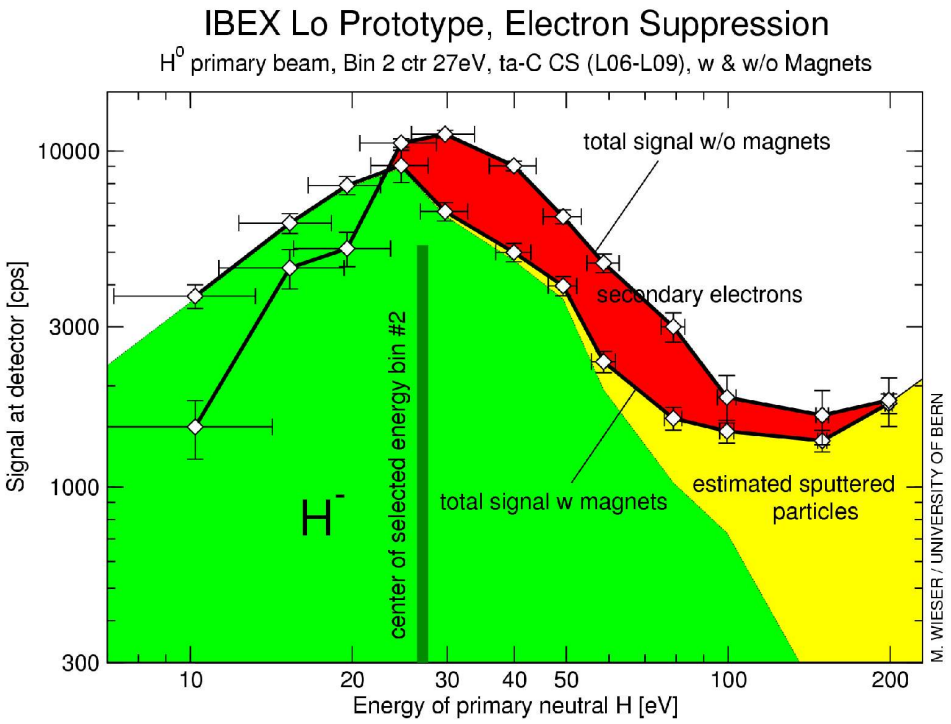

Figure 3.10

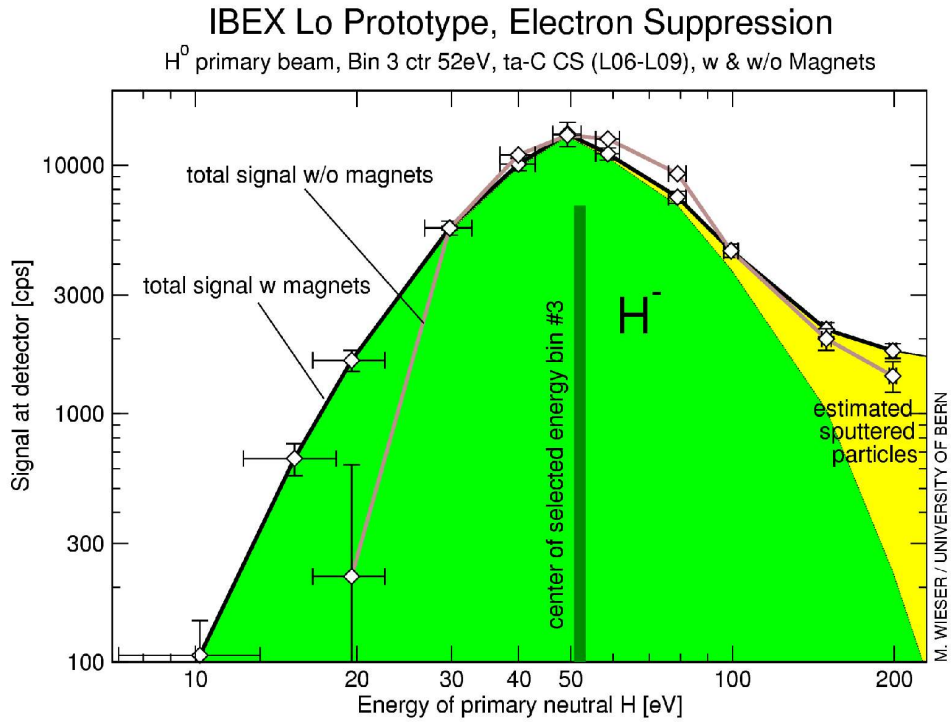

Figure 3.11

In energy bin #1 up to 60% of the signal at energies above the center energy consisted of electrons and could be removed. The actual electron suppression factor is much higher, but as the detector used does not provide mass resolution its exact value could not be determined. Time-of-Flight measurements would be needed to get the electron suppression factor.

In bin #2 (Figure 3.10) the suppression is less dominant as the secondary electron distribution created from impinging neutral particles on the CS and from other sources[4] peaks at a few eV and only its high energy tail is visible in bin #2 centered at 27eV.

In bin #3 (Figure 3.11) no effect of the magnets can be seen as expected.

In Figure 3.10 and Figure 3.11 both signal peaks measured without the magnets appear to be steeper on the low energy side of the center energy of the bin. This is an artifact; when considering the error bars (one sigma) the difference is not significant and both curves are identical below the center energy of the bin.

Sputtered particles were estimated from the shape of bin #1 and subtracted as shown in yellow in Figure 3.9 to 3.11.

[4] The main other source in the chamber were the collimator plates in front of the beam neutralizer where a 3keV beam > 1nA hits collector plates used for beam diagnostics.

3.3 Results for Oxygen

3.3.1 Energy Loss Model

Data analysis showed that the simple energy loss model for hydrogen (15% loss upon a reflection from the CS, valid over a wide energy range) is not valid for oxygen. Furthermore, the width of the energy distribution after scattering is not proportional to the primary energy below 300eV, but much larger. Figure 3.12 depicts an estimate of the mean energy loss expressed as fraction of the incident particle energy. Black points represent data obtained from scattering neutral and positive oxygen atoms off a MgO surface (data taken at the University of Osnabrück)[5]. The gray area represents the uncertainty of the data points obtained from IBEX prototype measurements.

To analyze all oxygen data the following simple empirical loss model was used:

$$E = E0 * (0.72 - 0.075*\ln(E0))$$

with:

E0: incident energy in eV
E: mean energy after scattering in eV

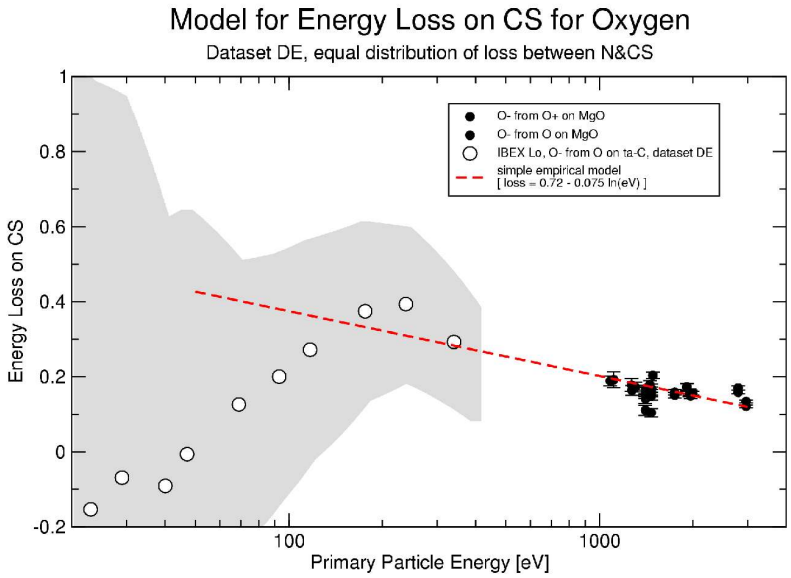

Figure 3.12

Corresponding bin center energies for oxygen and hydrogen as derived from the calibrations are shown in Table 3.1. Since the energy loss upon scattering

[5] Wieser M., P. Wurz, K. Büning and W. Heiland, Scattering of atoms and molecules off a magnesium oxide surface, *NIMB, 192 (4), 370-380 (2002)*

off the CS is larger for oxygen the energy bins are shifted to higher primary particle energies.

IBEX Lo Bin	*Center energy for hydrogen [eV]*	*Center energy for oxygen [eV]*
1	14	23
2	27	41
3	52	73
4	102	134
5	197	242
6	403	no IBEX proto data
7	780	no IBEX proto data
8	1500	no IBEX proto data

Table 3.1

3.3.2 Ionization Efficiency and Transmission

The figures below show ionization efficiency times transmission without (Fig. 3.13) and with secondary electron suppression magnets (Fig. 3.14). Unfortunately, the energy bins below 100eV are contaminated by sputtering cause by primary particles of higher energy. Since the oxygen atoms are heavier than the hydrogen atoms they cause considerable amounts of sputtering (which has already been observed with the NICE prototype) and these sputtered atoms from the CS can only be distinguished from the truly converted oxygen atoms with the help of a mass analyser. Most of the sputtered negative ions are carbon and hydrogen (see NICE prototype) after the CS is sufficiently clean.

The magnets prove to be effective also for secondary electron suppression caused by primary oxygen atoms. Considerable signal suppression between 10eV and 100eV is visible in Figure 3.14 compared to Figure 3.13. The signal in bin #1 and #2 of Figure 3.13 is to a large part due to secondary electrons causing a widening of the bins toward lower energies (comp. Fig. 3.13 and 3.14)

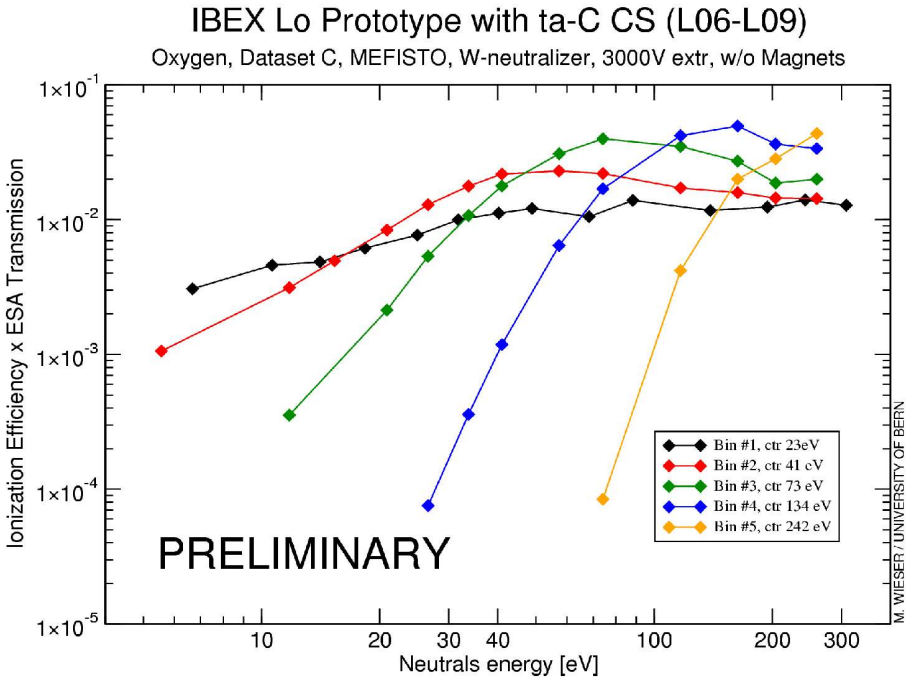

Figure 3.13

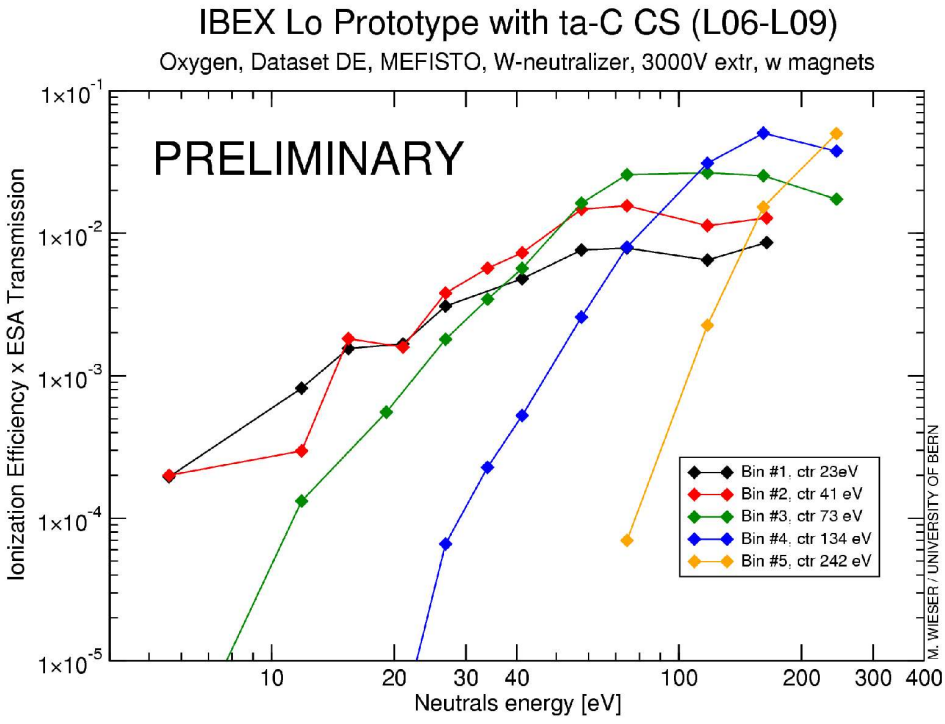

Figure 3.14

The signal drop below 100eV in Figure 3.14 is due to the drop in ionization efficiency of the CS. Data from the NICE prototype depict a drop of ionization efficiency for CVD diamond of one order of magnitude when reducing the primary energy from 100eV down to 20eV. This is compatible with the findings shown in Figure 3.14.

3.3.3 Energy Bin Shape

The energy bin shapes for oxygen shown in Figure 3.15 are much wider than what was obtained for hydrogen (Fig. 3.7). This is due to the contamination with sputtered particles and due to more energy spread for oxygen particles at the CS at low energies.

The effect of heating the CS to ~100°C for more than 24h on the shape of energy bin #3 for oxygen is shown in Figure 3.16. No significant difference depending on CS or beam neutralizer temperature could be found. The properties of the ta-C DLC conversion surface did not change in the temperature range between -20°C and +100°C.

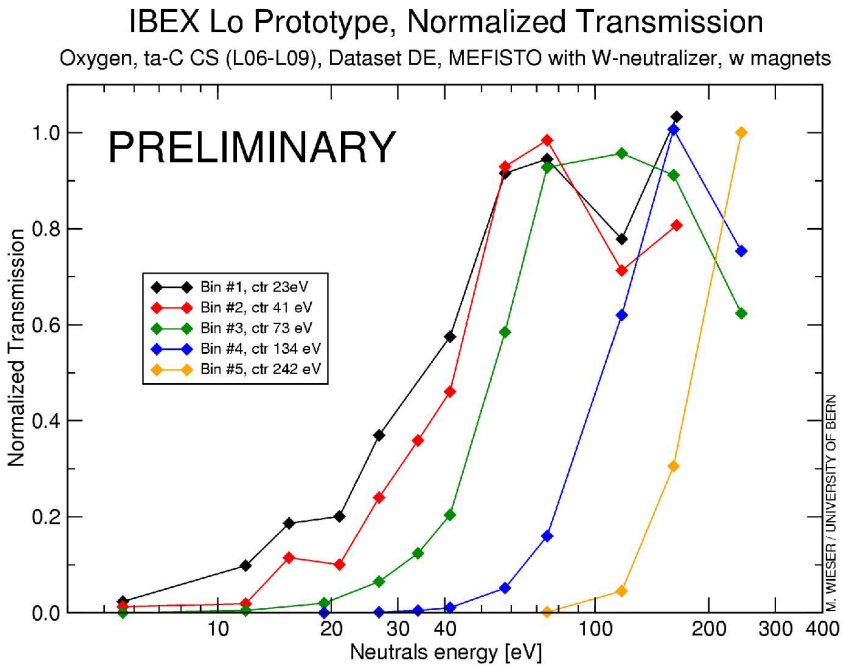

Figure 3.15

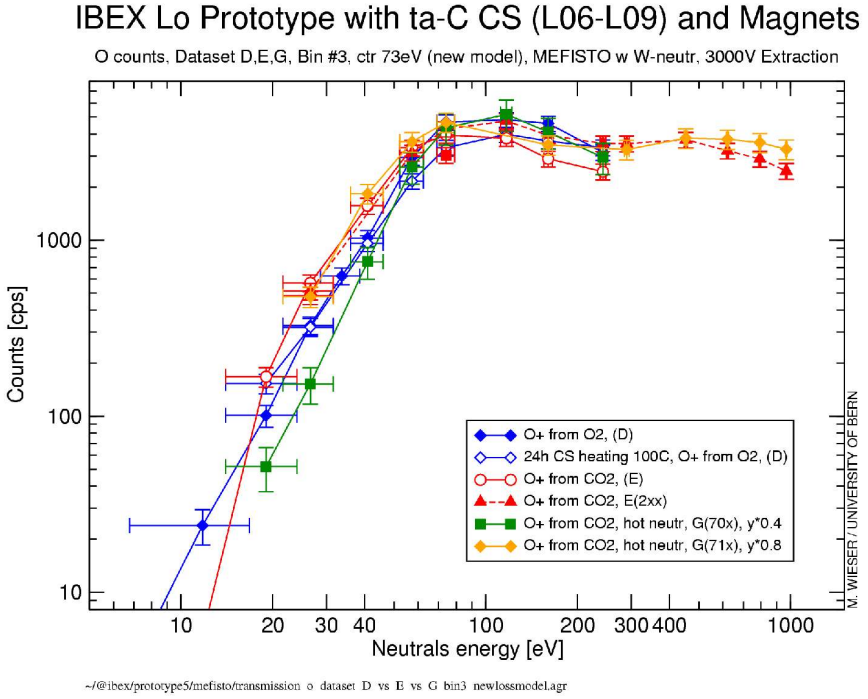

Figure 3.16

4 Outlook

The following measurements remain work in progress:

1. Response of energy bins #6 through #8 for both oxygen and hydrogen. This requires a detector that can be floated to at least 10kV above ground potential. For this, the optically coupled CEM detector will be used once replacement laser diodes, already received, can be installed. As a precaution to protect the diode, the CEM detector will not be operated below 10°C. Successful combination of data taken with the Quantar and CEM detectors has already been demonstrated using positive ions in the CASYMS chamber.

2. More detailed measurements are needed to better understand the energy distribution of scattered oxygen particles.

5 Summary

The detection efficiency of the prototype fitted with a ta-C DLC conversion surface for neutral hydrogen and oxygen was measured in energy bins #1 through #5 and found to be in good agreement with ion-optical simulations and theoretical predictions regarding particle scattering. The energy resolution of the system is close to that predicted by simulations. ta-C DLC conversion surfaces perform better in terms of ionization efficiency and angular scattering than any other practical CS candidate tested to date. Adequate scattered particle rejection has been demonstrated by implementing blackened surfaces and fins.

Neutral oxygen as primary particles requires a different energy loss model than neutral hydrogen. The energy losses when scattering oxygen atoms result in a shift of the nominal bin center energy towards higher values

Suppression of secondary electrons with static magnetic fields in the ion acceleration region proved to be successful in keeping them from reaching the detector. At the same time, the transmission for negative ions, even at the lowest energies of interest, is not measurably affected by these magnets.

Suppression of sputtered negative ions is not possible. These ions have to be identified by the TOF mass spectrometer. This needs a TOF section which can distinguish C (sputtered from ta-C) from O (truly converted). Thus, the post-acceleration of 20kV and thin carbon foils (1.5 $\mu g/cm^2$) are needed. The former is also necessary for maintaining the high ion-optical transmission at the highest primary particle energies.

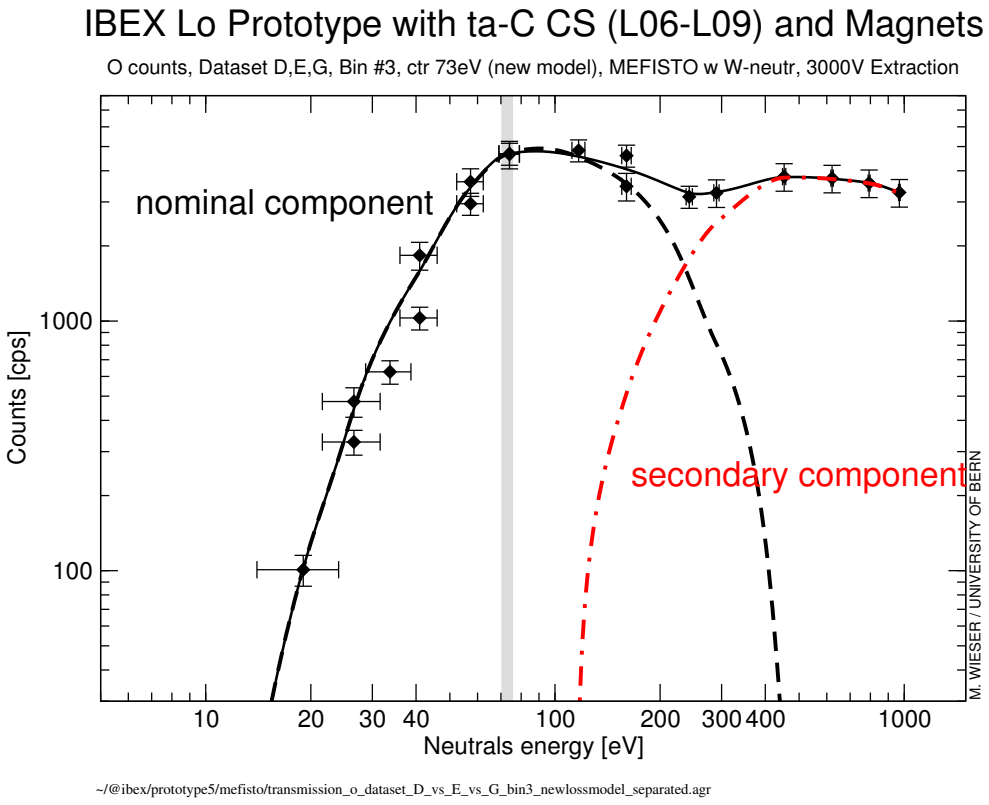

Figure 7.15: Response of the prototype to incident neutral oxygen with electrode potentials set to energy bin #3. The expected response is shown as a dashed black line. A additional secondary component was observed shown as red dotdashed line.

7.2.8 Prototype Response to Neutral Oxygen

As shown in the report reprinted in Section 7.2.7, the response of the instrument to neutral oxygen did not reproduce the energy bins as it did for incident neutral hydrogen. Figure 7.15 depicts an attempt to separate a nominal part from an additional secondary component. No mass resolution was available with the detector used thus the composition of the secondary component is not well known.

Several explanations for the secondary component were proposed:

1. Sputtering of oxygen, carbon, and hydrogen at the CS
2. Scattering and ionization of neutral atoms at the ESA and/or pre-acceleration electrodes
3. Secondary electrons generated further inside the ion-optics than the suppression magnets.

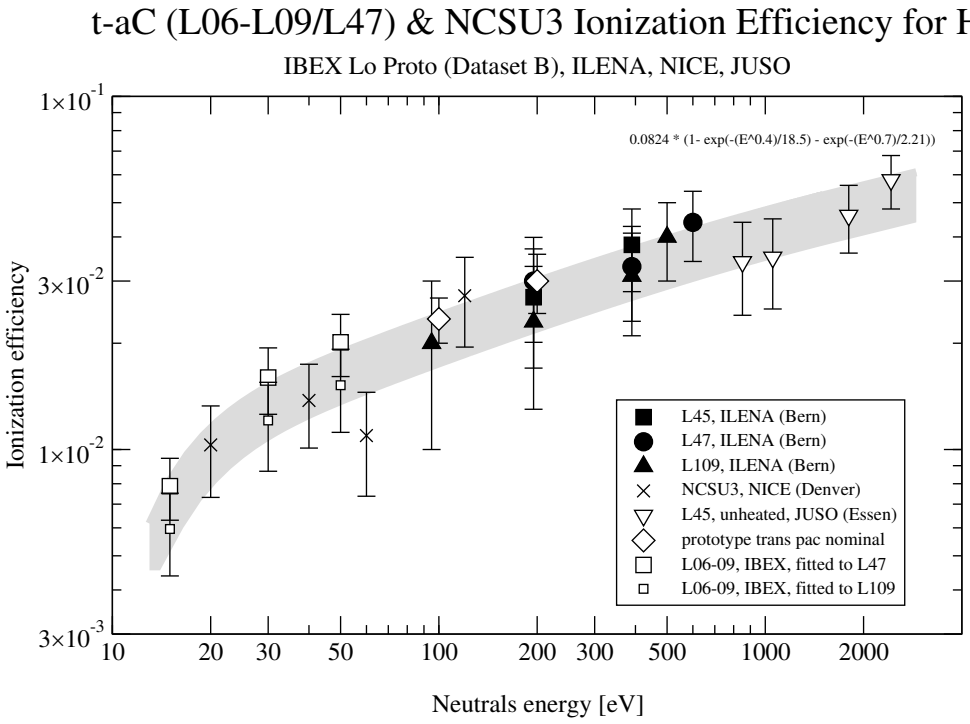

Figure 7.16: Compilation of negative ion yield from hydrogen for various CVD diamond surfaces at incidence angles between 5° and 15°. Data from four different experiments were combined. The gray area represents a fit shown to guide the eye.

Explanation 1 is supported by data from the NICE prototype, however mass resolved data is only available up to 300 eV compared to 1000 eV for the IBEX-Lo prototype data; explanation 2 will be addressed by blackening all remaining electrodes inside the prototype; and explanation 3 was ruled out by simulations, secondary electrons generated at the electrodes beyond the suppression magnets will splat at the inner ESA electrode. Further measurements with the prototype will allow to resolve this issue.

7.2.9 Ionization Efficiencies of Different CVD Diamond Surfaces

Experiments preceeding the IBEX-Lo prototype did also provide data about the negative ionization yield of CVD diamond surfaces for incident hydrogen. Figure 7.16 depicts a compilation of available data obtained from ILENA and JUSO experiments as well as NICE and IBEX-Lo prototypes. Although the data shown were obtained from different CVD diamond surfaces that were quite differently preparated, the values agree very well.

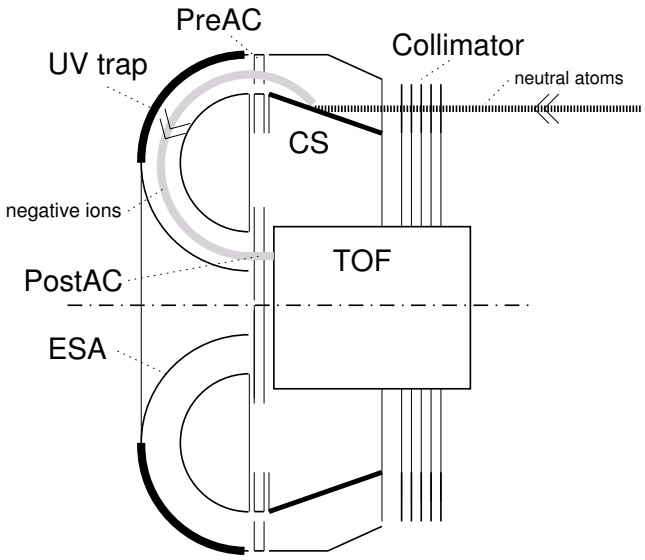

Figure 7.17: Ion-optical functional blocks of a flight like IBEX-Lo sensor design. The main differences to the prototype design are the flip of the CS to point outwards and the introduction of a ring-shaped TOF interface area. PreAC and PostAC indicate the pre-acceleration and post-acceleration sections respectively.

7.3 Flight Sensor Geometry

Parallel to tests with the prototype, a flight version of the IBEX-Lo sensor was developed. Major modifications to the prototype version were, as shown in Figure 7.17, the reorientation of the CS to pointing outwards and the replacement of the circular exit area of the ESA by a ring shaped area. The reorientation of the CS was done to get better UV suppression and also to maintain the ESA deflection radius when switching to a ring shaped interface to the TOF section. Better UV suppression is also obtained trough the added UV trap, i.e., the fins. Figure 7.18 shows a 3D-rendering of a flight like design, formally named AJ14, of the CS and ESA sections of the sensor as generated from geometry information used in SIMION. The collimator is not included in this image. The TOF is symbolized by the large yellow cylinder in the center with the circular entry aperture shown in a darker yellow.

Transmission and energy resolution were actively optimized using the ion-optics optimizer software. As for the design of the prototype, only negative ions starting at the CS were considered in the evaluation of the objective function. Negative ions started from the CS with realistic angular scattering profiles as obtained from scattering measurements from ta-C DLC surfaces in the ILENA experiment. To prevent the loss of energy resolution while increasing the overall transmission the particle population was split into three groups, with 45 eV, 100 eV, and 170 eV energy when starting at the CS. While particles from the 100 eV group that made it to the TOF interface improved the value of the objective function, particles from the two other groups with energies at the CS that are outside the band of transmission resulted in a penalty to the objective function as soon as they reached the TOF interface (Figure 7.19). The

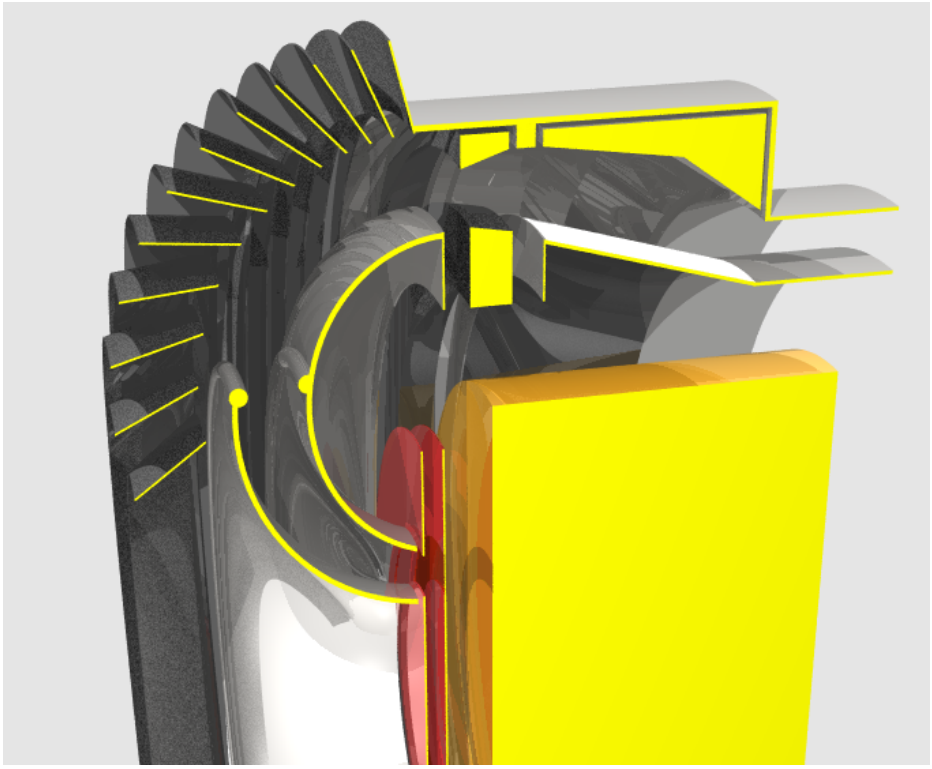

Figure 7.18: 3D-rendering of the ion-optics of the flight like IBEX-Lo sensor design AJ14. Neutral particles enter the system from the right through a collimator (not shown) and hit the conversion surface (white) where they are converted to negative ions. After energy analysis they pass through two shaping electrodes (shown in red) and enter the TOF section (yellow in the center). The fins act as neutral particle and UV trap.

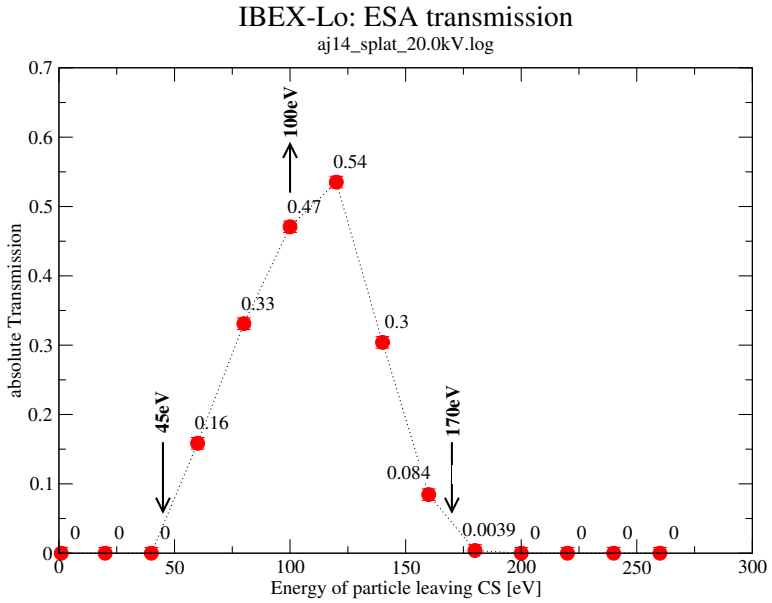

Figure 7.19: Energy resolution of design variant AJ14. Black arrows indicate where the ion-optics optimizer tries to 'pull' on the curve: particles reaching the TOF interface that started with 100 eV at the CS have a positive influence (upward pointing arrow) while particles reaching the TOF interface that started with 45 eV or 170 eV result in a penalty (downward pointing arrows) on the objective function.

angular spread of the trajectories at the TOF interface was monitored but not included into the objective function as it decreased anyway.

Several standard data products are routinely generated during the optimization. The energy resolution of the AJ14 design is shown in Figure 7.19. For simulation purposes the center energy of the ESA is nominally set to 100 eV, this corresponds approximately to energy bin number 4 (see Table 7.1). A shift of the peak of the pass band vom 100 eV towards higher energies can be observed. This is no problem as the electrode potentials will be rescaled anyway to fit the sensor's eight energy bins. Figure 7.20 depicts the transmission depending on where on the CS a neutral particle was negatively ionized. As expected, particles hitting the CS closer to the pre-acceleration section are more likely transmitted to the exit of the ESA. The angular scattering of ions reaching the TOF interface area is shown in Figure 7.21. The plot shows a histogram of the angles relative to the normal of the entry aperture. Low angles are important for particles not to be lost inside the TOF section. For the data shown the TOF was set to a potential of 20 kV relative to the CS.

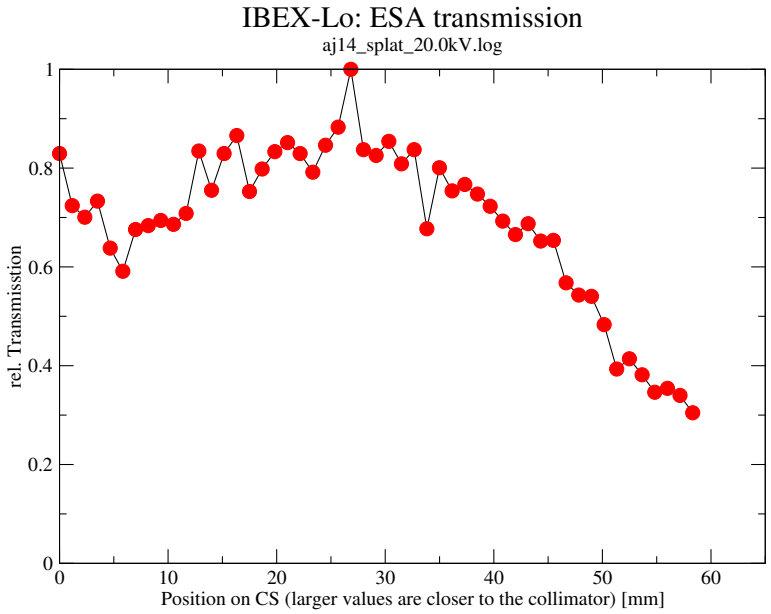

Figure 7.20: Transmission of flight like design variant AJ14 as a function of the position where a neutral particle was ionized at the CS.

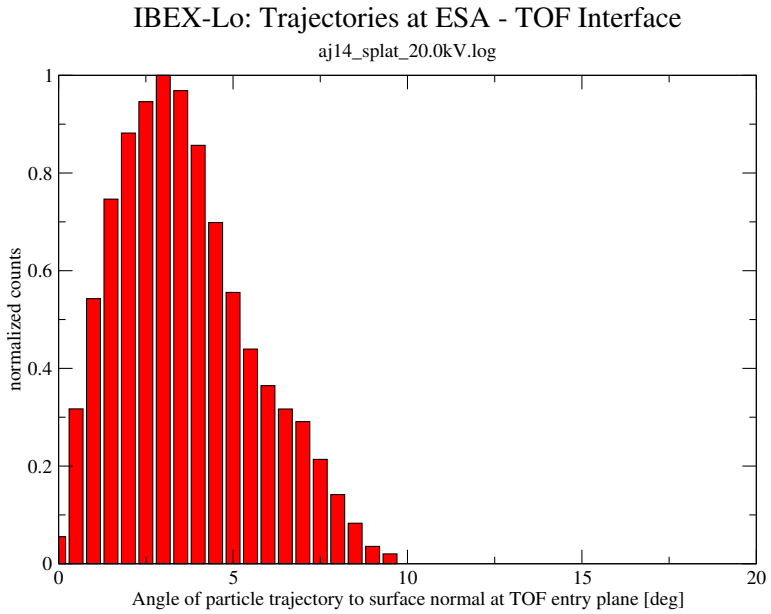

Figure 7.21: Histogram of the angles of the particle trajectories to the surface normal of the TOF interface plane.

7.4 Outlook

Most design related questions could be addressed by the prototype and by the further development of the flight like design up to the version AJ14. Some issues, however, still need to be solved, among them the influence of field penetration from the collimator's charged particle rejection system into the CS section. This is an issue mainly at the lower end of the IBEX-Lo energy range. More modeling will be done to fully understand the influence of these fields. Another not yet addressed problem is the division of the circular opening of the sensor in a 270° wide section with a $7^\circ \times 7^\circ$ FOV and a 90° sector with a $2^\circ \times 2^\circ$ FOV. Although the limitation of the FOV is done in the collimator and thus beyond the scope of the ion-optical design shown in the previous chapter, an effective way to suppress particles entering the wide angle FOV area when doing measurements with the narrow angle FOV is needed. In the current design the CS will be floated to a positive high voltage in the 270° sector in this case. Field termination plates will be needed to prevent a distortion of the potentials in the active narrow FOV sector. The shape and making of these terminators is still to be defined. Ideally they should reproduce the potentials very closely, not draw any current and also not cause any scattering of particles into the ESA section.

At the time of writing, about one and a half months of optimization time are remaining prior an ion-optical design freeze. Although the ion-optical design variant AJ14 is already very mature, further performance improvements of the sensor are expected until then.

Bibliography

Balogh, A., Bird, M., Blomberg, L., Bochsler, P., Bougeret, J.-L., Brückner, J., Iess, L., Guest, J., Langevin, Y., Milani, A., Sauvaud, J.-A., Schmidt, W., Sphon, T., von Steiger, R., Thomas, N., Torkar, K., Wänke, H. & Wurz, P. (2000), BepiColombo, A Interdisciplinary Cornerstone Mission to the Planet Mercury, Technical report, ESA-SCI(2000)1.

Barabash, S., Lundin, R., Andersson, H., Gimholt, J., Holström, M., Norberg, O., Yamauchi, M., Asamura, K., Coates, A., Linder, D., Kataria, D., Curtis, C., Hsieh, K., Sandel, B., Fedorov, A., Grigoriev, A., Budnik, E., Grande, M., Carter, M., Reading, D., Koskinen, H., Kallio, E., Riihela, P., Säles, T., Kozyra, J., Krupp, N., Livi, S., Woch, J., Luhmann, J., McKenna-Lawlor, S., Orsini, S., Cerrulli-Irelli, R., Mura, A., Milillo, A., Roelof, E., Williams, D., Sauvaud, J.-A., Thocaven, J.-J., Winningham, D., Frahm, R., Scherer, J., Sharber, J., Wurz, P. & Bochsler, P. (2004), 'The Analyzer of Space Plasmas and Energetic Atoms (ASPERA-3) for the Mars Express Mission', *ESA-SP 1240* pp. 121–139.

Benninghoven, A., Rüdenauer, F. G. & Werner, H. W. (1987), *Secondary Ion Mass Spectrometry*, Vol. 86 of *Chemical analysis*, Wiley, New York.

Berghen, F. V. (2004), Constrained, non-linear, derivative-free, parallel optimization of continuous, high computing load, noisy objective functions., PhD thesis, Université Libre de Bruxelles.

Burns, G., Daoud, R. & Vaigl, J. (1994), LAM: An Open Cluster Environment for MPI, *in* 'Proceedings of Supercomputing Symposium', pp. 379–386.
URL: *http://www.lam-mpi.org/download/files/lam-papers.tar.gz*

Collini Flühmann (n.d.), *Schering Rapid, CuS blackening*, Galv. Anstalt, Ringstrasse 9, Postfach 630, 8600 Dübendorf, Switzerland.
URL: *http://www.collini.ch/*

Fahr, H.-J. (2004), 'Global structure of the heliosphere and interaction with the local interstellar medium: three decades of growing knowledge', *Adv. Space Research* **34**, 3–13.

Fedorov, A. (2003), *TRACE*, Centre d'Etude Spatiale des Rayonnements, 9, avenue du Colonel ROCHE, 31028 TOULOUSE Cedex 4. Version 7.0.

Fox, B. & Ramey, C. (2002), *The GNU Bourne-Again SHell*. GNU bash, version 2.05.
URL: *http://www.gnu.org/software/bash/bash.html*

Ghielmetti, A. G., Balsiger, H., Bänninger, R., Eberhardt, P., Geiss, J. & Young, D. T. (1983), 'Calibration system for satellite and rocket-borne ion mass spectrometers in the energy range from 5 eV/q to 100 keV/q', *Rev. Sci. Instrum.* **54**, 425–436.

Ghielmetti, A. G. & Shelley, E. G. (1990), 'Angle, energy, and time-of-flight focusing with poloidal toroid electrostatic analyzers', *Nucl. Instr. and Meth.* **A298**, 181–188.

Ghielmetti, A. G., Shelley, E. G., Fuselier, S., Wurz, P., Bochsler, P., Herrero, F., Smith, M. F. & Stephen, T. (1994), 'Mass spectrograph for imaging low energy neutral atoms', *Opt. Eng.* **33**, 362–369.

Gruntman, M., Roelof, E., Mitchell, D., Fahr, H., Funsten, H. & McComas, D. (2001), 'Energetic neutral atom imaging of the heliospheric boundary region', *J. Geophys. Res.* **106**(A8), 15767–15781.

ISO (1997), *The Virtual Reality Modeling Language*, ISO/IEC 14772-1:1997 edn.
URL: *http://www.web3d.org/x3d/specifications/vrml/ISO-IEC-14772-IS-VRML97WithAmendment1/*

Jans, S. (1999), Ionization of Energetic Neutral Atoms for Application in Space Instrumentation, Master's thesis, University of Bern, Switzerland.

Jans, S., Wurz, P., Schletti, R., Brüning, K., Sekar, K., Heiland, W., Quinn, J. & Leuchter, R. (2001), 'Negative ion production by surface ionization at barium zirconate surface', *Nucl. Instr. Meth. B* **173**, 503–515.

Kazama, Y. & Barabash, S. (2003), Quick report on the design of the ENA instrument, Technical report, Swedish Institute of Space Physics.

Kennedy, J., & Eberhart, R. (1995), Particle swarm optimization, *in* 'Proceedings of the 1995 IEEE International Conference on Neural Networks (Perth, Australia)', IEEE Service Center, Piscataway, NJ, pp. 1942–1948.

Linsky, J. L. & Wood, B. E. (1996), 'The alpha Centauri Line of Sight: D/H Ratio, Physical Properties of Local Interstellar Gas, and Measurement of Heated Hydrogen (The 'Hydrogen Wall') Near the Heliopause', *Astrophysical Journal* **463**, 254.

Losch, A. & Niehus, H. (1999), 'Structure analysis of the KBr(100) surface - An investigation with a new method for surface analysis on insulators', *Surf. Sci* **420**, 148–156.

Lukka, T. J. & Stewart, J. (1998-2005), *FreeWRL, a VRML and X3D browser*.
URL: *http://freewrl.sourceforge.net/*

Marti, A., Schletti, R., Wurz, P. & Bochsler, P. (2001), 'New Calibration Facility for Solar Wind Plasma Instrumentation', *Rev. Sci. Instr.* **72**(2), 1354–1360.

McComas, D. J., Allegrini, F., Bochsler, P., Bzowski, M., Collier, M., Fahr, H., Fichtner, H., Frisch, P., Funsten, H., Fuselier, S., Gloeckler, G., Gruntman, M., Izmodenov, V., Knappenberger, P., Lee, M., Livi, S., Mitchell, D., Möbius, E., Moore, T., Reisenfeld, D., Roelof, E., Schwadron, N., Wieser, M., Witte, M., Wurz, P. & Zank, G. (2003), 'Interstellar Boundary Explorer', NASA SMEX AO 03-0SS-02.

McComas, D. J., Allegrini, F., Bochsler, P., Bzowski, M., Collier, M., Fahr, H., Fichtner, H., Frisch, P., Funsten, H., Fuselier, S., Gloeckler, G., Gruntman, M., Izmodenov, V., Knappenberger, P., Lee, M., Livi, S., Mitchell, D., Möbius, E., Moore, T., Reisenfeld, D., Roelof, E., Schwadron, N., Wieser, M., Witte, M., Wurz, P. & Zank, G. (2004), The Interstellar Boundary Explorer (IBEX), *in* V. Florinski, N. Pogorelov & G. Zank, eds, 'Physics of the Outer Heliosphere: Third International IGPP Conference', AIP Conference Proceedings 719, pp. 162–181.

Moestue, H. (1973), 'The field and geometrical factor of an annular curved plate electrostatic analyzer', *Rev. Sci. Instr.* **44**(12).

Moore, T., Chornay, D., Collier, M., Herrero, F., Johnson, J., Johnson, M., Keller, J., Laudadio, J., Lobell, J., Ogilvie, K., Rozmarynowski, P., Fuselier, S., Ghielmetti, A. G., Hertzberg, E., Hamilton, D., Lundgren, R., Wilson, P., Walpole, P., Stephen, T., Peko, B., van Zyl, B., Wurz, P., Quinn, J. & .R.Wilson, G. (2000), 'The Low-Energy Neutral Atom Imager for IMAGE', *Space Sci. Rev.* **91**, 155–195.

Möbius, E., Granoff, M., Couture, E., Karrer, R., Wieser, M. & Hertzberg, E. (2004), IBEX-lo Collimator Prototype, Design Concept Verification at UNH & Testing in Bern, Status Report, Technical Report 1, University of New Hampshire, University of Bern, and Lockheed Martin Advanced Technology Lab.

Nelder, J. & Mead, R. (1965), 'A Simplex Method for Function Minimization', *Comp. J.* **7**, 308–313.

Nier, A. O. (1940), 'A Mass Spectrometer for Routine Isotope Abundance Measurements', *Rev. Sci. Instr.* **11**(7), 212–216.

Peko, B. L. & Stephen, T. M. (2000), 'Absolute detection efficiencies of low energy H, H^-, H^+, H_2^+, and H_3^+ incident on an multichannel plate detector', *Nucl. Instr. Meth. B* **171**, 597–604.

Pesses, M. E., Eichler, D. & Jokippi, J. R. (1981), 'Cosmic ray drift, shock wave acceleration, and the anomalous component of cosmic rays', *Astrophysical Journal, Part 2 - Letters to the Editor* **246**, L85–L88.

Petitet, A., Whaley, R. C., Dongarra, J. & Cleary, A. (2004), *HPL - A Portable Implementation of the High-Performance Linpack Benchmark for Distributed-Memory Computers*, Innovative Computing Laboratory, University of Tennessee, Suite 413 Claxton, 1122 Volunteer Blvd, Knoxville TN 37996-3450, USA. HPL Version 1.0a.
URL: *http://www.netlib.org/benchmark/hpl/*

Research Systems, Inc. (2001), 4990 Pearl East Circle, Boulder, CO 80301, USA. Verion 5.5.
URL: *http://www.rsinc.com*

Rew, R., Davis, G., Emmerson, S. & Davies, H. (1997), *NetCDF User's Guide for C, An Interface for Data Access, Version 3*, University Corporation for Atmospheric Research/Unidata, P.O. Box 3000, Boulder, CO 80307-3000, USA.
URL: *http://my.unidata.ucar.edu/content/software/netcdf*

Rühl, A. (2004), GICLU PM - Gibb Cluster Performance Monitor, Abschlussarbeit für Informatiker (IPA), Technical report, Gewerblich-industrielle Berufsschule Bern. in German.

Scheer, J., Wieser, M., Wurz, P., Bochsler, P., Hertzberg, E., Fuselier, S., Koeck, F., Nemanich, R. & Schleberger, M. (2005), 'High negative ion yield from light molecule scattering', *Nucl. Instr. Meth. B* p. in press.

Schletti, R. (1996), Anwendung der Oberflächenionisation in Raumforschungsexperimenten, Master's thesis, University of Bern, Switzerland. in German.

Squyres, J. & Lumsdaine, A. (2003), A Component Architecture for LAM/MPI, *in* 'Proceedings, 10th European PVM/MPI Users' Group Meeting', number Lecture Notes in Computer Science *in* '2840', Springer-Verlag, Venice, Italy, pp. 379–387.

Stephen, T. M. & Pecko, B. L. (1998), 'Absolute calibration of a multichannel plate detector for low energy O, O^-, and O^+', *Rev. Sci. Instrum.* **71**(3), 1355–1359.

Stephen, T., van Zyl, B. & Amme, R. (1996), 'Generation of a Fast Atomic-Oxygen Beam from O^- Ions by Resonant Cavity Radiation', *Rev. Sci. Instrum.* **67**, 1478–1482.

Thomas, G. E. (1978), 'The insterstellar wind and its influence on the interplanetary environment', *Ann. Rev. Earth Planet* **6**, 173–204.

Wall, L. (2003), *perl, Practical Extraction and Report Language*. Version 5.8.
URL: *http://perl.org*

Wieser, M. (2001), Experimental Work for the Direct Measurement of Interstellar Neutral Gas, Master's thesis, University of Bern, Switzerland.
URL: *http://www.iapetus.ch/doc/diploma/*

Wieser, M., Wurz, P., Brüning, K. & Heiland, W. (2002), 'Scattering of atoms and molecules off a magnesium oxide surface', *Nucl. Instr. Meth. B* **192**, 370–380.

Wieser, M., Wurz, P., Nemanich, R. & Fuselier, S. A. (2005), 'Secondary electron emission of chemical vapor deposited diamond by impact of slow H^+, D^+, H_2^+, C^+, O^+, and O_2^+ ions', *J. Appl. Phys.* **submitted**.

Witte, M., Banaszkiewicz, M., Rosenbauer, H. & McMullin, D. (2004), 'Kinetic parameters of interstellar neutral helium: updated results from the ULYSSES/GAS-instrument', *Adv. Space Research* **34**, 61–65.

Witte, M., Rosenbauer, H., Keppler, E., Fahr, H., Hemmerich, P., Lauche, H., Loidl, A. & Zwick, R. (1992), 'The interstellar neutral-gas experiment on ULYSSES', *Astronomy and Astrophysics* **92**, 333–348.

Wurz, P. (2000), *The outer Heliosphere: Beyond the Planets*, Copernicus Gesellschaft e.V., chapter Detection of Energetic Neutral Particles.

Wurz, P., Aellig, M., Bochsler, P., Ghielmetti, A. G., Shelley, E. G., Fuselier, S. A., Herrero, F., Smith, M. F. & Stephen, T. S. (1995), 'Neutral atom imaging mass spectrograph', *Opt. Eng.* **34**(8), 2365–2376.

Wurz, P., Bochsler, P., Ghielmetti, A. G., Shelley, E. G., Herrero, F. & Smith, M. F. (1993), Concept for the HI-LITE neutral atom imaging instrument, *in* P. Varga & G. Betz, eds, 'Proceedings of the Symposium on Surface Science', Kaprun, Austria, pp. 255–230.

Wurz, P., Schletti, R. & Aellig, M. R. (1997), 'Hydrogen and oxygen ion production by surface ionization using diamond surfaces', *Surf. Sci.* **373**, 56–66.

Zank, G. P. & Pauls, H. L. (1996), 'Modelling the Heliosphere', *Space Sci. Rev.* **78**, 95–106.

List of Figures

List of Tables

List of Publications

1. M. Wieser, P. Wurz, K. Büning and W. Heiland, **Scattering of atoms and molecules off a magnesium oxide surface**, NIMB, 192 (4), 370-380 (2002)

2. M. Wieser, P. Wurz, P. Bochsler, E. Moebius, J. Quinn, S.A. Fuselier, J.N. DeFazio, T.M. Stephen, **Direct mass spectrometric measurement of interstellar neutral gas**, Proceedings of the Week of Doctoral Students 2002, (ed. J. Safránková), Charles University, Prague, Czech Republic, 275-280 (2002)

3. D. McComas, F. Allegrini, P. Bochsler, M. Bzowski, M. Collier, H. Fahr, H. Fichtner, P. Frisch, H. Funsten, S.A. Fuselier, G. Gloeckler, M. Gruntman, V. Izmodenov, P. Knappenberger, M. Lee, S. Livi, D. Mitchell, E. Moebius, T. Moore, D. Reisenfeld, E. Roelof, N. Schwadron, M. Wieser, M. Witte, P. Wurz, and G. Zank, **The Interstellar Boundary Explorer (IBEX)**, AIP Conference Proceedings 719 (2004) 162-181.

4. M. Wieser, P. Wurz, R.J. Nemanich, and S.A. Fuselier, **Secondary electron emission of chemical vapor deposited diamond by impact of slow H+, D+, H2+, C+, O+, and O2+ ions**, J. Appl. Phys. (2005), submitted.

5. M. Wieser, P. Wurz, P. Bochsler, E. Moebius, J. Quinn, S.A. Fuselier, A. Ghielmetti, J.N. DeFazio, T.M. Stephen, and R.J. Nemanich, **NICE: an instrument for direct mass spectrometric measurement of interstellar neutral gas**, Meas. Sci. Technol., (2005), submitted.

6. M.Wieser and P. Wurz, **Production of a low energetic neutral particle beam using surface neutralization**, Meas. Sci. Technol., (2005), submitted.

7. J.A. Scheer, M. Wieser, P. Wurz, P. Bochsler, E. Hertzberg, S.A. Fuselier, R.J. Nemanich, and M. Schleberger, **High Negative Ion Yield from Light Molecule Scattering**, Nucl. Instr. Meth. B (2005), in press.

8. J.A. Scheer, M. Wieser, P. Wurz, P. Bochsler, E. Hertzberg, S.A. Fuselier, R.J. Nemanich, and M. Schleberger, **Conversion Surfaces for Neutral Particle Imaging Detectors**, Adv. in Space Res. (2005), submitted.

List of Acronyms

AC	Alternating Current
ACR	Anomalous Cosmic Ray
ADC	Analog Digital Converter
CS	Conversion Surface
CVD	Carbon Vapor Deposited diamond
DAC	Digital Analog Converter
DC	Direct Current
DLC	Diamond Like Charbon
ENA	Energetic Neutral Atom
ESA	Electro Static Analyzer
FOV	Field Of View
GPIB	General Purpose Interface Bus, IEEE Standard Digital Interface for Programmable Instrumentation, IEEE-488.1 and IEEE-488.2
IEEE	Institute of Electrical and Electronical Engineers
IBEX	Interstellar Boundary Explorer
ILENA	Imager for Low Energy Neutral Atoms
MCP	Micro Channel Plate (also Multi Channel Plate)
MPI	Message Passing Interface
NICE	Neutral Interstellar Composition Experiment
S/C	Spacecraft
SSD	Solid State Detector

ta-C tetrahedral amorphous Carbon

TOF Time Of Flight

TS Termination Shock

VRML Virtual Reality Modeling Language

Acknowledgments

I deeply indebted to Prof. Dr. Peter Wurz for giving me the fascinating opportunity to develop neutral particle mass spectrometers. I appreciated in particular the many fruitful discussions I have had in the course of this work. I enjoyed working in his team. I also appreciate the frequent possibilities to travel abroad for various projects.

I also thank:

- Prof. Dr. Peter Bochsler for his support
- Prof. Dr. Eberhard Möbius for refereeing this work
- Dr. Urs Rohner for his work with SIMION and ion-optics optimizer related issues
- Dr. Jürgen Scheer for discussions about surface science and other issues
- Dr. James Whitby for valuable discussions and proofreading of this thesis
- Joseph Fischer for his continuous support in the development of all the prototypes and experiments
- Kurt Bratschi for all the drawings and his never ending patience with all my modification requests
- Martin Sigrist, Martin Rieder, and Beat Zahnd from the engineering office for their support
- Jürg Jost, René Liniger, Jakob Stettler, and Martin Neuenschwander from the electronics workshop for their continuous support
- Harry Mischler, Sascha Häusler, Heinz Spycher and the whole mechanics workshop for help
- Hans Lüthi for the glass parts used in my experiments and late night emergency modifications of instrument prototypes
- Reto Karrer for the help with measurements in the MEFISTO calibration facility
- Adrian Etter for operating the CASYMS calibration facility

- Dr. Fritz Bühler, Dr. Ruth Ziethe, Andrea Opitz, and all the other people from our office for valuable discussions on various subjects
- Reto Sollberger for making it possible to work at the Gewerblich-Industrielle Berufsschule Bern at a very flexible schedule during this thesis and for his enthusiasm regarding the cluster computer
- Adrian Rühl for his work on the cluster management software
- Dominique Leuenberger, Samuel Knutti, Thomas Anderegg, and the IT-team at the Gewerblich-Industrielle Berufsschule Bern for their work and support with the cluster
- Florian Leuenberger for organizing many visits to the cinema

And last but not least I also thank my parents for their long-standing and continuous support.

Curriculum Vitae

Name:	Wieser
First name:	Martin
Date of birth:	January 1, 1970
Native place:	Hasle bei Burgdorf, BE, Switzerland

Degrees

1990	Diploma as Elektroniker, Bern
1994	Federal maturity certificate
2001	Master's thesis in physics at the Physikalisches Institut, Space Research and Planetary Sciences, University of Bern *Experimental Work for the Direct Measurement of Interstallar Neutral Gas*
2005	PhD thesis in physics at the Physikalisches Institut, Space Research and Planetary Sciences, University of Bern *Detection of Energetic Neutral Atoms and its Application to Heliospheric Science*

Education

-1986	Primary and secondary school, Hasle-Rüegsau
1986 - 1990	Apprenticeship as Elektroniker, Gfeller AG, Bern
1990 - 1994	AKAD - distance learning course for maturity certificate
1996 - 2001	Studies at the University of Bern in physics, mathematics, and earth science
1999 - 2001	Diploma student in physics, University of Bern
2001 - 2005	PhD student in physics, University of Bern

Professional and scientific experience

1990 - 1994	Development of hard- and software for telecommunication systems at Ascom Business Systems AG, Bern
1994 - 1997	Teacher in electronics, physics, mathematics, and related subjects at Gewerblich-industrielle Berufsschule Bern, GIBB
1997 - 2005	Management, design, implementation, and support of campus wide computer network infrastructure at GIBB
2003 -	Participating scientist for NASA's IBEX mission